Design-Oriented Prediction of Operational Shock and Vibration for Hard Disk Drives

NANYANG TECHNOLOGICAL UNIVERSITY

Design-Oriented Prediction of Operational Shock and Vibration for Hard Disk Drives

HENDRI HARMOKO

HENDRI HARMOKO

SCHOOL OF MECHANICAL AND AEROSPACE ENGINEERING

2009

2009

Design-Oriented Prediction of Operational Shock and Vibration for Hard Disk Drives

HENDRI HARMOKO

School of Mechanical and Aerospace Engineering

A thesis submitted to the Nanyang Technological University
in fulfillment of the requirement for the degree of
Doctor of Philosophy

2009

Dedication

To God for making everything possible

To my family for their love and support

Acknowledgements

The author would like to thank both his supervisors; A/P Yap Fook Fah and A/P Nader Vahdati for their time, energy, and effort in making this project a success. For all the advice, suggestions, and support, the author is sincerely grateful.

The author also wants to thank his fellow researchers, especially Dr. Liu Mengjun, Dr. Ao Hong Rui, A/P Stephen Lee, and the dedicated staff of the Centre for Mechanics of Micro-Systems (Mr. Cheo and Ms. Hali) for their help in one way or another in this project so far.

The author then would like to thank Seagate Technology International, especially Dr. Quock, Mr. Samuel Gan, Mr. Terang Thia, and Mr. Joseph Lau for their support in this project. For their ideas, concern, and their help in experimental work, the author is very grateful.

Last but not least, the author would like to thank God, his family, and friends who have helped him during the hard and difficult times in his research.

Table of Contents

List of Figures

List of Tables

List of Symbols

x_d	position of contacting points on the dimple
x_s	position of contacting points on the dimple on the slider
k_d	linearized contact stiffness between the slider and the dimple.
$f(x_d, x_s)$	contact force acting on the flexure
$\Delta_x, \Delta_y, \Delta_z$	bearing relative displacements
α_x, α_y	bearing angular displacements
$F_x^{(b)}, F_y^{(b)}, F_z^{(b)}$	bearing force
$M_x^{(b)}, M_y^{(b)}$	bearing moment
$\mathbf{K}^{(b)}$	5×5 bearing stiffness matrices
$\mathbf{C}^{(b)}$	5×5 bearing damping matrices
(m, n)	disk mode having m nodal circles and n nodal diameter
$\mathbf{M}$	mass matrix
$\mathbf{C}$	gyroscopic matrix
$\mathbf{C}_m$	damping matrix from rotating and stationary part
$\mathbf{K}$	stiffness matrix from rotating and stationary part
$\mathbf{K}_m$	oscillatory matrix from rotation
$\mathbf{F}_B(\mathbf{q}, \dot{\mathbf{q}})$	generalized forces resulting from bearing force/moments
$\mathbf{f}_{RB}$	generalized force acting on stationary and the rotating parts
$\mathbf{f}$	generalized excitations from the base motion
p	pressure acting on slider surface
h	spacing between disk an slider
μ	air dynamic viscosity
U, V	local disk velocity in the x and y direction
$Q(Kn)$	slip model (a function of Knudsen number)
∇	differentiation operator
X and Y	non-dimensional coordinates (x/l and y/l)
l	slider length
D is	inverse Knudsen number ($\sqrt{\pi}/2Kn$)
Kn	$\lambda/h;\ \lambda = \mu\sqrt{2\pi RT_0}/2p$
R	gas constant
T_0	characteristic temperature
$Q_p(D)$	flow rate of Poiseuille flow
$\overline{Q}_p(D)$	relative flow of Poiseuille flow; $Q_p(D)/(D/6)$
P	non-dimensional pressure; p/p_a
p_a	ambient pressure
H	non-dimensional spacing; h/h_0
h_0	minimum (characteristic) spacing
$\vec{\Psi}$	disk velocity; $Ui + Vj$
ω_0	disk angular velocity
$\bar{\tau}$	non-dimensional time

α	surface accommodation coefficient
η	surface density of asperities
$\tilde{A}$	nominal contact area
E'	effective Young's modulus
β	radius of curvature of asperities
σ	standard deviation of the asperity heights
$F(h)$	scaled height distribution
h	standardized separation
s	standardized asperity height
$\Phi(s)$	standardized height distribution (Gaussian).
FH	Flying Height
IMF	Intermolecular Force
A, B	the effective Hamaker constants between the slider and the disk
h	Planck's constant
v_e	ionization frequency
ε_i	permittivity of material i
n_i	reflective index of material i
D	air thickness
T	thickness of disk lubricant
T'	thickness of DLC layer in the slider
ε_o	permittivity constant (8.85×10^{-12} F.m^{-1})
k_e	dielectric constant (1 for air)
V	potential difference between the slider and the disk.
TEC	Trailing Edge Centre
LEC	Leading Edge Centre
ζ	Damping
$\mathbf{R}^i$	a set of Cartesian coordinates that define the location of the origin of the body reference
$\boldsymbol{\theta}^i$	the set of Euler angles that describe the orientation of the selected body reference
$\mathbf{u}^i_p$	local position vector of point P expressed in $x''y''z''$
$x''y''z''$	body reference
$\mathbf{A}^i$	the transformation matrix between the body reference and the global reference
$\mathbf{u}^i_o$	the position of point P in the undeformed state in the body reference
$\mathbf{u}^i_f$	the displacement of point P due to elastic deformation
m	the number of mode shapes to be taken into account
N^i_k	k^{th} shape function of the corresponding element
φ^i_{jk}	j^{th} mode shape value evaluated at the nodal points of the element
n	the number of the shape functions of the element
T^i	the kinetic energy of the flexible body i
$\mathbf{M}^i$	the mass matrix of the flexible body i
ρ^i	the density of the body i
V^i	the volume of the body i

$\mathbf{K}_f^i$	the diagonal stiffness matrix associated with the elastic coordinates of the body *i*
$\mathbf{C}^i$	the damping coefficient matrix
$\mathbf{Q}_e^i$	the generalized force applied on the flexible body
$\mathbf{Q}_v^i$	the quadratic velocity vector
$\mathbf{C}_f^i$	the diagonal damping matrix associated with the elastic coordinates of the body
E	Young's modulus
v	Poisson's ratio
$\mathbf{B}^i$	the matrix whose columns are the partial derivatives of the vector $\mathbf{A}^i\mathbf{u}_p^i$
$\boldsymbol{\varphi}$	the normalized modal matrix
δ	the interference in the hertz elastic contact model
b	the slider width normalized by the slider length
F_{shp}	the shear forces in pitch direction
F_{shr}	the shear forces in roll direction
Γ	the diffusion coefficient
$\mathbf{u}$	the flow velocity vector
S	the source term
CV	control volume
P_e	Peclet number
CDS	Central Differencing Scheme
R_P	Residual of discretized Reynolds equation
σ	the squeeze number
S_{CV}	the area of the CV
Δt	the time step length
NL	Normal load of the air bearing
QS	Quasi-static
AB	Air bearing
PSD	Power Spectral Density
GRMS	Root mean square of acceleration in G unit (1 G = 9.81 m/s^2)
MIL-STD	Military Standard
MB	Megabytes
S_{yy}	Input PSD

Publications (International Journals)

1. F. Gao, F. F. Yap, Y. Yan, and H. Harmoko, "Shock Analysis of Non-Operating Hard Disk Drives Based on a Multi Body Dynamic Formulation," Microsystem Technologies, vol. 12, 2006, pp. 247-257. *(Journal impact factor: 0.673) (cited: 1)*

2. F. F. Yap, N. Vahdati, and H. Harmoko, "Design and Analysis of Vibration Isolation Systems for Hard Disk Drives," Journal of Magnetism and Magnetic Materials; 6th International Symposium on Physics of Magnetic Materials, vol. 303, 2006, pp. e52-e56. *(Journal impact factor: 1.212)*

3. M. Liu, F. F. Yap, and H. Harmoko, "Shock Response Analysis of Hard Disk Drive Using Flexible Multi Body Dynamics Formulation," Microsystem Technologies, vol. 13, 2007, pp. 1039-1045. *(Journal impact factor: 0.673)*

4. H. Harmoko, F. F. Yap, N. Vahdati, S. Gan, M. Liu, and B. J. Shi, "A More Efficient Approach for Investigation of Effect of Various HDD Components on the Shock Tolerance," Microsystem Technologies, vol. 13, 2007, pp. 1331-1338. *(Journal impact factor: 0.673)*

5. F. F. Yap, H. Harmoko, M. Liu, and N. Vahdati, "Modeling of Hard Disk Drives for Shock and Vibration Analysis – Consideration of Nonlinearities and Discontinuities," Nonlinear Dynamics, vol. 50, 2007, pp. 717-731. *(Journal impact factor: 0.902)*

6. H. Harmoko, F. F. Yap, N. Vahdati, C. Li, "Design and Analysis of Shock and Random Vibration Isolation of Operating Hard Disk Drive in Harsh Environment," Journal of Shock and Vibration (accepted) *(Journal impact factor: 0.173)*

7. M. Liu, F. F. Yap, and H. Harmoko, " Dimple-Flexure Contact Stiffness Effect on Operational Hard Disk Drive Shock Tolerance," Microsystem Technologies (accepted) *(Journal impact factor: 0.673)*

Publications (International Conferences)

1. F. F. Yap, N. Vahdati, H. Harmoko, “Design and analysis of vibration isolation systems for hard disk drives,” presented at 2005 International Symposium on Physics of Magnetic Materials (ISPMM), Singapore, 2005.

2. H. Harmoko, F. F. Yap, N. Vahdati, S. Gan, and L. Mengjun, "Investigation of Effect of Various Components in HDD on the Shock Tolerance," presented at 2006 ASME/JSME Joint Conference on Micromechatronics for Information and Precision Equipment (MIPE 2006), Santa Clara, California, USA, 2006.

3. M. Liu, F. F. Yap, and H. Harmoko, "Shock Response Analysis of Hard Disk Drive Using Flexible Multi Body Dynamics," presented at 2006 ASME/JSME Joint Conference on Micromechatronics for Information and Precision Equipment (MIPE 2006), Santa Clara, California, USA, 2006.

4. H. Harmoko, F. F. Yap, N. Vahdati, and M. Liu, "Toward Efficient Op-Shock Simulation," presented at 2006 Asia-Pacific Magnetic Recording Conference, Singapore, 2006. *(indexed at Inspec)*

Abstract

The hard disk drives have been increasingly used in consumer electronics and mobile computing, in which they may experience severe shock and vibration. Additionally, there is a fierce competition from the solid state drives. Hence, there is a need for rapid innovation, especially in the ever shorter drives design cycle. This in turn requires faster and accurate simulation method.

This dissertation focuses on the formulation of an efficient theoretical model for design parametric studies and optimization in modern hard disk drives. It integrates both drive structural model and air bearing model. The structural models are developed using flexible multi body dynamics formulation and state-space mode superposition theory. The air bearing model is developed using finite volume formulation and modified quasi-static concept. The coupled structural and air bearing models can simulate the shock response at drive level and also predict the operational shock tolerance effectively. Hertz elastic contact theory is incorporated to deal with structural discontinuities. A modified state-space formulation is also included to simulate the dynamic air bearing location due to disk rotation.

In the analysis of the quasi-static air bearing, it is found that air bearing equilibrium condition does not occur almost-immediately due to the squeeze term effect. Addition of optimized damping elements to quasi-static air bearing model can increase its accuracy and enable it to predict the same air bearing force as the finite volume model.

From parametric studies, it is found that lower contact stiffness between suspension (dimple) and slider (flexure) yield higher shock tolerance. A more rigid cover is also found to increase the shock tolerance.

Shock response analysis shows that the first-three most dominant actuator modes that affect the read/write head shock response are induced by the flexibility of suspension and flexure. It is also discovered that updating the position on the disk, at which the air bearing forces act, at every simulation time-step does not have significant effect on the shock response. Hence, it is not necessary to update the air bearing force location on the disk.

From HDD vibration isolation studies, it can be observed that to survive a harsh shock and random vibration defined in MIL-STD-810E, the natural frequencies of the external vibration isolation system should be between 10 to 20 Hz. The damping ratio required is relatively high (> 10%). To reduce the peak-to-peak displacement during shock event, combination of soft and stiff isolators can be used.

CHAPTER 1 INTRODUCTION

Hard disk drives (HDD) are non-volatile storage devices [1] which store digital data on rapidly rotating disks with magnetic surfaces. In the beginning the HDD had several detachable disks (that was how the word 'drives' comes [2]); however, modern HDD are typically a sealed unit with fixed media.

1.1 *Introduction to HDD mechanical components*

The structure of a typical hard disk drive is illustrated in Figure 1.1. From a mechanical point of view, the major components of HDD include: spindle motor assembly, disks, voice coil motor (VCM), head-actuator assembly (HAA), and the device housing. Digital data is stored on the disks. During operation, the disks spin at high speed and the HAA moves across the disk surface to read or write data on tracks.

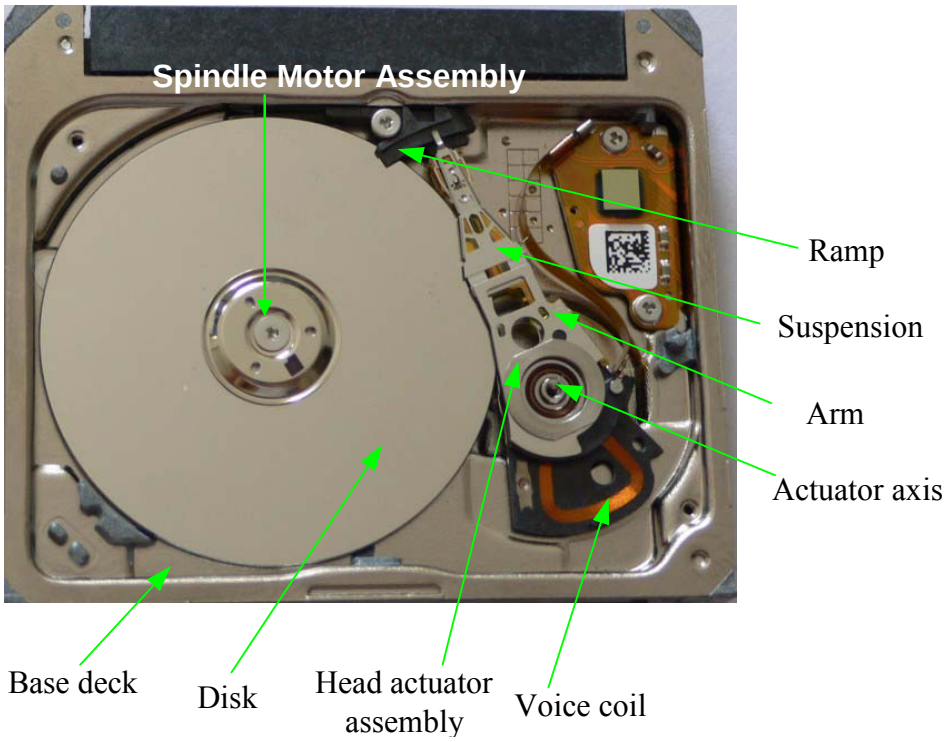

FIGURE 1.1 THE STRUCTURE AND COMPONENTS OF A HARD DISK DRIVE

1.1.1 Spindle Motor Assembly

The function of the spindle motor assembly is to rotate the disks. It provides stable, reliable and consistent turning power. Previously, there were two kinds of bearings used in spindle motor assembly: ball bearing and fluid dynamic bearing. The fluid-dynamic bearing (FDB) has less non-repeatable run-out error, lower noise level, better non-operational shock resistance, and greater speed control. This is due to the higher damping possessed by FDB as a result of the viscosity of the lubrication oil between the sleeve and the stator. The ball bearing was then rapidly replaced by the FDB. Presently, all the spindle motor assemblies use FDB. Figure 1.2 shows the cross-sectional view of an FDB with rotating-shaft spindle used in most of the portable HDD.

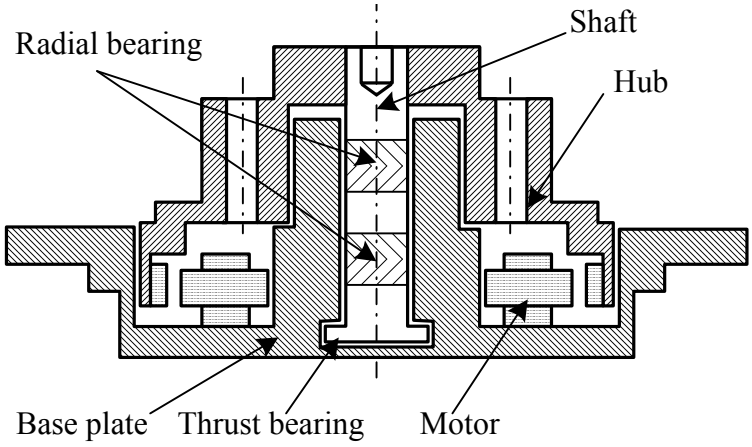

FIGURE 1.2 THE CROSS-SECTIONAL VIEW OF A TYPICAL FDB WITH ROTATING-SHAFT SPINDLE

1.1.2 Disks

All HDD contains one or more flat disks. The disk is composed of two main substances: a substrate material that forms the bulk of the disk and gives it structural rigidity, and a magnetic media coating which holds the magnetic data. The disks are mounted through a centrally cut hole and stacked onto a spindle. Today the four

most common disk sizes (form factor) used in PCs and other consumer electronic devices are 3.5 inch, 2.5 inch, 1.8 inch, and 1 inch. Their spinning speed usually ranges from 3,600 rpm up to about 20,000 rpm.

1.1.3 VCM/actuator Assembly

The VCM/actuator assembly is made up of a head-gimbal assembly (HGA), an actuator and a voice coil motor (VCM). The HGA (for example, see Figure 1.4) consists of a slider where the read/write head is attached, and a suspension. The actuator consists of suspension arms and pivot assembly. The HGA together with the actuator is usually called the head-actuator assembly (HAA). The VCM is composed of a magnetic coil and two yoke plates where permanent magnets are bonded in place. The read/write heads are attached to the slider. The T-limiter and the dimple are used to restrict the movement of the slider. In steady reading/writing process, due to the preload force generated by the suspension and the opposite force generated by air bearing under the slider, the slider stays in contact with the dimple (the air bearing is shown in Figure 1.5). However, the slider and the dimple may separate under shock or severe vibration.

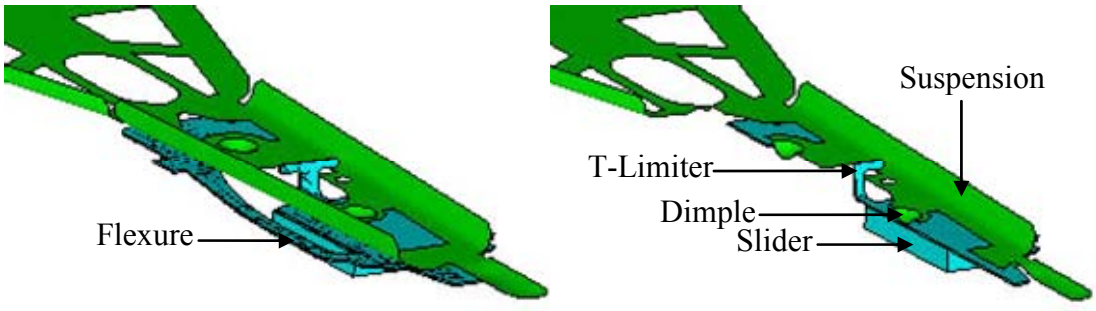

FIGURE 1.3 HEAD-GIMBAL ASSEMBLY DEVICE I

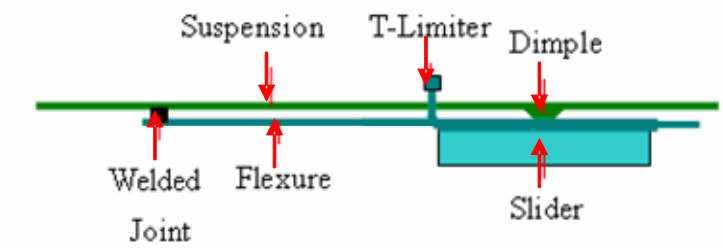

FIGURE 1.4 HEAD-GIMBAL ASSEMBLY DEVICE II

1.1.4 Head-disk Interface

Figure 1.5 describes a typical head-disk interface, in which the air bearing is formed between the slider and the disk due to the relative motion between them. The air bearing can follow the disk roughness of micrometer level within angstrom level. It also can tolerate high acceleration track seeking without significant variation in the flying height. Air bearing is voted in 1999 as one of the most successful technologies in the HDD [3].

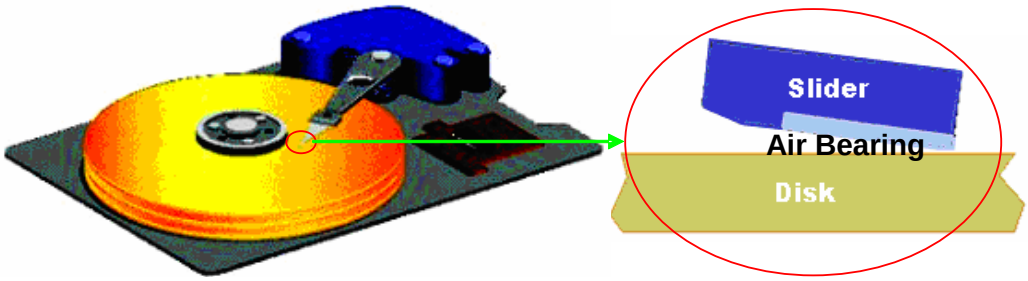

FIGURE 1.5 A TYPICAL HEAD-DISK INTERFACE IN HDD

1.1.5 Device Housing

The device housing usually consists of two parts: the base plate and the top cover. The housing provides features for mounting the spindle motor/disks assembly, the VCM/actuators assembly, and printed circuit board. The actuator shaft is usually mounted on the drive base plate and supported by the cover through a screw. The base and the cover also keep contamination from external environment low.

1.2 *Overview of HDD Industry and Technology*

The HDD were originally developed for use with desktop computers. In the 21st century, the HDD have been used in entertainment systems such as digital video recorders, digital audio players, personal digital assistants, digital cameras, and video game consoles. In 2005 the first mobile phones to include HDD were introduced by Samsung and Nokia [4]. Figure 1.6 shows these HDD growth in various applications over the last few years and projected to 2010 [5].

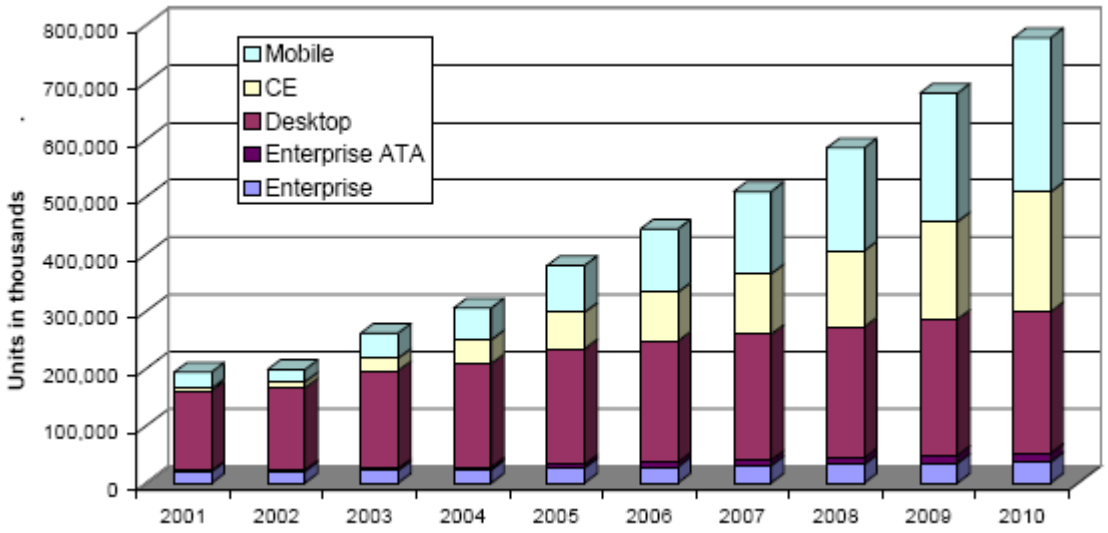

FIGURE 1.6 HISTORY AND PROJECTIONS FOR HDD GROWTH TO 2010 PER MARKET SEGMENT [5]

The first reason for the HDD widespread in many digital applications is that its disk size (form factor) can be as small as 0.85 inch. The smallest form factor, 0.85-inch Microdrive (Figure 1.7) can store 4 Gigabytes with a projection of 10 Gigabytes in the near future [6]. Form factor evolution to smaller sizes has been accomplished without loss of capacity and often has resulted in higher performance and lower power dissipation [7].

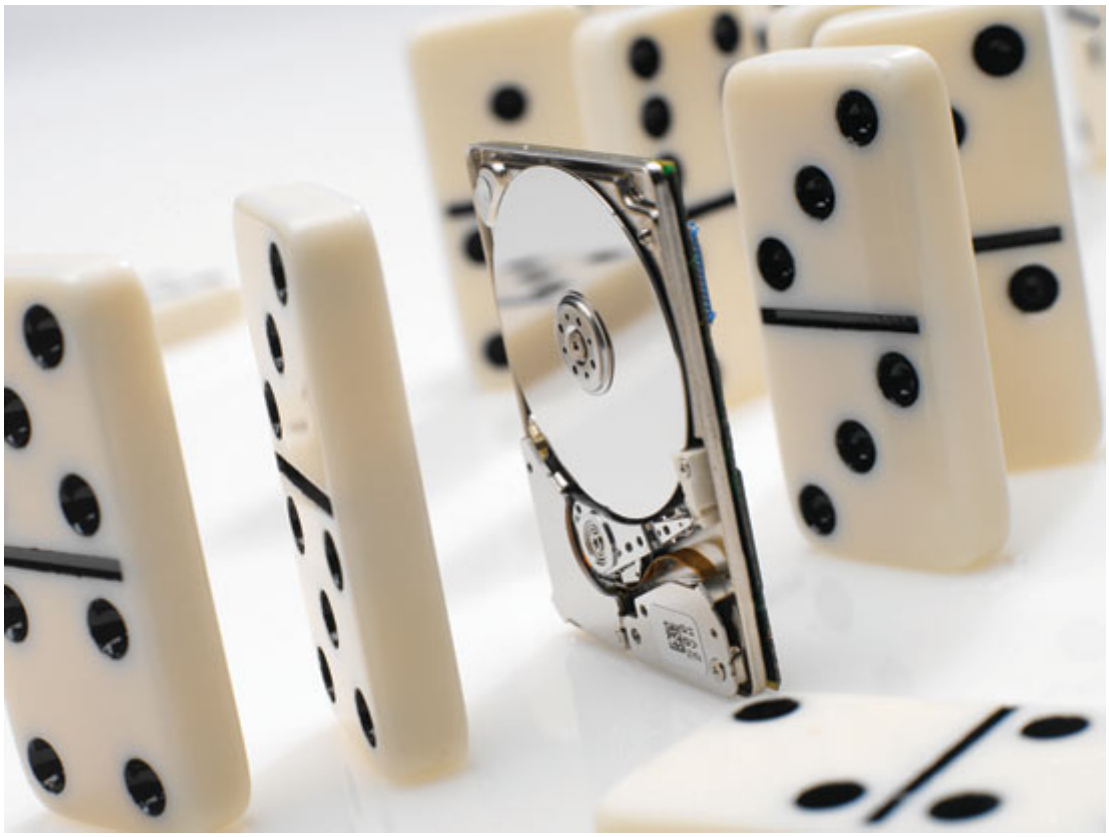

FIGURE 1.7 A 0.85-INCH TOSHIBA MICRODRIVE [8]

At the same time HDD pricing has stabilized substantially. Figure 1.8 shows the average selling price (ASP) of 3.5-inch HDD for Seagate, Maxtor, and Western Digital since 1998 (these three companies represent 59% of the total drive market in 2005) [5]. From Q4 ’98 to Q3 ’02 the HDD prices fell due to excessive inventory, extreme price competition between HDD manufacturers, and heavy pressure by customers for lower price. Since 2003 the price did not vary much and in 2004 till 2006 the prices show good stability.

One of the reasons for the increase in the price stability is significant industry consolidation. With the merger of Maxtor and Quantum [9], the integration of Hitachi and IBM drive operations [10], and the recent acquisition of Maxtor by Seagate [11], there are fewer rivalries in this very competitive market. Hence, a chance that one

player trying to gain more market share by undercutting the prices is less than before the industry consolidation.

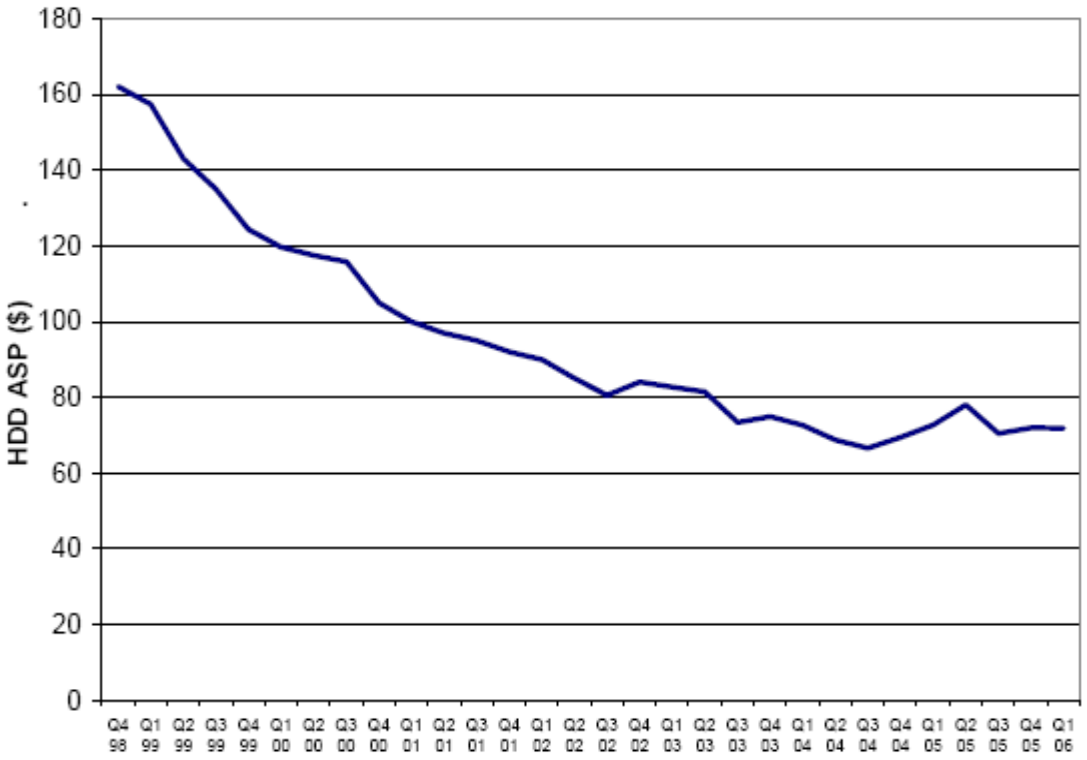

FIGURE 1.8 AVERAGE SALES PRICE (USD) FOR SEAGATE, WESTERN DIGITAL, AND MAXTOR

Another cause for the price stability is a critical shortage of HDD components, especially the disks. The shortage of the components (as reported in [12]) limits the industry's ability to produce the drives. This shortage is acting as external constraint to HDD supply and thus helps stabilizing the price.

Although the HDD price does not change much, the data density increases substantially. Figure 1.9 shows the growth of areal density over the past few decades [13]. More specifically, the areal density has increased by a factor of 35 million since the first disk drive, RAMAC, was introduced in 1957. Since 1991, the rate of increase has accelerated to 60% per year, and since 1997 this rate has further accelerated to an incredible 100% per year [14]. The areal density of hard disk media continues to

increase at an astonishing rate even exceeding some of the optimistic predictions of a few years ago; the density doubles easily every two years and sometimes every year, faster even than the chip progress described by Moore's Law [15].

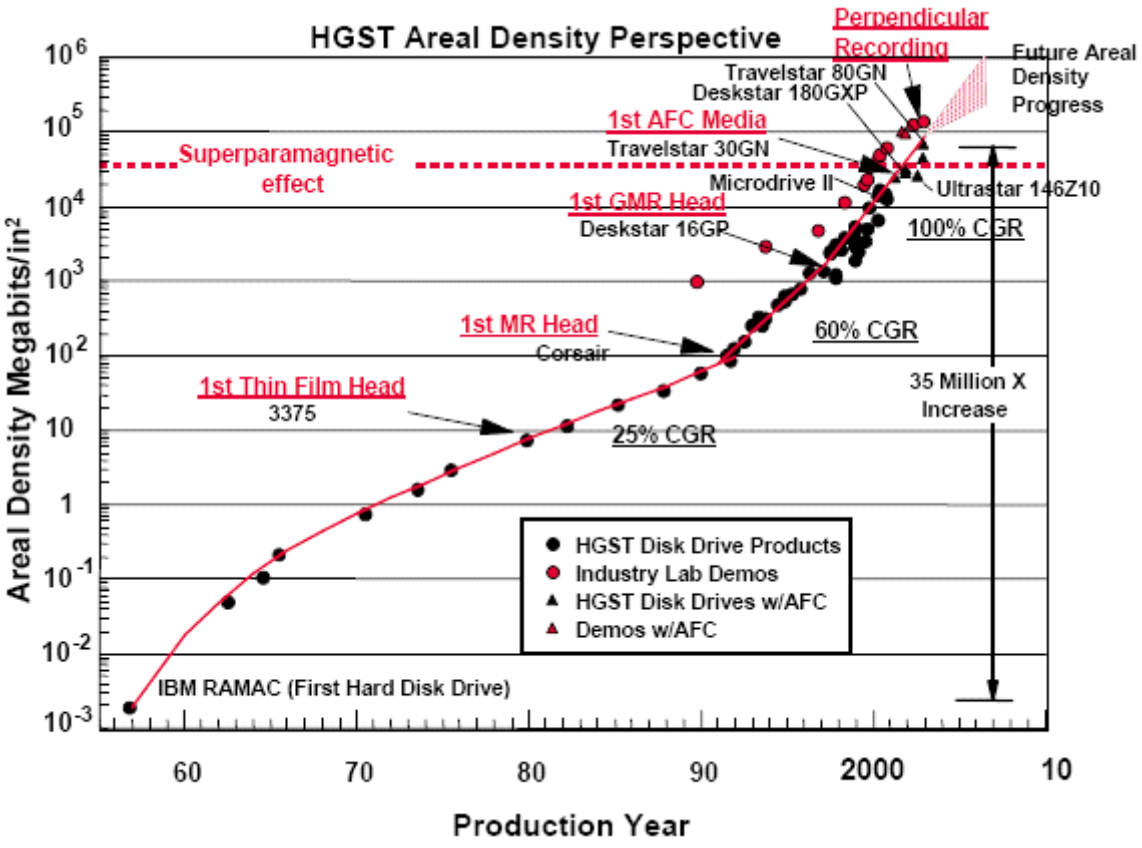

FIGURE 1.9 THE PROGRESS OF AREAL DENSITY

The impressive increase in the HDD areal density is the result of several important technologies. The most prominent one is the magneto-resistive read heads in 1991 and then followed by giant magneto-resistive (GMR) read heads in 1997. The "giant" in GMR doesn't refer to the size of the head but the large change in resistance that occurs when magnetic fields are applied. Different resistance levels can be tagged as ones and zeros of data. The discovery of this GMR has bestowed the 2007 physics Nobel prize to Albert Fert and Peter Grünberg [16].

Advances in disk/media technologies have also contributed to the increase in areal density. Old longitudinal magnetic recording disk has been changed to perpendicular magnetic recording (PMR) disk [17] that can squeeze ten times more data [18]. In 2006, Seagate demonstrated a storage areal density of 421 Gbits/in^2 using this PMR technology [19], almost 2.5x the density that Toshiba demonstrated just three months before it [20]. The areal density of PMR disk has been further enhanced by discrete track recording (DTR) technique [21]. By 2010, using heat-assisted magnetic recording (HAMR) technology Seagate believes it can produce 50 Tbits/in^2 hard disk drives [22, 23].

To accommodate the increase in the areal density, the read/write heads are required to fly progressively closer to the disk surface (as described in Figure 1.10). This allows the fields created during the write process, and subsequently read, to be focused into a smaller space as areal density increases. However, continued spacing decrease requires a greater physical stability during the read-write operation. This requirement limits the physical shock tolerance of the HDD. Currently, the operational shock tolerance of a typical 2.5-inch HDD is up to 325 G [24].

The significant increase in the drives capacity accompanied by increase in price stability enables the HDD to have lowest cost per Gigabytes compared to other digital storages technology (~ 100 times cheaper than solid state memory). This allows the small form factor HDD to play a major role in many portable digital applications. However, the use of HDD in mobile environment expose it to severe shock ranging from 800 G to 4000 G [25, 26], capable of disturbing the read/write process in HDD.

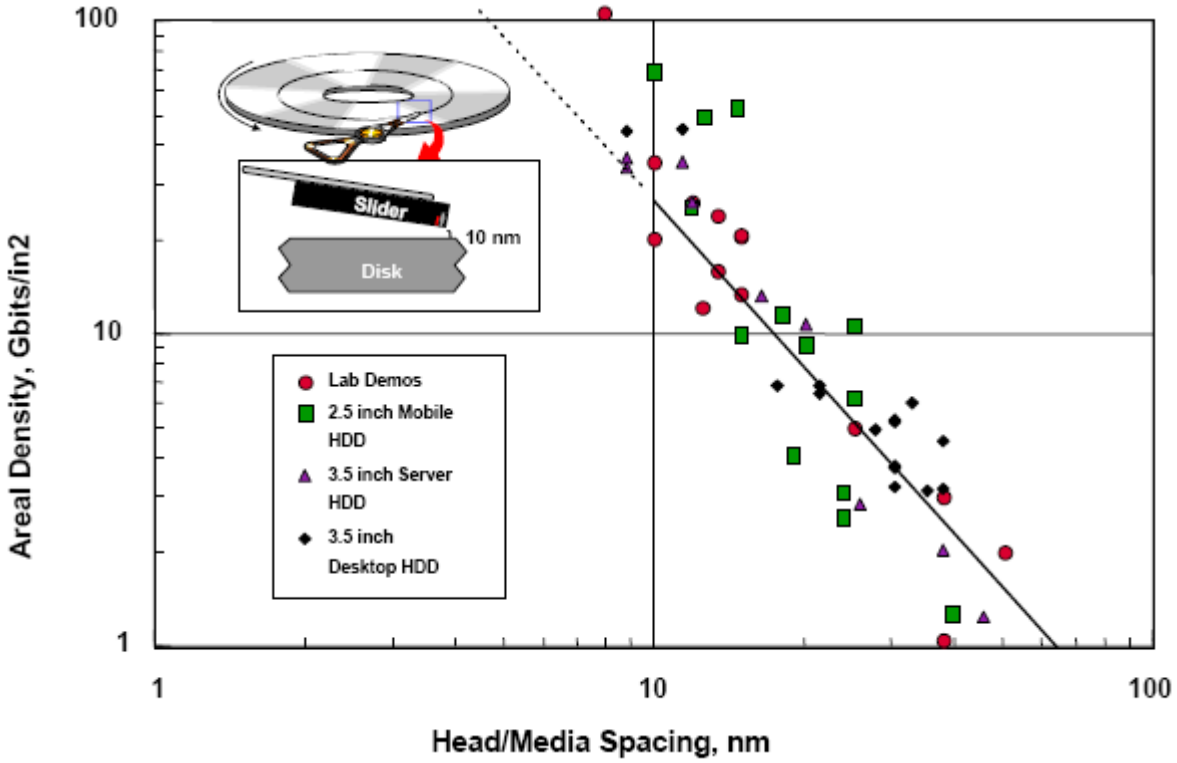

FIGURE 1.10 SPACING-AREAL DENSITY PERSPECTIVE [27]

At the same time, the solid state memory devices (one of HDD competitors in digital storage market), which have an exceptional operational shock tolerance up to 1300 G [28], has become cheaper and cheaper [29]. This gives considerable pressure to HDD industry to increase the shock tolerance of HDD.

In summary, the maximum magnitude of the shock excitation during the usage is higher than the shock tolerance of the HDD. Since the way the consumers handle the HDD cannot be controlled, the best way to prevent the HDD from being damaged is to increase its operational shock tolerance.

1.3 *Formulation of Research Objectives*

There are several ways to increase the operational shock tolerance of the HDD. The first one is to design robust mechanical system. The mechanical system can be seen as

the 'body' of the HDD. The mechanical component that has a large influence on the shock tolerance is the suspension/gimbal assembly (Figure 1.11). Its influence is becoming more significant as the drives are getting smaller [30].

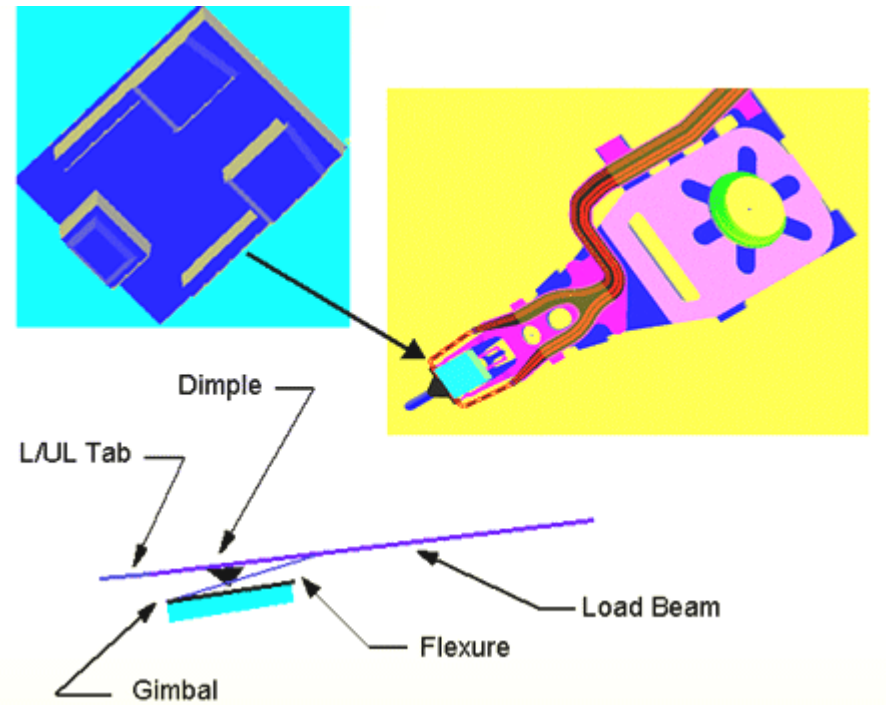

FIGURE 1.11 AIR BEARING SLIDER AND SUSPENSION [31]

Over the years, the suspension shape has changed considerably due to various optimization processes. The profile of the current suspension is relatively complicated with several mechanical discontinuities or nonlinearities. The suspension itself is connected with the rest of HDD structures (also having a high degree of complexities) by bearing joints. It is a challenge to formulate the theoretical model of these complex & interconnected HDD structures considering the suspension nonlinearities and strong shock excitation.

The second way to increase the operational shock tolerance of the HDD is to design robust head disk interface (HDI). The HDI can be considered as the 'heart' of the HDD. The shock robustness of the HDI largely depends on the performance of the

air bearing slider. To improve shock resistance of the drive, the slider has been evolved with time based on requirement to reduce the overall mass of the slider/suspension assembly [32]. The evolution of the slider/air bearing surface is shown in Figure 1.12. It can be seen that as the slider becomes smaller, its complexity is increasing.

In predicting the air bearing shock response using a conventional way (finite volume method), a relatively huge grid size is needed to model the modern air bearing. The big grid size means that a large number of degrees-of-freedom needs to be processed during the shock simulation. Hence, the simulation may not be time-efficient [33]. It is then useful to develop a new concept that enables us to create a time-efficient dynamics model of the air bearing.

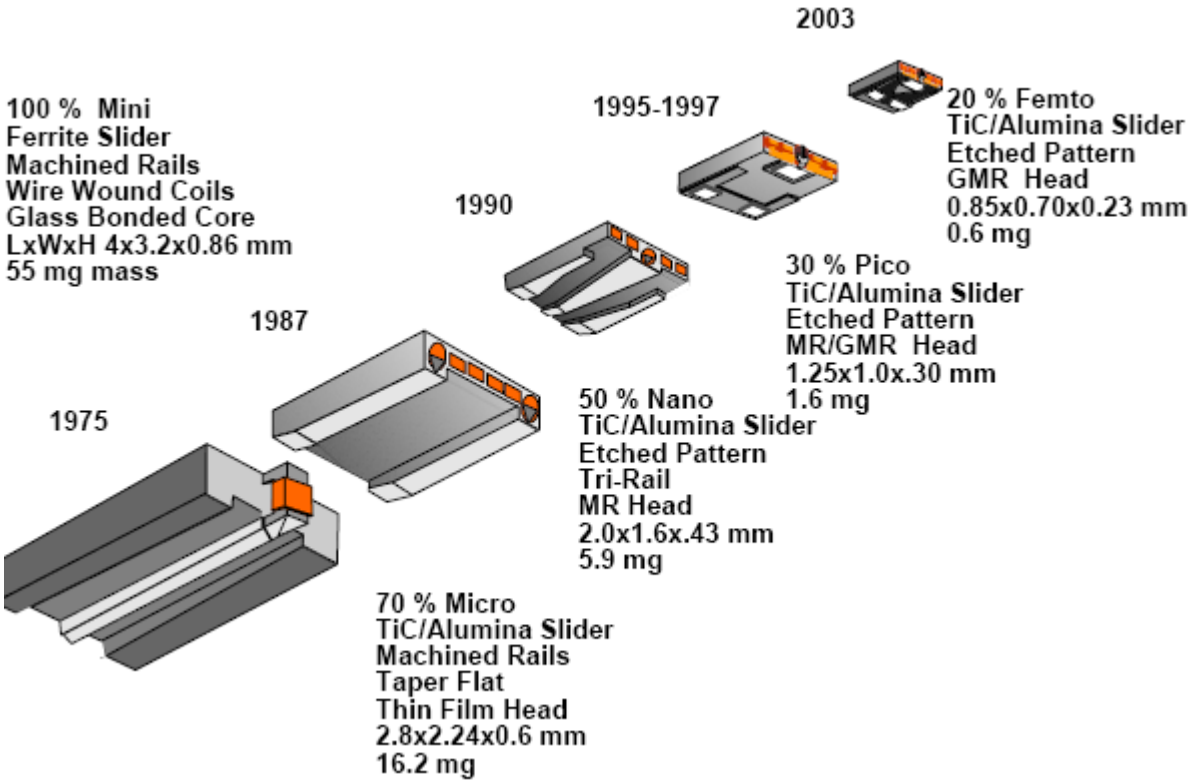

FIGURE 1.12 EVOLUTION OF SLIDER/AIR BEARING SURFACE [32]

The third method to increase the shock tolerance of the HDD is to design an effective shock and vibration isolation for the HDD. The isolation acts as HDD 'skin', protecting it from external excitation. The idea of "vibration isolation as HDD skin" appears more concrete in the current portable drives as shown in Figure 1.13; the figure portrays a mobile HDD wrapped with rubber isolator.

The knowledge and theory on how to design, test, and evaluate shock isolation system for the HDD, subject to severe shock and random vibration based on known standards, is important. To demonstrate the need of the vibration isolation, a random vibration test on several bare HDD (HDD without vibration isolation) was conducted. It is found that a random vibration with excitation level as low as 3.5 GRMS (G root-mean-square) is enough to cause read/write error in the HDD [34].

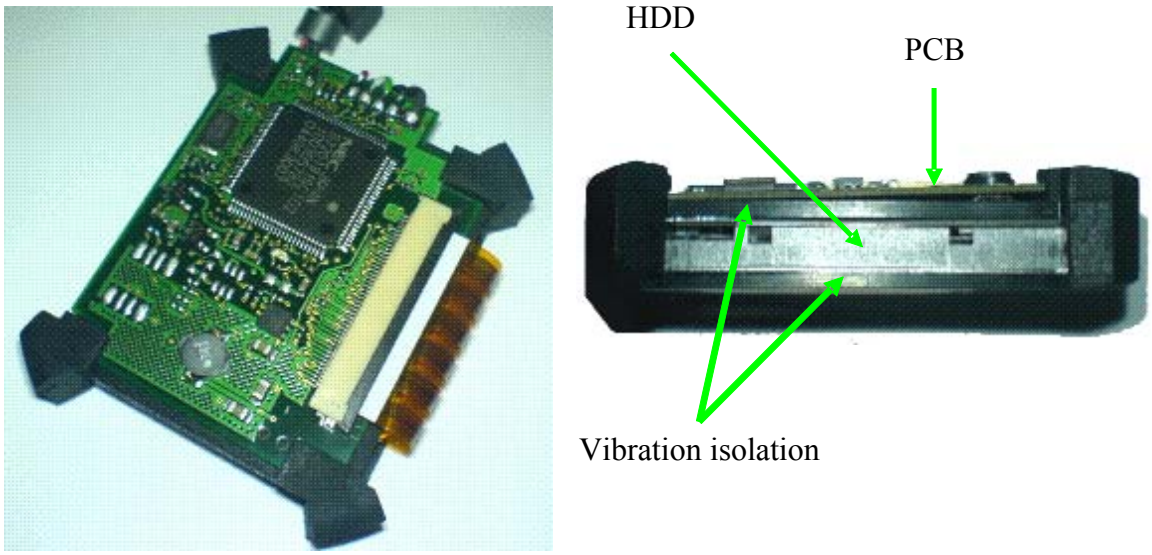

FIGURE 1.13 A PORTABLE HDD

Therefore, this research project aims to create novel and effective techniques/methods to predict the operational shock and vibration response of hard disk drives for design parametric studies and optimization.

1.4 *Scope*

To accomplish the objective above, the project covers:

1. Formulation of theoretical model of complete operational HDD including the nonlinear suspension/gimbal assembly

2. Formulation of theoretical model of the air bearing for efficient operational shock simulation

3. Development of the appropriate fluid and structural coupling method, followed by HDD design parametric studies & optimization

4. Formulation of theory/concept on how to design, test and evaluate effective shock/vibration isolation system for HDD subject to severe shock and random vibration defined in a known standard.

1.5 *Chapter Organization*

The thesis is organized as follows.

1. Extensive literature review on theoretical dynamics models of air bearing & HDD structures and investigation on the HDD shock and vibration design (Chapter 2)
2. Flexible multi body dynamics formulation and development of time-efficient state-space mode superposition theory of operational HDD subject to shock excitation (Chapter 3)
3. Formulation of air bearing dynamics model based on full Reynolds compressible gas equation using finite volume method, followed by formulation and investigation of quasi-static concept of the air bearing (Chapter 4)

4. Development of direct coupling method for structural & fluid interaction at the head-disk interface, prediction of HDD shock tolerance, verification of the theoretical model, and parametric studies plus optimization (Chapter 5)

5. Formulation of theory/concept for design, test, and evaluation of shock and vibration isolation system for HDD operating in harsh mechanical environment as defined in MIL-STD-810E (Chapter 6)

1.6 *Chapter Summary*

Summary of the HDD industry/technologies and the formulation of research objectives are given in the following two flow diagrams.

1.6.1 Summary on the HDD Industry and Technologies

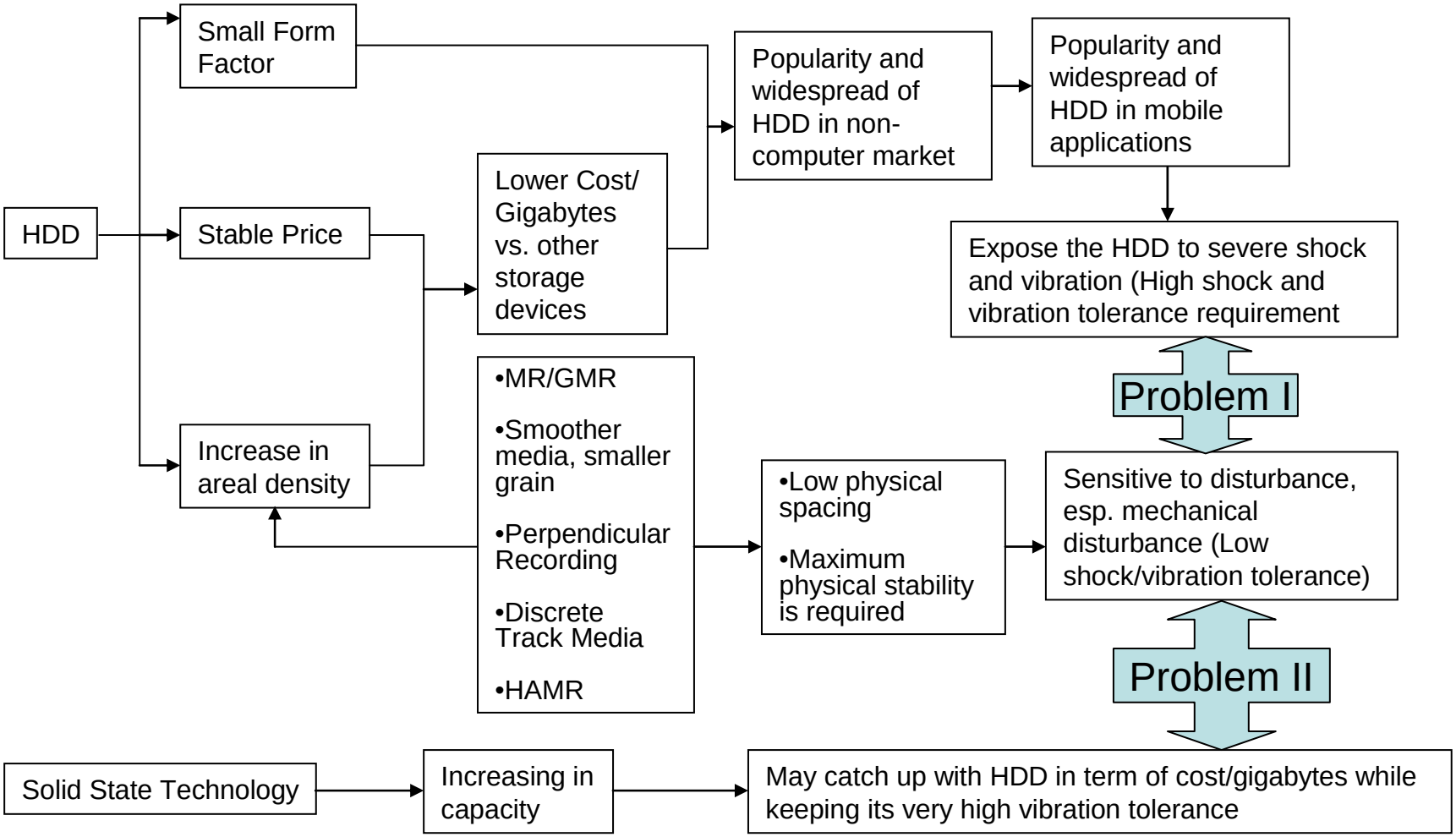

1.6.2 Summary on the Research Objectives Formulation

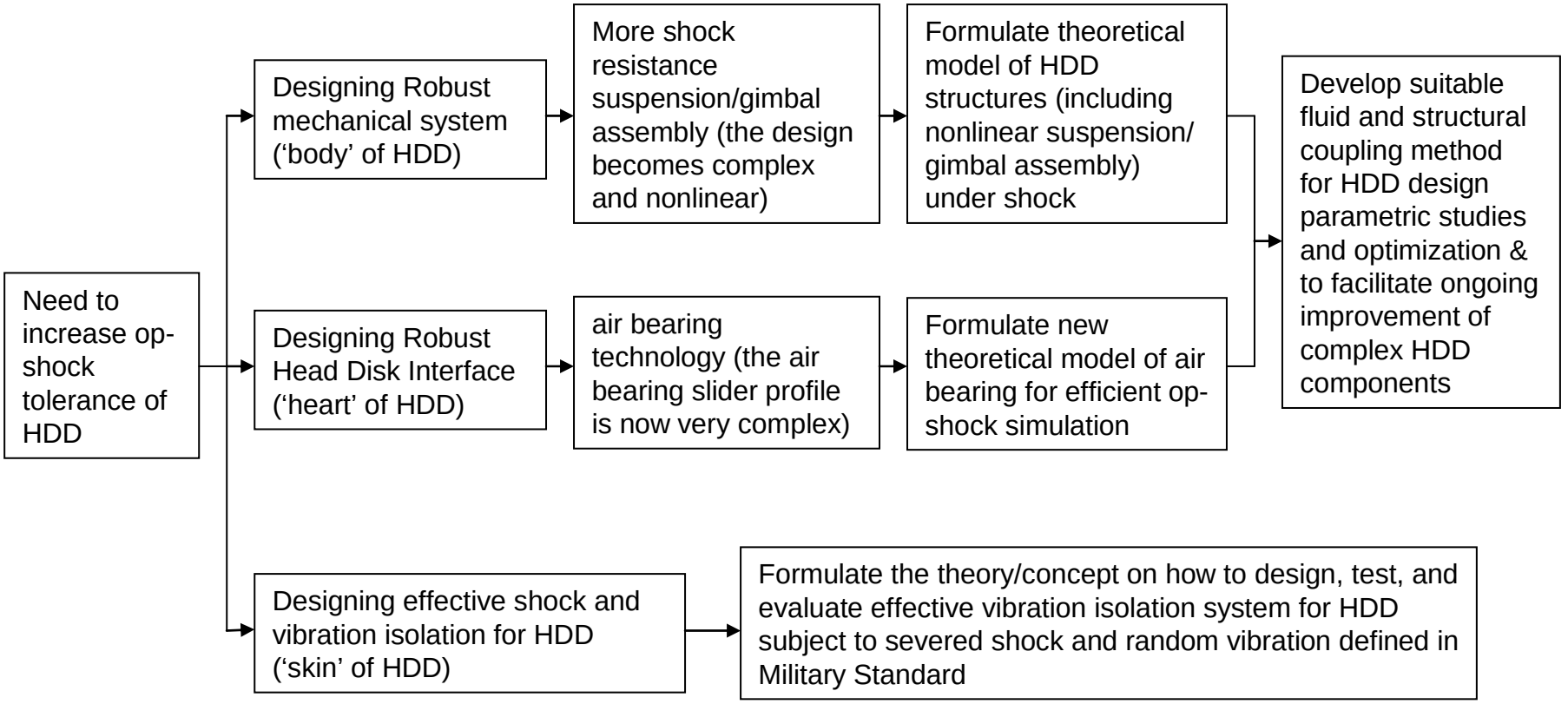

CHAPTER 2 LITERATURE REVIEW

Basically the objectives of the research project, as mentioned in Chapter 1, are to formulate theoretical models of operational HDD subject to shock excitation and to develop theories on how to design, test, and evaluate the vibration isolation of the HDD subject to strong shock and random vibration. The first necessary step required to achieve these objectives is a thorough literature review to find out the existing related works. This review covers the theoretical models of HDD structures and the air bearing, and the HDD shock and vibration isolation.

2.1 *Theoretical Model of HDD Structures for Shock Simulation*

Before discussing the modeling theories for the HDD structural shock simulation, the review of the mechanics of each HDD structures is given below.

2.1.1 Mechanics of HDD Structures

There are three important structures in the HDD that affect its shock response; they are head actuator assembly (HAA), disks-spindle assembly, and drive casing [30]. The mechanics of HAA, rotating disk, and disk-spindle assembly are presented individually in the following sub-sections

2.1.1.1 Head Actuator Assembly

Generally, when HDD is in operation, the dimple and the slider keeps in contact while the T-limiter is disengaged from the suspension. When a shock takes place, the dimple and the slider may separate. When the shock is very severe, the T-limiter may engage the suspension preventing further separation of slider and dimple. This means there is a

discontinuity in the overall stiffness of the suspension.

Contact dynamics can be used to model these discontinuities. For a simple case, the force between the dimple and the slider can be modeled as a spring force when contact takes place. A model of the suspension dimple and slider is shown in Figure 2.1.

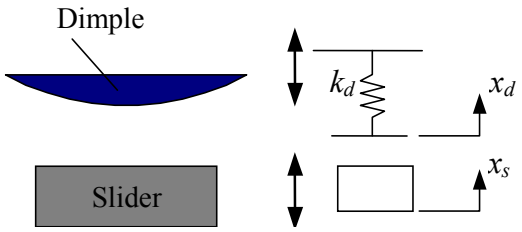

FIGURE 2.1 MODELING DIMPLE-SLIDER CONTACT

The equation of the force acting on the slider is

$$f(x_d, x_s) = \begin{cases} k_d(x_d - x_s) & x_d \le x_s \\ 0 & x_d > x_s \end{cases} \tag{2.1}$$

where x_d and x_s are the positions of contacting points on the dimple and on the slider, respectively. k_d is the linearized contact stiffness between the slider and the dimple. The contact force acting on the dimple is $-f(x_d, x_s)$. A similar approach can be used to model the T-limiter. A more accurate contact model like mentioned in [35] or Hertz theory of elastic contact [36] can also be utilized to handle this nonlinearity.

2.1.1.2 Rotating Disk

The dynamic characteristics of the spinning disk in HDD have been widely studied [37]. When the disk is spinning, there are nonlinear couplings between the transverse vibration and the in-plane vibration of the disk. With the increase in spinning speed, the nonlinear coupling will have a greater effect on the dynamics of the disk.

In [38], the vibration of a spinning disk is studied considering the effect of the in-plane inertia. Vibration of a spinning flexible disk-spindle system supported by ball bearings has also been studied in [39] considering the non-linearity of the spinning disk. The analysis results for 2.5 inch HDD, shown in Figure 2.2, illustrates that the discrepancy between the natural frequencies obtained from linear and non-linear models increases with the increase of the disk spinning speed, and that when the spinning speed is higher than 6,000 rpm, the nonlinearity should be considered to predict the natural frequencies of an HDD spindle system more accurately.

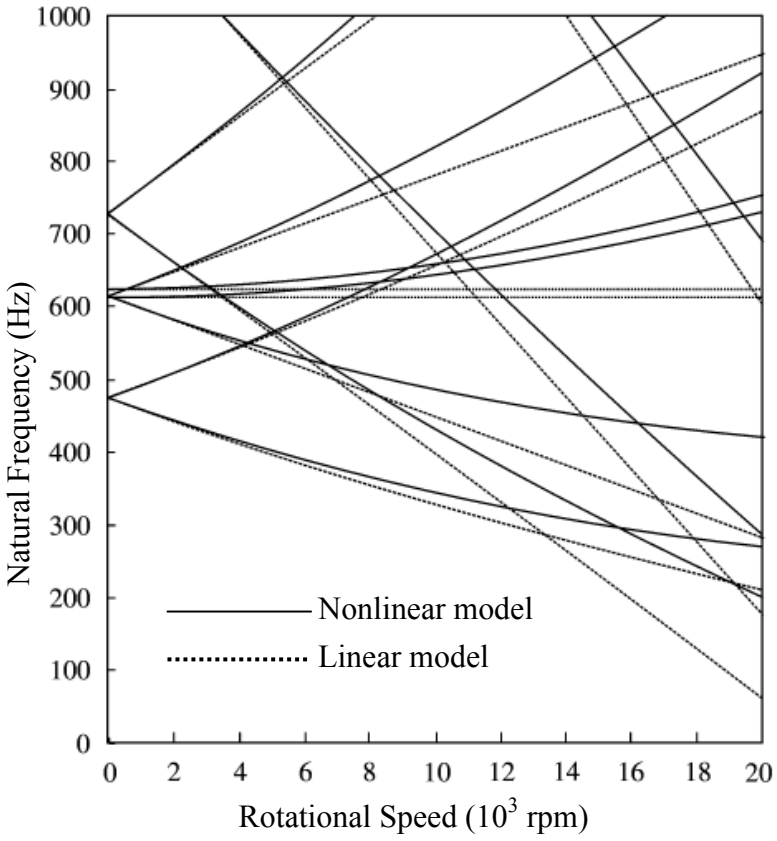

FIGURE 2.2 NATURAL FREQUENCIES DUE TO DISK NON-LINEARITY [39]

Another issue for attention is the flutter of a spinning disk. When a disk is spinning at a high speed in a fluid, the elastic coupling between the flexible disk vibration and the air around the disk may lead to the disk flutter. In that case, even though the disk is perfectly

balanced, a small disturbance to the disk will be amplified and the vibration amplitude of the disk will grow in time because of the energy supply from the air film. In HDD, the flutter of the disk will contribute directly to the track position errors of the read/write head and significant noise [40]. The flutter of rotating disks in enclosed fluids has been studied in [41, 42]. In [43, 44], an experimental method was developed to predict the onset of the disk flutter. The disk flutter problem in HDD was investigated in [45, 46]. At high spinning speed some of the eigenvalues of the system governing equation will have negative imaginary values (negative damping), meaning that fluttering will happen. By calculating plotting the eigenvalues with respect to disk rotational speed, the flutter speed can be predicted as shown in Figure 2.3; the disk has 0.178 m radius and 0.775 mm thickness. (m, n) corresponds to disk mode having m nodal circles and n nodal diameter [47]. When the disk rotates, modal distribution is characterized by pairs of waves propagating in opposite directions circumferentially for a ground-based observer (FTW: forward traveling wave and BTW: backward traveling wave).

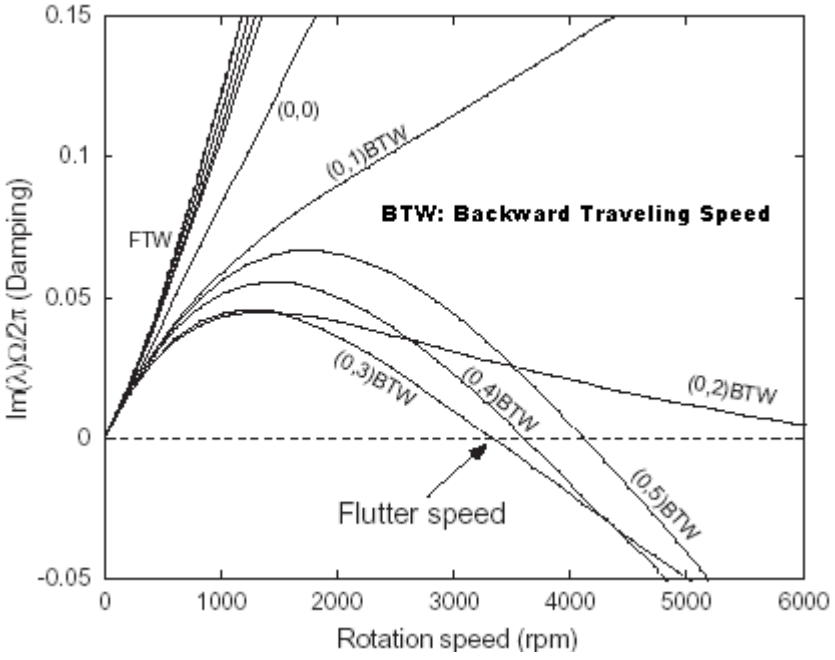

FIGURE 2.3 IMAGINARY PART OF EIGENVALUES OF MODES VS. ROTATION SPEED OF THE DISK [46]

2.1.1.3 Disk-Spindle Assembly

A summary on the development of the disk/spindle vibration before 2000 can be found in Shen I. Y.'s paper [48]. Presently, although there is a lot of literature on the nonlinearity of the fluid dynamic bearing (FBD) used in the disk-spindle assembly, only a few papers discuss the shock response of the spindle with nonlinear FDB. In [49] a method on how to incorporate fluid bearing nonlinearity to HDD spindle models without substantially increasing computational effort is demonstrated. In that paper, a linear spindle model by Tseng *et al* [50] was modified considering the bearing nonlinearity. The method is described as follows.

At each bearing (radial or thrust), the relative displacements $(\Delta_x, \Delta_y, \Delta_z)$ and angular displacements (α_x, α_y) of the stationary part and the rotating part can be determined. If the bearing is linear, corresponding to $(\Delta_x, \Delta_y, \Delta_z)$ and (α_x, α_y), the bearing forces $(F_x^{(b)}, F_y^{(b)}, F_z^{(b)})$ and bearing moments $(M_x^{(b)}, M_y^{(b)})$ can be obtained as

$$\begin{aligned}\left(F_x^{(b)}, F_y^{(b)}, F_z^{(b)}, M_x^{(b)}, M_y^{(b)}\right)^T = \\ -\mathbf{K}^{(b)}\left(\Delta_x, \Delta_y, \Delta_z, \alpha_x, \alpha_y\right)^T - \mathbf{C}^{(b)}\left(\dot{\Delta}_x, \dot{\Delta}_y, \dot{\Delta}_z, \dot{\alpha}_x, \dot{\alpha}_y\right)^T\end{aligned} \tag{2.2}$$

where $\mathbf{K}^{(b)}$ and $\mathbf{C}^{(b)}$ are 5×5 stiffness and damping matrices. The formulation is valid for different kinds of bearings, including FDB. When the bearing nonlinearity is considered, the bearing force/moment vector $\left(F_x^{(b)}, F_y^{(b)}, F_z^{(b)}, M_x^{(b)}, M_y^{(b)}\right)^T$ will becomes a nonlinear matrix function of $\left(\Delta_x, \Delta_y, \Delta_z, \alpha_x, \alpha_y\right)$ and its derivative. Although the explicit form of the nonlinear function varies and depends on the nonlinear mechanisms, the force/moment vector $\left(F_x^{(b)}, F_y^{(b)}, F_z^{(b)}, M_x^{(b)}, M_y^{(b)}\right)^T$ can still be exactly

calculated. After the bearing force/moment was obtained, using the Lagrangian mechanics, the motion equation can be derived as

$$\mathbf{M}\ddot{\mathbf{q}} + [\mathbf{C} + \mathbf{C}_{\mathrm{m}}]\dot{\mathbf{q}} + [\mathbf{K} + \mathbf{K}_{\mathrm{m}}]\mathbf{q} + \mathbf{F}_{\mathrm{B}}(\mathbf{q}, \dot{\mathbf{q}}) = \mathbf{f}_{\mathrm{RB}} + \mathbf{f} \tag{2.3}$$

where **M** is the mass matrix, **C** is the gyroscopic matrix, $\mathbf{C}_{\mathrm{m}}$ is the damping matrix from the rotating part and the stationary part, **K** is the stiffness matrix from the rotation part and stationary part, $\mathbf{K}_{\mathrm{m}}$ is oscillatory matrix from rotation, $\mathbf{F}_{\mathrm{B}}(\mathbf{q}, \dot{\mathbf{q}})$ is the generalized forces resulting from the nonlinear bearing forces/moments $\left(F_x^{(b)}, F_y^{(b)}, F_z^{(b)}, M_x^{(b)}, M_y^{(b)}\right)^T$ and linear/angular deformation $\left(\Delta_x, \Delta_y, \Delta_z, \alpha_x, \alpha_y\right)$, $\mathbf{f}_{\mathrm{RB}}$ is the generalized force acting on the stationary parts and the rotating parts and **f** is the generalized excitations from the base motion. The shock responses of a linear and a nonlinear FDB model were compared. From the comparison studies, it can be seen that the FDB nonlinearity appears like stiffening springs and dampers. The amplitude of its shock response is less than the one obtained from the linear model.

After the mechanics of HAA, spinning disk, and disk-spindle assembly have been presented, some existing theories on how they are incorporated together in HDD structural shock simulation models are described below.

2.1.2 Existing Theoretical Shock Model of HDD Structures

There are several theories that have been developed so far to model the HDD experiencing shock. They are full finite element theories, reduced mass and stiffness matrices, flexible multi body concepts, and state-space formulation based on mode superposition theory.

2.1.2.1 Full Finite Element Theories

Head-actuator assembly (HAA) and disk are often modeled based on the finite element theory [51-54]. In [51] two finite element software codes (LS-DYNA and ABAQUS/Explicit) were used to simulate the response of a non-operational hard disk drives subjected to tilt-drop. The simulation results were then directly compared with the experimental results. It is shown that the two finite element codes perform reasonably well. In [55] a finite element model of non-operational HDD was created using ANSYS software package. In the analysis, a half sinusoidal shock was applied perpendicular to the disk surface. The minimum shock amplitude required to lift the head off the disk was determined for different shock pulse width. The effects of cover stiffness, disk thickness, actuator arm stiffness, and bearing stiffness on the HDD non-operational shock performance were also investigated.

The effects of linear shock and rotary shock are investigated in [56] also using a full finite element model. The simulation was done using three software packages, Pro/E to develop the geometry, Hypermesh to do the pre- and post-processing and LS-DYNA to do the transient analysis. In [52], the finite element analysis is used to investigate the effect of shock pulse-width on the HDD shock response.

Recently, a free vibration model of a complete HDD was developed using finite element method [57]. In the model, the spinning spindle-disk system with fluid dynamic bearing, the head-actuator-assembly and the base are considered. Result shows the important effect of the motion of the disk on the vibration of the whole HDD.

Due to the complexities of the components, the finite element model may have 100,000 degrees of freedom or more. Hence, using finite element model to analyze the HDD shock response for parametric design studies is time consuming. However, the finite element method is very versatile; it can be used to calculate stress distribution, predict

modal properties of intricate structures, and performed various static analyses. For this reason, other methods usually rely on the finite element technique to obtain some data of the HDD structures.

2.1.2.2 Reduced Mass and Stiffness Matrices

In order to increase the computational efficiency, reduced mass and stiffness matrices are utilized to model the HDD structural components in [58, 59]. However, the mass and stiffness matrices cannot model the large rotational movement [60], and the effect of disk rotation that causes the position of air bearing force to change over time with respect to the disk. The rotational movement/disk rotation is not very important in the vertical linear shock simulation as shown later in section 5.2.4. However, in the rotational shock simulation, it is significant.

2.1.2.3 Flexible Multi Body Dynamics Concept

A theoretical model, that is more comprehensive than the reduced mass/stiffness matrices and also more time-efficient than the full finite element theory, can be formulated using flexible multi body dynamics concepts. Theoretical model of the disk-spindle model of the HDD [61-63] has been developed by Prof Shen based on this theory. This modeling only focuses on the HDD vibration analysis and not the HDD shock response. Using similar concept, the author has created a theoretical model of non-operational HDD with a linear head-actuator assembly [64]. However, the flexible multi body dynamics model of the operational HDD, considering the nonlinearity of the head-actuator assembly and the shock excitation has not been formulated yet.

2.1.2.4 State Space Formulation based on Mode Superposition Theory

In order to predict the HDD vertical-shock response within a few milliseconds, the flexible multi body dynamics concept is 'overkill' [60] because the total rotational movement of the structures will be minute. A more time efficient model can be developed based on mode superposition theory. State space equations based on this theory has been developed for a very simple HAA without considering the disk response and the discontinuities of the HAA [65].

In short, the four existing theories on how the HDD structures can be mathematically modeled for the shock simulation have been described. They are full finite element theory, reduced mass & stiffness matrices, flexible multi body dynamics concept, and state-space mode superposition theory. In the next section, some possible research contributions are stated.

2.1.3 Contribution to the Theoretical Shock Model of HDD Structures

Based on literature review on the existing theoretical models, it is realized that there are two possible significant theoretical advances that can be contributed in the area of HDD structural shock modeling. They are:

2.1.3.1 Flexible Multi Body Dynamics Formulation for HDD Operational Shock Tolerance Prediction; Considering the Discontinuities of HAA

A complete operational-HDD model for shock simulation will be formulated using flexible multi body dynamics concept. Three flexible structural components (*nonlinear* HAA, disk & its spindle and base plate) are considered in this formulation. The structural models are then coupled with the air bearing model.

For the tilt-drop tests calculation, where the rotational movement of HDD is relatively big, the accurate formulation of large rotational motion is important. Hence, the flexible multi-body dynamics formulation provides significant contribution especially because the tilt-drop tests are widely used to assess the shock hardness of disk drives.

The advantages expected from this contribution are that the HDD operational shock model can simulate the large rotational motion accurately and it can have high computational efficiency (better than the full finite element model).

2.1.3.2 State Space Formulation of Operational HDD based on Mode Superposition Theory; Considering the Disk Response & the Discontinuities of the HAA

The accurate simulation of large rotational motion is not efficient for the relatively short (few milliseconds) linear drop-test calculations. That is why a more effective formulation using state-space mode superposition theory is necessary. Advanced state-space formulation based on mode superposition principle will be developed to model modern operational HDD. The nonlinearity of the head-actuator assembly and disk response will be considered. This state-space HDD model will also be coupled with the air bearing model. With this contribution, the HDD operational shock model is expected to be very time-efficient while maintaining reasonable accuracy.

It is worth to note that the two proposed theoretical models mentioned above will be universal; means that their application is not limited to HDD with small form factor.

2.2 *Theoretical Model of the Air Bearing for Shock Simulation*

Before the theoretical dynamics model of air bearing under shock is presented, it is

essential to be aware of the two different processes, in which the air bearing plays its role. They are load/unload process and read/write process (operational state).

2.2.1 Air Bearing in Load/Unload Process

First, the background of the load/unload process is shown, and then followed by the dynamics of air bearing slider during this load/unload.

2.2.1.1 Background of Load/Unload Technology

Load/unload (L/UL) technology [66] is used to protect the slider and the disk during the non-operational mode. In the HDD using this L/UL technology, the slider rests on a ramp located beside the disk (see Figure 1.1). Compared with contact-start/stop (CSS) technology, where the slider rests on the disk surface in a CSS zone (located at the inner part of the disk), the L/UL technology has a number of advantages. Firstly, it completely eliminates the stiction between the slider and the disk during the start-up of the disk. By eliminating the direct contact between the slider and the disk, the L/UL HDD designs are exposed to less wear and usually tolerate more start/stop cycles than their CSS counterparts. Second, the shock tolerance of the HDD in idle mode is improved. This is especially important in small-form-factor HDD which are often used in a dynamic environment due to their portability.

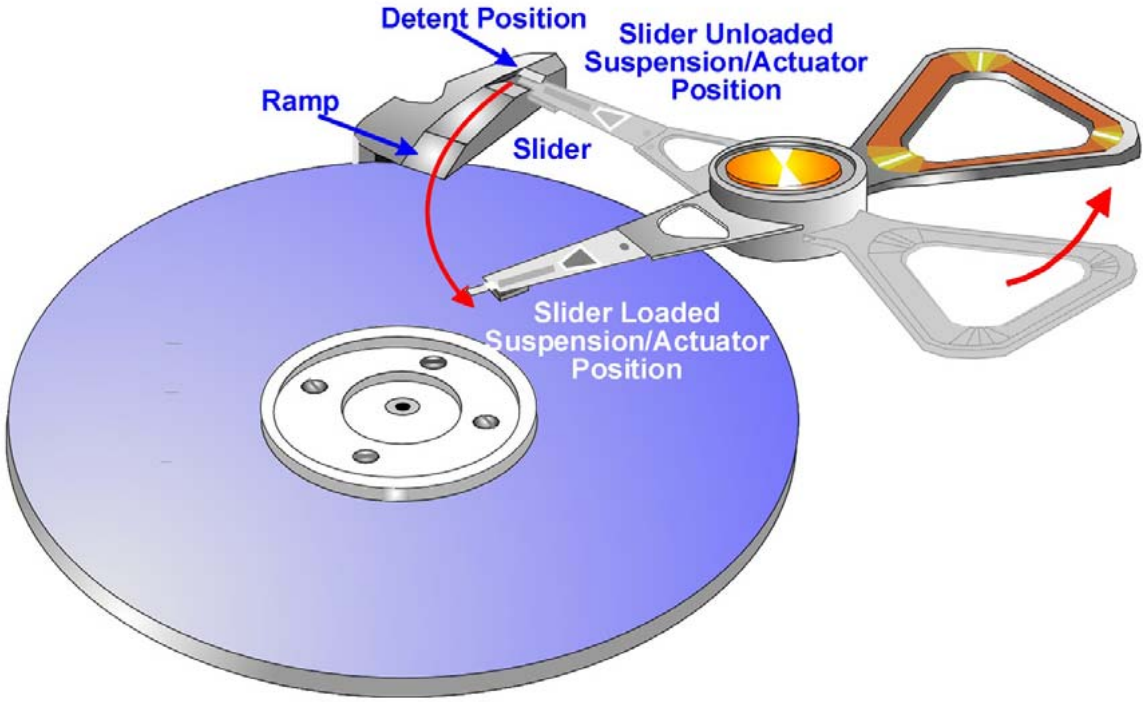

FIGURE 2.4 LOAD/UNLOAD DYNAMICS [67]

2.2.1.2 Dynamics of Air Bearing in Load/Unload Process

During the load or unload process, the onset or disappearance of the air bearing significantly affects the system stiffness. Without the air bearing, the dynamic characteristic of the slider is determined by the structural stiffness of the suspension. However, when the air bearing is present; as during the late stage of the loading process or the early stage of the unloading process; the slider will have a higher resonant frequency due to the very high air bearing stiffness. In this situation, the suspension may be assumed as a static load. The appearance of the air bearing will present some difficulty to the dynamic analysis of the whole U/UL process.

Zeng and Bogy [68-73] evaluated the effect of suspension design, shape of the air bearing surface, disk speed, and vertical slider velocity using numerical simulation. Experiment was set up to directly measure the air bearing forces during the unload process. In [68,

72], a 4-DOF suspension model for L/UL simulation is presented and applied to simulate the L/UL process of a pico slider.

In [74], two different sub-ambient pressure type sliders were investigated during the loading and unloading numerically and experimentally. The FE model presented in [75] was adopted in the numerical simulation. The actual HDD components such as the disks, heads VCM and ramp blocks were used in the experiment. The experiment is elaborately designed so that the wear caused by load and unload can be observed separately. The results show that the wear of the disk surface caused by loading is not greatly affected by the number of cycles, the rotational disk speed, or the air bearing design. However, during unloading, it was found that the disk wear increases with increasing number of unload cycles, increasing vertical unload velocity, and increasing disk rotational speed. In general, wear during unloading was larger than wear during loading in all their experiments. Properly designed ramps can improve the unloading performance. A larger dimple preload can suppress the pitch oscillation during loading, thereby improving the loading performance.

The load/unload process typically takes place in less than 100 milliseconds. Shock response prediction during load/unload process is not important because external shock excitation very seldom happens during the load/unload. The shock excitation mostly happens when the air bearing slider is in read/write process (operational mode).

2.2.2 Dynamics of Air Bearing Slider in Operational Mode

During normal operational mode, the slider is supported by the air bearing as it flies over the disk surface. All the forces acting on the slider are shown in Figure 2.5. They are air bearing force, suspension force and moment, shear and drag forces, contact force,

intermolecular force, and electrical force.

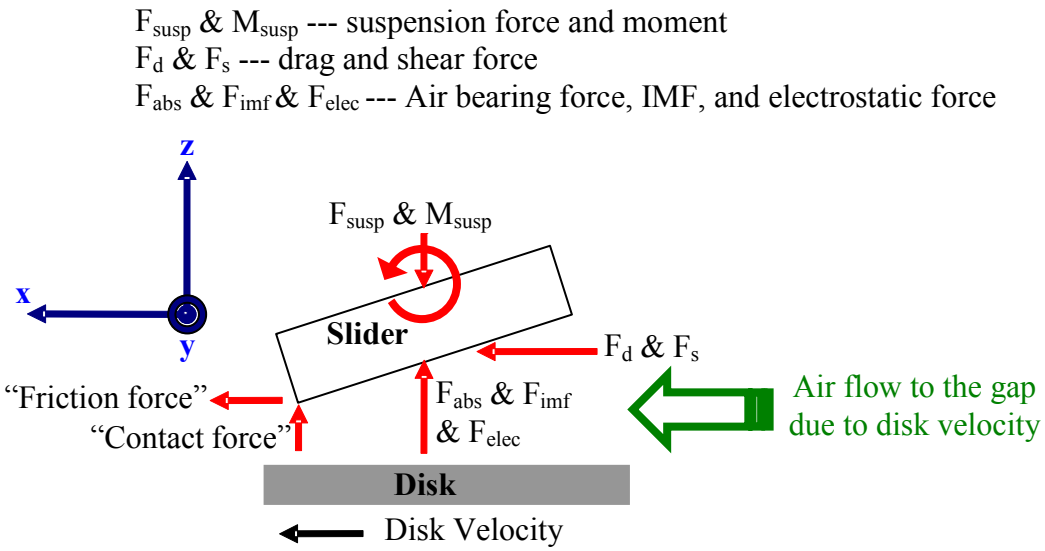

FIGURE 2.5 A FREE BODY DIAGRAM OF THE FORCES ACTING ON THE SLIDER BODY

In Figure 2.5 the moments are considered indirectly; the forces in the free body diagram are applied not at the CG of the slider but at a certain distance (moment arm) from the slider CG. To further illustrate this, the example of the air bearing force is used as follows. Figure 2.6(a) shows the air bearing response obtained in term of its pressure value. The pressure can be converted into point force acting on certain distance from slider CG (Figure 2.6 (b)). This type of force is the one shown in Figure 2.5 and hence there is no need to show the moments. In the actual calculation, the force and moments acting on CG (Figure 2.6 (c)) are considered.

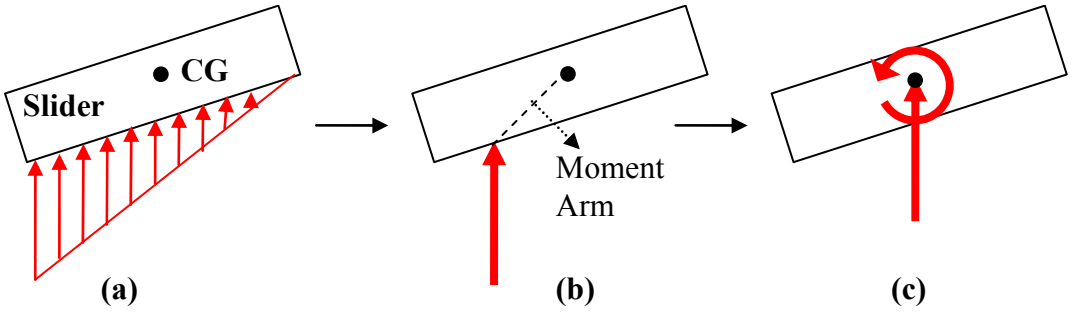

FIGURE 2.6 FORCES APPLICATION IN THE FREE BODY DIAGRAM OF THE SLIDER

The next two parts of this section give insights on how to calculate these forces. The first part presents the theory behind the air bearing force and the next part describes the rest of the force that affect the air bearing.

2.2.2.1 Air Bearing Force

The air bearing force depends on the pressure distribution exerted by the air on the slider surface and it is governed by gas lubrication equation (compressible Reynolds equation) shown in (2.4) [76].

$$\frac{\partial}{\partial x}\left(ph^3 \frac{\partial p}{\partial x} \right) + \frac{\partial}{\partial y}\left(ph^3 \frac{\partial p}{\partial y} \right) = 6\mu\left(U\frac{\partial ph}{\partial x} + V\frac{\partial ph}{\partial y} \right) + 12\mu\frac{\partial ph}{\partial t} \tag{2.4}$$

where p is the pressure acting on slider surface, h is the spacing between disk an slider, μ is air dynamic viscosity, U and V are the local disk velocity in the x and y direction.

In gas lubrication problem under submicron spacing, the flow in the gas film can not be considered as continuum flow because the molecular mean free path is not negligible compared with the spacing [77]. For that reason, it is treated as rarefied gas flow based on kinetic theory. One of the important parameters in the gas theory is the Knudsen number (ratio of molecular mean free path to the characteristic length of the flow or in this case the spacing). When the Knudsen number is greater than 0.01, a slip correction factor Q is added to account for rarefaction effect or slip at the boundaries as shown in (2.5) [78].

$$\frac{\partial}{\partial x}\left(Q(Kn)ph^3 \frac{\partial p}{\partial x} \right) + \frac{\partial}{\partial y}\left(Q(Kn)ph^3 \frac{\partial p}{\partial y} \right) = 6\mu\left(U\frac{\partial ph}{\partial x} + V\frac{\partial ph}{\partial y} \right) + 12\mu\frac{\partial ph}{\partial t} \tag{2.5}$$

where $Q(Kn)$ is a slip model (a function of Knudsen number).

There are various slip models that have been proposed and one of the most popular is

described by Fukui [79], in which the Boltzmann equation is used to study the characteristics of the flows with arbitrary Knudsen numbers. The equation is approximated with the assumption that the velocity distribution of the flow is in isotropic equilibrium (the Mach number is much smaller than one). Taking into consideration the flow rate of the lubricant, which is estimated using a variational method, a generalized lubrication equation is obtained as shown in (2.6).

$$\nabla \bullet \left[\overline{Q}_p(D)PH^3\nabla P\right] = \frac{6\mu l}{p_a h_0^{\,2}}\nabla \bullet (\bar{\Psi}PH) + \frac{12\mu\omega_0 l^2}{p_a h_0^{\,2}}\left(\frac{\partial(PH)}{\partial\bar{\tau}}\right) \tag{2.6}$$

where ∇ is the differentiation operator, X and Y are the non-dimensional coordinates (x/l and y/l), D is inverse Knudsen number ($\sqrt{\pi}/2Kn$), $Kn = \lambda/h$; where $\lambda = \mu\sqrt{2\pi RT_0}/2p$; R is gas constant and T_0 is characteristic temperature, $Q_p(D)$ is the flow rate of Poiseuille flow, $\overline{Q}_p(D)$ is the relative flow of Poiseuille flow; $Q_p(D)/(D/6)$, P is the non-dimensional pressure; p/p_a, p_a is the ambient pressure, H is the non-dimensional spacing; h/h_0, h_0 is the minimum (characteristic) spacing, l is the slider length, $\bar{\Psi}$ is the disk velocity; $Ui + Vj$, ω_0 is the disk angular velocity, and $\bar{\tau}$ is the non-dimensional time.

When surface accommodation coefficient α is nearly equal to one $Q_p(D)$ can be calculated as follows.

$$Q_p(D) = -\frac{1}{D} + \frac{1}{\Delta}\left(C_{11} - \frac{D^2}{6}C_{12} + \frac{D^4}{144}C_{22}\right) \tag{2.7}$$

where $C_{11} = \frac{1}{\sqrt{\pi}}\left\{8 - \frac{\sqrt{\pi}}{12}D^3 + \frac{D^4}{16} - (8D + 2D^3)T_0(D) - \left(16 + 8D^2 + \frac{D^4}{8}\right)T_1(D) - D(16 + D^2)T_2(D)\right\}$,

$C_{22} = \frac{1}{\sqrt{\pi}}\{1 - 2T_1(D)\}$,

$C_{12} = \frac{1}{\sqrt{\pi}}\left\{2 - \frac{\sqrt{\pi}}{2} + \frac{D^4}{4} - 2DT_0(D) - \left(4 + \frac{D^2}{2}\right)T_1(D) - 2DT_2(D)\right\}$,

and $\Delta = C_{11}C_{22} - C_{12}^2$. The function, $T_n(x)$, is the Abramowitz function defined by $T_n(x) = \int_0^\infty t^n \cdot e^{\left(-t^2 - \frac{x}{t}\right)} dt$

In practice, several interpolation functions or Poiseuille flow rate databases for different α are often employed to calculate $Q_p(D)$ in computer simulations [80, 81].

2.2.2.2 Other Forces Affecting the Air Bearing Slider

The suspension force and moment acting on the slider can be derived from the structural analysis theories described in section 2.1.2 above. The drag force and friction force, including the moments they create, are negligible due to the relatively small pitch angle (in the order of 10^{-5} radians) [82]. However, the viscous shear force contributed by the air flow is quite significant [83, 84].

The contact force can be obtained using Greenwood-Williamson contact model [85], in which the roughness of the disk surface is considered as an accumulation of asperities whose apexes have the same radius. It is then assumed that the heights of asperities follow a Gaussian distribution and there is no interaction between asperities. The contacts are considered elastic in this model. The contact force P is then given by:

$$P = \frac{4}{3}\eta\tilde{A}E'\beta^{\frac{1}{2}}\sigma^{\frac{3}{2}}F_{\frac{3}{2}}(h); \qquad F_{\frac{3}{2}} = \int_h^\infty (s-h)^{\frac{3}{2}}\Phi^*(s)ds; \qquad \Phi^*(s) = \frac{1}{\sqrt{2\pi}}e^{-\frac{s^2}{2}} \qquad (2.8)$$

where η is surface density of asperities, $\tilde{A}$ is nominal contact area, E' is the effective Young's modulus, β is radius of curvature of asperities, σ is standard deviation of the asperity heights, $F(h)$ is scaled height distribution, h is standardized separation, s is standardized asperity height, and $\Phi(s)$ is standardized height distribution (Gaussian).

When the flying height (FH) of the slider is very low (less than 6 nm), it has been shown experimentally that the HDI may become unstable [86-88]. Two forces were found to be the possible cause of this instability - intermolecular forces (IMF) and electrostatic forces.

The intermolecular forces ($F(r)$) are close range forces. They consist of a relatively long range attractive force and a short range repulsive force, and they can generally be modeled by the Lennard-Jones' equation below.

$$F(r) = \left(-\frac{A}{6\pi r^3} + \frac{B}{45\pi r^9} \right) \Delta x \Delta y \tag{2.9}$$

A and B are the effective Hamaker constants between the slider and the disk. r is the distance between the particles/ molecules/ atoms. $\Delta x \Delta y$ is the effective area of element on which the slider and the disk interact. From (2.9) it can be seen that the attractive components of intermolecular force is determined by the Hamaker constant A. A typical range of this attractive force is about 10 nm [87] while the range of the repulsive force is around 0.05 nm. Since the typical FH is from 3 to 18 nm, the repulsive force can be neglected.

For the HDI having multiple layers (as shown in Figure 2.7), the Hamaker constant A_{ijkl} is given by a multilayer model derived for four layers interaction.

$$A_{ijkl} = \frac{3hv_e}{8\sqrt{2}} \frac{(n_i^{\,2} - n_j^{\,2})(n_k^{\,2} - n_l^{\,2})}{(n_i^{\,2} + n_j^{\,2})^{1/2}(n_k^{\,2} + n_l^{\,2})^{1/2}\left\{(n_i^{\,2} + n_j^{\,2})^{1/2} + (n_k^{\,2} + n_l^{\,2})^{1/2}\right\}} \tag{2.10}$$

where h is Planck's constant; 6.626×10^{-34} J.s, v_e is ionization frequency; 3×10^{15} Hz, ε_i is permittivity of material i ($C^2.J^{-1}.m^{-1}$), and n_i is reflective index of material i.

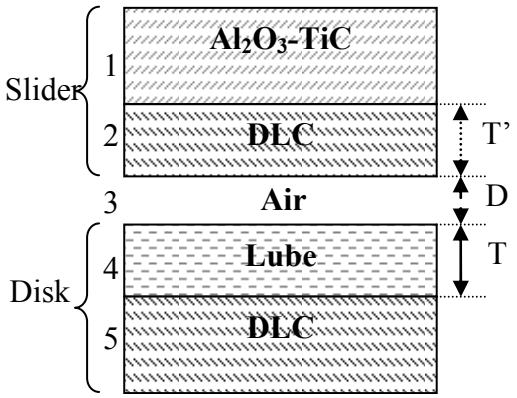

FIGURE 2.7 CROSS SECTION OF MULTILAYER HDI

The intermolecular force $F(D)$ is then given by a multilayer model equation (Matsuoka et al. as cited in [87]).

$$F(D) = -\frac{1}{6\pi}\left[\frac{A_{2343}}{D^3} + \frac{A_{2353}}{(D+T)^3} + \frac{A_{1343}}{(D+T')^3} + \frac{A_{1353}}{(D+T+T')^3}\right]\Delta x\Delta y \tag{2.11}$$

where D is air thickness, T is thickness of disk lubricant, and T' is thickness of DLC layer in the slider.

The second force that causes the HDI instability is the electrostatic force. The electrostatic force is an attractive force due to the electrostatic interaction between the disk and the slider [88], which can be calculated as

$$F_{elec}(D) = -\frac{\varepsilon_o k_e V^2 \Delta x \Delta y}{z^2} \tag{2.12}$$

where ε_o is permittivity constant (8.85×10^{-12} F.m^{-1}), k_e is dielectric constant (1 for air), V is potential difference between the slider and the disk.

In conclusion, when the slider is flying at a relatively low separation from the disk, the significant forces acting on it are the suspension force, the shear force, the contact force, the air bearing force, the intermolecular force, and the electrostatic force. After all the forces acting affecting the air bearing slider has been described, how these forces are represented and predicted in the HDD shock simulation are given next.

2.2.3 Existing Theoretical Shock Models of Air Bearing

The existing theoretical shock models can be classified into two existing groups. The first one is the constant stiffness model (linear spring model) and the second one is the full air bearing model.

2.2.3.1 Constant Stiffness Model (Linear Spring Model)

Some researchers have used simple linear springs combinations (Figure 2.8) to represent the air bearing in the HDD shock simulation [89, 90]. The stiffness value is calculated by solving (2.5) at the steady state condition. The purpose of using the linear spring as air bearing is to increase the simulation-time efficiency. But this linear-springs model is not appropriate for shock simulation because during shock the air bearing behavior is actually nonlinear [91, 92] as depicted in Figure 2.9.

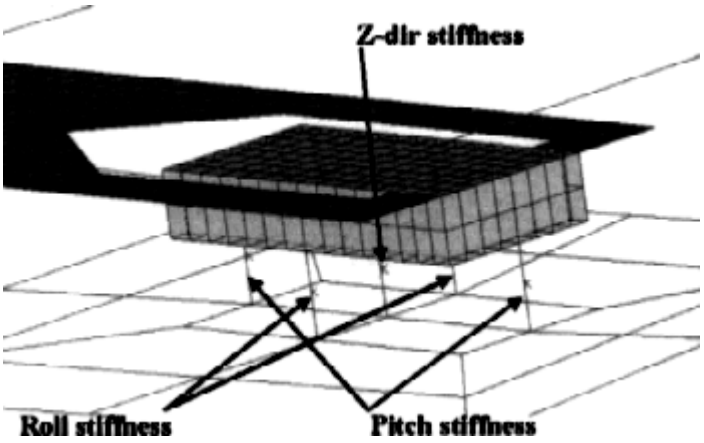

FIGURE 2.8 LINEAR SPRING COMBINATION TO REPRESENT AIR BEARING

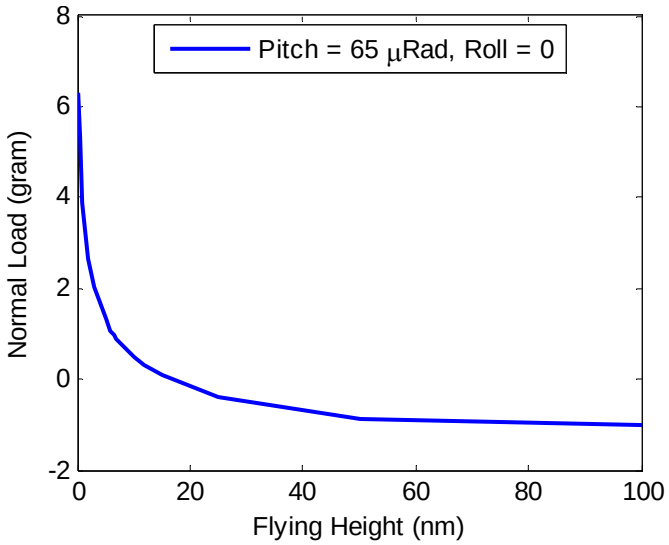

FIGURE 2.9 NONLINEAR RELATIONSHIPS BETWEEN FLYING HEIGHT AND AIR BEARING FORCE

The flying height is the spacing between the trailing edge center (TEC) of the slider and the disk. Pitch is the transverse angle formed by the disk surface and slider surface in micro-radians. Roll is the longitudinal angle formed by the disk surface and slider surface in micro-radians.

From Figure 2.9 it can be seen that for flying height below 10 nm, the air bearing force shows significant nonlinearity with respect to the flying height. Additionally, the air bearing force also behaves nonlinearly with respect to pitch angle and roll angle as shown

in Figure 2.10 and Figure 2.11.

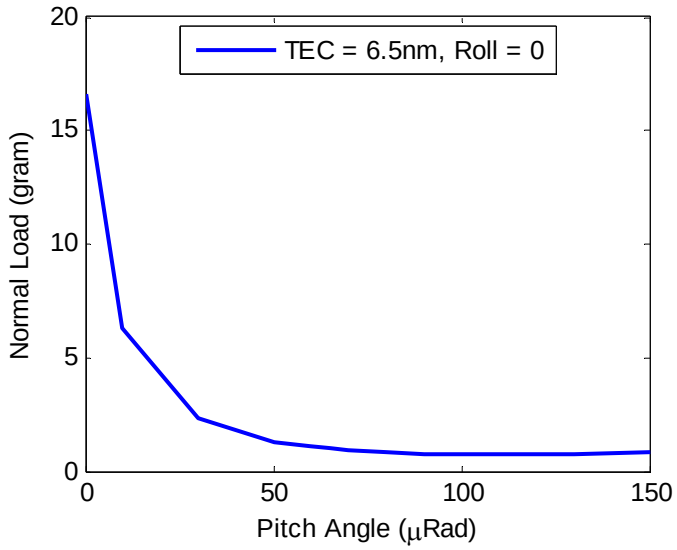

FIGURE 2.10 NONLINEAR RELATIONSHIPS BETWEEN PITCH ANGLE AND AIR BEARING FORCE

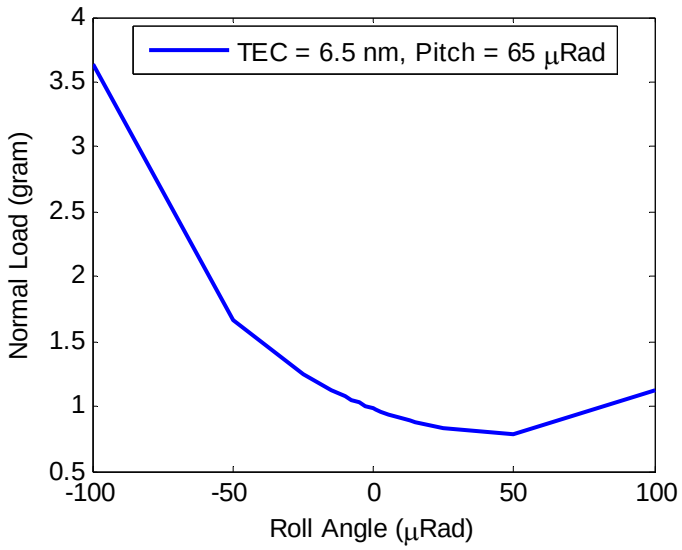

FIGURE 2.11 NONLINEAR RELATIONSHIPS BETWEEN ROLL ANGLE AND AIR BEARING FORCE

When strong shock happens, the air bearing spacing is expected to experience a relatively large variation; the spacing can then reach a quite low value (less than 10 nm). This means that during the shock, the air bearing stiffness should change. The changes in the air bearing stiffness values give rise to different air bearing forces and moments response

as shown in [76].

In summary, the use of linear spring to represent air bearing in the shock simulation results in inaccurate forces and moments, and incorrect slider movement.

2.2.3.2 Full Air Bearing Shock Model

Basically, the full air bearing shock model calculates the air bearing response by solving various related mathematical equations described in section 2.2.2. The most complex one is the compressible Reynolds equation. Usually finite volume method [93-95] is used to solve it. The advantage is that the air bearing response can be calculated with high accuracy. However, the shock response simulation takes considerably long period of time because at every time step the compressible Reynolds equation needs to be reevaluated. Also, additional computation time will be needed when the air bearing slider profile is more complicated. Hence, full model may not be an efficient method for design optimization studies where many parameters are involved and time is limited.

From the review above, it can be seen that the existing air bearing shock models consists of two extremes. The first one (the linear spring model) oversimplifies the air bearing dynamics, resulting in inaccurate prediction. On the other hand the full model complicates the shock simulation by reevaluation of governing equations at every time step, causing low computational-efficiency.

2.2.4 Contribution to the Air Bearing Shock Modeling

Based on the previous literature review, it appears that a possible significant contribution, which can be made to the development of the theoretical shock model of the slider plus air bearing, lies in setting up method or concept that can lead to time-efficient shock

response simulation having reasonable accuracy. The basic analytical consideration for the concept is given as follows.

It is understood that the slider and the air bearing form a dynamic system that can react very fast, relative to the duration of the shock event and the significant motions of other HDD components [96]. This comes from observing that the dominant frequency associated with a 0.5 ms half-sinusoidal pulse excitation is up to 2 kHz [97], whereas the fundamental air bearing resonance frequency is typically well over 100 kHz in modern HDD. Therefore, from the perspective of the air bearing, the dynamic response of HDD structural components merely causes a change in boundary conditions that happen slow enough for air bearing equilibrium to be maintained (in the absence of head disk contact).

From a constant mass-spring-damper system point of view, it can be seen that if the fundamental frequency of the air bearing is 100 kHz and the excitation pulse is 2 kHz, then the air bearing response falls in the stiffness controlled region as depicted in Figure 2.12. In that region, the air bearing dynamics response (x) is expected to be the same as its static response (δ_{static}), regardless of large variation of damping ζ. This almost-static (quasi-static) notion, if applied in air bearing shock modeling, is expected to accelerate the dynamics response calculation and at the same time produce quite accurate result. The quasi-static treatment has also been used in [98], in which the CML air bearing program was used to determine the air-bearing compliance matrix at different slider attitude. The compliance-matrix data were then transformed to force-displacement, force-rotation, moment-displacement, and moment-rotation curves. The result shows that the velocity profiles between the linear and non-linear air bearing are quite different. This paper however is very brief and does not give comparison with full finite volume air bearing

model.

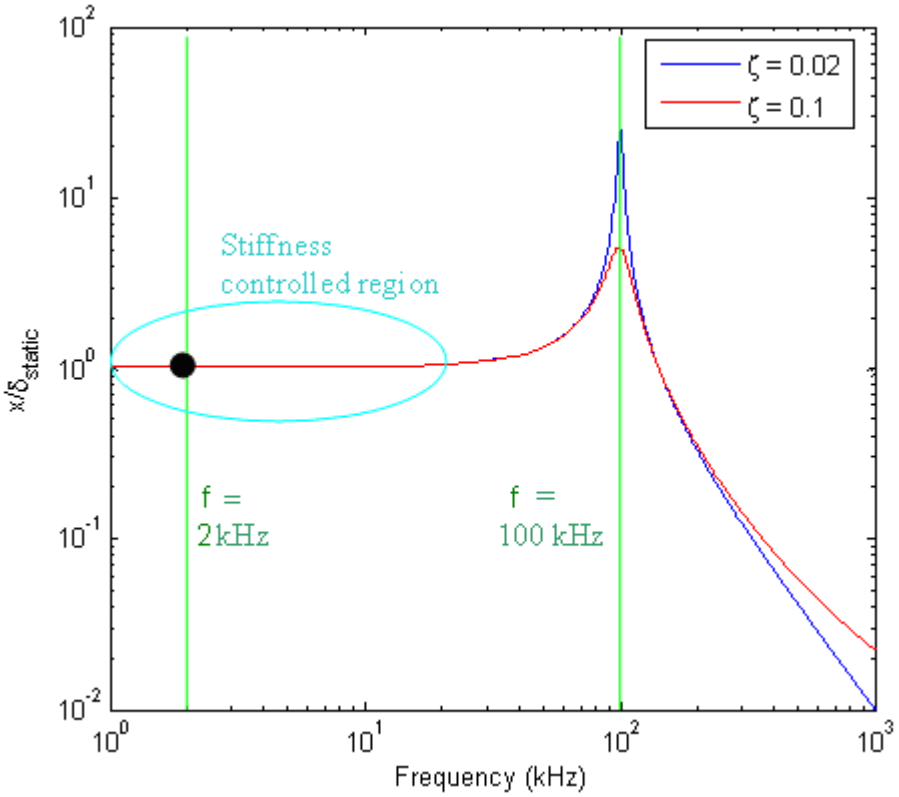

FIGURE 2.12 ESTIMATED TRANSMISSIBILITY CURVE FOR AIR BEARING

In chapter 4, this quasi-static concept will be investigated in detail by comparing the quasi-static air bearing shock model with a complete finite volume air bearing model. Subsequently, the quasi-static concept will be extended to increase its accuracy.

2.3 *Coupled Structural and Air Bearing Model*

HDD shock tolerance is defined as the minimum half-sine shock magnitude that causes damages on the magnetic surface on the disk. To predict the shock tolerance of HDD, the structural model and the air bearing model needs to be coupled with each other.

2.3.1 Existing Coupled Model

There are three types of coupled models that have been used in the HDD shock simulation; basic coupled model, indirectly coupled model, and directly coupled.

2.3.1.1 Basic Coupled Model

Finite element (FE) structural shock model is combined with the linear-springs air bearing model to simulate the shock response of the HDD. Usually FE transient analysis is used to solved the shock response (as in [90]). This is not the best approach for predicting the shock tolerance; it is time consuming when performing analysis at the system level, since the system involves many degrees of freedoms. Besides that, the use of the linear springs to represent the air bearing is not appropriate because during shock the variation in the flying height is relatively large; at low flying height region, the nonlinear behavior of the air bearing becomes significant [91].

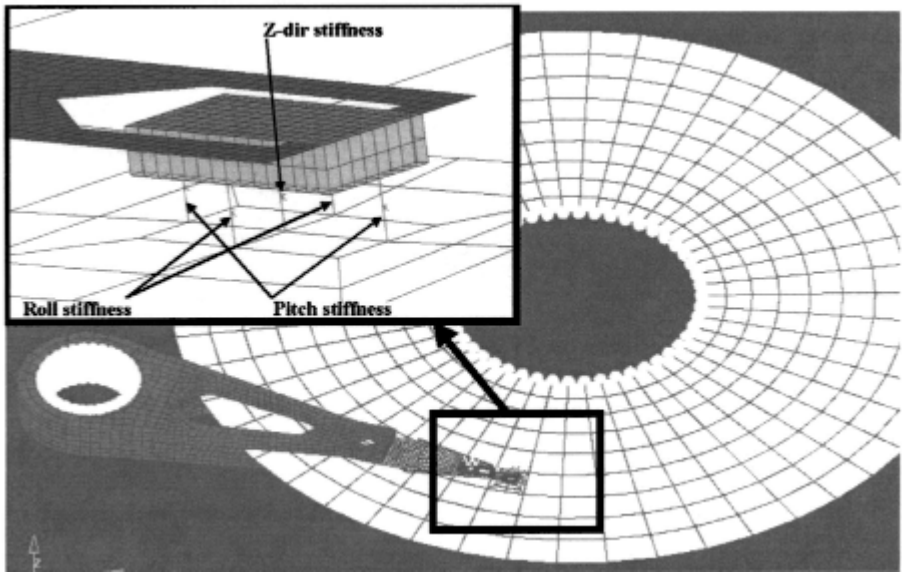

FIGURE 2.13 BASIC COUPLED MODEL (FE STRUCTURAL MODEL + LINEAR SPRING AIR BEARING)

This basic model has been improved and optimized over the years in the HDD industry due to its simplicity and ease of modeling. HDD engineers can straightforwardly

produce the FE model from available solid models. Then, several spring elements can be added immediately to the FE model to represent the air bearing. Next, the mode superposition method is used to reduce the computation time. With an appropriate selection of air bearing stiffness [99], this basic model can predict the *trend* of air bearing force response with reasonable accuracy.

This improved basic model is good to predict whether certain design changes reduce or increase the variation of air bearing force during shock event. However, to predict the shock tolerance, knowing the trend of the air bearing force response is not sufficient; more comprehensive air bearing models are necessary [96].

2.3.1.2 Indirect Coupled Model

Subsequently, the FE structural model is indirectly coupled with an air bearing model as in [76, 100-104]. This method is widely used because the air bearing is relatively very stiff that any sufficiently stiff linear spring will hold the slider to the disk. Besides that, the forces fed back to the arm are too small to affect arm response significantly.

The shock simulation is divided into two steps. In the first step, a finite element model of the disk, suspension, slider and air bearing is used to find the structural force response. In the finite element model, the linear springs are used to represent the air bearing. In the second step, the structural force response obtained in the first step is used as input data for the air bearing simulation and the dynamic flying attitudes are calculated. This kind of two-step method was later used in the optimization of air bearing contours for the shock performance of HDD [105].

A similar method [96] was also used to investigate the shock response of the HDD. The difference was that the motions of the disks/arm were obtained experimentally by the laser Doppler vibrometer (LDV), not by the finite element method.

The use of the linear springs as air bearing model in the finite element analysis and the indirect coupling method do not represent the real system where the air bearing behaves nonlinearly and the coupling between the air bearing and the structural components happen simultaneously. A direct coupling method is then preferred.

2.3.1.3 Direct Coupled Model

In [58, 59, 106] the air bearing model and the HDD structural model are directly coupled. At every time-step the two models communicate with each other. The air bearing modeling is done using the CML dynamics air bearing simulator software, while the ANSYS finite element analysis is used to calculate the structure response (in [59]) or to generate mass and stiffness matrices of the structures (in [58, 106]). The method used in [59] was computationally expensive because at each time step data should be exchanged between ANSYS and CML. To increase the computational efficiency, the mass and stiffness matrices obtained from ANSYS are embedded into the CML dynamics simulator and used to obtain structural response [58, 106]. Still, the shock response simulation takes considerably long computation time because at every time step the compressible Reynolds equation needs to be reevaluated. Hence, it may not be an efficient method for design optimization studies where many parameters are involved.

The direct coupling method used in [58, 59] also requires some modifications to the structural model; the slider needs to be modified into a mass element connected to the flexure by some rigid beams (as shown in Figure 2.14) [33].

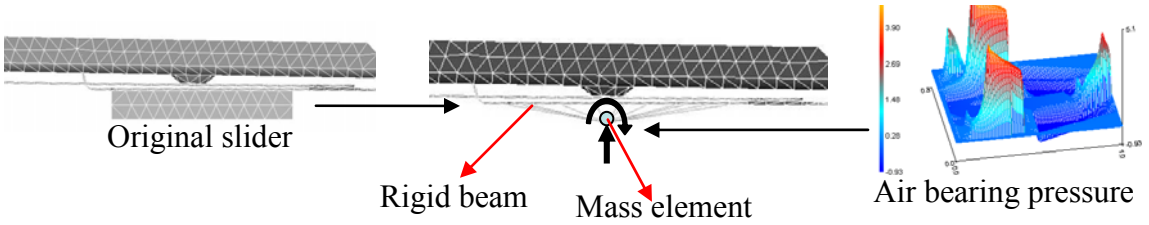

FIGURE 2.14 A DIRECT COUPLING METHOD

It should also be noted that in the models mentioned above the effect of the disks spin is not included (the locations of the forces acting on the disks (e.g. from the air bearing) are fixed).

Summing up, there have been various coupled model developed: basic model, indirectly coupled model, and directly coupled model. The direct coupled model is preferred due to its superiority in representing the actual fluid and structural interaction in the head-disk interface. In the next sub-section, several possible contributions to the diversity of direct coupled model are given.

2.3.2 Contribution to Diversity of Direct Coupled Models

There are two additional coupled models that will be contributed. The first one is the combination between the flexible multi body dynamics structural model and full air bearing model. The second one is the coupling between the state-space structural model (formulated based on mode superposition theory) and the quasi-static air bearing model. The first model will be able to give comprehensive prediction on both structural and air bearing shock response, while the second coupled model will be able to predict the HDD shock tolerance in a highly time-efficient manner.

So far in the literature review, the theoretical shock model of the HDD structures (the 'body'), the air bearing (the 'heart'), and their couplings have been discussed. With good theoretical shock model, the shock robustness of the structures and the air bearing can

be further optimized. Having a robust 'body' and 'heart' is excellent, but without appropriate 'skin' (vibration isolator) the HDD still has a high chance to fail.

2.4 *Design and Analysis of Vibration Isolation for HDD*

In this section the existing researches with the purpose of solving the vibration problems of the HDD, is presented. It is then followed by the possible contributions that can be made to advance the vibration isolation in HDD.

2.4.1 HDD Vibration Problem

Before discussing the existing theories/method related with solving HDD vibration problems, it is important to examine the source of vibration in the HDD. Four major noise and vibration sources in the HDD are the spindle-disk assembly, VCM/HAA system, base/cover, and external environment.

2.4.1.1 Vibration from Spindle-disk Assembly

The spindle-disk assembly consists of a number of disks mounted on a spindle motor, which is enclosed by a hub. A typical spindle motor has a stator firmly attached to a spindle shaft. The stator is energized by a voice coil system inside the hub. When the stator is energized, the hub and disks rotate simultaneously. Bearings separate the hub from the shaft and keep rotation smooth. As the demand for higher storage capacity and better performance has increased, the track density has reached 100,000 tracks per inch (TPI) [107]. The drive speed has exceeded 15,000 rpm. Accordingly, the spindle-disk assembly is subjected to increased amounts of acoustic and mechanical energy. A great amount of this energy is transmitted to the components of the spindle-disk assembly, where it causes reliability and performance problems, such as whirling-mode vibration

which increases the degree of non-repeatable run-out (NRRO) caused by bearing defects. The amplitudes of the NRRO generally increase with increasing drive speeds, and are creating substantial problems in today's high-speed drives [48].

2.4.1.2 Vibration VCM/HAA System

The actuator subsystem contains the actuator arm and the rotary ball-bearing component. When the voice coil is energized by the input current from flex circuit cable (magnetization process), it creates a magnetic field between the top and bottom magnetic plates and applies a mechanical torque to the actuator. The torque from the voice coil motor causes the actuator arm and the head-gimbal assembly (HGA) to rotate simultaneously (seeking motion). The magnetization of the voice coil not only generates significant acoustic noise, but also contributes considerable mechanical disturbance to the actuator element.

2.4.1.3 Cover/Bases Vibration

Disk drive covers and bases are normally made of thin aluminum or stainless steel, which easily resonates at higher rotational speeds. The vibration and acoustic noise that come from drive operation (HAA seeking motion) would also run through the edges of the cover and base and the screw holes.

2.4.1.4 Vibration from External Environment

The vibration level from the external of the HDD is quite high when the HDD is used in mobile applications. Severe shock is experienced by the HDD when its user accidentally drops it to the hard floor. The HDD also undergoes harsh vibration when it is being used in rough environment such as battlefields. All this external excitation may damage the

HDD if proper vibration isolation system is not used.

After discussing the four major noise and vibration sources in the HDD (the spindle-disk assembly, VCM/HAA system, base/cover, and external environment), let us take a look on the existing method/theories to deal with them.

2.4.2 Existing Theories/Method to Overcome HDD Vibration Problem

Besides optimizing the structural and air bearing design parameter, the research efforts in handling the HDD vibration problems can be categorized into three big groups; the first group develops more robust HDD servo, the second group devises more reliable drop/free fall detection method, and the third one designs better HDD vibration isolation/damping.

2.4.2.1 Robust HDD Servo Control

The first group basically deals with the development of robust servo control algorithm/mechanism. There have been *numerous* researches done in this group, such as reduction of external vibration in hard disk drives using adaptive feed-forward control [108], compensation of the HDD vibration during jogging/walking using low frequency disturbance feed forward control [109], use of MEMS based accelerometers for the compensation of the effects of self-induced and external vibrations in HDD [110], rejection of narrow-band disturbances using a general second-order phase lead peak filter [111], suppression of vibration during short-span seeking mode in HDD based on multi-rate feed-forward control [112], etc.

2.4.2.2 Reliable Drop/Free Fall Detection

The objective of drop/free fall detection is to reliably detect a fall and ‘park’ the

read/write head prior to impact event. The conventional approach (to measure the acceleration using the acceleration sensor and react based on acceleration threshold with timing reaction) is found ineffective in predicting the free fall [26]. Hence, more advanced algorithms are being developed, such as the one in [113]. The free fall detection is performed not only depending on the acceleration, but also depending on the calculated area value between the acceleration threshold and the current acceleration measurement below the threshold.

Better drop sensors are also employed. A predictive drop sensor, composed of a thermal accelerometer and an electronic controller, has been shown to achieve fast response in predicting the impending fall and enables the protection function before real impact occurs [114]. By the optimization of filter weighting coefficients, predictions of up to 35 ms have been demonstrated and that can provide reliable protection against drop shock.

However, this drop detection is more complicated than one first imagine because most of the time the drop motion is not a simple free-fall. It often mixes with spinning motion. Not only that, the center of mass may not be constant (such as in flip-phones and laptop) and real-life motions (tapping with thumbs, dancing, running, etc.) add further *complexity* [26].

2.4.2.3 Effective Vibration Isolation

There have been many basic theories formulated on how to optimally isolate/damp vibrations in/experienced by an object [115-122]. However, to create an effective vibration isolation of complicated machinery such as the HDD, more advanced theories/methods need to be developed. That is why there are many published research work devoted to HDD vibration isolation [123].

The research in the HDD vibration isolation is further classified based on the locations of vibration sources (spindle-disk assembly, VCM/HAA, base/cover, external environment).

(a) Vibration Isolation for Spindle-Disk Assembly

To solve the problems related to the spindle-disk assembly vibration, various damping treatments have been evaluated. For example, a whirl damper design addresses the whirling-mode vibration [124]. The whirl damper, made of a layer of viscoelastic damping polymer and a layer of stainless steel, works like a circular washer. Other interesting ideas for solving the problem of spindle motor vibration include damping treatments on the stator/spacer. Various designs of this type of damper have been proposed in [125]. Test results show that disk vibration is significantly lowered when a constrained-layer damper is added to the spacer.

Investigations of fluid-film or hydrodynamic bearings for spindle motors continue to appear in the literature [50, 126-130]. The advantages of these fluid-like bearings include improvement of non-repeatable run-out and reduction in acoustic noise. These are especially important for drives rotating at high speeds.

The other important source of spindle-disk assembly vibration is the disks themselves. Disk vibration (or disk flutter) results from unsteady airflow, or windage, over the disk surface. The problem is made worse when thinner and lighter disks are used. To reduce the effects of disk flutter on tracking performance, damping is added into disk substrates. The damped disk is made of two thin layers of aluminum with a layer of high-performance viscoelastic polymer in the middle. The new damped disk increases the damping properties of the disk and considerable improvements in tracking performance have been achieved by using this new damped-disk design [131]. Effect of adding

dynamics absorbers on the rotating disks was also examined in [132], in which the relationship between the location of the dynamics absorber and the effect in the vibration control was investigated numerically.

(b) Vibration Isolation for VCM/HAA assembly

To overcome the undesirable motion caused by vibration resonance in the HAA components, lighter and stiffer suspension that have higher natural frequencies have been manufactured. A smaller and lighter slider design further reduces the amount of inertial force, making the slider more stable during flying. The trend to decrease the size of the head-gimbal assembly to improve shock performance is limited by the current materials and manufacturing technology available. It is also limited by cost. HDD engineers then look for other possible solutions, such as passive damping treatments.

Suspension dampers have been widely used to reduce head-gimbal assembly (HGA) resonance. One of the works in suspension damping involves the insertion of a damping polymer into the multilayer suspension element [133]. This yields a damped suspension element where damping been designed into the suspension structure. However, adding damping element in suspension increases the effective mass of HGA, and subsequently reduces the shock performance of HDD [30].

Recently, damping is used in the arm and VCM. The damping devices are installed on the arm and hollow space within the voice coil motor on the HDD to suppress the quasi-rigid body mode caused by the flexibility of the arm pivot [134]. In [135] a dynamic absorber is introduced to assist in controlling the acceleration of the actuator arm. Subsequently, a dual-mass dynamic absorber is embedded within the VCM to restrain the VCM vibration modes and the quasi-rigid vibration of the HAA [136].

Advanced alloys with high damping such as High Damping Stainless Alloy (HIDAS) were developed and applied for suppression of noise or vibration in the HDD. These alloys have high strength (1400Mpa) as well as high damping capacity (10-20%). All data obtained showed better results compared with other materials [137]. High cost and quality control would be the remaining problems.

(c) Vibration Isolation for Base/Cover

Disk drive covers and bases are normally made of thin stainless steel, which easily resonates at higher rotational speeds. The acoustic noise that would come from drive operation would also run through the edges of the cover and base and the screw holes. Significant progress has been seen in controlling the noise and vibration transmitted through these areas. The popular cover damper used in hard disk drives was first introduced in 1993 when the drive speed increased to 5400 rpm [123]. The cover damper, based on the constrained-layer damping treatment [138] was strategically placed on the cover above the spindle motor area to reduce resonance. Recently, a piezoelectric bimorph was designed and also placed on the drive cover above the spindle motor area to effectively suppress the unwanted vibration of the disk-spindle system [139, 140].

(d) HDD External Vibration Isolation

The vibration isolation placed inside the HDD mainly helps to reduce the vibration caused by the disk spin and/or the HAA seeking motion (self-induced). To effectively protect the HDD from strong external excitation (having magnitude much bigger then the self-induced vibration), an external vibration isolation is a must [141]. In literatures, little attentions have been given to the external vibration isolation of HDD. So far, rubber mounts/pads have been investigated and optimized for HDD vibration protection [142-

144]. However, they do not offer a theory and principles on how to design, test, and evaluate external vibration isolation systems for HDD subject to both shock and random vibration based on well know standard.

2.4.3 Possible Contribution to the Field of HDD Vibration Isolation

From the review above, it is clear that the area of HDD external vibration isolation has not been well addressed. Hence, a research work on how to design, simulate, test and evaluate the vibration isolation systems for operating HDD subject to severe shock and random vibrations based on a well-known standard (such as military standard) will be a significant contribution in the field of HDD vibration isolation. Design concepts on how to achieve satisfactory shock and vibration isolation for HDD will be formulated. The concepts will then be tested and further enhanced by several design case studies.

2.5 *Chapter Summary*

Summary on the theoretical shock model of HDD structures (the ‘body’), the theoretical shock model of the air bearing (the ‘heart’), their coupled model, and the HDD shock and vibration isolation (the ‘skin’) are presented next in several flow diagrams.

2.5.1 Theoretical Model of HDD Structures for Shock Simulation

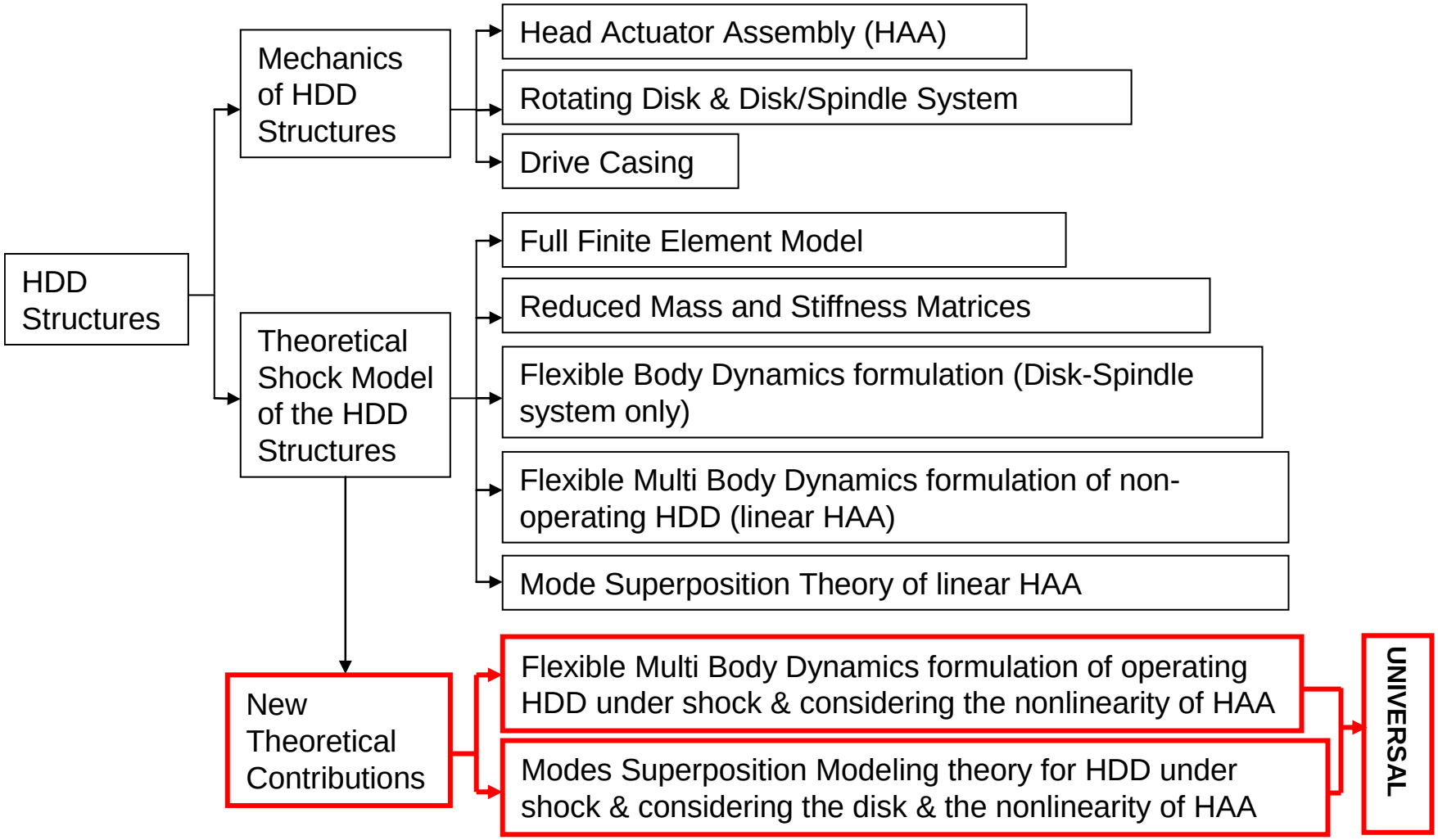

2.5.2 Theoretical Model of the Air Bearing for Shock Simulation

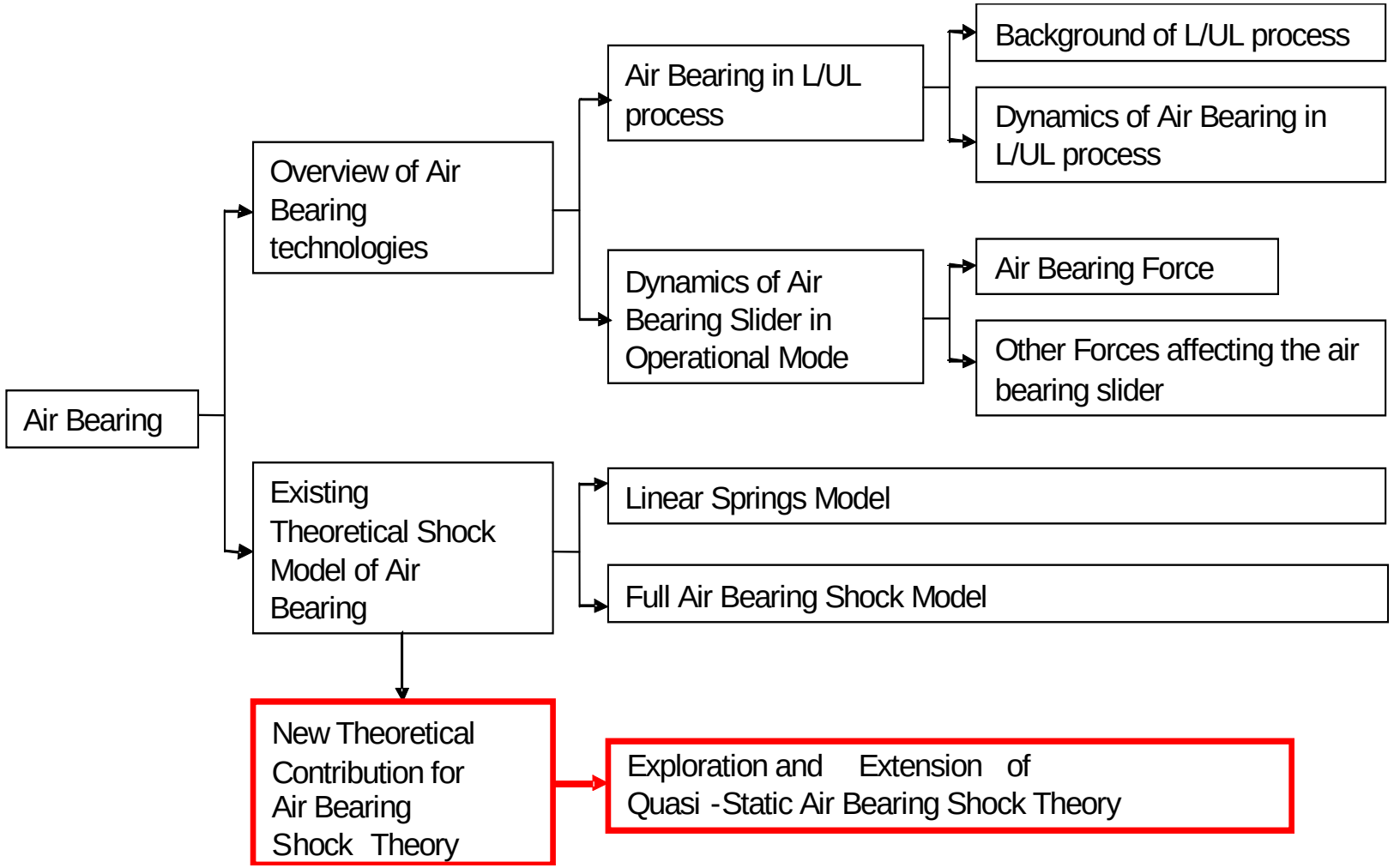

2.5.3 Coupled Structural and Air Bearing Model

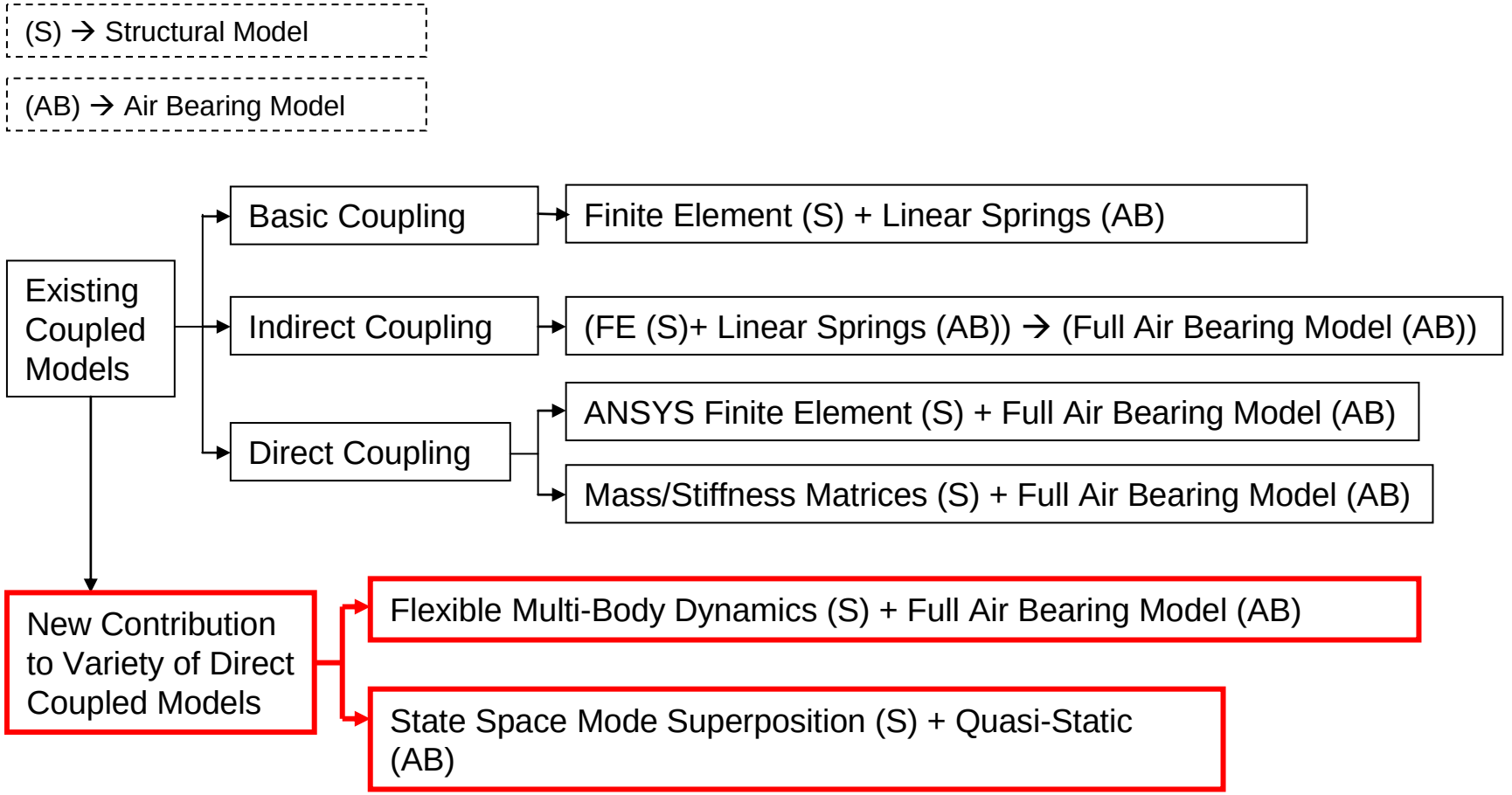

2.5.4 Design and Analysis of Vibration Isolation for HDD

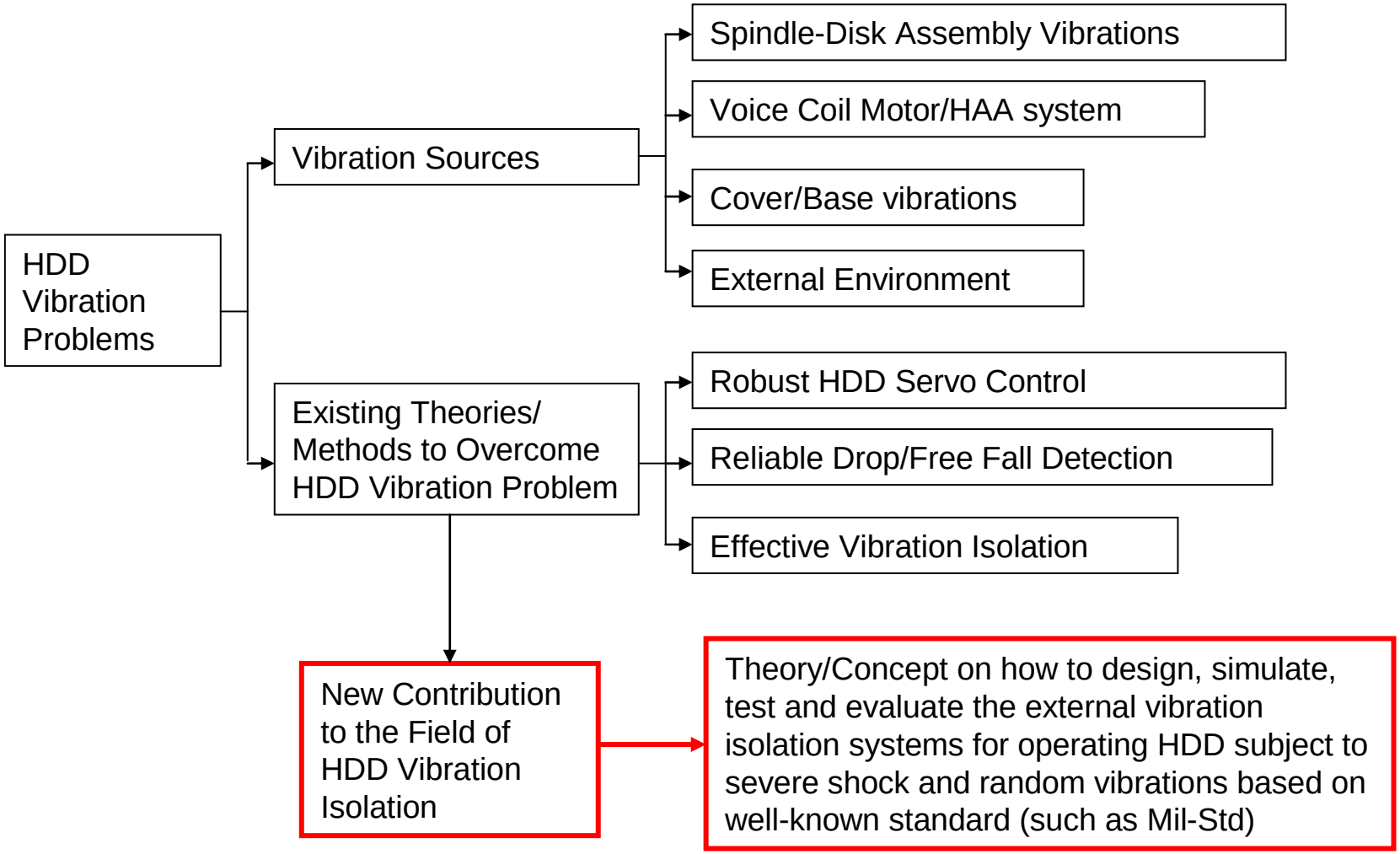

CHAPTER 3 STRUCTURAL MODELING OF OPERATIONAL HDD SUBJECT TO SHOCK

In the first part of this chapter, an operational HDD structural model for shock simulation is developed using flexible multi body dynamics formulation. Three flexible structural components (nonlinear head actuator assembly, disk-spindle and base plate) are considered in this model. The advantages of the flexible multi body dynamics formulation are: it can simulate the large rotational motion accurately and its computational efficiency is better than the full finite element model.

If only the vertical-shock response in the few milliseconds after shock happens is needed, then flexible multi-body dynamics is overkill. Hence, in the next part a more time-efficient operational-HDD structural model is developed using a state-space formulation based on mode superposition principle to predict the HDD vertical-shock response within a few milliseconds. The discontinuity of the head actuator assembly is considered. The effect of the disk spin on the air bearing location is included. The advantage of the formulation is the reduced computation time and the ease in doing the parametric studies.

In the last section, modeling and verification of the head actuator model is depicted to complete the formulation of the theoretical shock model of the HDD structures.

3.1 *Flexible Multi Body Dynamics Formulation of HDD*

The HDD experiencing the shock can be modeled as different flexible bodies which are connected to each other by bearing joints. These bodies include the VCM-head actuator assembly, the disk-spindle assembly and the housing, as shown in Figure 3.1

[145].

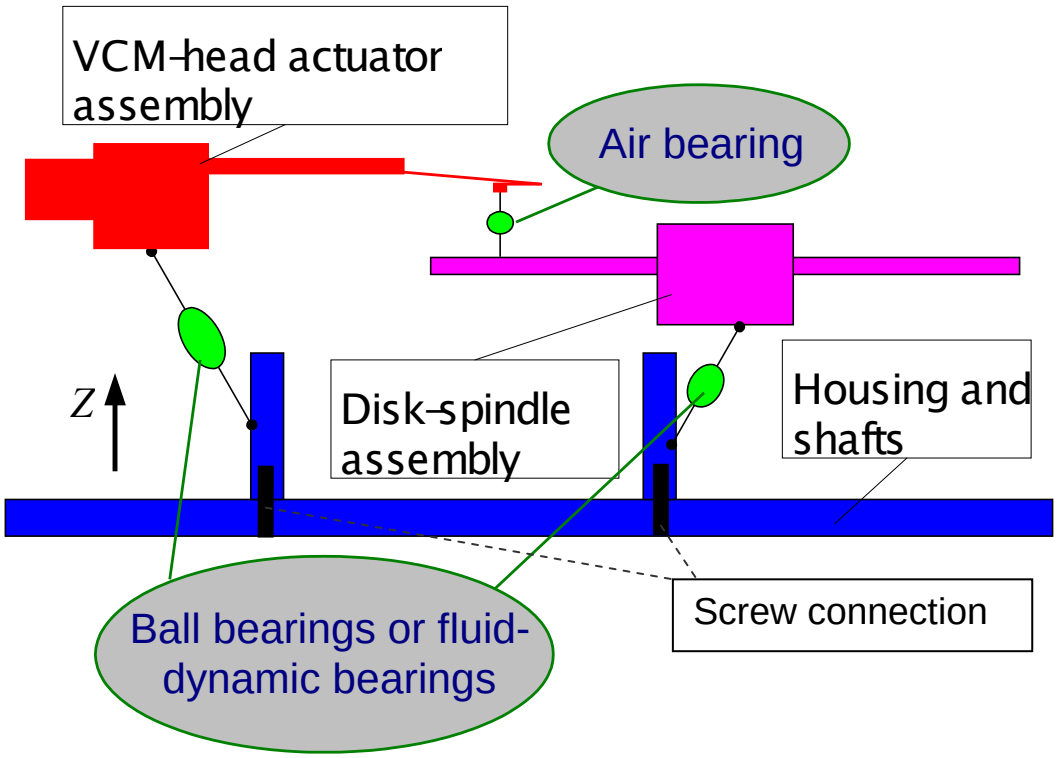

FIGURE 3.1 FLEXIBLE MULTI BODY MODEL OF HDD

The whole formulation is divided into two main parts. The first part is the formulation of dynamics properties of each flexible body (mass, damping, & stiffness matrices as well as quadratic velocity vector). The second part is the formulation of the generalized force applied on flexible bodies.

3.1.1 Formulation of Dynamics Properties of Flexible Body

For any flexible body in the HDD, as shown in Figure 3.2, the body reference o^i"x^i"y^i"z^i" is selected. Here, the superscript i denotes the i^{th} body. The location and orientation of the body reference with respect to the global coordinate system $OXYZ$ are defined by a set of coordinates $\mathbf{q}_r^i$. The vector $\mathbf{q}_r^i$ can be written in a partitioned form as

$$\mathbf{q}_r^i = [\mathbf{R}^{i\mathrm{T}} \quad \boldsymbol{\theta}^{i\mathrm{T}}]^{\mathrm{T}} \tag{3.1}$$

where $\mathbf{R}^i$ is a set of Cartesian coordinates that define the location of the origin of the body reference and $\boldsymbol{\theta}^i$ is the set of Euler angles that describe the orientation of the selected body reference.

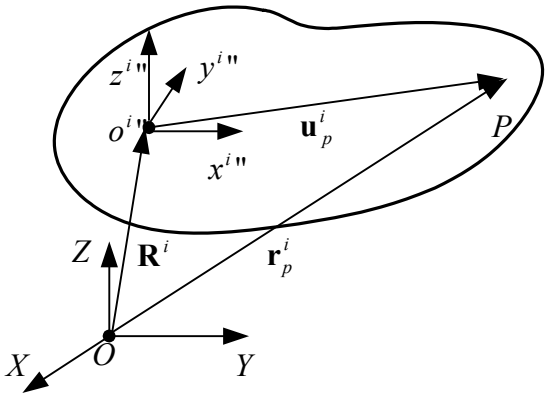

FIGURE 3.2 DISPLACEMENT VECTOR OF ARBITRARY POINT *P* ON ONE FLEXIBLE BODY IN THE HDD

Then for an arbitrary point P on the body, its global position vector $\mathbf{r}_p^i$ can be written as [60]

$$\mathbf{r}_p^i = \mathbf{R}^i + \mathbf{A}^i \mathbf{u}_p^i \tag{3.2}$$

where $\mathbf{u}_p^i$ is the local position vector of point P expressed in $x''y''z''$ and $\mathbf{A}^i$ is the transformation matrix between the body reference and the global reference (see appendix A.1); $\mathbf{A}^i$ is a function of $\boldsymbol{\theta}^i$, and $\mathbf{u}_p^i$ is the *vector sum* of $\mathbf{u}_o^i$ (the position of point P in the undeformed state in the body reference) and $\mathbf{u}_f^i$ (the displacement of point P due to elastic deformation).

Next, the displacement of point P due to elastic deformation can be approximated as

$$\mathbf{u}_f^i = \mathbf{S}^i(x^i'', y^i'', z^i'')\mathbf{q}_f^i(t) \tag{3.3}$$

where $\mathbf{S}^i(x^i", y^i", z^i") = [\phi_1^i \quad \phi_2^i \quad \cdots \phi_m^i]$ is space-dependent shape matrix, and $\mathbf{q}_f^i(t) = [q_{f1}^i \; q_{f2}^i \cdots q_{fm}^i]^{\mathrm{T}}$ is vector of time-dependent elastic generalized coordinates known as modal coordinates. *m* is the number of mode shapes to be taken into account.

The mode shapes of each HDD flexible component are obtained through finite element analysis. The boundary conditions for each component when the mode shapes are calculated are shown in Figure 3.3 below. For the head actuator assembly its spindle is fixed, no constraint is applied between the dimple and the flexure. For the disk, its spindle is also fixed. For the base plate its two side edges are fixed. The air bearing is not considered in the modes extraction state.

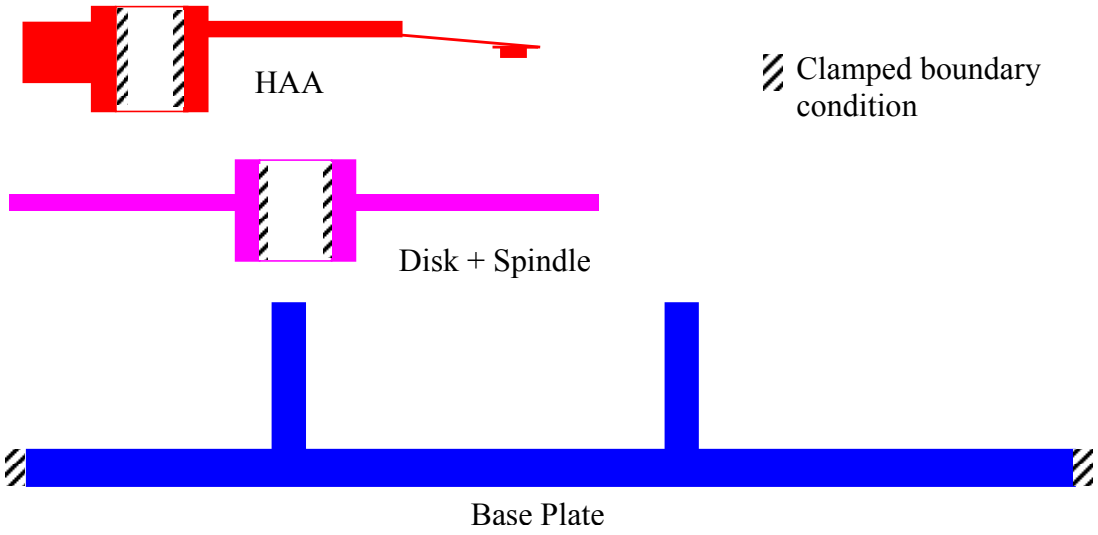

FIGURE 3.3 THE BOUNDARY CONDITION DURING MODE EXTRACTION

The j^{th} mode shape value $\phi_j^i(x^i", y^i", z^i")$ at any point can then be obtained by interpolation as in (3.4).

$$\phi_j^i(x^i", y^i", z^i") = \sum_{k=1}^{n} N_k^i \varphi_{jk}^i \tag{3.4}$$

where N_k^i is the k^{th} shape function of the corresponding element, φ_{jk}^i is the j^{th} mode shape value evaluated at the nodal points of the element, and n is the number of the shape functions of the element.

Expanding (3.2) the global position of point P can be further describes as

$$\mathbf{r}_p^i = \mathbf{R}^i + \mathbf{A}^i(\mathbf{u}_o^i + \mathbf{S}^i\mathbf{q}_f^i) \tag{3.5}$$

The total vector of the generalized position of point P can then be written as

$$\mathbf{q}^i = \begin{bmatrix}\mathbf{R}^{i\mathrm{T}} & \boldsymbol{\theta}^{i\mathrm{T}} & \mathbf{q}_f^{i\mathrm{T}}\end{bmatrix}^{\mathrm{T}} \tag{3.6}$$

By differentiating (3.5) with respect to time, the velocity of point P can be obtained as

$$\dot{\mathbf{r}}_p^i = \mathbf{L}^i\dot{\mathbf{q}}^i \tag{3.7}$$

where $\mathbf{L}^i$ is a time- and space-dependent matrix. Subsequently, the kinetic energy T^i of the flexible body i is represented in terms of $\dot{\mathbf{q}}^i$

$$T^i = \frac{1}{2}\dot{\mathbf{q}}^{i\mathrm{T}}\mathbf{M}^i\dot{\mathbf{q}}^i \tag{3.8}$$

where $\mathbf{M}^i$ is the mass matrix of the flexible body i and is defined as

$$\mathbf{M}^i = \int_{V^i}\rho^i\,\mathbf{L}^{i\mathrm{T}}\mathbf{L}^i dV^i \tag{3.9}$$

where ρ^i and V^i are the density and the volume of the body i, respectively.

By using the modal frequencies, the potential energy caused by the elastic deformation is written as

$$P_E^i = \frac{1}{2}\mathbf{q}^{i\mathrm{T}}\begin{bmatrix}\mathbf{0} & \mathbf{0} & \mathbf{0}\\ \mathbf{0} & \mathbf{0} & \mathbf{0}\\ \mathbf{0} & \mathbf{0} & \mathbf{K}_f^i\end{bmatrix}\mathbf{q}^i \tag{3.10}$$

where $\mathbf{K}_f^i$ is the diagonal stiffness matrix associated with the elastic coordinates of the body

$$\mathbf{K}_f^i = \mathrm{diag}(\omega_1^{i2} \quad \omega_2^{i2} \quad \cdots \quad \omega_m^{i2}) \tag{3.11}$$

Here ω_k^i is the k^{th} modal frequency.

Upon the application of the Lagrange's equations

$$\frac{d}{dt}\frac{\partial T^i}{\partial \dot{q}_j^i} - \frac{\partial T^i}{\partial q_j^i} + \frac{\partial P_E^i}{\partial q_j^i} = Q_j^i \quad j = 1, 2, \cdots, 6+m \tag{3.12}$$

and with the consideration of the modal damping, the equations of the body motion can be obtained as

$$\mathbf{M}^i\ddot{\mathbf{q}}^i + \mathbf{C}^i\dot{\mathbf{q}}^i + \mathbf{K}^i\mathbf{q}^i = \mathbf{Q}_e^i + \mathbf{Q}_v^i \tag{3.13}$$

where $\mathbf{C}^i$ is the damping coefficient matrix, $\mathbf{Q}_e^i$ is the generalized force applied on the flexible body, and $\mathbf{Q}_v^i$ is the quadratic velocity vector resulting from the differentiation of the kinetic energy with respect to time and body coordinates.

$$\mathbf{C}^i = \begin{bmatrix}\mathbf{0} & \mathbf{0} & \mathbf{0}\\ \mathbf{0} & \mathbf{0} & \mathbf{0}\\ \mathbf{0} & \mathbf{0} & \mathbf{C}_f^i\end{bmatrix}$$

where $\mathbf{C}_f^i$ is the diagonal damping matrix associated with the elastic coordinates of

the body

$$\mathbf{C}_f^i = \text{diag}(2\zeta_1^i\omega_1^i \quad 2\zeta_2^i\omega_2^i \quad \cdots \quad 2\zeta_m^i\omega_m^i)$$

Here ζ_1^i is the k^{th} modal damping.

$\mathbf{Q}_v^i$ contains the gyroscopic force and the Coriolis force components.

$$\mathbf{Q}_v^i = -\dot{\mathbf{M}}^i\dot{\mathbf{q}}^i + \frac{1}{2}\frac{\partial}{\partial \mathbf{q}^i}\left(\dot{\mathbf{q}}^{iT}\mathbf{M}^i\dot{\mathbf{q}}^i\right) \tag{3.14}$$

In a similar way, the governing equations of the other flexible bodies in the HDD are formulated.

After the mass, damping, & stiffness matrices plus the quadratic velocity vector of each flexible body have been formulated, it is time to formulate the generalized force $\mathbf{Q}_e^i$ in equation (3.13).

3.1.2 Formulation of the Generalized Force

Before the generalized force can be formulated, the physical forces acting on HDD component need to be identified and computed. These forces are generated at pivot bearings, air bearing, and dimple/flexure contact surfaces.

3.1.2.1 Pivot Bearings Forces

Ball bearings (between head actuator assembly (HAA) and base) and fluid bearings (between disk-spindle and base) are modeled as springs-dampers system. A node is determined at the center of each bearing as illustrated in Figure 3.4.

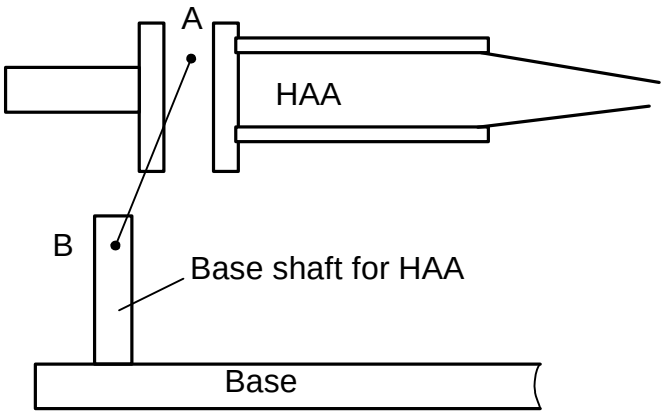

FIGURE 3.4 BEARING NODE POSITION

Nodes *A* and *B* are at positions where the outer ring center and inner ring center of the bearing located, respectively. Distance between *A* and *B* are later used to measure the deformation of the bearing. Once the distance and the relative velocity between nodes *A* and *B* are obtained, the bearing force can be obtained through the stiffness and damping matrix function. The stiffness and damping matrix functions were obtained from the respective manufacturer. In case this information cannot be obtained, the matrices can be approximated from experiments. In the same way, the force between the disk-spindle and the base can be obtained.

3.1.2.2 Air Bearing Forces

Air bearing forces [95] acting on the slider surface and on the disk surface can be found using theoretical models described in literature review chapter. Additionally, in chapter 4, the author presents the finite volume formulation and quasi-static air bearing model to calculate the air bearing force in the shock simulation. Then, in chapter 5, the way to couple the air bearing model with the flexible multi body dynamics structural model is discussed.

3.1.2.3 Dimple/Flexure Contact Forces

If the HDD experiences severe vibration or shock, the dimple and the flexure may separate. This means there is a discontinuity in the overall stiffness of the head actuator assembly. These discontinuities can be modeled using a contact model.

In the current study, Hertz model [36] for circular point contact is adopted since the diameter of the dimple is smaller compared to the flexure's length and width. Figure 3.5 illustrates the model; the dashed line is the shape of the dimple and the flexure before deformation.

From the Hertz elastic contact theory, the relations between the contact force P and the interference δ is

$$P = k_c \delta^{\frac{3}{2}} \tag{3.15}$$

where k_c is the stiffness coefficient and it can be approximated as:

$$k_c = \frac{4E^*\sqrt{R}}{3}, \quad E^* = \left(\frac{1-\nu_1^2}{E_1} + \frac{1-\nu_2^2}{E_2} \right)^{-1} \tag{3.16}$$

E_1, E_2 are the Young's modules of the flexure and load beam and ν_1, ν_2 are the Poisson ratios. R is the radius of the dimple.

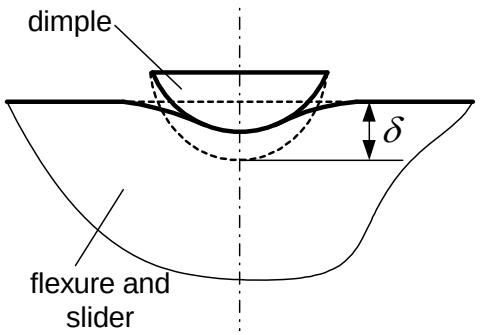

FIGURE 3.5 CONTACT BETWEEN DIMPLE AND FLEXURE

After the forces exerted by the bearings and by the contacts between the dimple and the flexure have been formulated, they are considered as external forces $\mathbf{F}^i(\mathbf{q}^i,t)$ defined in the global coordinate system. If $\mathbf{F}^i(\mathbf{q}^i,t)$ is applied at point *P*, the virtual work done is defined as

$$\delta W^i = \mathbf{F}^i \delta \mathbf{r}_p^i \tag{3.17}$$

And δW^i can be written in a partitioned form as

$$\delta W^i = \mathbf{F}^{iT} \begin{bmatrix} \mathbf{I} & \mathbf{B}^i & \mathbf{A}^i\mathbf{S}^i \end{bmatrix} \begin{bmatrix} \delta\mathbf{R}^i \\ \delta\boldsymbol{\theta}^i \\ \delta\mathbf{q}_f^i \end{bmatrix} \tag{3.18}$$

Then the generalized force $\mathbf{Q}_e^i$ applied on the body caused by the force $\mathbf{F}^i(\mathbf{q}^i,t)$ can be formulated as

$$\mathbf{Q}_e^i = \begin{bmatrix} \mathbf{F}^{iT} & \mathbf{F}^{iT}\mathbf{B}^i & \mathbf{F}^{iT}\mathbf{A}^i\mathbf{S}^i \end{bmatrix}^T \tag{3.19}$$

where $\mathbf{B}^i$ is the matrix whose columns are the partial derivatives of the vector $\mathbf{A}^i\mathbf{u}_p^i$ with respect to the body reference rotational coordinates.

After the generalized force $\mathbf{Q}_e^i$ has been formulated, the governing equation for each flexible body (3.13) can be completed. Additional details on the flexible multi body dynamics formulation is given in Appendix A. The proposed simulation procedure is described in Chapter 5.

The flexible multi body dynamics is good to represent the system experiencing relatively large rotation (when the shock applied is rotational shock or the simulation time is relatively long). This method is also computationally efficient. If one

component in the HDD is changed, only mode shapes and frequencies of that component need to be re-calculated and used in the formulation to obtain the system's response. However, if only the vertical-shock response (the shock direction is perpendicular to the disk surface) in the next few milliseconds after shock happens is needed, then mode superposition theory expressed in the state-space system can be used to develop the dynamic model of the HDD for further increase of the computational efficiency.

3.2 *State-Space Formulation for HDD Vertical Shock Analysis*

The description on the state-space formulation is divided into two main sections. The first part explains the basic state-space mode superposition theory including the formulation of system matrix. And, the second part describes in detail the modified formulation of input and output matrix of each important HDD components

3.2.1 General Concept & Formulation of System Matrix [65]

The diagram of the state-space model is given in Figure 3.6 [146]. The structural state-space models take forces as inputs and gives response of the structure (displacements, velocities, and accelerations) as outputs. The state-space models are formulated using the mode shapes and the natural frequencies of the structures of interest. The formulation is based on mode superposition principle [147]. Damping is assumed to be proportional to mass/stiffness matrices. For most metal (e.g. stainless steel) the damping is ~ 2 %.

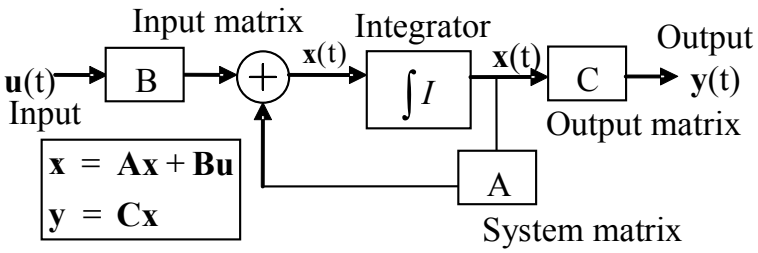

FIGURE 3.6 STATE-SPACE DIAGRAM

The shock response due to vertical shock (perpendicular to the disk surface) is the focus in the subsequent formulations, as HDD is most prone to failure in that direction [101, 104]. The experiment result in Table 6.2 further shows that indeed the HDD is more vulnerable to the vertical vibration than horizontal vibration.

The formulation of system matrix **A** is as follows. The equation of motion in the modal coordinates is shown in (3.20).

$$\ddot{q}_i + 2\zeta_i\omega_i\dot{q}_i + \omega_i^2 q_i = F_{i1}u_1 + \ldots + F_{im}u_m \tag{3.20}$$

$\ddot{q}_i, \dot{q}_i,$ and q_i are acceleration, velocity, and displacement of i^{th} mode. ζ_i and ω_i are proportional damping ratio and natural frequency of i^{th} mode, respectively. F_{ij} is generalized force component of i^{th} mode corresponding to input j. The F_{ij} is equal to $\boldsymbol{\varphi}^{\mathrm{T}} F_{pj}$, where $\boldsymbol{\varphi}$ is the normalized modal matrix. u_j and F_{pj} are magnitude and unit vector of input j in the physical coordinates, respectively. m is the number of physical forces acting on the structures.

Equation (3.20) can be written as:

$$\begin{aligned} \dot{q}_i &= \dot{q}_i \\ \ddot{q}_i &= F_i - 2\zeta_i\omega_i\dot{q}_i - \omega_i^2 q_i \end{aligned} \tag{3.21}$$

Writing (3.21) in matrix form, (3.22) is obtained.

$$\begin{pmatrix} \dot{q}_i \\ \ddot{q}_i \end{pmatrix} = \begin{bmatrix} 0 & 1 \\ -\omega_i^{\,2} & -2\zeta_i\omega_i \end{bmatrix} \begin{pmatrix} q_i \\ \dot{q}_i \end{pmatrix} + \begin{pmatrix} 0 \\ F_{i1} \end{pmatrix} u_1 + \ldots + \begin{pmatrix} 0 \\ F_{im} \end{pmatrix} u_m \tag{3.22}$$

By defining that $\mathbf{x} = [q_1, \dot{q}_1, q_2, \dot{q}_2, \ldots, q_n, \dot{q}_n]$ and recalling that $\dot{\mathbf{x}} = \mathbf{Ax} + \mathbf{Bu}$, system matrix **A** can be formulated as in (3.23) where *n* is number of modes used.

$$\mathbf{A} = \begin{bmatrix} 0 & 1 & 0 & 0 & \cdots & \cdots & 0 & 0 \\ -\omega_1^{\,2} & -2\zeta_1\omega_1 & 0 & 0 & \cdots & \cdots & 0 & 0 \\ 0 & 0 & 0 & 1 & \cdots & \cdots & 0 & 0 \\ 0 & 0 & -\omega_2^{\,2} & -2\zeta_2\omega_2 & \cdots & \cdots & 0 & 0 \\ \vdots & \vdots & \vdots & \vdots & \ddots & \ddots & \vdots & \vdots \\ \vdots & \vdots & \vdots & \vdots & \ddots & \ddots & \vdots & \vdots \\ 0 & 0 & 0 & 0 & \cdots & \cdots & 0 & 1 \\ 0 & 0 & 0 & 0 & \cdots & \cdots & -\omega_n^{\,2} & -2\zeta_n\omega_n \end{bmatrix}_{2n \times 2n} \tag{3.23}$$

The formulations of input matrix **B** and output matrix **C** depend on the characteristic of structures modeled and will be presented in the next sections.

3.2.2 State-Space Formulation of Head Actuator System Considering Structural Discontinuities

The state-space formulation of the head actuator system is divided into three parts. The first part explains about the procedure for required modal analysis. The second part shows the input and output matrix formulation. And, the third part discusses how to handle the discontinuities in the head actuator assembly.

3.2.2.1 Modal Analysis

The configuration and the boundary conditions of the structural model of the head actuator assembly system (Figure 3.12) for modal analysis are described as follow.

The model follows the configuration of the head actuator assembly system during HDD normal operating condition. There is no constraint applied between the dimple and the slider. The slider is free to move, while the arm pivot (the nodes coupled with the mass element in Figure 3.12) is only allowed to move in the vertical direction.

3.2.2.2 Input Matrix and Output Matrix Formulation

The input matrix **B** converts the physical forces to modal forces. Its formula can be derived from (3.22) and (3.23).

$$\mathbf{B_{HAA}} = \begin{bmatrix} 0 & 0 & \dots & 0 \\ F_{11} & F_{12} & \dots & F_{1m} \\ 0 & 0 & \dots & 0 \\ F_{21} & F_{22} & \dots & F_{2m} \\ \vdots & \vdots & \ddots & \vdots \\ \vdots & \vdots & \ddots & \vdots \\ 0 & 0 & \dots & 0 \\ F_{n1} & F_{n2} & \dots & F_{nm} \end{bmatrix}_{2n \times m} \tag{3.24}$$

To couple the HAA with the air bearing and to handle the nonlinearity of the structure, the vertical displacements of several points on the HAA are needed. The points consist of the nodes on the slider corner, dimple, limiter, arm pivot, and lift tab. Let the output $\mathbf{y} = [z_1, z_2 \dots z_k]$ where z is the vertical displacement of the points, k is the number of the points, and n is number of modes used.

Matrix **C** can then be formulated as in (3.25).

$$\mathbf{C_{HAA}} = \begin{bmatrix} \varphi_{z11} & 0 & \varphi_{z12} & 0 & \dots & \dots & \varphi_{z1n} & 0 \\ \varphi_{z21} & 0 & \varphi_{z22} & 0 & \dots & \dots & \varphi_{z2n} & 0 \\ \vdots & \vdots & \vdots & \vdots & \ddots & \ddots & \vdots & \vdots \\ \varphi_{zk1} & 0 & \varphi_{zk2} & 0 & \dots & \dots & \varphi_{zkn} & 0 \end{bmatrix}_{k \times 2n} \tag{3.25}$$

where φ_{zji} is the head actuator assembly normalized-mode-shape-value corresponding to the vertical displacement of point j in i^{th} mode.

3.2.2.3 Handling Structural Discontinuity

During shock event, the dimple may be separated from the slider as in Figure 3.7. At any time step when the dimple and slider are in contact with each other, contact force F_c is applied to each contacting element as depicted in Figure 3.8.

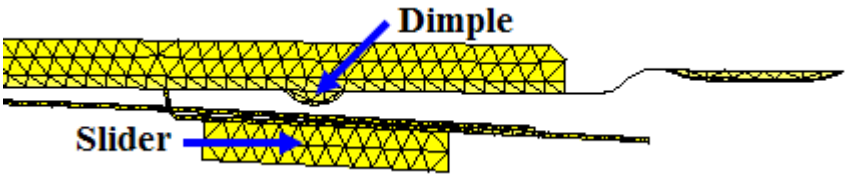

FIGURE 3.7 DIMPLE-SLIDER SEPARATION

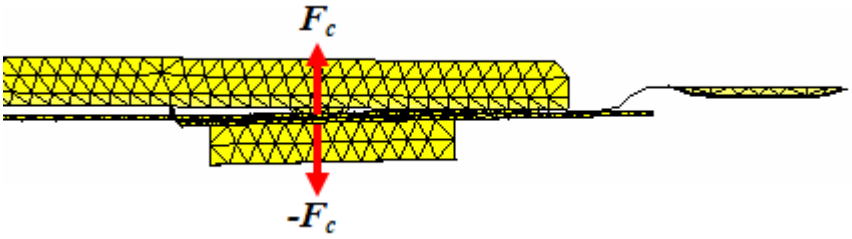

FIGURE 3.8 FORCES APPLIED DURING DIMPLE-SLIDER CONTACT

The contact force is approximated by using Hertz elastic contact stress formula (3.26). E^* and R are described in Figure 3.9.

$$F_c = \frac{4E^*\sqrt{R}}{3}\delta^{\frac{3}{2}} \;;\; \delta \text{ is } interference \tag{3.26}$$

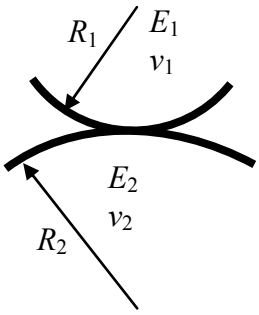

$$\frac{1}{R} = \frac{1}{R_1} + \frac{1}{R_2}$$

$$E^* = \left(\frac{1 - v_1^{\,2}}{E_1} + \frac{1 - v_2^{\,2}}{E_2} \right)$$

FIGURE 3.9 DIMPLE-SLIDER CONTACT AS CIRCULAR POINT CONTACT

The force response of this nonlinear spring is treated as external physical force to the HAA. The force is then translated into the generalized forced ($F_{ij}u_j$) in the equation of motion in the modal coordinates (3.20).

After the HAA state-space model has been formulated, the next section will show how the state-space model of the disk, which includes the effect of disk rotation on the air bearing position, can be formulated.

3.2.3 State Space Formulation for Disk Considering Spinning Effect on Air Bearing Position

The state-space formulation of the disk is divided into three parts. The first part explains about the procedure for required modal analysis. The second part shows the input matrix formulation. And, the third part describes the output matrix formulation

3.2.3.1 Modal Analysis

The boundary conditions of the disk (Figure 3.10) for modal analysis are described as follows. The outer edge of the disk is free. The inner edge is coupled with a mass element and is allowed to move only in the vertical direction. First, the static analysis is done to obtain the stress distribution due to disk spin. Modal analysis is then carried

out by considering stress stiffening and spin softening effect.

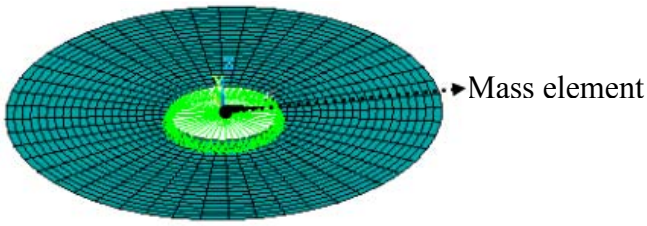

FIGURE 3.10 STRUCTURAL MODEL OF DISK

3.2.3.2 Formulation of Input Matrix of Spinning Disk

The part of the disk surface that makes direct contact with the air bearing changes as the disk rotates. Hence, the position on the disk at which the air bearing forces act needs to be updated at every time step. To facilitate this, matrix **B** is formulated as in (3.27). This formulation directs the state-space model of the disk to take modal forces instead of physical forces as inputs.

$$\mathbf{B_{DISK}} = \begin{bmatrix} 0 & 0 & \dots & 0 \\ 1 & 0 & \dots & 0 \\ 0 & 0 & \dots & 0 \\ 0 & 1 & \dots & 0 \\ \vdots & \vdots & \ddots & \vdots \\ \vdots & \vdots & \ddots & \vdots \\ 0 & 0 & \dots & 0 \\ 0 & 0 & \dots & 1 \end{bmatrix}_{2n \times n} \tag{3.27}$$

The modal forces **FM** can be calculated using (3.28).

$$\mathbf{FM} = \begin{bmatrix} \varphi_{z11}' & \varphi_{z21}' & \cdots & \varphi_{zm1}' \\ \varphi_{z12}' & \varphi_{z22}' & \cdots & \varphi_{zm2}' \\ \vdots & \vdots & \ddots & \vdots \\ \varphi_{z1n}' & \varphi_{z2n}' & \cdots & \varphi_{zmn}' \end{bmatrix}_{n \times m} \times \begin{Bmatrix} F_{v1} \\ F_{v2} \\ \vdots \\ F_{vm} \end{Bmatrix}_{m \times 1} \tag{3.28}$$

F_{vj} (j = 1, 2, …, m) is the magnitude of vertical force i acting on the disk. φ_{zji}' is the i^{th} mode normalized-mode-shape-value corresponding to vertical displacement of the disk section where F_{vj} acts on at the current simulation time.

To facilitate the computation of φ_{zji}', the mode shapes of the disk are stored using circular coordinates (radial positions r and circumferential positions θ). Figure 3.11 shows the plot of one of the disk modes in circular coordinates. Since the disk rotates with a known speed, the position of the forces with respect to the disk can be found at any time step. Subsequently, φ_{zji}' is retrieved using lookup and interpolation method [148].

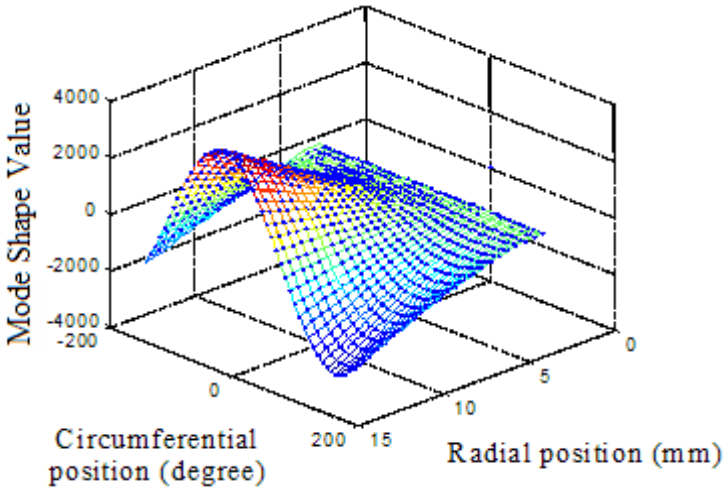

FIGURE 3.11 (0,1) DISK MODE IN CIRCULAR COORDINATES

3.2.3.3 Formulation of Output Matrix of Spinning Disk

The displacement of the disk area under the slider must be calculated in order to find the spacing of the air bearing. However, this area changes as the disk spins. To facilitate the calculation of its displacement, the output matrix **C** is formulated as in (3.29). In this way, the state-space model of the disk gives modal displacement **q** =

$[q_1, q_2, \ldots, q_n]$ as the output.

$$\mathbf{C_{DISK}} = \begin{bmatrix} 1 & 0 & 0 & 0 & \ldots & \ldots & 0 & 0 \\ 0 & 0 & 1 & 0 & \ldots & \ldots & 0 & 0 \\ \vdots & \vdots & \vdots & \vdots & \ddots & \ddots & \vdots & \vdots \\ 0 & 0 & 0 & 0 & \ldots & \ldots & 1 & 0 \end{bmatrix}_{n \times 2n} \tag{3.29}$$

The part of disk surface directly under the slider can be predicted based on the disk spinning speed and its vertical displacement **y** can be obtained from (3.30).

$$\mathbf{y} = \begin{bmatrix} \varphi_{z11}' & \varphi_{z12}' & \cdots & \varphi_{z1n}' \\ \varphi_{z21}' & \varphi_{z22}' & \cdots & \varphi_{z2n}' \\ \vdots & \vdots & \ddots & \vdots \\ \varphi_{zm1}' & \varphi_{zm2}' & \cdots & \varphi_{zmn}' \end{bmatrix}^{\mathrm{T}}_{m \times n} \times \mathbf{q} \tag{3.30}$$

After formulation for each flexible body has been completed, in Chapter 5 they are combined together with the air bearing. The state-space formulation that has been developed is computationally efficient because only mode shapes value at the point of interest are needed during the simulation and very high frequency modes can be truncated. Besides that, the formulation can model the dynamics air bearing position due to disk rotation.

3.2.4 Further Discussion

In this subsection, how to apply the shock pulse to the state-space model and how many modes are necessary to get acceptable accuracy in shock simulation are described.

3.2.4.1 Applying Shock Excitation in State Space Model

Since the magnitude of the shock applied to the HDD is usually given in terms of

acceleration (for instance 250 G), there is a need to convert acceleration input to force. To facilitate this, a mass element is added to the structural component. This mass element should be much heavier than the structural components (~ 1000 times) so that the mass of the structures can be neglected. The element is then coupled to the structure nodes at which the shock pulse will be applied. Figure 3.12 depicts how this technique can be applied to a head actuator assembly: A mass element of 5 kg is added at the location shown in the figure. The 5 kg value is chosen because it is sufficiently bigger than HAA mass, which is ~ 5 gram only. The lines between the mass element and its surrounding nodes symbolize the couplings. Applying a force with magnitude of 250×9.81×5 Newton at the mass element node will produce 250 G acceleration at the coupled nodes.

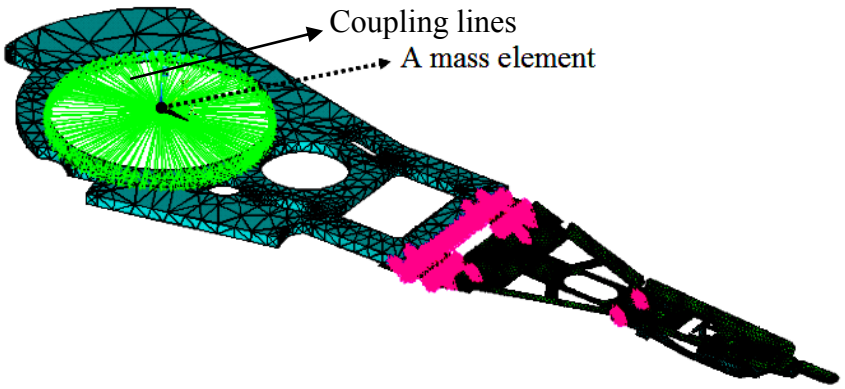

FIGURE 3.12 STRUCTURAL MODEL OF HEAD ACTUATOR ASSEMBLY (HAA)

3.2.4.2 Required Number of Mode Shapes

To determine the number of modes to be included in the shock response simulation, a convergence test was carried out. A half sine shock with magnitude 200 G and pulse width 0.5 ms was applied to several HAA models. Each model uses different number of modes. It was observed that using 100 modes give good convergence; the displacement of the trailing edge center of the slider differs by less that 0.5 nm when

compared to the model that uses 250 modes.

In the flexible multi body dynamics formulation and in the development of the state-space model described above, it can be seen that only the modal property of individual HDD components is needed. Since the head actuator assembly (HAA), as one of the HDD components, has a quite intricate shape and also a significant effect on the shock tolerance, its modeling and experimental verification will be included in the next section for clarity and completeness in describing the theoretical shock models of HDD structures.

3.3 *Modeling and Verification of Head Actuator Assembly*

To ensure reliable shock model, the structural models used need to be verified by experiments. One of the ways to verify them is by comparing its numerical modal analysis result with experimental result [149].

First, the finite element modeling of *complete* head actuator assembly (HAA) is presented, followed by its modal analysis. Then, the experimental modal analysis of the HAA and the disk are shown and last is the verification of the HAA model.

3.3.1 Finite Element Modeling of Complete HAA

Finite element model of HAA developed from its solid CAD model is shown in Figure 3.13. All body is meshed using Solid92 element (a tetrahedral element). The FE software used to perform the numerical modal analysis is ANSYS Version 10.0 [35].

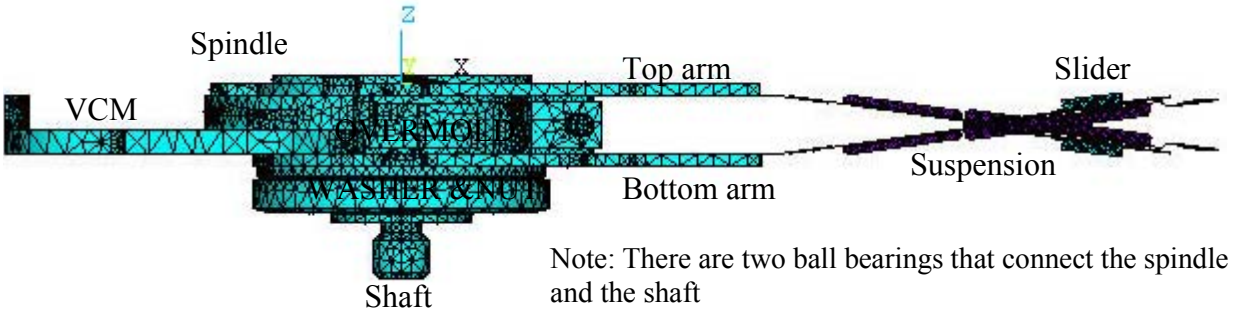

FIGURE 3.13 FE MODEL OF COMPLETE HAA

Two bearing models were considered for this HAA model. Their stiffness is determined from experiments as follows [150]. In Figure 3.14a below, force F_A is applied to the bearing while its shaft is fixed. The force F_A needed to produce 1 mm downward displacement was recorded. For the bearing that we modeled, the F_A is 1119 N. Hence, bearing axial stiffness is 1119 N/mm.

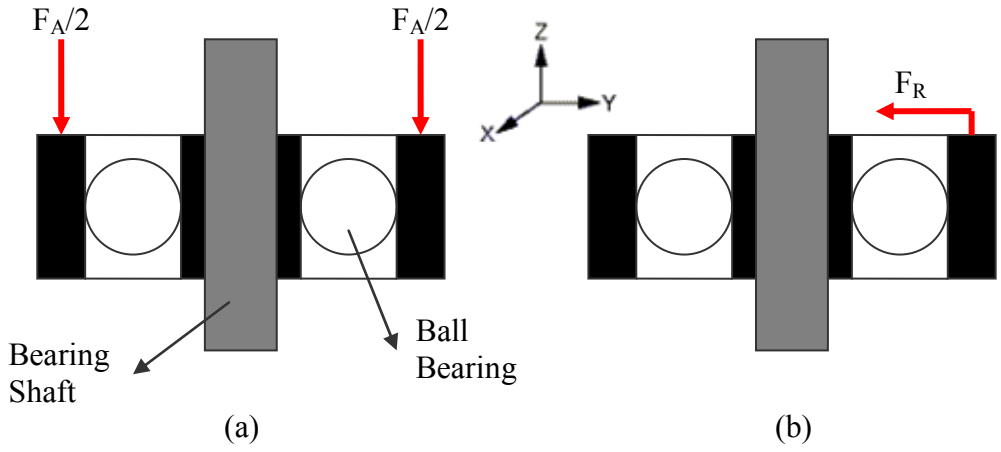

FIGURE 3.14 EXPERIMENTAL SETUP FOR BEARING STIFFNESS DETERMINATION

The radial stiffness can be obtained through the same method. F_R (see Figure 3.14b) is the force needed to produce 1 mm radial displacement. The bearing radial stiffness was obtained accordingly as 4062 N/mm.

The first model is depicted in Figure 3.15. Nine spring elements are used to represent

the nine metal balls inside the bearings. Hence, every spring element has a vertical stiffness (k_Z) of 124.33 N/mm, stiffness in x-axis (k_X) of 451.33 N/mm and stiffness in y-axis (k_Y) of 451.33 N/mm. The rotational stiffness is zero.

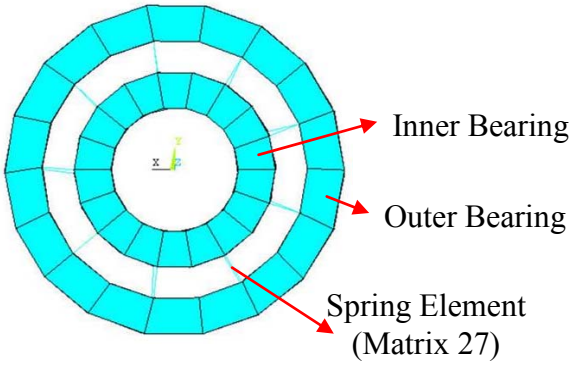

FIGURE 3.15 BEARING MODEL I

Another bearing model is described in Figure 3.16. The inner bearing and the outer bearing are connected to one spring element using rigid links. Hence, k_Z = 1119 N/mm and $k_X = k_Y$ = 4062 N/mm. The rotational stiffness in vertical axis is zero because the bearing is supposed to rotate freely. To find the rotational stiffness in x- and y-axis, the bearing is tilted (hypothetically) at 0.01 radians with respect to one of the horizontal axes. Since the axial stiffness of each ball in the bearing is $k_Z/9$ = 124.33 N/mm, the total reaction moment as the results of tilting the bearing 0.01 radians can be calculated as 13.75 Nm. Hence, the rotational stiffness in x- and y-axis can be estimated as 1375 Nm/radian.

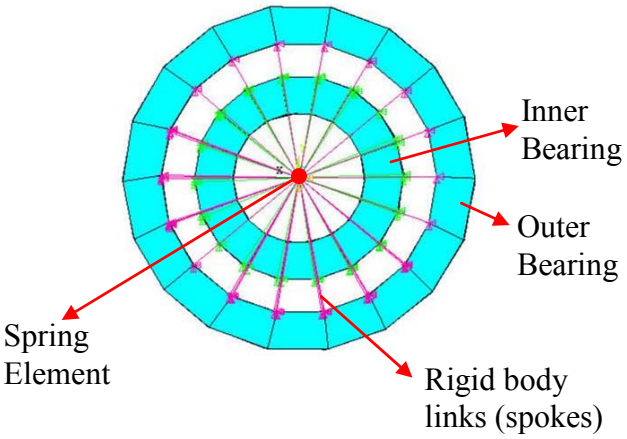

FIGURE 3.16 BEARING MODEL II

The two bearing models give almost the same result during modal analysis. However, the second model was deemed more appropriate because it can give a free rotation about the bearings axis while the first one cannot.

3.3.2 Finite Element Modal Analysis of HAA (Pre-stressed)

The HAA is first loaded onto the disk (Figure 3.17). Stress then develops in the hinge. This stress can be obtained by static analysis. It is afterwards included in the modal analysis (pre-stressed modal analysis).

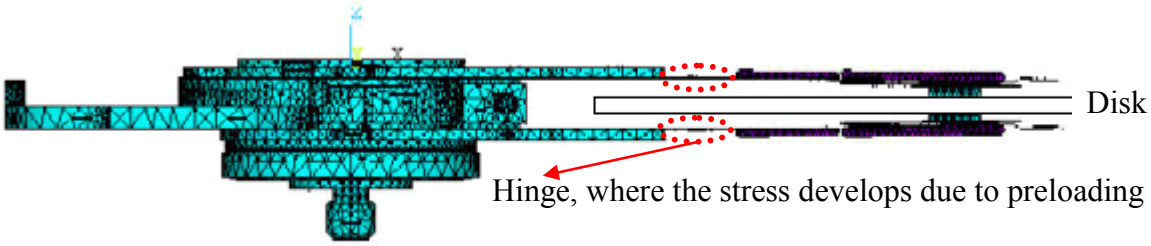

FIGURE 3.17 COMPLETE HAA LOADED ONTO THE DISK

The natural frequencies of the first two modes are 3,494 Hz (suspensions first bending in-phase) and 3,990 Hz (suspensions first bending out-of-phase). The corresponding mode shapes are shown in Figure 3.18 and Figure 3.19.

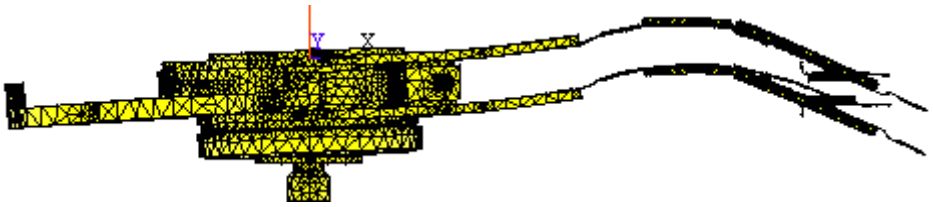

FIGURE 3.18 SUSPENSIONS FIRST BENDING IN-PHASE

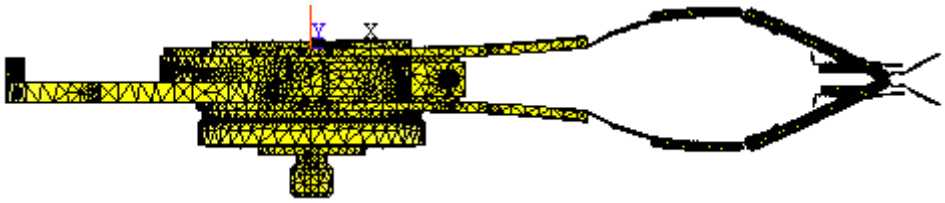

FIGURE 3.19 SUSPENSIONS FIRST BENDING OUT-OF-PHASE

If the stress in the hinge is not included in the modal analysis, the natural frequencies shift up (3,506 Hz and 4,016 Hz). This is due to the preload induced pre-strain and pre-stress in the suspension hinge [151]. The percentage changes are 0.35% for the first mode and 0.65% for the second mode.

After the numerical analysis has been presented, the experimental modal analysis will described next.

3.3.3 Experimental Modal Analysis of the Disk and the HAA

Experimental modal analysis have been well established as described in [149, 152]. In this subsection, the experimental setup is portrayed and then the modal analysis results of the disk and the HAA are presented.

3.3.3.1 General Experimental Setup

The experiment setup for modal analysis is shown in Figure 3.20. To enable the shaker to give input vibration with correct magnitude and frequency, a closed loop control is used.

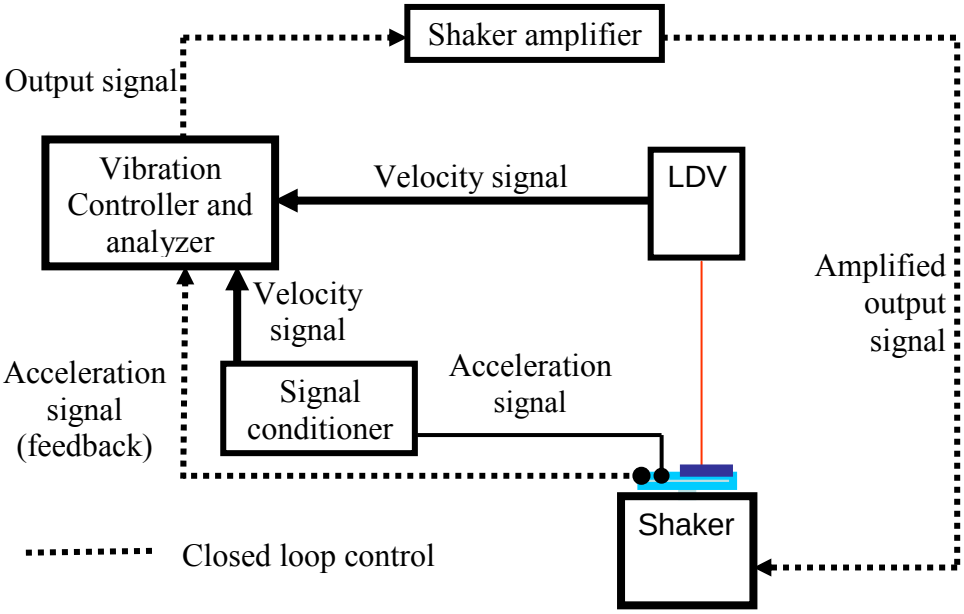

FIGURE 3.20 EXPERIMENT SETUP FOR MODAL ANALYSIS

Figure 3.21 shows an HDD fixed onto a shaker using several clamps. The accelerometer labeled with "control" provides the feedback signal to the vibration controller. Another accelerometer provides input signal (acceleration signal) which is converted to velocity by a signal conditioner and then fed to the vibration controller. The laser Doppler velocimetry (LDV) captures the velocity the HDD components and sends the output signal to the vibration controller. The transmissibility (velocity signal from LDV divided by velocity signal from signal conditioner) is calculated and then plotted against the frequencies.

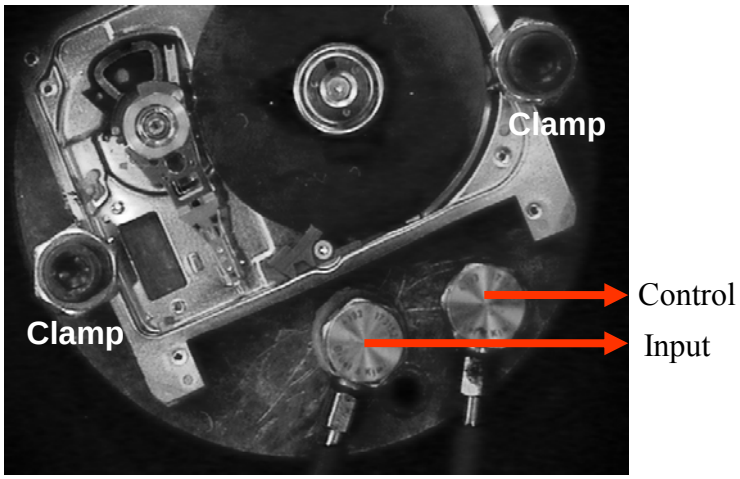

FIGURE 3.21 EXPERIMENT SETUP – CLOSE UP

A fixture is needed to hold the HDD firmly while doing the modal analysis. Instead of clamping the HDD (Figure 3.21), gluing the HDD using epoxy (Figure 3.22) can give better grip to the shaker platform.

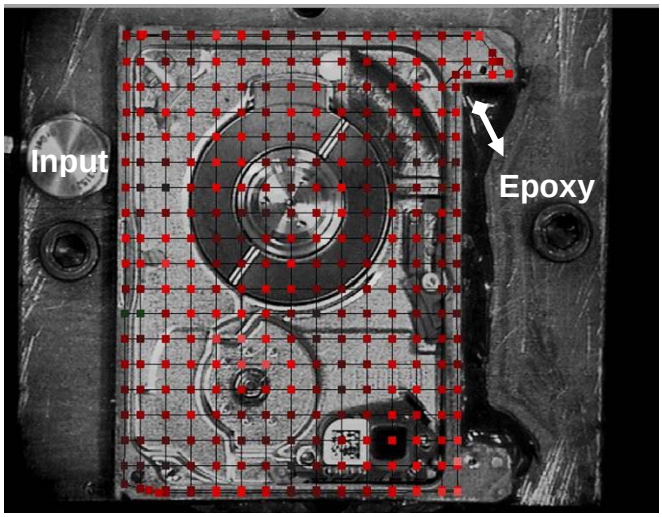

FIGURE 3.22 SHAKER AND BASE GLUED TOGETHER

The network of dots in Figure 3.22 and the several subsequent figures indicates the scan points of the LDV. After the general experimental set up has been described, next the modal analysis results of the disk and the HAA are given.

3.3.3.2 Experimental Modal Analysis Results of the Disk

The modes of the disk were then obtained using the LDV scanning utility. The setup is shown in Figure 3.23.

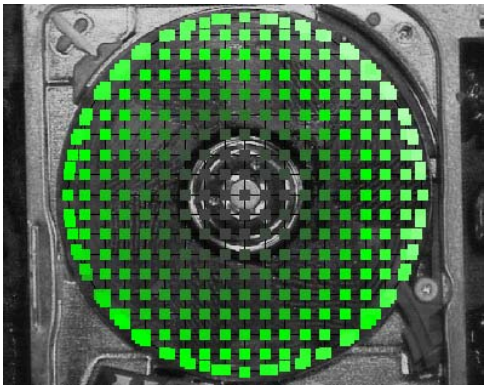

FIGURE 3.23 SETUP FOR DISK MODAL EXTRACTION

Figure 3.24 shows the first three modes. There are no 0-1 balanced modes or 0-0 balanced modes because there is only one disk in this HDD.

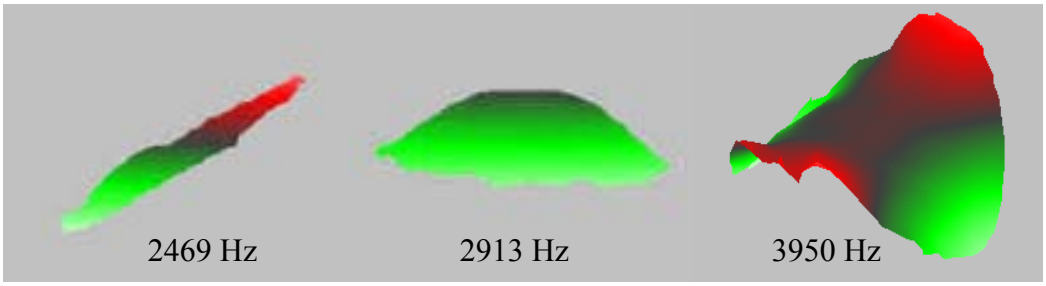

FIGURE 3.24 MODE 0-1, MODE 0-0, MODE 0-2 OF THE DISK

The natural frequencies of the disk depend on the boundary condition. When the same disk is clamped using a different boundary condition (using a washer tightened with a screw as shown in Figure 3.25), the resulting natural frequencies (Table 3.1) are different compared to one using the original clamp shown in Figure 3.23. This is due to the difference in the clamp dimension and clamp symmetrical properties; the original clamp is wider and more symmetric than the washer.

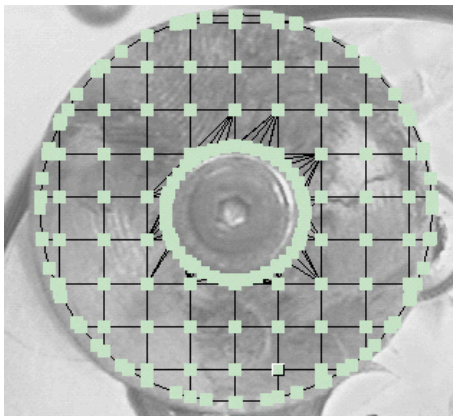

FIGURE 3.25 DISK WITH DIFFERENT BOUNDARY CONDITION

TABLE 3.1 NATURAL FREQUENCIES OF THE DISK WITH A DIFFERENT CLAMP

Mode Shape	Using Original Clamp (Figure 3.23)	Using Washer and Screw (Figure 3.25)
(0,0) mode	2913 Hz	2150 Hz
(0,1) mode	2469 Hz	2425 Hz
	2469 Hz	2774 Hz
(0,2) mode	3950 Hz	3750 Hz
	3950 Hz	3906 Hz

3.3.3.3 Experimental Modal Analysis Results of the HAA

The mode shapes of an HAA with a free head-gimbal assembly (Figure 3.26) are first obtained.

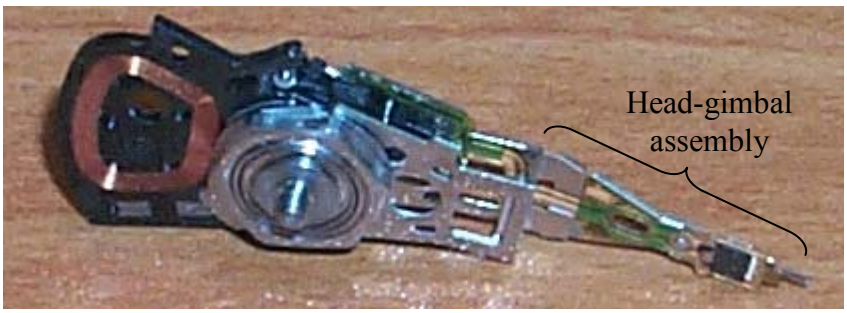

FIGURE 3.26 HAA WITH A FREE HGA

The mode shapes obtained from setups shown in Figure 3.27 and Figure 3.28 are given in Figure 3.29.

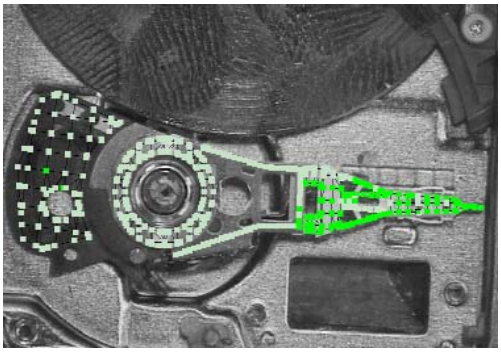

FIGURE 3.27 MODAL ANALYSIS SETUP I FOR HAA WITH FREE HGA

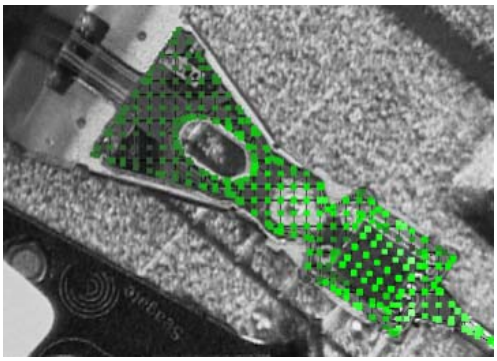

FIGURE 3.28 MODAL ANALYSIS SETUP II FOR HAA WITH FREE HGA

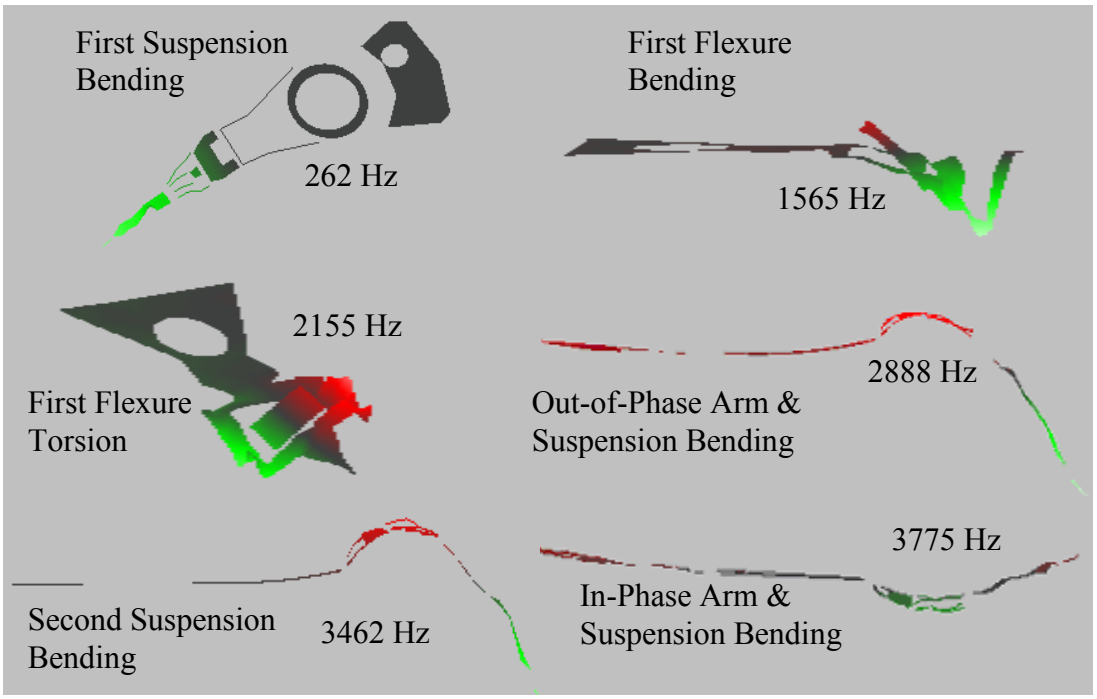

FIGURE 3.29 MODES OF HAA WITH ONE SUSPENSION ONLY

Figure 3.30 shows the setup for modal extraction setup of the HAA on the disk (the disk was not rotating and fully clamped).

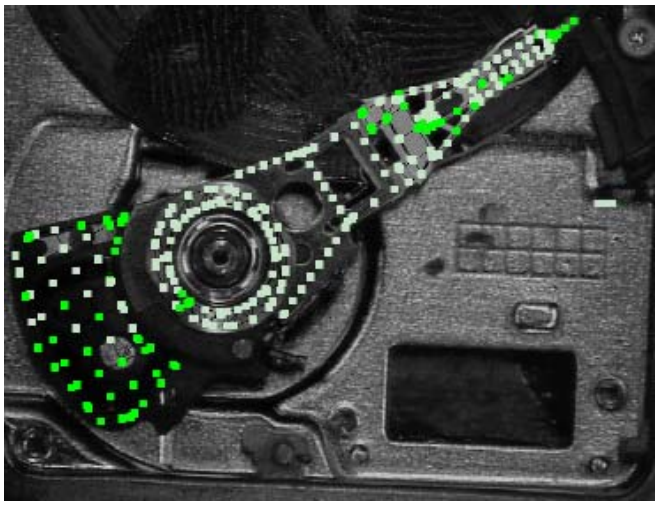

FIGURE 3.30 HAA ON DISK

The mode shapes obtained are presented in Figure 3.31 and Figure 3.32.

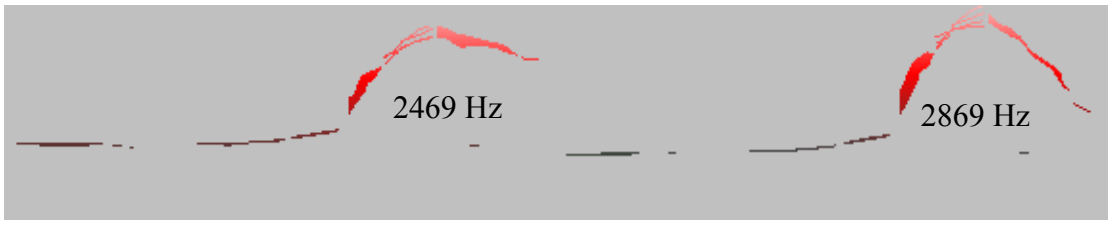

FIGURE 3.31 FIRST AND SECOND MODE OF HAA ON DISK

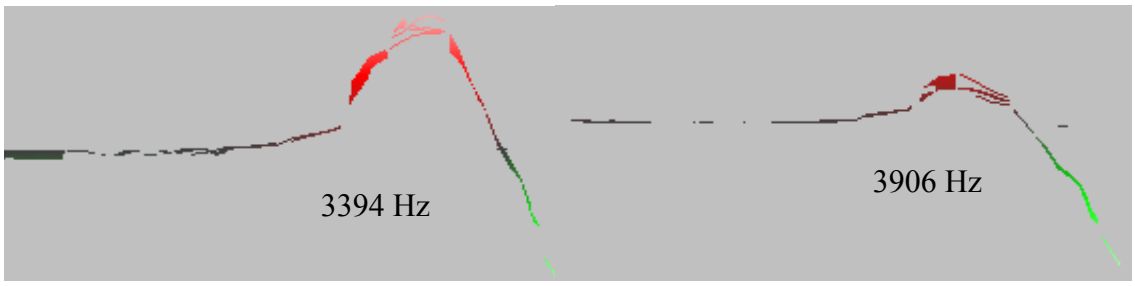

FIGURE 3.32 THIRD AND FOURTH MODE OF HAA ON DISK

It appears that the first and second modes are induced by disk modes (0-1 modes and 0-0 modes), while the third and fourth modes is caused by the HAA bending modes.

3.3.4 Experimental Verification of HAA FE model

The natural frequencies and the mode shapes of the analytical model of the HAA (with its pivot and the slider fixed) are then compared with the related experimental result. The comparison results are presented in Table 3.2 and Table 3.3. It can be seen that the finite element model is quite accurate, within 2-3 %.

TABLE 3.2 FIRST MODE COMPARISON

First Mode	Real model	FE model
Mode shape	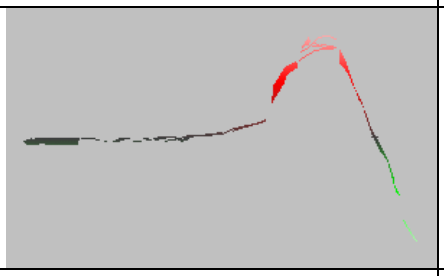	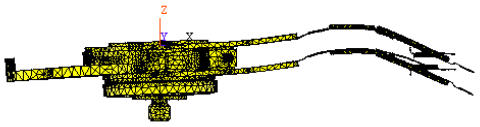
ω_n	3394 Hz	3494 Hz (+ 3 %)

TABLE 3.3 SECOND MODE EXPERIMENTAL VERIFICATION

Second Mode	Real model	FE model
Mode shape	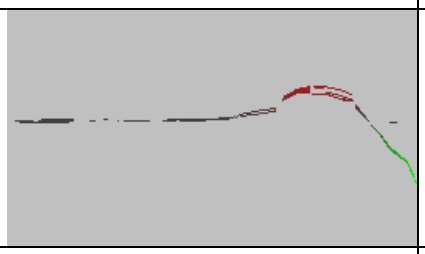	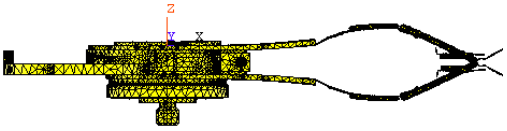
ω_n	3906 Hz	3990 Hz (+ 2 %)

After the models have been verified, they are used to generate the modal properties (natural frequencies and mode shapes) required in the flexible multi body dynamics formulation and in the development of the state-space mode superposition model.

3.4 *Chapter Summary*

The summaries on the flexible multi body dynamics formulation of HDD, the development of the state-space model for HDD vertical shock analysis, and the HAA modal analysis are given below in the form of flow diagram.

3.4.1 Flexible Multi Body Dynamics Formulation of HDD

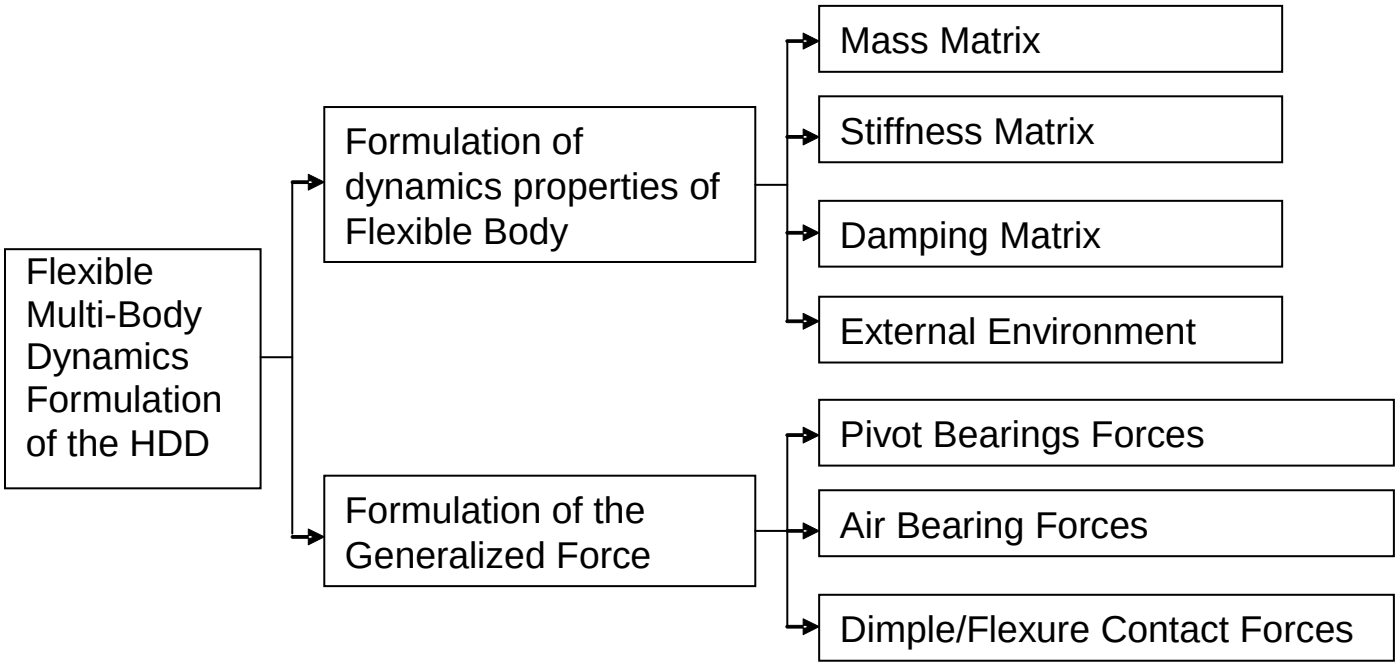

3.4.2 State Space Formulation for HDD Vertical Shock Analysis

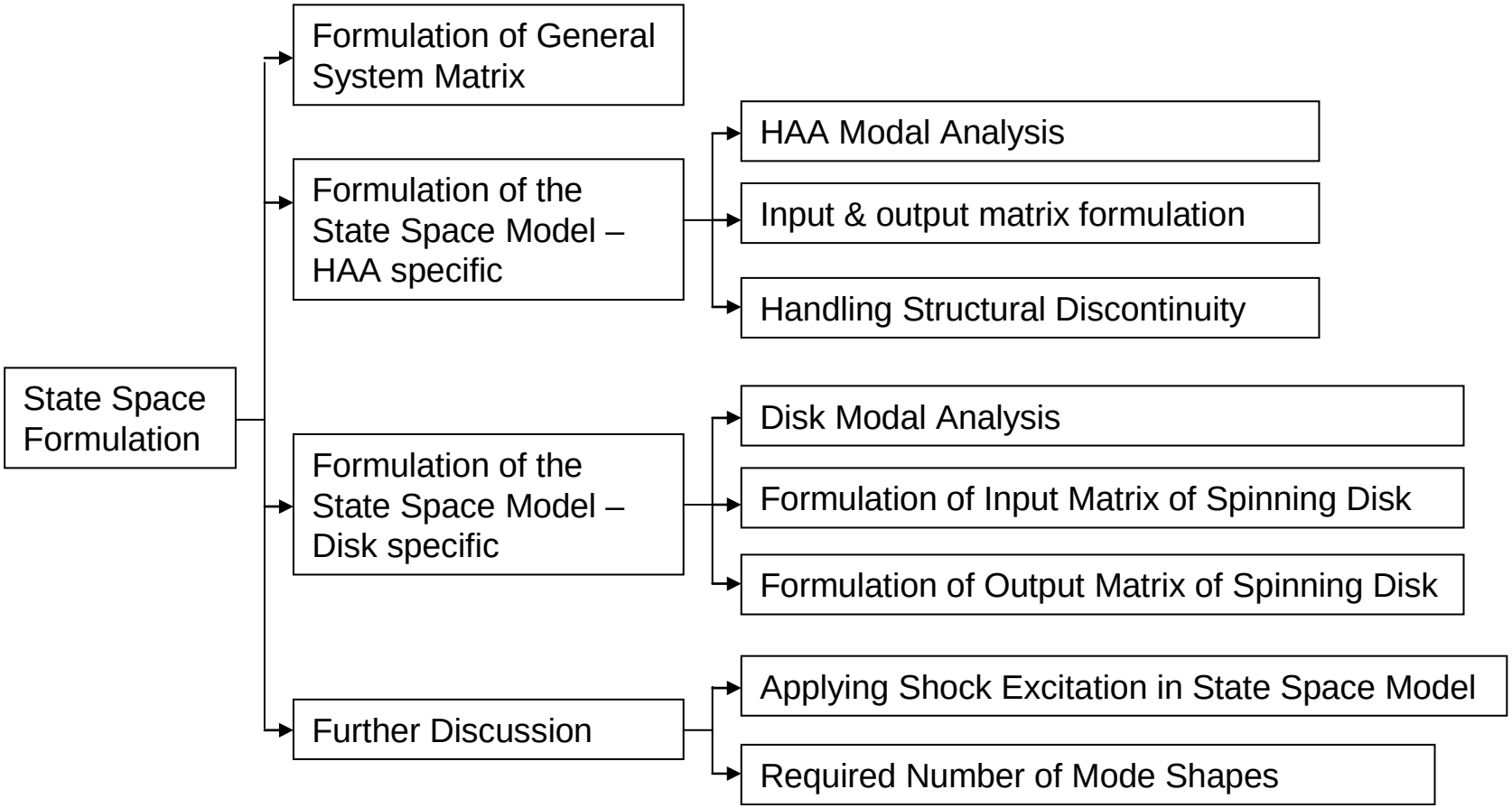

3.4.3 HAA Modal Analysis

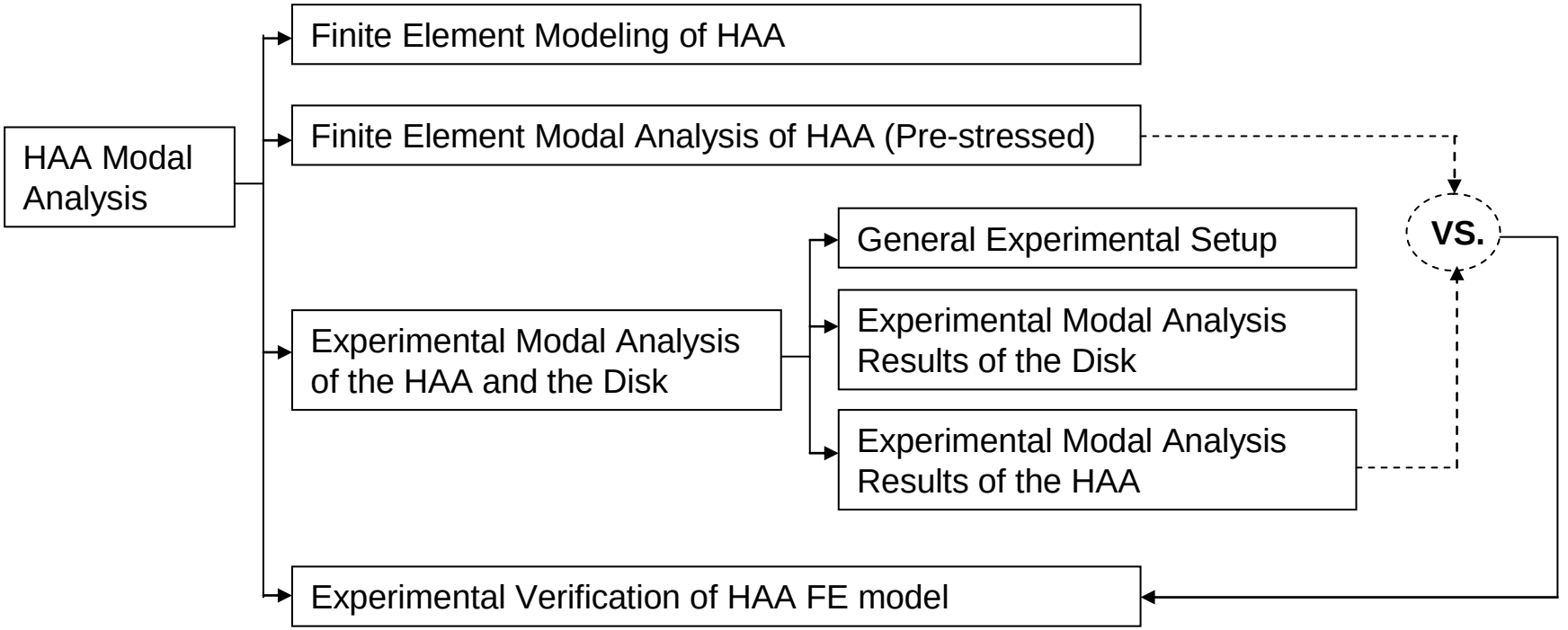

CHAPTER 4 QUASI - STATIC CONCEPT FOR AIR BEARING SHOCK MODELING

This chapter aims to introduce and investigate the quasi-static concept of the air bearing for the HDD shock simulation. The chapter is divided into three major parts. In the first part, the analytical consideration that leads to the quasi-static notion is explained. Then, the development of full air bearing shock model based on finite volume method, considering viscous shear force & intermolecular is presented. In the last part an air bearing model is built based on the quasi-static idea and the model is subsequently compared with the full air bearing model.

4.1 *Analytical Consideration*

The basic analytical considerations for the quasi-static concept are explained as follows: The duration of the shock pulse and the motions of HDD structural components are relatively much slower than the response of the dynamic system formed by the slider and the air bearing. This can be concluded by observing that the dominant frequency associated with half-sinusoidal excitation is around 1,000 Hz for shock with 0.5 ms pulse width, whereas the fundamental air bearing resonance frequency is typically well over 100 kHz in modern HDD [96]. Since the motion of the HDD structures do not happen on a time scale that is significantly faster than the shock pulse, these components can be dynamically excited. Therefore, from the point of view of the air bearing, the shock response of HDD components only causes slow enough alteration in its boundary condition that the air bearing equilibrium is maintained during the shock event (in the absence of head disk contact).

To further explain this concept, a mass-spring-damper system viewpoint is used below. Referring to Figure 2.12, if the fundamental frequency of the air bearing is 100 kHz and the excitation pulse has maximum significant frequency content up to 2 kHz, then the air bearing response lies in stiffness controlled region [116, 147]. In that region, the air bearing dynamics response is expected to be the same as its static response (quasi-static), regardless of large variation of damping ζ.

However, the various related literatures [49, 78, 153-159] have shown that the air bearing behavior is nonlinear. Hence, its fundamental natural frequencies can change. This is further demonstrated in the next figure; Figure 4.1 displays the variation in air bearing force with respect to flying height. It shows that the air bearing fundamental natural frequencies varies from ~ 36 kHz to ~ 140 kHz when the flying height changes from 50 nm to 2 nm (the slider mass is 0.006 gram and its position is 30 mm from disk pivot; the pitch angle and roll angle are fixed at 80 μ-radians and 0 radians, respectively).

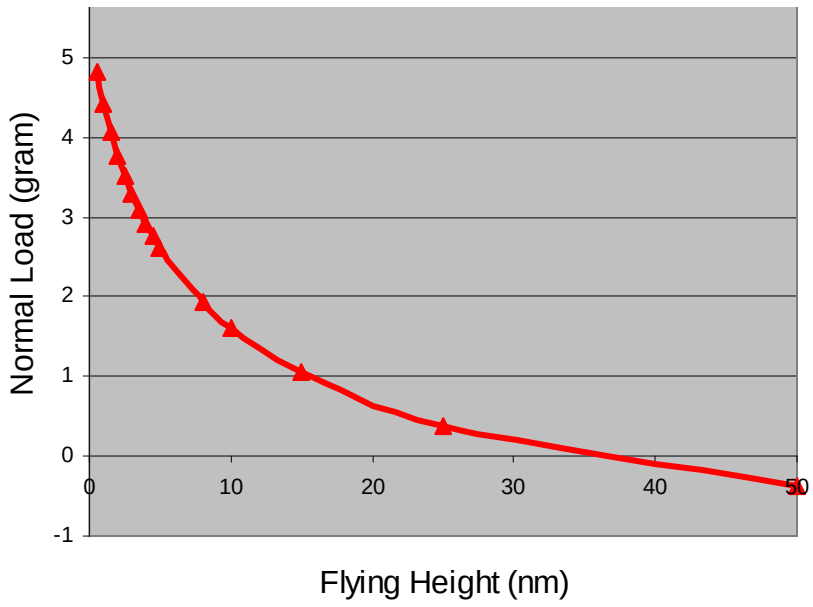

FIGURE 4.1 RELATIONSHIPS BETWEEN FLYING HEIGHT AND BEARING FORCE

From a mass-spring-damper system point of view, the variation of the fundamental frequencies of the air bearing does not significantly affect the quasi-static nature of the air bearing response. This is further explained in Figure 4.2, which shows that the air bearing response is still much the same with the static response, although its fundamental frequency has changed from 140 kHz to 36 kHz.

Nevertheless, the actual air bearing shock response is expected to be quite complex because not only the flying height that varies during shock event, the pitch and roll angle also fluctuate. Hence, the best way to test the quasi-static concept in the air bearing dynamics application is to build both the full model & the quasi-static model, and then compare their shock responses.

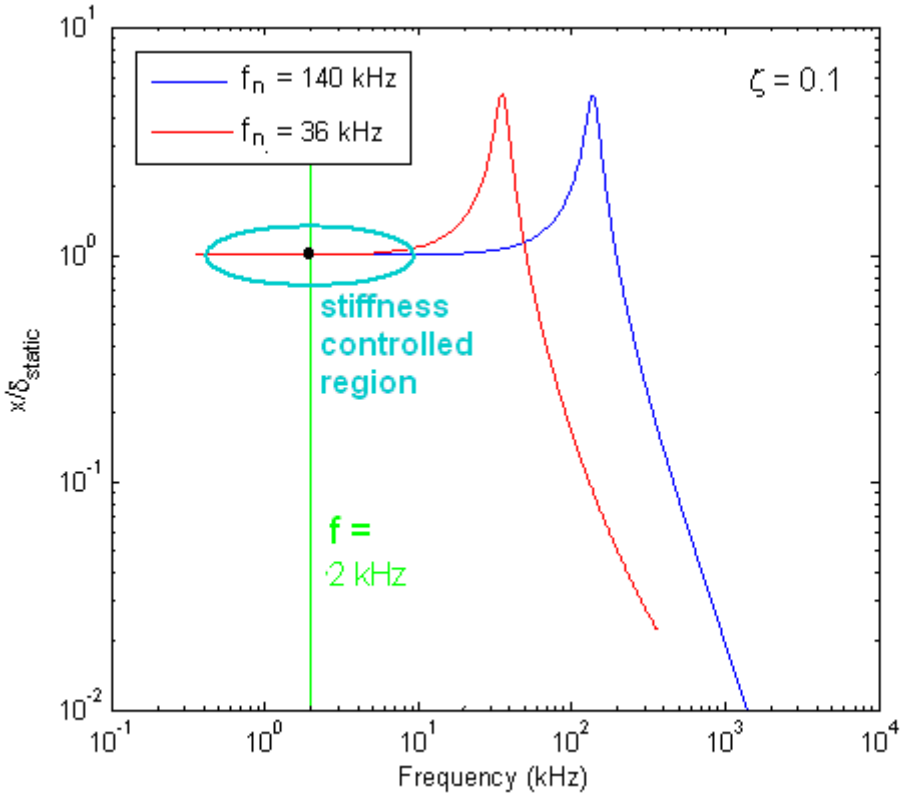

FIGURE 4.2 AIR BEARING TRANSMISSIBILITIES AT DIFFERENT FUNDAMENTAL FREQUENCIES

The development of the full finite volume model of the air bearing are presented in the next section and then followed by the formulation of quasi-static air bearing model.

4.2 *Full Finite Volume Air Bearing Modeling*

The finite volume method (FVM) can be applied to a general class of convection-diffusion problem (case independent). Here, the FVM is adapted to model the air bearing dynamics. In the first part of this section, the governing equations for the air bearing are presented. The next two parts contain the finite volume formulation and its verification using another well established numerical model.

4.2.1 The Governing Equations for the Air Bearing

In this study, three forces in the air bearing are considered. The first one is the air pressure governed by Reynolds compressible gas equation; the other two are viscous shear force and intermolecular force. The formulations of all those forces have been previously shown in the literature review [95, 160]. In the followings, they will be explained with more detail and clarity to facilitate subsequent finite volume formulation.

4.2.1.1 Reynolds Compressible Gas Equation

The pressure distribution exerted by the air bearing on the slider is governed by gas lubrication equation [161] i.e. compressible Reynolds equation that can be written as

$$\frac{\partial}{\partial x}\left(ph^3 \frac{\partial p}{\partial x}\right)+\frac{\partial}{\partial y}\left(ph^3 \frac{\partial p}{\partial y}\right)=6\mu\left(U\frac{\partial ph}{\partial x}+V\frac{\partial ph}{\partial y}\right)+12\mu\frac{\partial ph}{\partial t} \tag{4.1}$$

where p is the pressure acting on slider surface, h is the spacing between disk an slider, μ is air dynamic viscosity, U and V are the local disk velocity in the x and y direction. Since the air bearing thickness is very small compared to the lateral dimension of the slider, the pressure can be assumed to be constant across the film thickness.

The above Reynolds equation cannot be used directly when the spacing between the slider and the disk is in submicron order. If the air bearing spacing between the disk and slider is very small and comparable to the molecular mean free path, the rarefaction effect of the gas (the slip effect) has to be taken into account. The slip correction factor Q for the steady state air bearing condition can be put into the following non-dimensional form of Reynolds equation [162, 163].

$$\frac{\partial}{\partial X}\left(QPH^3\frac{\partial P}{\partial X}-\Lambda_x PH\right)+\frac{\partial}{\partial Y}\left(QPH^3\frac{\partial P}{\partial Y}-\Lambda_y PH\right)=0 \qquad (4.2)$$

where $P=p/p_a$ and $H=h/h_m$ are dimensionless parameters of air pressure and air bearing spacing, respectively; p_a is the ambient pressure and h_m is the reference spacing between the trailing edge center of the slider and the disk, $X=x/L$ and $Y=y/L$ are dimensionless coordinates in slider length and width direction; L is the length of the slider. $\Lambda_x=6\mu UL/p_a h_m^2$ and $\Lambda_y=6\mu VL/p_a h_m^2$ are the bearing numbers in X and Y direction respectively, which represent the relative importance between convection effect and diffusion effect. μ is the dynamic viscosity of the gas, U and V are the disk velocity components in X and Y direction respectively. Q is the slip term; different Q function reflects different slip order as shown in Table 4.1.

TABLE 4.1 VARIOUS SLIP MODEL

Non-slip model	Q = 1
First-order slip model	$Q = 1 + 6aK_n/(PH)$
Second-order slip model	$Q = 1 + 6K_n/PH + 6(K_n/PH)^2$
1.5-order slip model	$Q = 1 + 6\alpha K_n/PH + (8/3)(K_n/PH)^2$
Fukui-Kaneko model	$Q = f(K_n/PH)$

Here, $a = (2-\alpha)/\alpha$ is a numerical constant where α is the surface accommodation coefficient, $K_n = \lambda/h_m$ is the Knudsen number and λ is the molecular mean free.

$$\lambda = \frac{\mu\sqrt{2\pi RT}}{2p} \tag{4.3}$$

where R is the gas constant, T is the temperature and p is the gas pressure.

The Fukui-Kaneko approximation model [81] is used in this simulation because its validity has been confirmed by the Direct Simulation Monte Carlo method [164]. The corresponding slip term Q can be expressed as

$$Q = \frac{Q_p}{Q_{con}} \tag{4.4}$$

where

$$\begin{aligned} Q_p &= D/6 + 1.0162 + 1.0653/D - 2.1354/D^2 \text{ for } (D \geq 5) \\ Q_p &= 0.13852D + 1.25087 + 0.15653/D - 0.00969/D^2 \text{ for } (0.15 \leq D < 5) \\ Q_p &= -2.22919D + 2.10673 + 0.01653/D - 0.0000694/D^2 \text{ for } (0.01 \leq D < 0.15) \end{aligned} \tag{4.5}$$

and

$$Q_{con}(D) = D/6 \tag{4.6}$$

D is the inverse Knudsen number

$$D = \frac{\sqrt{\pi}}{2K_n} = D_0 PH \tag{4.7}$$

and D_0 is a characteristic inverse Knudsen number.

$$D_0 = \frac{p_a h_m}{\mu\sqrt{2RT_0}} \tag{4.8}$$

The non-dimensional form of the unsteady state (dynamics) Reynolds equation can be written as

$$\frac{\partial}{\partial X}\left(QPH^3\frac{\partial P}{\partial X} - \Lambda_x PH\right) + \frac{\partial}{\partial Y}\left(QPH^3\frac{\partial P}{\partial Y} - \Lambda_y PH\right) = \sigma\frac{\partial}{\partial T}PH \tag{4.9}$$

where $\sigma = 12\mu\omega L^2/(p_a h_m^2)$ is the squeeze number, $T = \omega t$, and ω is an appropriate angular frequency used for the dimensionless process of time t.

4.2.1.2 Viscous Shear Force Formulation

With the development of the HDD, the flying height keeps reducing and the spinning speed of the disk keeps increasing. When the flying height is small enough, the shear force generated by the air flow under the slider may become significant. The shear force also increases as the spinning speed of the disk increases. The shear force, normalized by $p_a L^2$, can be calculated with the following formula.

$$F_{shp} = \frac{h_m}{L}\int_0^b\int_0^1\left(\frac{H}{2}\frac{\partial P}{\partial X} + \frac{\Lambda_x}{6(H+2K_n)}\right)dXdY \tag{4.10}$$

$$F_{shr} = \frac{h_m}{L}\int_0^b \int_0^1 \left(\frac{H}{2}\frac{\partial P}{\partial Y} + \frac{\Lambda_y}{6(H+2K_n)} \right) dXdY \tag{4.11}$$

where b is the slider width normalized by the slider length. F_{shp} and F_{shr} are the shear forces in pitch and roll direction, respectively. To obtain their contribution to pitch and roll moment, the shear forces are multiplied with the slider thickness.

4.2.1.3 Intermolecular Force Formulation

When the flying height of the slider is less than 10nm, the contribution of the intermolecular force between the slider and the disk to the air bearing instability cannot be neglected. For two infinite half spaces, if the distance between the two center planes of the surface atoms or molecules is h, then the intermolecular adhesion *stress* P_i between these two half spaces can be expressed as

$$P_i = Ah^{-3}/(6\pi) - Bh^{-9}/(45\pi) \tag{4.12}$$

where A is the Hamaker constant and B is another constant. The first term in (4.12) is the attractive term and the second term is the repulsive term. In this study, the Hamaker constant A is taken to be 10^{-19} J and B is taken to be 10^{-76} J.m^6 [165].

After the three governing equations have been given, the finite volume formulation is given next.

4.2.2 Finite Volume Formulation

The finite volume formulation starts by formation of the computational grid containing finite number of control volume. The compressible Reynolds equation is then generalized and integrated over each side of the control volume [95]. After that,

the integrated equations are evaluated using hybrid interpolation scheme. The evaluated equations of all the control volumes are put together to form a general matrix equation and solved using two level iteration scheme.

4.2.2.1 Formation of Computational grid

The grid distribution in finite volume method (FVM) plays an important role in obtaining a meaningful solution. This is especially true in the air bearing study where the slider profile has a relatively complicated geometry. There are not only clearance discontinuities, but also sudden changes of the surface slope. Generally, if a more accurate pressure solution is wanted, denser grid will be needed. However, the increase of the grid number will introduce other problems, such as longer computational time. Hence, non-uniform grid is always used to address this problem; more computational grids are assigned at the positions where accurate pressure solutions is wanted (at areas with discontinuities/ abrupt changes) while fewer grids are put at other unimportant position (e.g. shallow region). It is also important to align a grid line at the position where there are clearance or slope discontinuities. In the subsequent section, the term “key position” will be used as the name of the position where there is a clearance or slope discontinuities.

A grid scheme base on the geometric progression [166] is adapted in this study. Since it is important to put a computational node at the key positions, they are firstly extracted out from the slider profile data. After all the key positions have been known, the computational domain is then divided into several intervals using these key positions in both directions. In each interval, the geometric progression can be used. In Figure 4.3, the grids number distribution for an interval is shown. In this figure, the

total grids number is $n_1 + n_2 + n_1$. The first n_1 grids are expanding grids with the geometric progression ratio q while the last n_1 grids are shrinking grids with the geometric progression ratio 1/ q. The n_2 grids in the middle are uniform grids with grid size equals to the size of the last grid in the first n_1 grids. The length of this interval is $AB = l$. The following relation can be found.

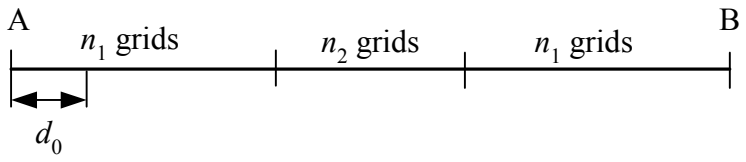

FIGURE 4.3 GRIDS NUMBER IN AN INTERVAL

$$2\frac{d_0(1-q^{n_1})}{1-q} + n_2 d_0 q^{n_1-1} = l \tag{4.13}$$

Then the first grid size d_0 can be expressed as

$$d_0 = \frac{l(1-q)}{2(1-q^{n_1}) + n_2(1-q)q^{n_1-1}} \tag{4.14}$$

After the computational grid has been established, the governing equation for each control volume in the grid can be formulated.

4.2.2.2 Integration of Generalized Compressible Reynolds Equation

The general class of convection-diffusion equation can be written as

$$\frac{\partial}{\partial t}(\rho\phi) + \mathrm{div}(\rho\mathbf{u}\phi) = \mathrm{div}(\Gamma\,\mathrm{grad}\,\phi) + S \tag{4.15}$$

where ϕ is the dependent variable, ρ is the density of the fluid, Γ is the diffusion coefficient, **u** is the flow velocity and S is the source term. In (4.15), the first term in

the left hand side is called transient term and the second term is called *convection* term. The first term in the next side is *diffusion* term and the second is source term.

When considering the two dimensional case, the steady state Reynolds equation (4.2) can be written as:

$$\frac{\partial f_x}{\partial X} + \frac{\partial f_y}{\partial Y} = 0 \tag{4.16}$$

where f_x and f_y are the total fluxes defined by

$$f_x \equiv \rho u \phi - \Gamma \frac{\partial \phi}{\partial X} \tag{4.17}$$

$$f_y \equiv \rho v \phi - \Gamma \frac{\partial \phi}{\partial Y} \tag{4.18}$$

where u and v are the X and Y components of **u**

Clearly, it can be seen that (4.2) is a special case of (4.15), with $\phi = P$, $\rho = H$, $u = \Lambda_x$, $v = \Lambda_y$ and $\Gamma = QPH^3$.

In finite volume method, the solution domain is subdivided into a finite number of small control volumes (CVs), as shown in Figure 4.1. The integration of equation (4.16) over a CV gives

$$F_e + F_n - F_w - F_s = 0 \tag{4.19}$$

where F_e and F_w are the integration of flux f_x over the CV face e and face w, respectively; F_w and F_s are the integration of flux f_y over the CV face n and face s, respectively.

Each integrated flux is then separated back into convective flux F^c and diffusive flux F^d to ease the subsequent formulation.

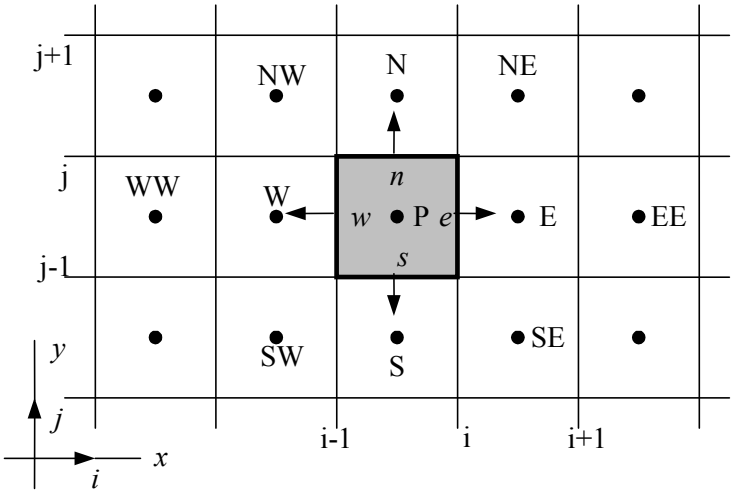

FIGURE 4.4 A TYPICAL CV USED FOR A CARTESIAN 2D GRID

The approximations to F^c and F^d require the values of the variables at the locations other than computational nodes (CV centers). They can be expressed in terms of the nodal values by interpolation. Numerous interpolation schemes are available, such as central differencing scheme, upwind differencing scheme, hybrid differencing scheme, power-law scheme, and higher order schemes. In this study, central difference scheme is used and stabilized using hybrid scheme. The hybrid system has been proven to be the one of the most effective stabilizing schemes [95].

4.2.2.3 Evaluation of Flux by Central Differencing Scheme (CDS)

The general steady state convection-diffusion equation without source (4.20) can be obtained by integrating (4.15) over the sides of the CV.

$$\int_S \rho\phi\mathbf{v}\cdot\mathbf{n}dS = \int_S \Gamma \operatorname{grad}\phi\cdot\mathbf{n}dS \tag{4.20}$$

In the above equation, the term on the left is the convective flux F^c and the right term is the diffusive flux F^d. The convective flux F^c can be approximated as a product of the mass flux and the mean value of ϕ, for example, on the 'e' face of the CV in Figure 4.3:

$$F_e^c = \int_{S_e} \rho\phi\mathbf{v}\cdot\mathbf{n}dS \approx \dot{m}_e\phi_e \tag{4.21}$$

where $\dot{m}_e$ is the mass flux through the 'e' face:

$$\dot{m}_e = \int_{S_e} \rho\mathbf{v}\cdot\mathbf{n}dS \approx (\rho u)_e \Delta y \tag{4.22}$$

ϕ_e is obtained by using the linear interpolation between the two nearest nodes as:

$$\phi_e = \phi_E\lambda_e + \phi_P(1-\lambda_e) \tag{4.23}$$

where λ_e is the linear interpolation factor and it is defined as:

$$\lambda_e = \frac{x_e - x_P}{x_E - x_P}. \tag{4.24}$$

Then the convective flux can then be written as:

$$F_e^c = \dot{m}_e(1-\lambda_e)\phi_P + \dot{m}_e\lambda_e\phi_E \tag{4.25}$$

The mass flux $\dot{m}_n$ through the 'n' face can be calculated as

$$\dot{m}_n = \int_{S_n} \rho\mathbf{v}\cdot\mathbf{n}dS \approx (\rho u_y)_n \Delta x \tag{4.26}$$

Analogous expressions for the convective fluxes of other CV faces are:

$$F_w^c = \dot{m}_w(1-\lambda_w)\phi_P + \dot{m}_w\lambda_w\phi_W \tag{4.27}$$

$$F_n^c = \dot{m}_n(1-\lambda_n)\phi_P + \dot{m}_n\lambda_n\phi_N \tag{4.28}$$

$$F_s^c = \dot{m}_s(1-\lambda_s)\phi_P + \dot{m}_s\lambda_s\phi_S \tag{4.29}$$

The total convective flux can then be written as

$$\begin{aligned}&\int_S \rho\phi\mathbf{v}\cdot\mathbf{n}dS = F_e^c + F_w^c + F_n^c + F_s^c \\ &= (A_P^c + \dot{m}_e + \dot{m}_w + \dot{m}_n + \dot{m}_s)\phi_P + A_E^c\phi_E + A_W^c\phi_W + A_N^c\phi_N + A_S^c\phi_S\end{aligned} \tag{4.30}$$

where

$$\begin{aligned}&A_E^c = \dot{m}_e\lambda_e; \quad A_W^c = \dot{m}_w\lambda_w \\ &A_N^c = \dot{m}_n\lambda_n; \quad A_S^c = \dot{m}_s\lambda_s \\ &A_P^c = -(A_E^c + A_W^c + A_N^c + A_S^c)\end{aligned} \tag{4.31}$$

Note that $\dot{m}_w$ and λ_w for the CV centered on node P are equal to $-\dot{m}_e$ and $1-\lambda_e$ for the CV centered on node W, respectively.

The diffusive flux integral is evaluated using the midpoint rule and CDS approximation of the normal derivative. For example, on the 'e' face of the CV in Figure 4.3, the diffusive flux is:

$$\begin{aligned}F_e^d &= \int_{S_e} \Gamma\,\mathrm{grad}\,\phi\cdot\mathbf{n}dS \approx \left(\Gamma\frac{\partial\phi}{\partial x}\right)_e \Delta y \\ &= \frac{\Gamma\Delta y}{x_E - x_P}(\phi_E - \phi_P)\end{aligned} \tag{4.32}$$

In (4.32), the diffusion coefficient Γ is interpolated linearly between the nodal values at P and E. Note that for a same CV, Γ is different at different CV faces.

Analogously, the diffusive flux integral over other CV faces can be obtained as:

$$F_w^d = -\frac{\Gamma \Delta y}{x_P - x_W}(\phi_P - \phi_W) = \frac{\Gamma \Delta y}{x_P - x_W}(\phi_W - \phi_P) \tag{4.33}$$

$$F_n^d = \frac{\Gamma \Delta x}{y_N - y_P}(\phi_N - \phi_P) \tag{4.34}$$

$$F_s^d = -\frac{\Gamma \Delta x}{y_P - y_S}(\phi_P - \phi_S) = \frac{\Gamma \Delta x}{y_P - y_S}(\phi_S - \phi_P) \tag{4.35}$$

The diffusive flux over the whole CV can then be written as:

$$\begin{aligned} \int_S \Gamma \operatorname{grad}\phi \cdot \mathbf{n} dS &= F_e^d + F_w^d + F_n^d + F_s^d \\ &= -(A_P^d \phi_P + A_E^d \phi_E + A_W^d \phi_W + A_N^d \phi_N + A_S^d \phi_S) \end{aligned} \tag{4.36}$$

where

$$\begin{aligned} A_E^d &= -\frac{\Gamma \Delta y}{x_E - x_P}; \quad A_W^d = -\frac{\Gamma \Delta y}{x_P - x_W} \\ A_N^d &= -\frac{\Gamma \Delta x}{y_N - y_P}; \quad A_S^d = -\frac{\Gamma \Delta x}{y_P - y_S} \\ A_P^d &= -(A_E^d + A_W^d + A_N^d + A_S^d) \end{aligned} \tag{4.37}$$

Finally, for a generic node P, the integral equation (4.20) becomes:

$$A_W \phi_W + A_S \phi_S + A_P \phi_P + A_E \phi_E + A_N \phi_N = Q_P \tag{4.38}$$

where $A_l = A_l^c + A_l^d$; l represents any of the indices P, E, W, N, S and $Q_P = 0$.

The stability of the CDS depends on the Peclet number that measures the relative strength between convection and diffusion. It is defined as

$$P_e = A^c / A^d \tag{4.39}$$

When $|P_e| > 2$, the CDS will lead (4.38) to divergence [167]. To stabilize this, hybrid scheme method is used. When $|P_e| \le 2$, the Hybrid scheme is equivalent to the original CDS. When Peclet number $|P_e| > 2$, the Hybrid scheme dictates that the upwind differencing scheme is used to calculate convection flux and the diffusion flux set to be zero. Under this scheme, the coefficients in (4.38) are re-expressed as

$$\begin{aligned} A_E &= \min(\dot{m}_e, 0, A_E^c + A_E^d); \quad A_W = \min(\dot{m}_w, 0, A_W^c + A_W^d) \\ A_N &= \min(\dot{m}_n, 0, A_N^c + A_N^d); \quad A_S = \min(\dot{m}_s, 0, A_S^c + A_S^d) \\ A_P &= -(A_E + A_W + A_N + A_S) + (\dot{m}_e + \dot{m}_w + \dot{m}_n + \dot{m}_s) \end{aligned} \tag{4.40}$$

where the coefficients A_E^c, A_W^c, A_N^c and A_S^c are defined by equation (4.31) while the coefficients A_E^d, A_W^d, A_N^d and A_S^d are defined by equation (4.37).

After all the flux equations at each CV has been established using CDS with hybrid scheme, all their coefficients are assembled and used to solve the pressure value at each CV center. In last two subsections, the pressure solution at any given slider configuration and the unsteady state pressure solution are given.

4.2.2.4 Solving the Pressure at Given Slider Attitude

Equation (4.38) is nonlinear because its coefficients are functions of the unknown dependent variable ϕ. To solve these equations, a two level iteration scheme is employed. The outer iteration updates the coefficients using the most current values of the pressure and the inner iteration solves the linear outer-iteration-generated system of equation. For the inner iteration, the alternating direction line-by-line method is used.

When solving the equation (4.38), an approximate convergence criterion should be given. For each grid point, the residual R_P can be defined as

$$R_P = A_W\phi_W + A_S\phi_S + A_P\phi_P + A_E\phi_E + A_N\phi_N - Q_P \tag{4.41}$$

When R_P at all grid point is smaller than a preset value, (4.38) is deemed converged. In this report, the convergence criterion is written as

$$R = \frac{\sum_P |R_P|}{\sum_P |A_P\phi_P|} < \varepsilon \tag{4.42}$$

where ε is a given small number used as the convergence criterion number. The usual value of ε is ~ 10^{-7}.

4.2.2.5 Pressure solution for Unsteady State Air Bearing

When the HDD is working in a vibrating environment, the vibration of the HDD structures will cause the change of the flying attitude of the air bearing. The change of the flying attitude will cause the change of the air bearing pressure. The unsteady state Reynolds equation (4.9) should be used to find the air bearing pressure.

Fully implicit scheme is adopted to solve the unsteady state Reynolds equation. For an unsteady state, if at time step *n* the pressure is ϕ^n and the clearance is h^n, while at time step *n*+1, the pressure is ϕ^{n+1} and the clearance is h^{n+1}, the discretization of (4.9) results in as

$$A_W\phi_W^{n+1} + A_S\phi_S^{n+1} + A_{Pu}\phi_P^{n+1} + A_E\phi_E^{n+1} + A_N\phi_N^{n+1} = Q_P^n \tag{4.43}$$

A_l (l represents any of the indices E, W, N, S) has the same form as in (4.38),

$$A_{Pu} = A_P + \frac{\sigma h^{n+1}}{\Delta t} S_{CV}, \tag{4.44}$$

and

$$Q_P^n = \frac{\sigma h^n}{\Delta t} S_{CV} \phi^n \tag{4.45}$$

where σ is the squeeze number, h is the air bearing spacing, S_{CV} is the area of the CV, and Δt is the time step length.

Equation (4.43) is then solved using the same two-level-iteration scheme introduced in section 4.2.2.4.

After the pressure and the air bearing spacing have been solved, the contribution of the intermolecular force and the viscous shear force to total air bearing response can be easily calculated using (4.12), (4.10), and (4.11).

4.2.3 Verification of the Finite Volume Model of Air Bearing

In this section, the verification of the finite volume formulation shown in the previous section is presented. First, the slider used in the verification study is described. The dynamics process that was simulated is then described. Lastly, the dynamics response of the air bearing model is compared with the results obtained from an established model.

4.2.3.1 Description of the Slider Used in the Verification

The slider used in the verification process is shown in Figure 4.5. It is a current slider in the market used in a one-inch Micro drive. Its profile is quite complicated.

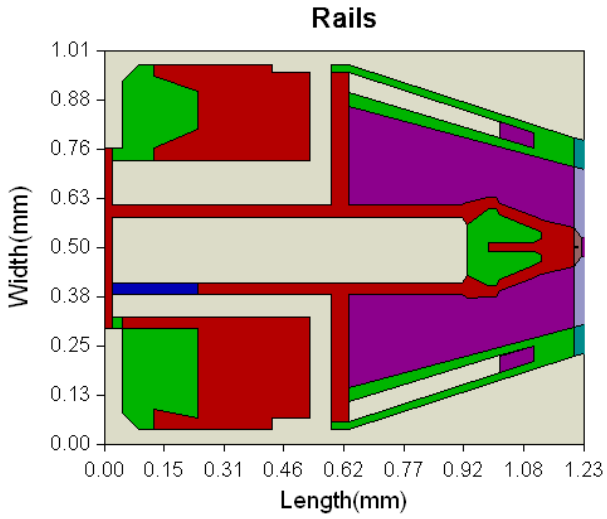

Preload = 1.25 gram

RPM = 3600

Radial Position = 12 mm

Skew angle = 11.34 degrees

Steady State FH = ~ 6 nm

Steady State pitch = ~ 45 μrad

Steady State roll = ~ 1 μrad

FIGURE 4.5 SLIDER DESIGN AND PARAMETERS [33]

The other corresponding parameters are slider mass $m = 0.006$ gram, pitch moment of inertia $I_p = 2.18 \times 10^{-10}$ kg.m^2, roll moment of inertia $I_r = 1.36 \times 10^{-10}$ kg.m^2 gas viscosity $\mu = 2.08 \times 10^{-5}$ Pa$\cdot$s, ambient pressure $P_0 = 1.01 \times 10^5$ Pa, and surface accommodation coefficient α =1.

4.2.3.2 Dynamic Process Simulated

The slider is given initial TEC height 15 nm, initial pitch angle 150 micro radians, and initial roll angle 0. The initial air pressure is uniform and at the same level as ambient pressure. The disk is perfectly rigid and flat. The mesh size is 128 × 128.

The slider center of gravity is at the base of the slider profile and it can only move vertically (up and down). At time t = 0, the preload of 1.25 gram is given at the slider center of gravity and the simulation starts. The results of the simulation and its comparison with other model are given next.

4.2.3.3 Comparison with another Dynamic Model

The same slider and the same dynamic process described previously were simulated using our model and using CMLAir32 v6.56a. The CMLAir32 is an air bearing commercial design program created by Computer Mechanics Laboratory in University of California, Berkeley. It has been used extensively in the HDD industry to analyze air bearing design and its analysis results shows good correlation with experimental results [33].

The comparison of the dynamic of the slider attitudes and the air bearing force are given in Figure 4.6 and Figure 4.7. It can be seen that our model agrees quite well with CMLAir32 v6.56a; the differences that appear between the two models are most probably contributed by the slight differences in both the computational grids used and the mathematical formulation (e.g. the interpolation scheme).

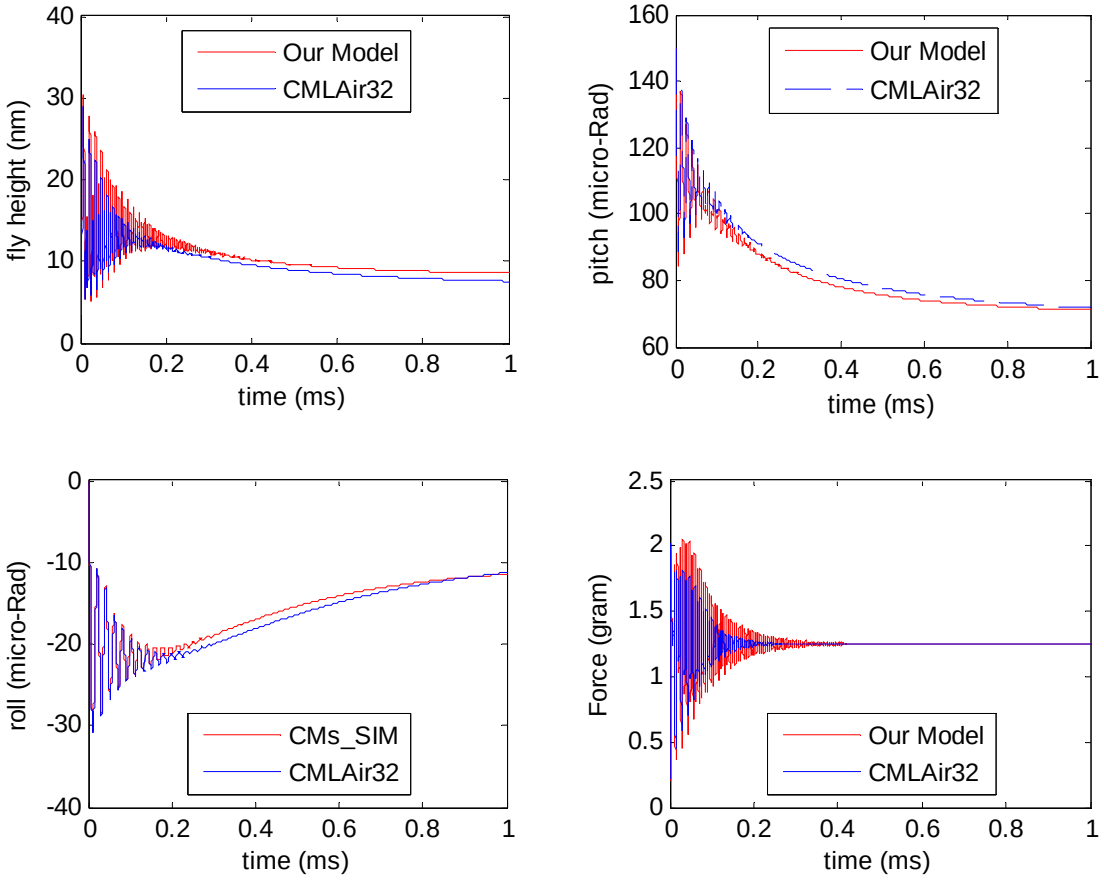

FIGURE 4.6 COMPARISON WITH CMLAIR32

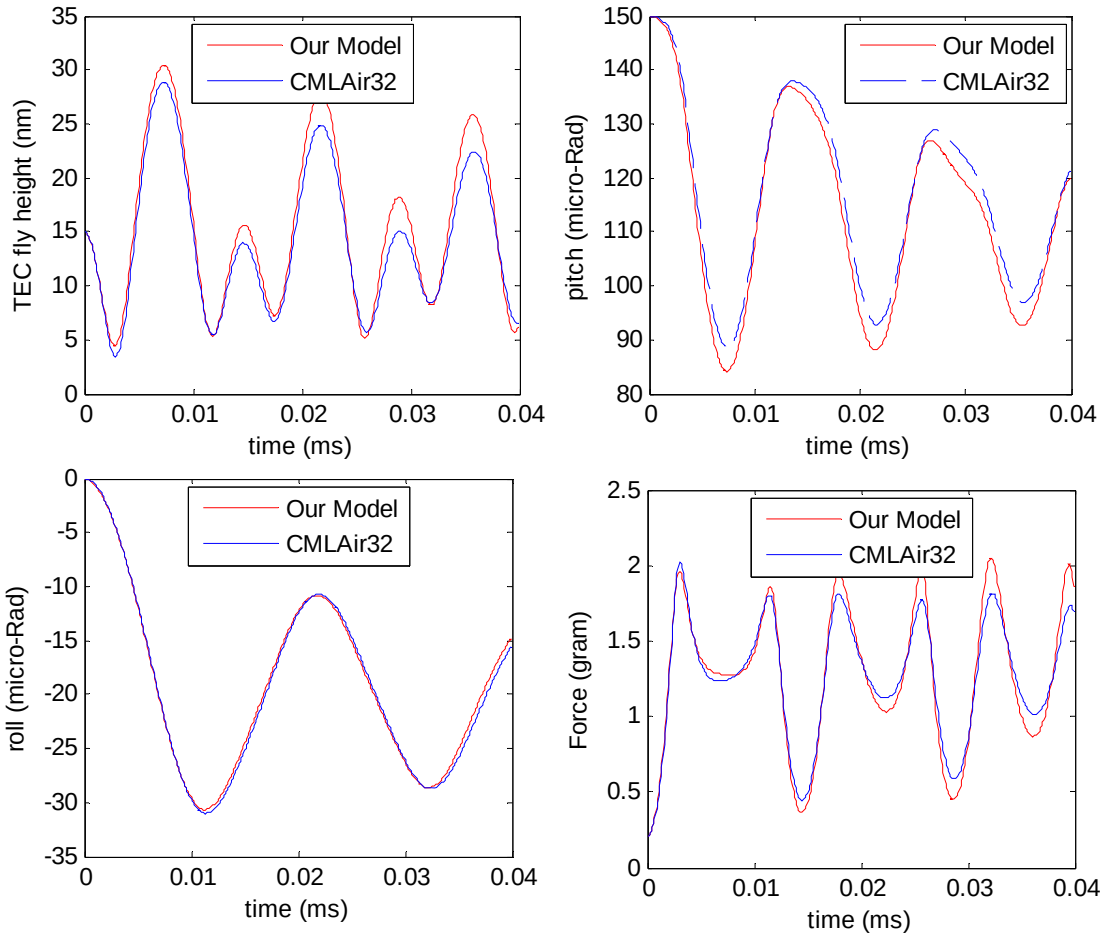

FIGURE 4.7 DETAILED COMPARISON WITH CMLAIR32

Since our finite volume model agrees quite well with the established model, it can be said that the model is accurate enough to be used in investigating the quasi-static concept introduced in section 4.1. In the next section, the quasi-static idea will be used to build an air bearing model. The model will be subsequently compared with the full finite volume model.

4.3 *Quasi-static Concept for Air Bearing Modeling*

In brief, when the fundamental frequency of a dynamic system is much higher than the frequency of excitation, its response will mostly depend on the static governing equation. Referring to the main governing equation of the air bearing (the

Reynolds compressible equation), the quasi-static concept suggests that the squeeze term (the time dependent term) can be considered as negligible because the equilibrium condition of the air bearing system is considered to happen almost instantaneously.

In the following subsection, the development of air bearing model based on the quasi-static concept is first described. Then, its shock response is compared with the full model.

4.3.1 Development of 3D Air Bearing Model based on Quasi-Static Idea

Figure 4.8 illustrates the mechanism of air bearing model; given any spacing configuration (fly height, pitch, and roll) as the input, the model should be able to give its force response (normal force, pitch & roll moment) to the structures.

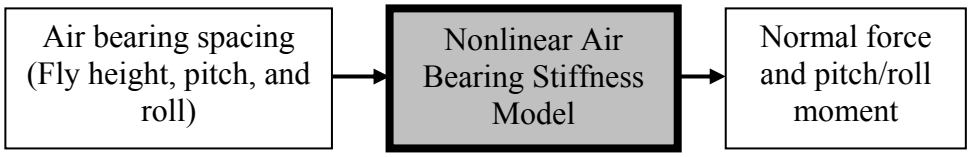

FIGURE 4.8 MECHANISM OF THE AIR BEARING MODEL

Unlike in full finite volume model where the compressible Reynolds equation is evaluated from at each simulation-time-step, quasi-static air bearing model has its force and moment response pre-calculated.

Initially, the pressure distribution on the slider air bearing surface is obtained by solving the static compressible Reynolds (4.2) at various slider attitudes using finite volume method.

Next, normal load (N_L), pitch moment load (P_M), and roll moment load (R_M) acting on the slider are computed for each spacing configuration. The data are then saved in lookup tables (one for each load). The parameters of a lookup table are illustrated in Figure 4.9. The intervals for the lookup tables depend on the degree of accuracy required; smaller interval means more accuracy in deciding the air bearing response during shock simulation. N_L, P_M, and R_M of the air bearing configurations inside the interval are obtained by interpolation (N_L is the net vertical force acting on the slider; P_M and R_M is calculated with respect to slider geometric center).

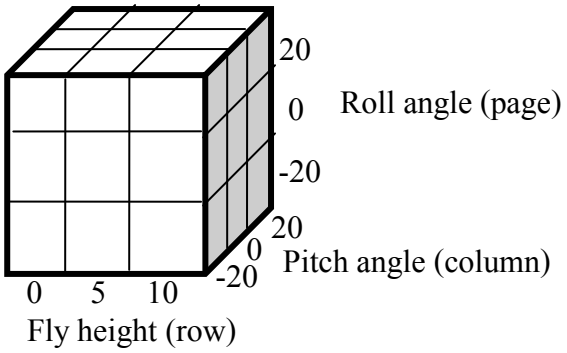

FIGURE 4.9 SIMPLE LOOKUP TABLE

The fly height axis of the lookup tables may range from 0 to 100 nm (100 nm is chosen because above this value the air bearing behave almost linearly; the linear interpolation will be able to give good prediction of the air bearing response). To capture the nonlinear behavior of the air bearing, the axis-interval at the low fly height region should be small. For instance, the fly height axis can be set as 0, 0.5, 1, 2, 3, 4, 5, 6, 7, 8, 9, 10 (smaller interval), 12, 15, 25, 50, and 100 nm (larger interval). The pitch and roll axes of the lookup tables may range from -100 micro-radians to 100 micro-radians with 20 micro-radians interval; the air bearing shock responses are expected to fall inside these ranges.

There will be some spacing configurations in the lookup tables where the slider-disk-contact is detected. At these configurations the air bearing responses are not computable using the static Reynolds equation. To complete the lookup tables, linear extrapolation method can be used. The interpolation is done for each roll angle value and for each load type. The figure below shows a typical lookup table for air bearing normal load (NL) for a certain roll angle configuration. The flying height and the pitch angle has uniform interval.

TABLE 4.2 LOOKUP TABLE

Row *j* \ Column *i*		Flying Height				
		1	2	3	…	n
Pitch Angle	1	NL	NL	NL	…	NL
	2	NL	NL	NL	…	NL
	3	NL	NL	NL	…	NL
	…	…	…	…	…	…
	m	NL	NL	NL	…	NL

= interval where slider-disk contact happens (as the results, its value cannot be predicted using static Reynolds equation)

= interval where static Reynolds equation can be used to determine its value.

The expansion process starts by filling the unknown values at the bottom edge and the right edge of the table.

$$NL_{(m,j)} = 2NL_{(m,j+1)} - NL_{(m,j+2)} \text{ and } NL_{(i,n)} = 2NL_{(i+1,n)} - NL_{(i+2,n)} \quad (4.46)$$

Then, the rest of the unknown values are extrapolated as

$$NL_{(i,j)} = NL_{(i+1,j)} + NL_{(i,j+1)} - NL_{(i+1,j+1)} \quad (4.47)$$

The extrapolation is then repeated for the rest of roll angle. The same method is also

used for moment load.

The completed lookup table functions as 3D quasi-static air bearing model in the shock simulation; providing air bearing force response at any given slider attitudes (flying height, pitch angle, and roll angle).

After both full model and quasi-static model have been shown, in the next subsection the shock response of the two models are compared.

4.3.2 Comparison between Quasi-static Model and Full Model

To investigate the accuracy of the quasi-static model, its shock response is compared with the full air bearing model. In this comparison a same structural model is coupled to both full model and quasi-static air bearing model (the details on the coupling process is given in the next chapter).

Figure 4.10 gives the response of the quasi-static air bearing and the full air bearing model to 200 G and 0.5 ms shock input. It appears that the shock responses of the full air bearing model is significantly lower compared to the response of the quasi-static air bearing.

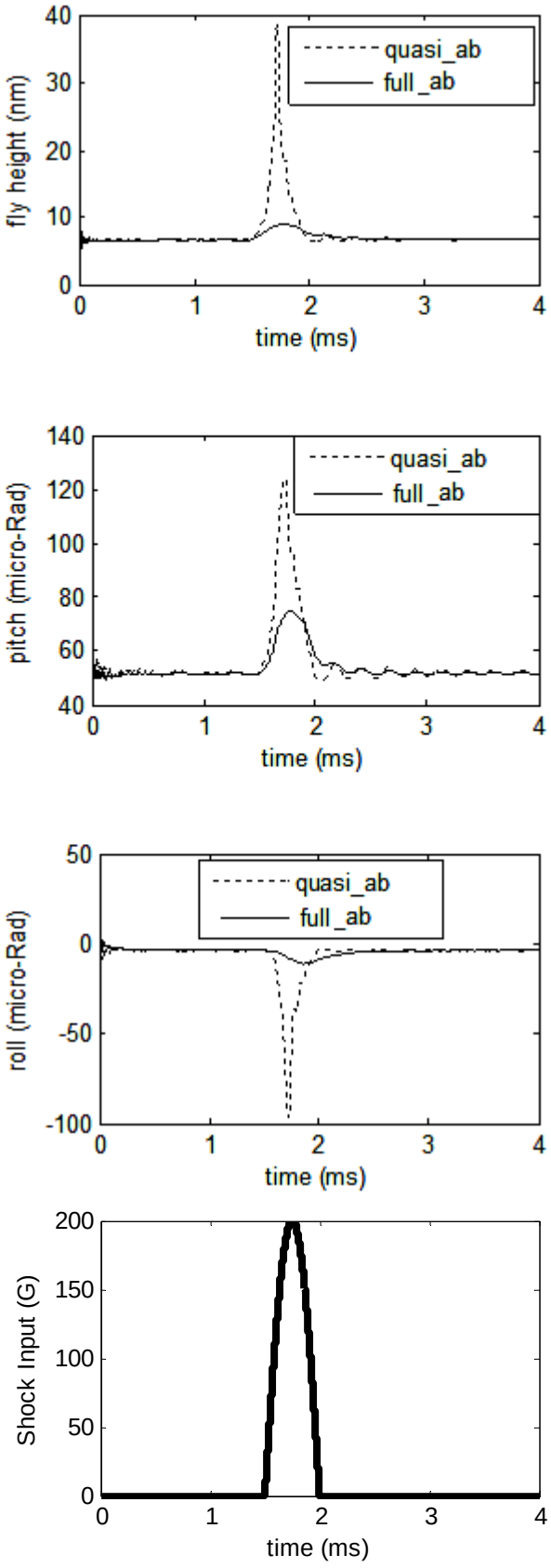

FIGURE 4.10 COMPARISON OF SLIDER RESPONSE BETWEEN QUASI-STATIC AND FULL AIR BEARING (AB) MODEL

A relatively high amount of damping is present in the shock response of the full air bearing model. This is in conflict with the analytical consideration in section 4.1 that shows that damping variation is not supposed to affect the air bearing response. The answer to this conflict lies in the squeeze term effect that is included in the full model; the damping/stiffness due to the squeeze term appears to have significant influence on the dynamics of the air bearing at the low frequency range.

4.3.3 Modification of Quasi-static Air Bearing Model

Modifying the interval of the lookup tables and/or changing the interpolation method used in quasi-static air bearing model do not significantly improve the accuracy of the model. Other ways to improve the accuracy of quasi-static air bearing model were investigated. It is found that adding viscous damping can increase accuracy of the quasi-static model considerably. The best places to put the damping elements and how much damping should be applied were investigated and the conclusion is presented as follows.

A linear viscous damping is best placed between the slider trailing edge center and the disk (position ‘A’ in Figure 4.11). Position ‘B’ (under the slider center) is not recommended because at that position the damping reduces pitch response much more than the fly height response. It means that by putting the damper at position ‘B’, the required pitch response may be obtained but the fly height response is still higher. A rotational damper is needed only at the rolling axis. The rotational damper in pitching axis is not necessary because the linear damper affects pitch response at the same time.

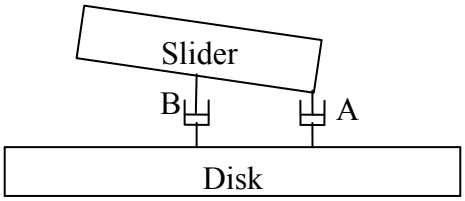

FIGURE 4.11 ADDITION OF VISCOUS DAMPING ELEMENT IN QUASI-STATIC MODEL

The damping values depend on the slider profile and its related parameters. The approximation function for the damping values is too complex to derive considering the intricacy of the slider profile. Hence, the next sensible solution is using an optimization method with the objective to minimize the difference in the maximum shock response between the quasi-static air bearing and finite volume air bearing. In this study, trial-and-error method is used in optimizing the damping values. Since the time needed to run shock simulation using the quasi-static air bearing is very fast (in term of minutes), the trial-and-error technique is quite efficient. For the slider shown in Figure 4.5, the linear damping needed is found to be around 800 $N.s.m^{-1}$ and the rotational damping is around 10^{-7} $N.m.s.rad^{-1}$. These values may be used as references for the damping optimization of another similar slider.

4.3.4 Modified Quasi-Static Model vs. Full Air Bearing Model

The shock response of the quasi-static model (with optimized viscous damping) and the full model at 200 G shock with 0.5 ms pulse-width are given in Figure 4.12. It can be seen that the shock response of the quasi-static model is much improved with the addition of damping. It is interesting to note that the force response of the quasi-static model and the full model (Figure 4.13) are virtually the same. This indicates that the quasi-static air bearing (AB) can accurately predict the change in air bearing force.

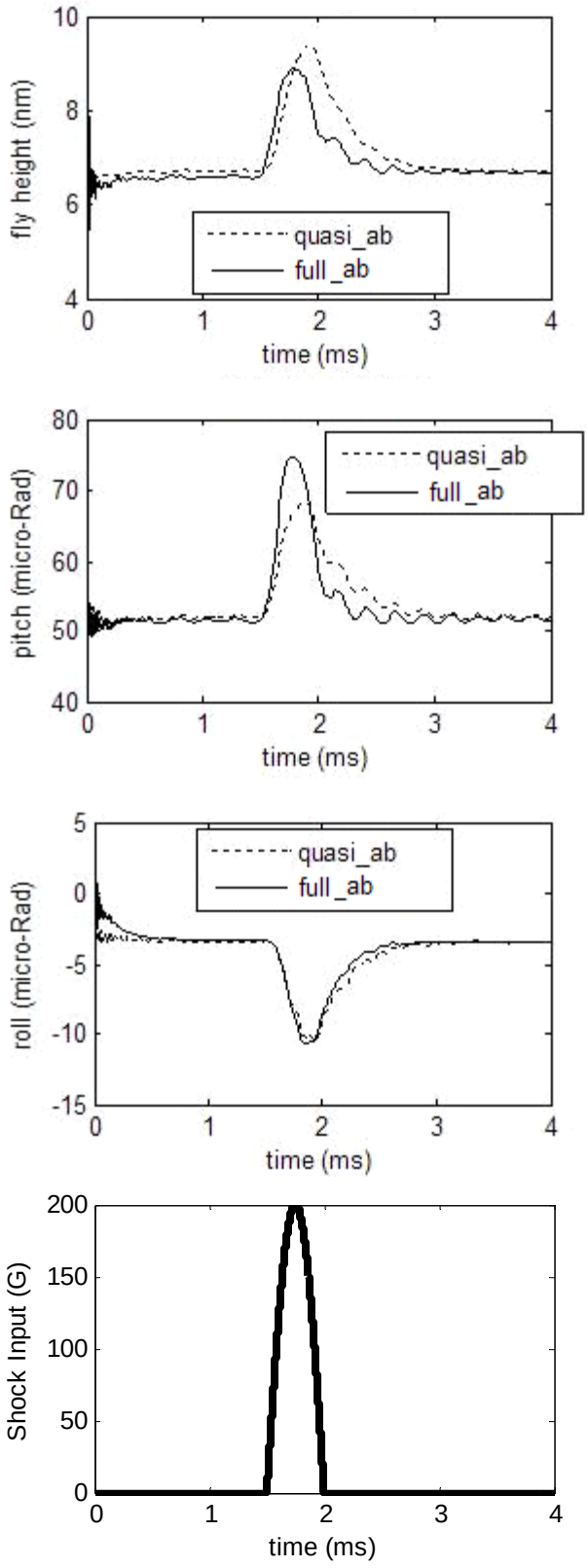

FIGURE 4.12 COMPARISON OF SLIDER RESPONSE BETWEEN QUASI-STATIC MODEL (WITH DAMPING) AND FULL AB MODEL

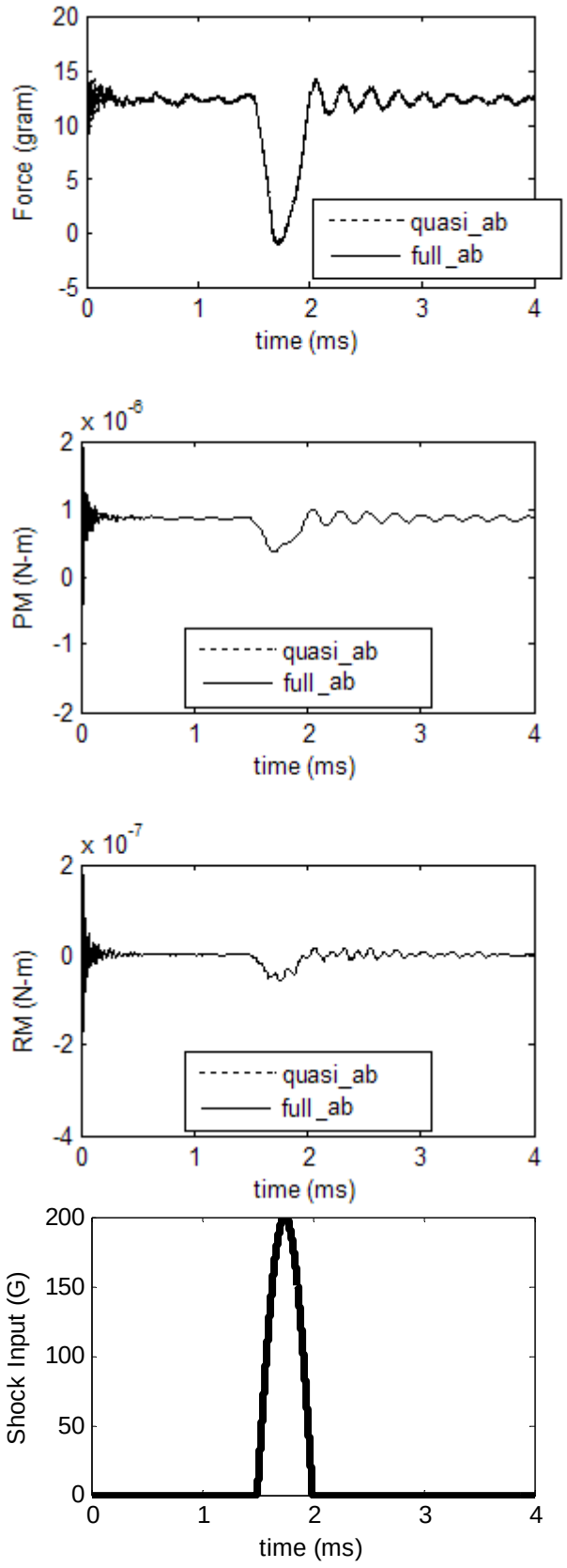

FIGURE 4.13 AIR BEARING FORCE COMPARISON BETWEEN QUASI-STATIC MODEL (WITH DAMPING) AND FULL AB MODEL

Figure below shows the comparison between model without and with modification. It can be seen that the response of the air bearing is reduced due to this modification.

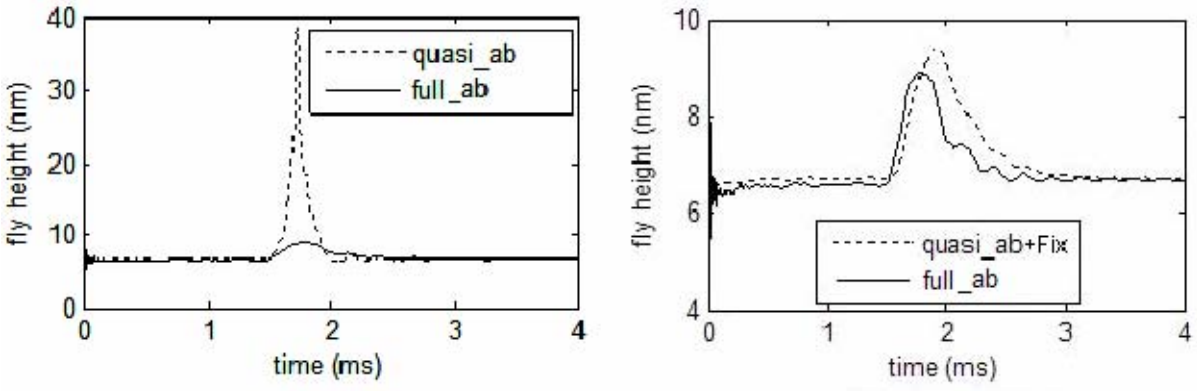

FIGURE 4.14 COMPARISON BETWEEN QUASI-STATIC MODEL WITHOUT AND WITH FIX

The effect of the modification on Figure 2.12 is depicted as the figure below. It is similar to that of over-damped damper, reducing the slider response even at the low frequency region.

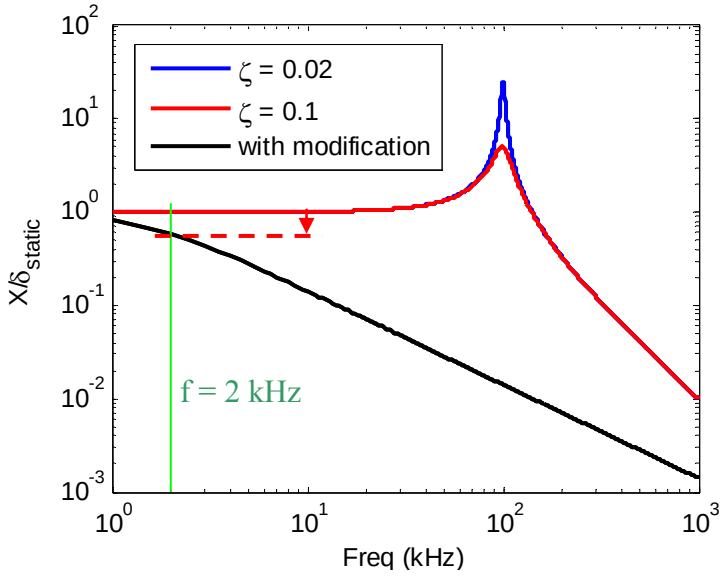

FIGURE 4.15 EFFECT OF MODIFICATION FROM SDOF POINT OF VIEW

The same fitted damping value was tried at pulses with different widths and heights. It was found that the same damping can be used to obtain acceptable results for a variety

of pulse parameters. The comparison results are shown below (Figure 4.16 to Figure 4.21). It can be seen that the flying height difference is less than 2 nm and the maximum pitch angle difference is ~ 10 μrad. For the roll angle the difference is less than 4 μrad. Note that without the damping fix (see Figure 4.10) the error is up to 30 nm for the flying height, 40 μrad for the pitch angle, and ~ 90 μrad for the roll angle.

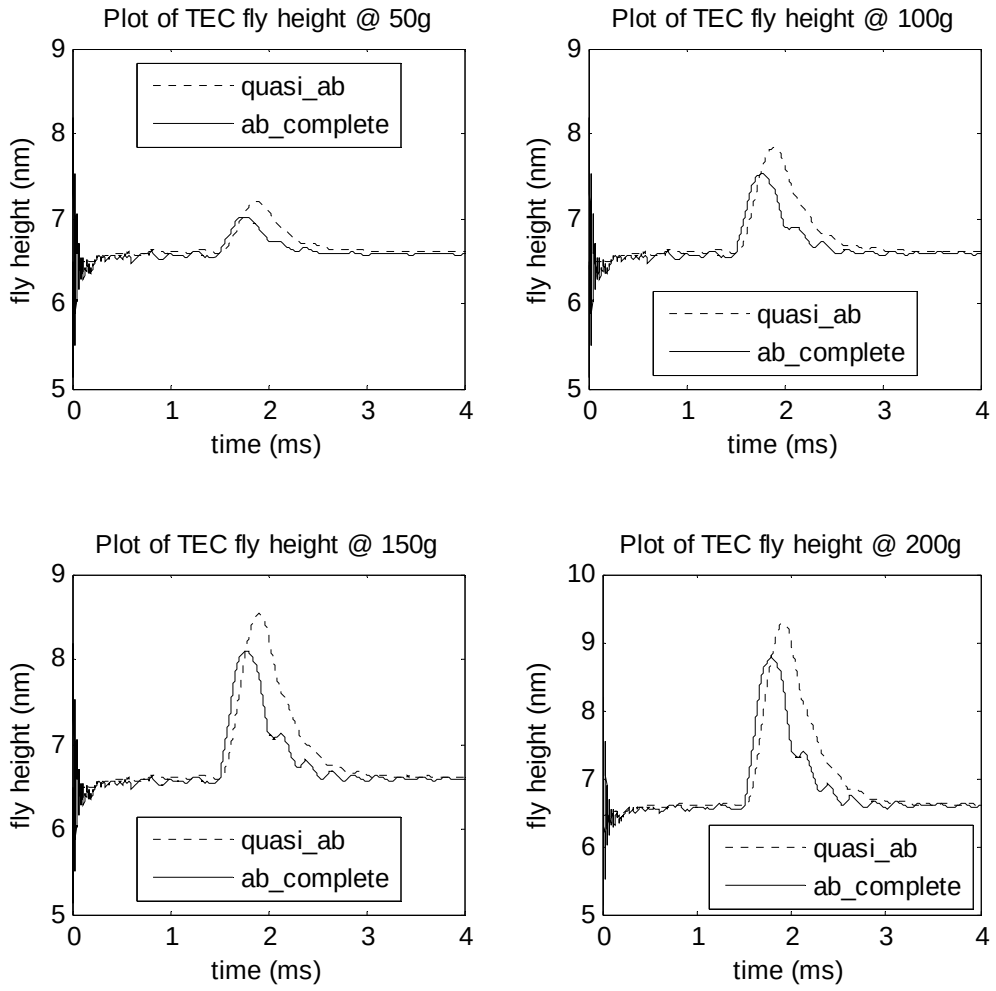

FIGURE 4.16 FLYING HEIGHT COMPARISON 0.5MS PULSE WIDTH @ DIFFERENT G LEVEL

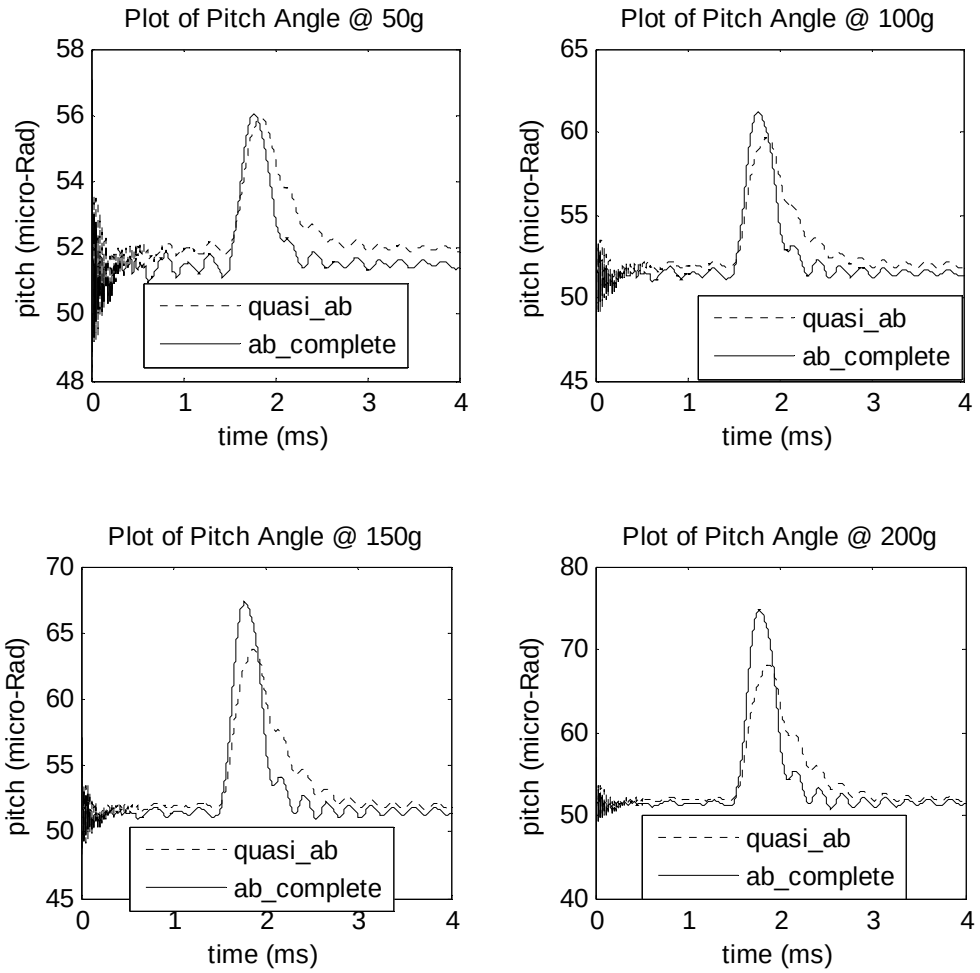

FIGURE 4.17 PITCH ANGLE COMPARISON 0.5MS PULSE WIDTH @ DIFFERENT G LEVEL

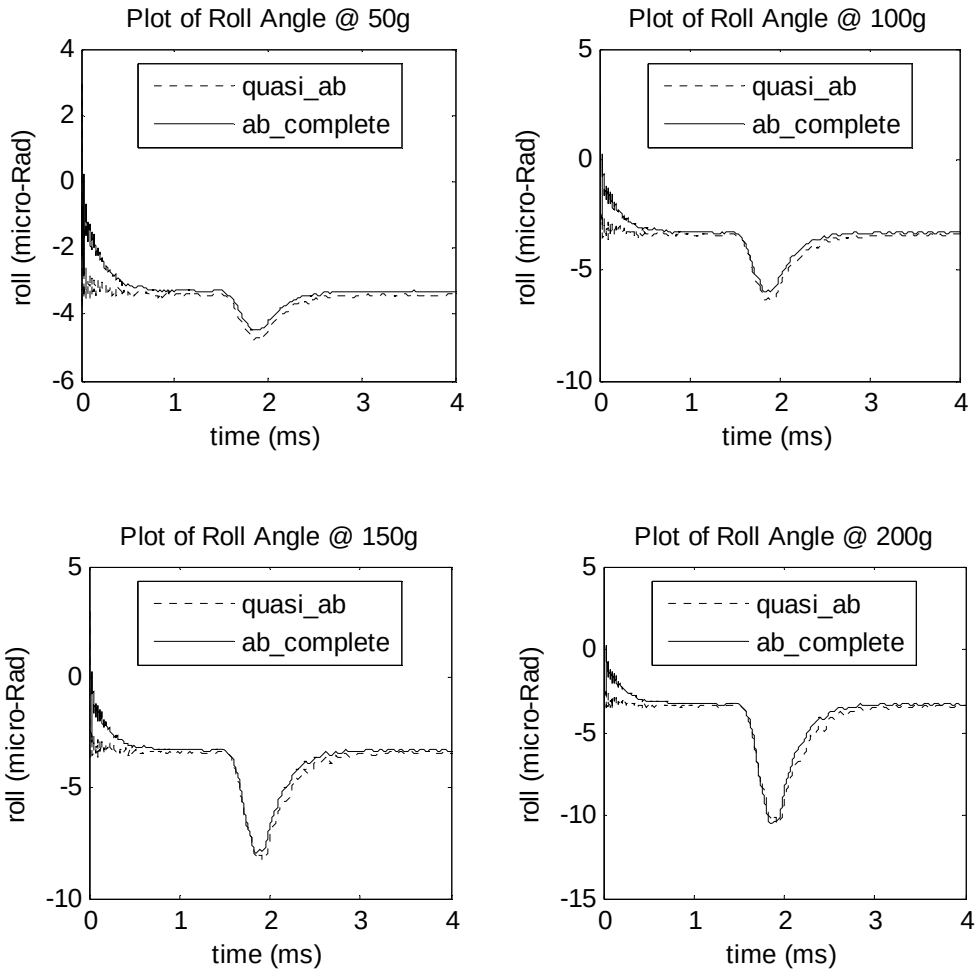

FIGURE 4.18 ROLL ANGLE COMPARISON 0.5MS PULSE WIDTH @ DIFFERENT G LEVEL

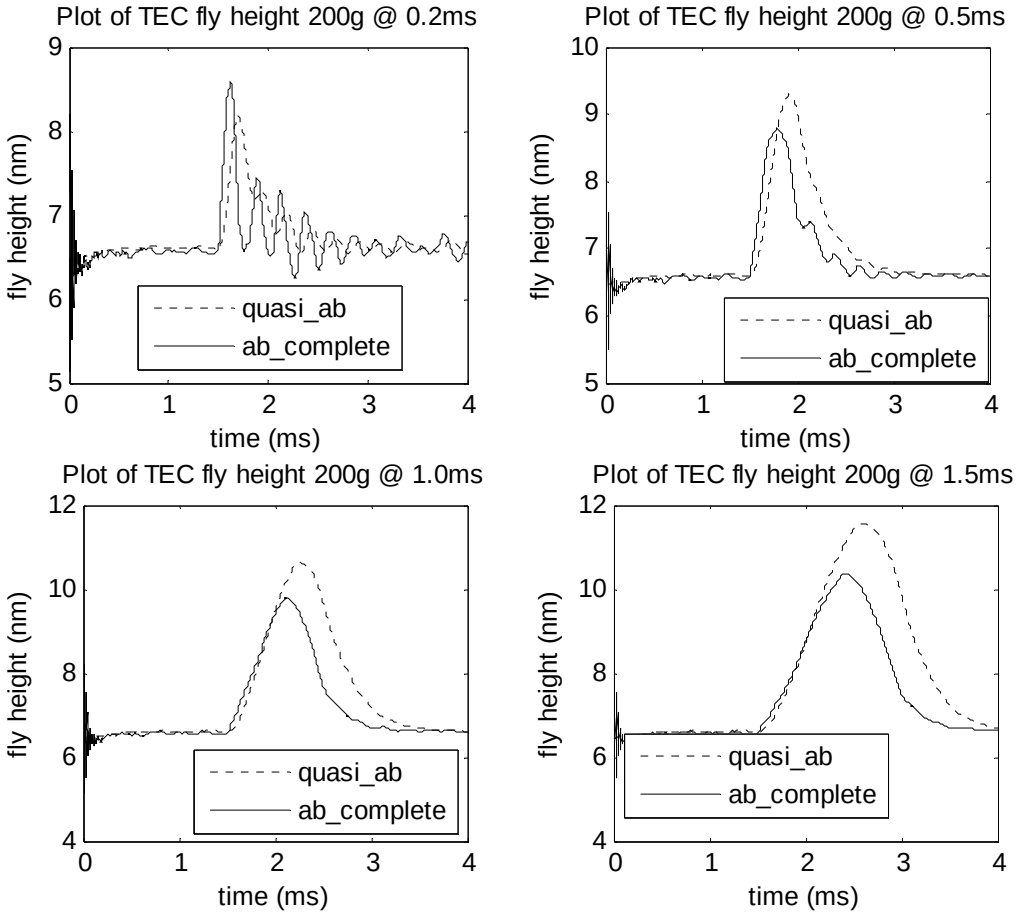

FIGURE 4.19 FLYING HEIGHT COMPARISON @ DIFFERENT PULSE WIDTH

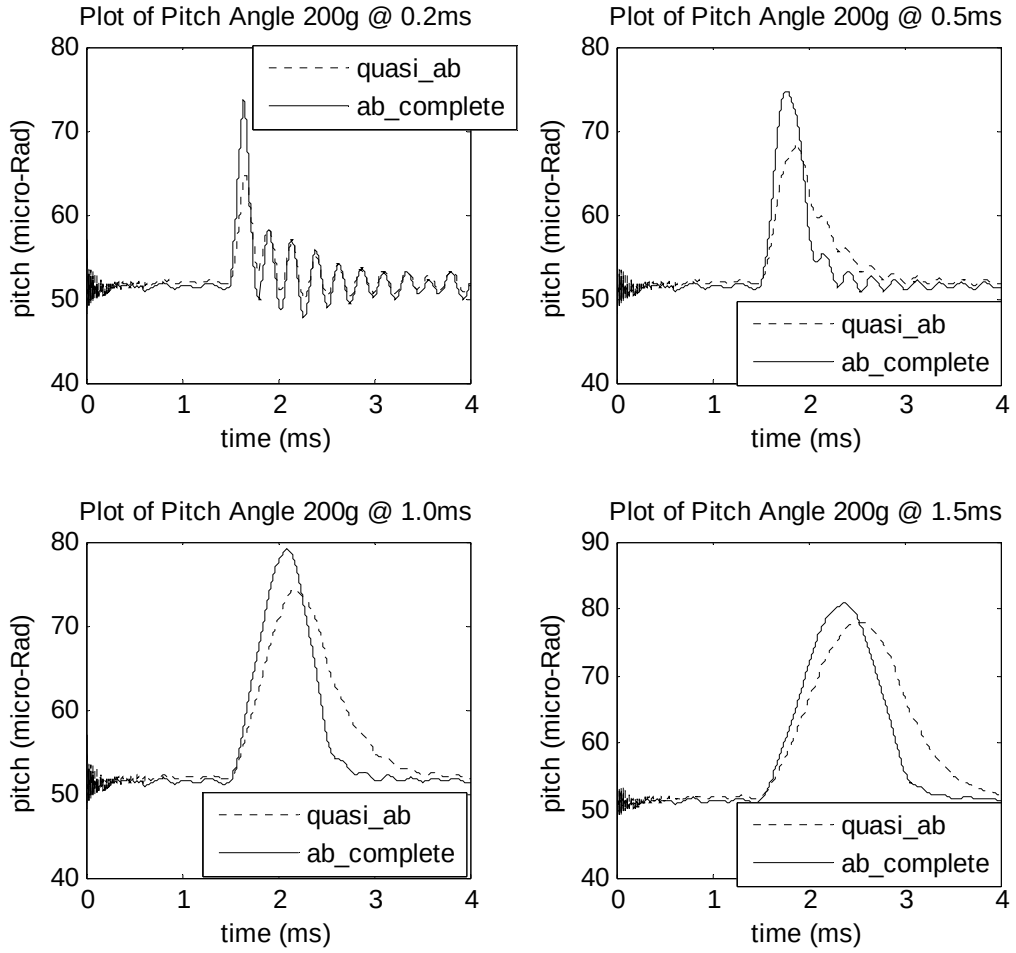

FIGURE 4.20 PITCH ANGLE COMPARISON @ DIFFERENT PULSE WIDTH

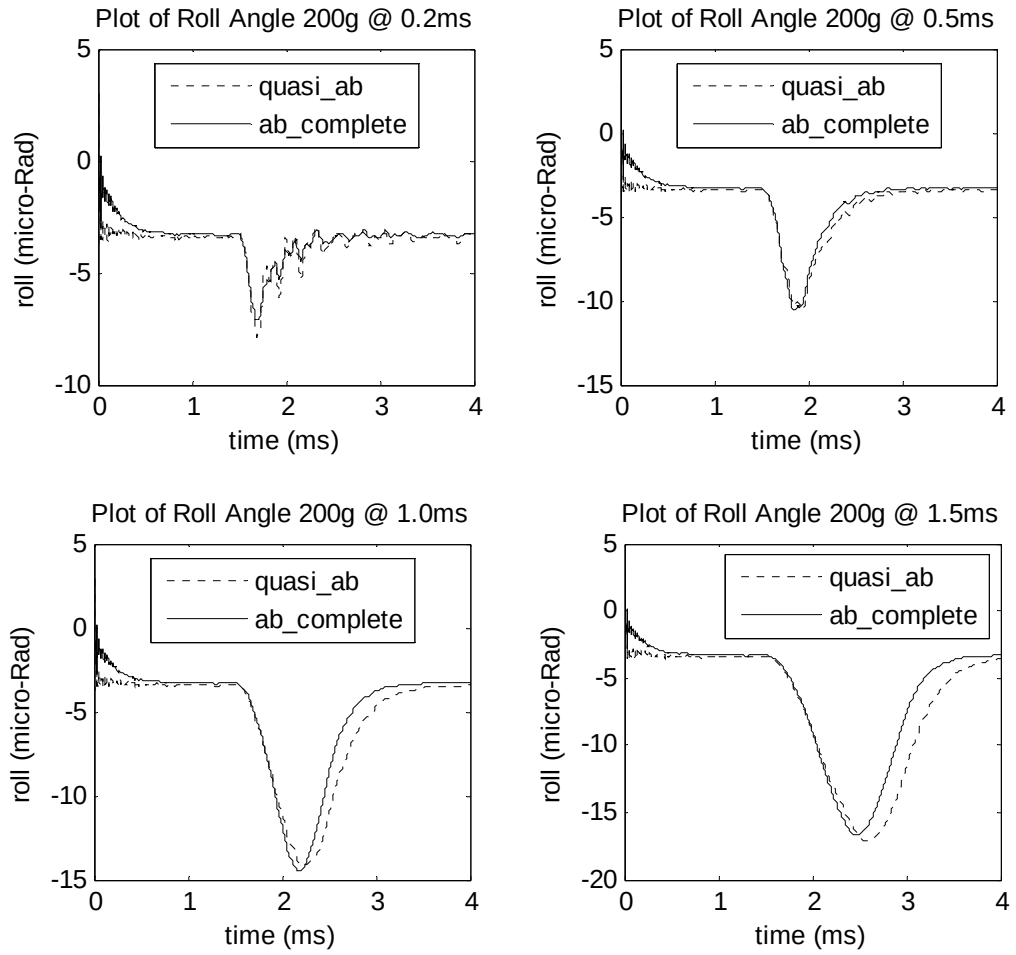

FIGURE 4.21 ROLL ANGLE COMPARISON @ DIFFERENT PULSE WIDTH

4.3.5 Advantages and Disadvantages of Modified Quasi-Static

The advantages of the modified quasi-static concept in air bearing shock simulation are: the air bearing response can be obtained very quickly and with reasonably good accuracy. The force and moments response are virtually the same with the full air bearing. This approach is more realistic than the linear spring model and can be used for HDD with any form factor. The drawback is that significant amount of time is needed to prepare the modified quasi-static air bearing model before it can be used in the shock simulation. However, the preparation steps only need to be done once for each type of slider.

4.4 *Chapter Summary*

The quasi-static concept of the air bearing for shock simulation has been introduced. It has been used to build a quasi-static air bearing model. The quasi-static model was then compared with the full finite volume model. The results show that the quasi-static notion alone is not accurate in representing the air bearing dynamics due to the significance damping contributed by the squeeze effect. An optimized damping was then added to the original quasi-static model and the modified model then shows relatively high accuracy especially in predicting the air bearing force and moment response. Overall summary of the work presented in this chapter is presented in the following flow diagram.

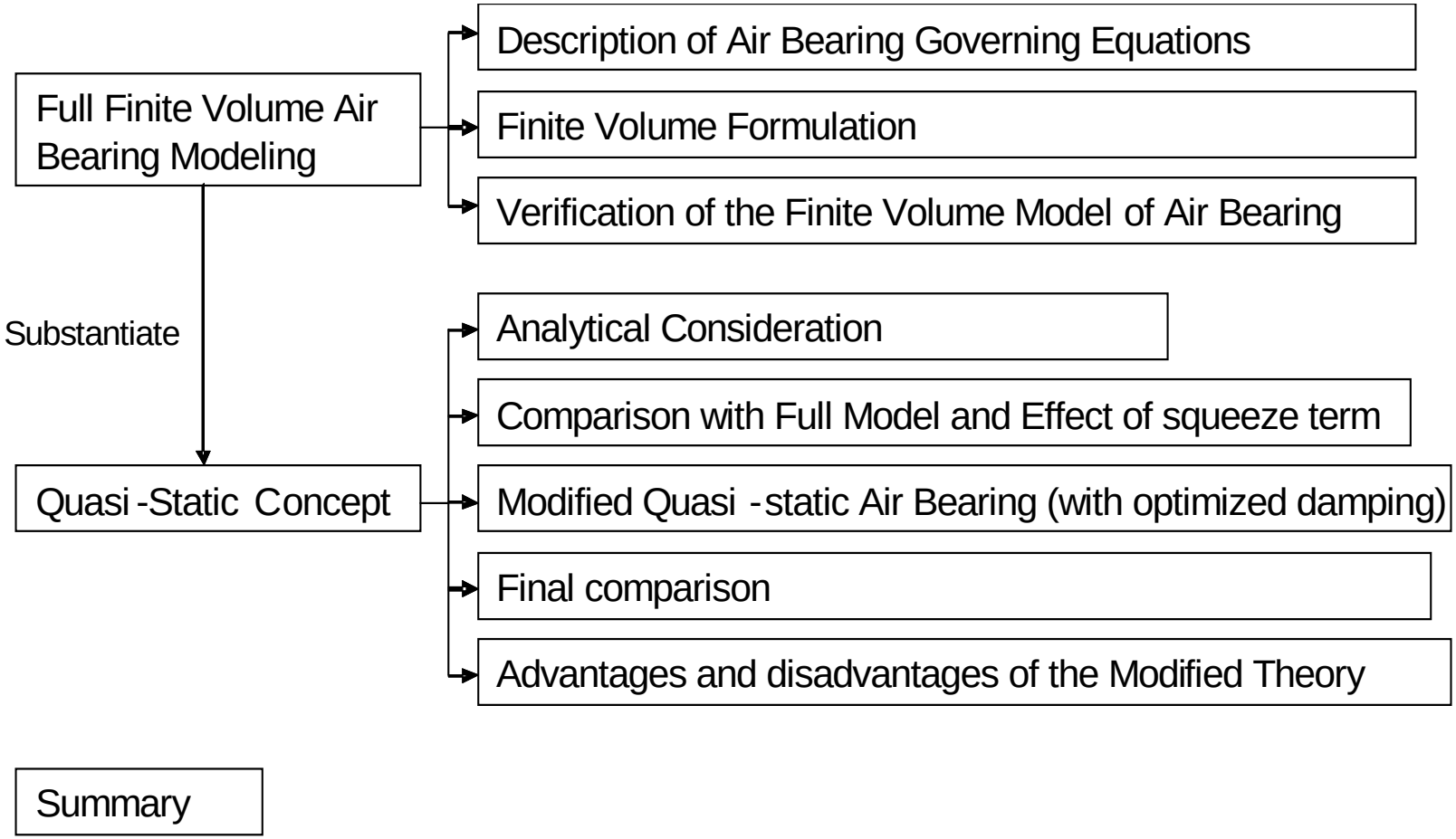

CHAPTER 5 FLUID AND STRUCTURAL COUPLING, VALIDATION, AND PARAMETRIC STUDIES

This chapter is divided into two main sections. In the first section two types of coupled models, which are formed from the combination of the HDD structural models and the air bearing models presented in previous two chapters, are described and validated. HDD design and simulation parameter studies follow in the last section.

5.1 *Coupled Models (Structural plus Air Bearing)*

The two coupled models are presented here. The first coupled model is the combination between the flexible multi body structural model and the full finite volume air bearing model. The second one is the state-space structural model combined with quasi-static air bearing model.

5.1.1 Flexible Multi Body & Full Air Bearing Coupled Model

This subsection is divided into three parts. In the first part the method for coupling the air bearing pressure into the flexible multi body structural model is described. Then, the shock simulation procedure is presented. Lastly, the validation of the coupled model is given.

5.1.1.1 Air Bearing Pressure Coupling Method

After the discrete air pressure and the intermolecular stress have been obtained at each time step by finite volume formulation of the air bearing, it is transformed into the point forces applied on the centers of the slider edges (Figure 5.1). The centers are labeled as LEC (leading edge center), TEC (trailing edge center), OEC (outer edge

center) and IEC (inner edge center). *OXYZ* is the general coordinate system of the HDD and *oxyz* is the slider coordinate system. The transformation of air bearing pressure into point forces is based on the almost-perfectly-rigid property of the slider (due to its small size and relatively high Young's modulus).

Since the slider coordinate system *oxyz* does not always coincide with the general coordinate system *OXYZ* of the HDD, the four point forces should be transformed into the general HDD coordinate in the multi body dynamics formulation.

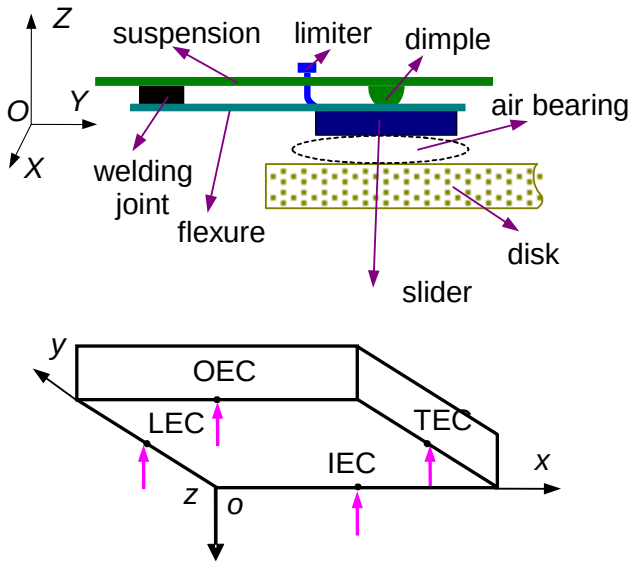

FIGURE 5.1 SKETCH OF AIR BEARING & STRUCTURES COMBINED

5.1.1.2 Shock Simulation Procedure

Considering that the air bearing has a higher stiffness compared to the structure, the numerical differentiation formula (ode15s as described in [168]) is used in the time-stepping. After the slider vibration has reached steady state, half-sinusoidal acceleration shock in the *Z*-direction is then applied to the two short edges of the base cover. If the shock duration is *T* and the shock amplitude is *A*, then the velocity *v* and displacement *s* of the base cover is given in (5.2) and (5.1), and their profiles (with *T*

= 0.5 ms an A = 1 G) are depicted in Figure 5.2.

$$\begin{cases} v = -\dfrac{AT}{\pi}(\cos\dfrac{\pi}{T}t - 1) & t \le T \\ v = \dfrac{2AT}{\pi} & t > T \end{cases} \tag{5.1}$$

$$\begin{cases} s = \dfrac{AT}{\pi}(t - \dfrac{T}{\pi}\sin\dfrac{\pi}{T}t) & t \le T \\ s = \dfrac{AT}{\pi}(2t - T) & t > T \end{cases} \tag{5.2}$$

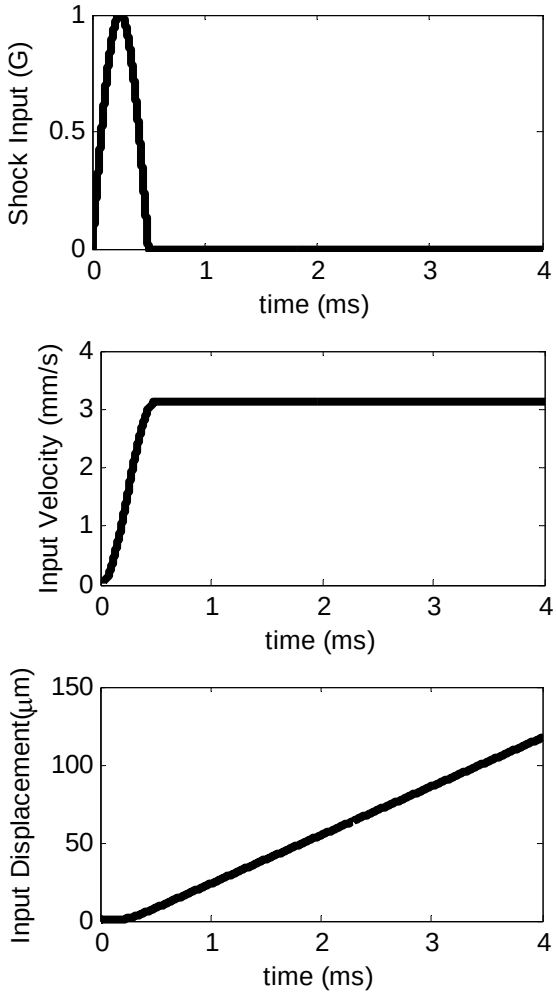

FIGURE 5.2 SHOCK (ACCELERATION, VELOCITY AND DISPLACEMENT)

5.1.1.3 Model Validation

The validation was done by comparing the shock tolerance predicted by the coupled model with the actual shock tolerance of the HDD. The highest half-sine shock amplitude that the HDD can withstand without disk damage is called shock tolerance. The damage is considered happen when the slider touches disk surface.

According to its manufacturer specification, the shock tolerance of the one-inch HDD that have been modeled here is 200 G @ 1ms. In fact, its actual tolerance is about one-third higher than the specification given to the consumer (which is ~ 267 G) [33].

The simulation result predicts the shock tolerance to be 223 G, which is quite closed to the actual shock tolerance. The difference in the prediction may be caused by the difference between the base model used and the real base; the real base has printed circuit board and electronic controller unit embedded in it, making it stiffer.

The first coupled model has been described and validated in the above section. The second coupled model (the combination of the state-space structural model & quasi-static air bearing model) are presented next.

5.1.2 State Space Structural & Quasi-Static Air Bearing Model

This subsection is divided into three parts. In the first part, the method for coupling the quasi-static air bearing force and moments into the state-space structural model is described. Then, the shock simulation procedure is presented. In the third part, the global validation of the coupled model is given together with its comparison with two other existing coupled models.

5.1.2.1 Quasi-Static Air Bearing Coupling Method

A coupling method, to enable the state-space structural model and the quasi-static air

bearing model to communicate with each other, is formulated as follows. The state-space equations take forces as inputs and give displacements as output, while the quasi-static air bearing model takes fly height, pitch, and roll as inputs and gives the loads (N_L, P_M, and R_M) as outputs. To couple them together in the shock simulation, the structural displacements are converted to the fly height, pitch, and roll, whereas the force and moment loads are transformed to point forces (as in Figure 5.3). The conversion from the structural displacements to the fly height, pitch, and roll is relatively easy. To transform the N_L, P_M, and R_M to the point forces, the conversion formula (5.3) is used. The formula is valid because the slider is almost perfectly rigid.

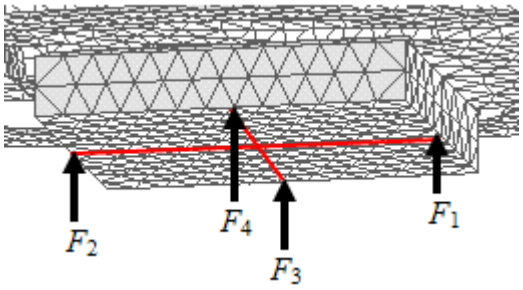

FIGURE 5.3 POSITION OF THE POINT FORCES ON THE SLIDER

$$\begin{aligned} F_1 &= N_L / 2 + P_M /(L\cos\alpha) \\ F_2 &= N_L / 2 - P_M /(L\cos\alpha) \\ F_3 &= R_M /(W\cos\beta) \\ F_4 &= -F_3 \end{aligned} \tag{5.3}$$

F_1, F_2, F_3, and F_4 are the point forces acting on the slider as depicted in Figure 5.3; F_1 and F_2 act at the trailing edge center and the leading edge center respectively, while F_3 and F_4 act on the mid point of the inner edge and the outer edge of the slider respectively. L and W are slider length and width. α and β are pitch and roll angles, respectively. Equal and opposite forces are also applied to the four points on the disk directly under the four points on the slider.

The advantage of this coupling method and the method presented in section 5.1.1.1 is that no structural modification is required on the slider model (unlike in coupling method used in [59]).

5.1.2.2 Shock Simulation Procedure

Several time-stepping methods had been tried for its efficiency & stability. It was found that for Ode45 solver (Dormand-Prince) with variable time-step and error tolerance of 10^{-7} (absolute) and 10^{-4} (relative) is also quite time-efficient and stable in advancing the simulation time this coupled model.

The time needed for 6-ms shock simulation in MATLAB® SIMULINK environment is less than 25 minutes using a computer with an Intel® dual-core T2300 processor. In this coupled model, the shock excitation is applied at the HAA and disk pivots.

5.1.2.3 Validation and Comparison with Other Models

To validate the method, experimentally measured shock tolerance of the 1" HDD that have been modeled was compared with simulation results. The comparison studies with other available methods were also conducted.

Experiment Results

The actual shock is measured by drop test. First, the HDD base was *fully* clamped to the fixture on the drop table (the base vibration can be neglected). A drop table was used to produce 0.5 ms half-sine shock pulse to the HDD. The shock amplitudes, measured by an accelerometer placed on the HDD motor hub, were increased with 50 G increments (100 G, 150 G, 200 G …). After each test, the slider head was programmed to scan the disk for hard errors. It was observed that the disk damages

mostly happen at 300 G shock amplitude.

Simulation Results

The shock input to the model is increased at 10 G interval. At 310 G level, the leading edge of the slider starts to touch the disk. Hence, at 310 G the disk may be damaged. The predicted shock tolerance (310 G) is quite close with the actual tolerance (300 G). The air bearing response at 310 G, 0.5 ms shock pulse is shown in Figure 5.4.

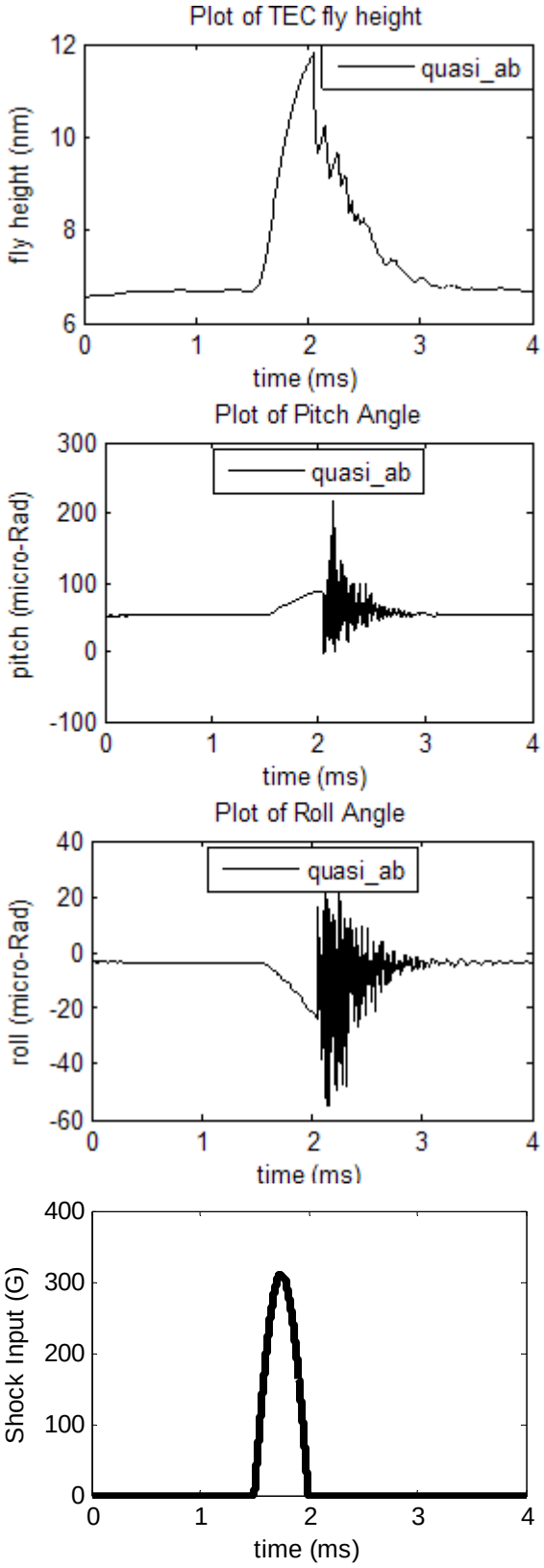

FIGURE 5.4 SLIDER RESPONSE AT 310 G, 0.5 MS HALF-SINE SHOCK

Comparison Studies with Other Methods

The computation time and accuracy of the proposed method are compared with

1. Full finite element method using LS-DYNA as its dynamics solver
2. CML HDD Dynamics Events Simulator [58, 59, 106]

Only the following components are modeled in these studies:

1. A head-actuator assembly (as in Figure 3.26)
2. A disk (ρ = 2553 kg.m^{-3}, E = 83.5 GPa, thickness = 0.381 mm, ID = 7.01 mm, OD = 27.4 mm)
3. Air bearing (described in Figure 4.5)

The disk is not spinning. The boundary conditions of the disks and the head actuator assembly are shown in Figure 5.5.

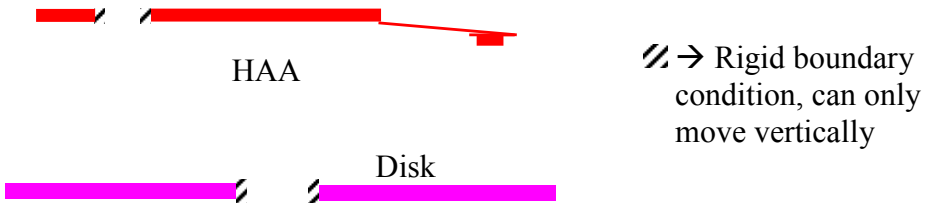

FIGURE 5.5 BOUNDARY CONDITIONS OF DISK AND HAA

In the HDD model for comparison (refer to Figure 5.6) the disk is connected to the air bearing model. The air bearing model is then connected to the slider in the HAA. Next, a half sine shock pulse with magnitude 200 G and pulse width 0.5 ms are applied at both the disk and the HAA (indicated by blue arrows in Figure 5.6).

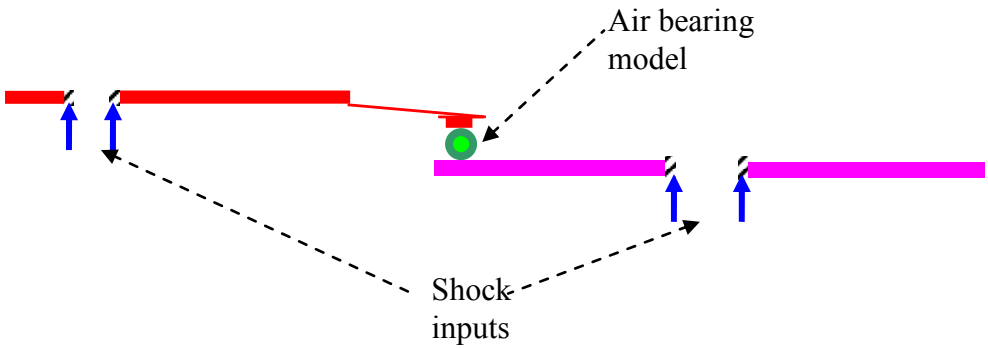

FIGURE 5.6 HDD MODEL FOR METHOD COMPARISON

The studies were carried out using a computer with Intel ® Xeon ™ CPU 2.20 GHz, 512 MB of RAM. The three models were run one at a time to predict 6 ms time history of HDD shock response. Full CPU utilization for each method was observed. The shock input started at simulation time = 3ms. Summary of the results is shown in Table 5.1.

In Table 5.1, the CML shock tolerance of 300G is based on the contact force exceeding 10g, whereas the author's shock tolerance of 310G is based on the slider touching the disk. The justification for this comparison is that both definitions supposedly mean the same thing, which is the slider-disk contact. The rule of predicting shock tolerance based on 'contact force exceeding 10g' comes from the CML programmer himself. This 10g force is used to increase the correlation between the CML results and the experimental results. For the author, the slider-disk contact simply means: the slider touches the disk (the minimum spacing between the slider and the disk surface is zero) and that is what the author used in predicting the shock tolerance.

TABLE 5.1 COMPARISON RESULTS BETWEEN THE PROPOSED METHOD AND TWO EXISTING METHODS

Task	Computation Time		
	Full Finite Element Model with LS-DYNA solver	CML's HDD Dynamics Event Simulator	State Space Structural model with Quasi-static air bearing model
Air bearing modeling	Using linear springs; the stiffness was obtained from air bearing steady state analysis (~ 1 minute). To be done only once.	The air bearing finite volume model has been set; can directly proceed to the next task.	Using lookup tables to represent air bearing; time needed to create the tables and to optimize the damping was ~14 hours. To be done only once.
Structural model preprocessing	Not required	Substructuring the finite element model to 250 dof and obtaining mass and stiffness matrices (~12 minutes)	Modal analysis to extract 250 modes (~6 minutes)
Shock simulation run	Time step: decided by LS-DYNA program Total dof : ~20,000 Time for 6 ms run: ~6 hours	Time step: 10^{-7} s Air bearing mesh: 161 x 161 Normalized residual for Reynolds equations: 10^{-7} Time for 6 ms run: ~7.5 hours	Time step: variable (ode45) 10^{-6} to 10^{-11} s Error tolerance: 10^{-3} (relative), 10^{-7} (absolute) Time for 6 ms run: ~ 1.25 hours
Total time (3 factors structural DOE – 8 runs)	~ 48 hours	~62 hours	~ 24 hours **(Fastest time)**
Accuracy	The linear springs are very stiff. Even at 800 G the slider hardly moved	Predicted shock tolerance is 300 G (based on contact force > 10 gram force after head lift event)	Predicted shock tolerance is 310 G (based on slider touching the disk)

5.1.3 Comparison between Two Coupled Models

The state-space/quasi-static model (SS/QS) and the multi-body/finite-volume model (FMBD/FVM) are compared using the same setup as in section 5.1.2.3. First, the comparison of the initial transient response (before shock) is shown in Figure 5.7. Then, the shock responses of the two models are compared in the Figure 5.8.

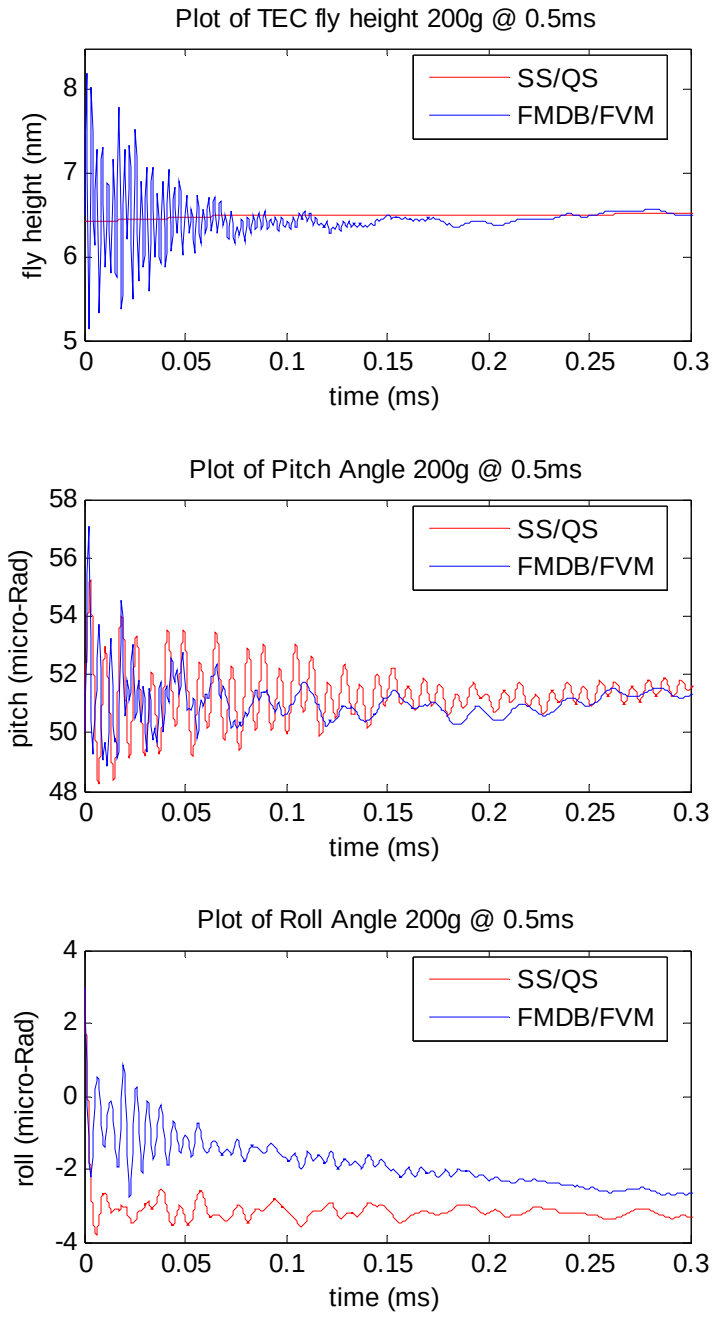

FIGURE 5.7 DIRECT COMPARISON OF RESPONSE HISTORY (INITIAL RESPONSE)

Overall the early responses are different because in the FMDB/FVM the initial air bearing pressure starts from uniform value (ambient pressure), while in SS/QS the air bearing pressure starts directly from the static-equilibrium value.

In addition, the flying height in SS/QS achieves the equilibrium much faster than in the FMDB/FVM. This is due to the addition of high damping between the TEC and the disk in the QS model (refer to section 4.3.3). For the roll and pitch motion both models reach equilibrium almost at the same time. Nevertheless, after ~0.3 ms both models converge to relatively same value.

Next, the shock responses of the two models are shown below. Both models show relatively good resemblance; the maximum flying height error is ~ 1 nm and the pitch difference is less than 10 μrad. The roll response are almost the same (error is less than 1 μrad).

In summary, the differences of the two coupled models are caused mainly by the air bearing models. The structural models practically give the same outputs because only the linear shock input is considered.

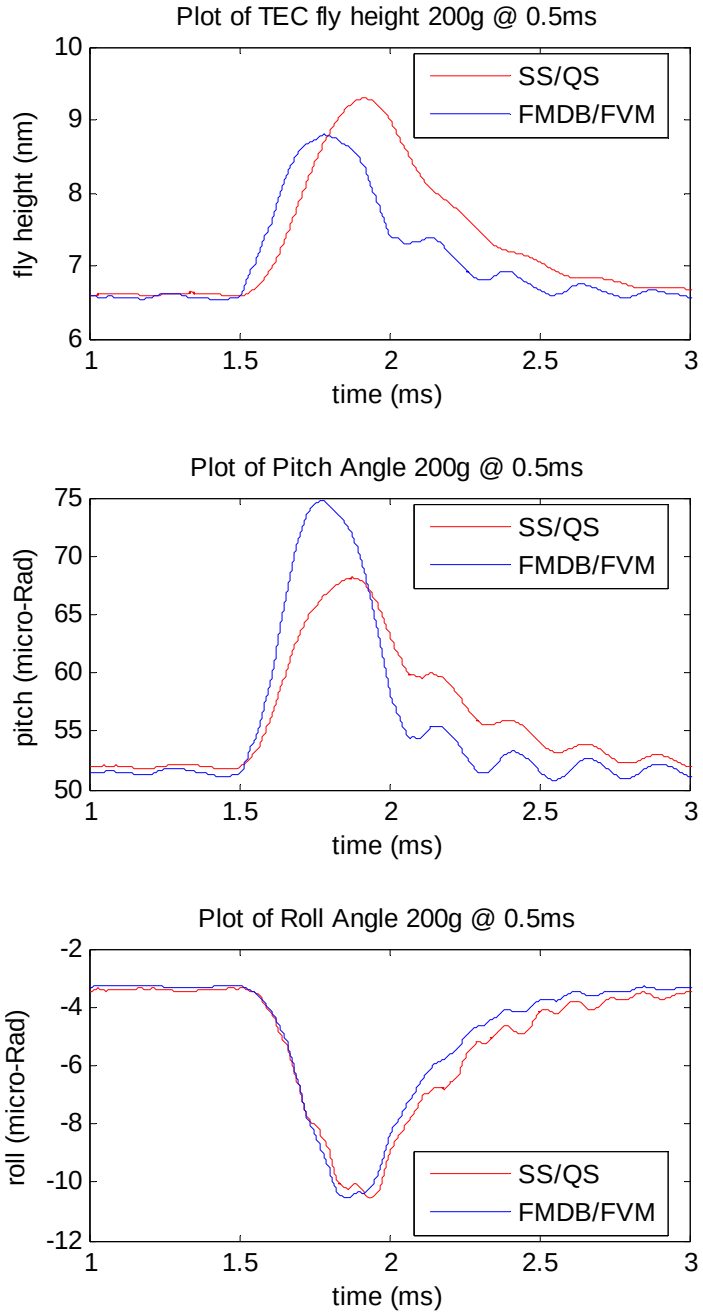

FIGURE 5.8 DIRECT COMPARISON OF RESPONSE HISTORY (SHOCK RESPONSE)

5.1.4 Summary of Two Coupled Models

The second coupled model (the combination of the state-space structural model & quasi-static air bearing model) is particularly efficient for studying HAA/disk design parameters such as thickness and shape of the arm/suspension; once the quasi-static air bearing model has been created, it can be used over and over again in the

structural studies. But, when the design parametric studies involve the changes in the air bearing parameter (such as slider profile or disk velocity), the quasi-static model needs to be updated to cater for every change; this process will take relatively long time. Hence, for the parametric studies involving air bearing parameters, the first coupled model developed shown in section 5.1.1 is more appropriate.

The descriptions of the two coupled models together with their validation and the comparison with two other models have been given in the above section. In the next section, various parametric studies on HDD design and shock simulation are shown.

5.2 *Design and Simulation Parameter Studies*

The HDD design parametric studies comprise the investigation of the effect of the dimple/flexure contact stiffness and the flexibility of the bases on the shock tolerance. In addition, the effect of considering the intermolecular force and the ever-changing air bearing location in the HDD shock simulation are presented.

5.2.1 Study and Optimization of Dimple/Flexure Contact Stiffness

In this study, the shock pulse-width is fixed at 0.5 ms, while the contact stiffness coefficient between the dimple and the flexure (Figure 5.9) k_c is set as controlled variable. The base is considered rigid for simplification. The base here refers to the base-plate. Since the base is considered rigid, the shock pulse experienced by the base will be transmitted to the disk and HAA without any changes. This means that the shock pulse can be directly applied to the disk and the HAA. The shock pulse starts after 0.5 ms simulation time. This is to allow the air bearing to reach the steady state condition.

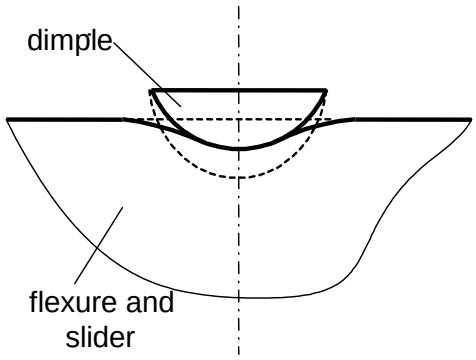

FIGURE 5.9 CONTACT BETWEEN DIMPLE AND FLEXURE

Figure 5.10 shows the slider flying attitude, air bearing force and dimple spacing response to 500 G shock when the contact stiffness coefficient k_c is 10^6 N/m. TEC is trailing edge center of the slider as depicted in Figure 5.1.

Figure 5.10d shows the displacement of the TEC on the slider and its projection on the disk, with respect to HDD shaft. In Figure 5.10d, it appears that after the shock begins both the slider and the disk start to lift up. After this, from Figure 5.10f it can be seen that the dimple and the flexure separate and subsequently get in contact again. The flying height are in nm scale as depicted in Figure 5.10a. Hence, the two curves in Figure 5.10d are relatively very close.

Figure 5.10f shows the dimple-slider spacing response (the relative distance between the dimple and the flexure/slider). It is possible for the suspension (the dimple) to move at relatively higher distance than the slider (the TEC) movement. As the results, in Figure 5.10f it can be seen that the dimple is being separated from the slider at a distance of 250μm max, while the TEC only moves 30μm max with respect to HDD shaft (in Figure 5.10d).

The separation and contact between the dimple and the flexure happen repeatedly. As the dimple hits the slider (when the dimple spacing is below zero in Figure 5.10f),

the contact force is produced between the dimple and the slider. The air bearing reacts with this contact force, generating the air bearing force response as shown in Figure 5.10e.

When the dimple hits the flexure, there is a sudden change of the flying height, pitch angle and roll angle. However, in this case (k_c=10^6 N/m) the sudden change does not lead to the slider touching the disk (the minimum clearance in Figure 5.10a is more than zero).

Figure 5.11 shows the slider flying attitude, air bearing force and dimple spacing response to the same shock (500 G) when the contact stiffness coefficient k_c is increased to 10^7 N/m. It appears that now the slider touches the disk (Figure 5.11a). The sudden change of the flying attitude is big enough, leading to the impact between the slider and disk. If the shock amplitude is less than 450 G, the impact will not happen.

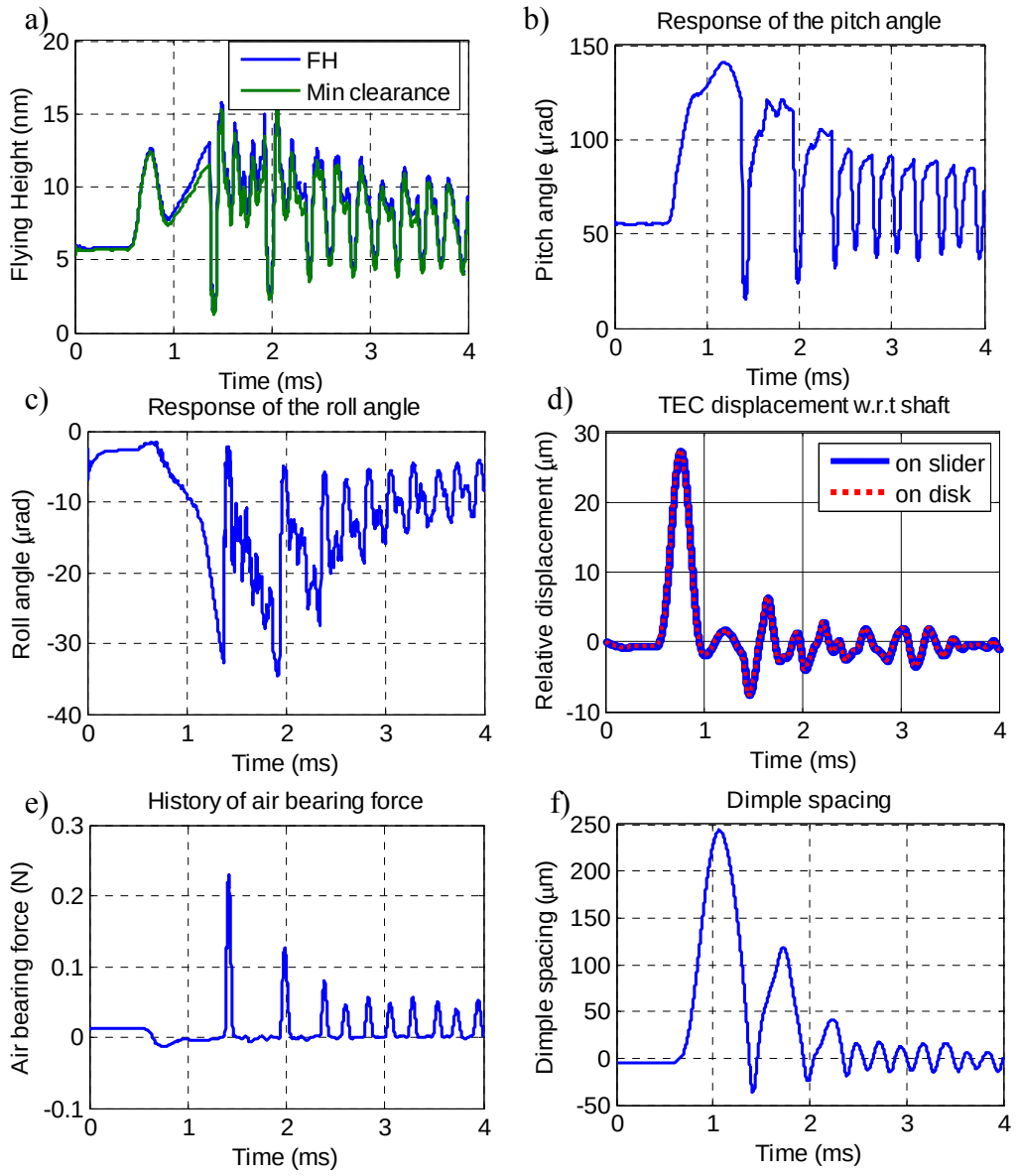

FIGURE 5.10 SLIDER, AIR BEARING, AND DIMPLE SPACING @ 500 G WITH $k_c = 10^6$ N/M

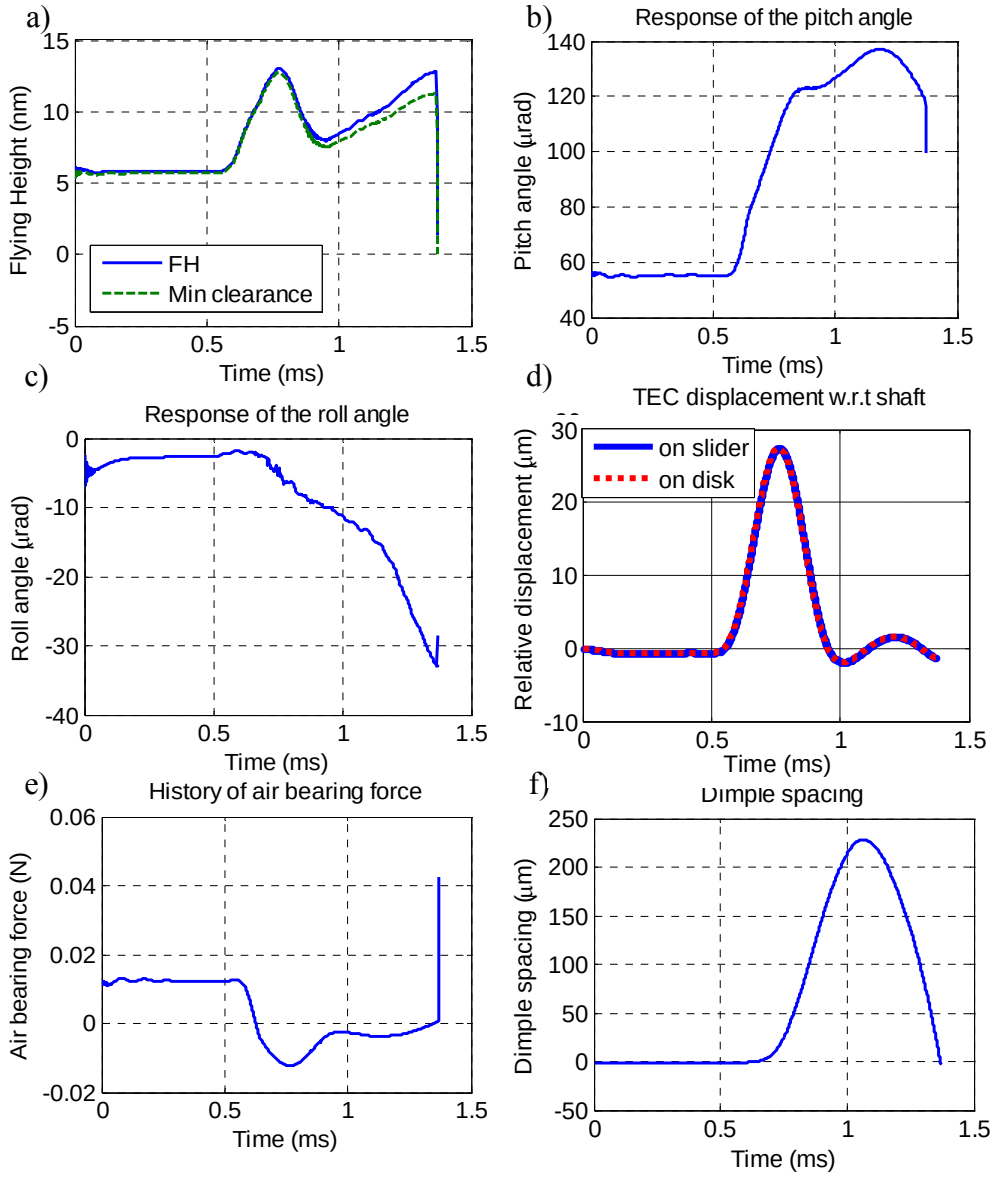

FIGURE 5.11 SLIDER, AIR BEARING FORCE, AND DIMPLE SPACING @ 500 G AND $k_c = 10^7$ N/M

Figure 5.12 shows the flying height responses when the contact stiffness coefficient k_c is further increased to 10^8 N/m and the shock amplitudes are 250 G and 280 G respectively; the dimple spacing response is shown in Figure 5.13. It is observed that severe vibration happens after the dimple contacts the flexure. This is due to repeated contacts between the dimple and the flexure. However, at 250 G this vibration does not lead to the slider/disk impact. By increasing the contact stiffness coefficient k_c to

10^9 N/m, at shock amplitude 250 G, the impact between the slider and the disk happens.

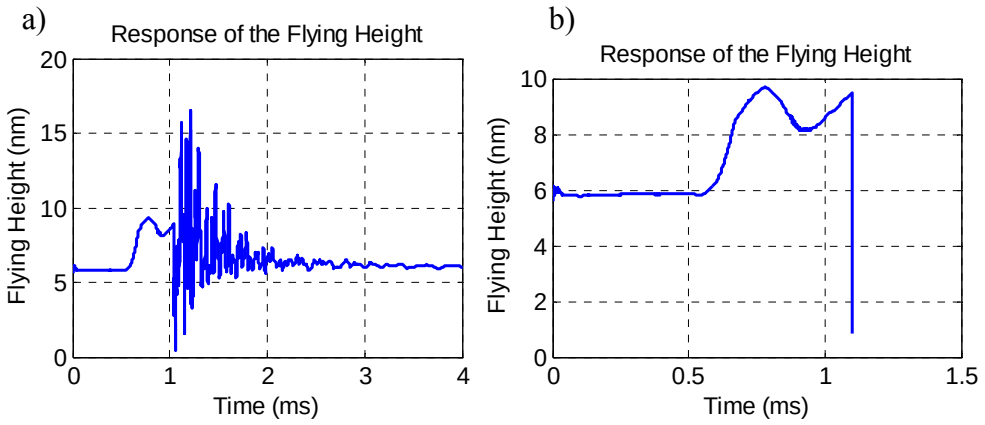

FIGURE 5.12 FLYING HEIGHT FOR SHOCK WITH AMPLITUDE A) 250 G B) 280 G, $k_c = 10^8$ N/M

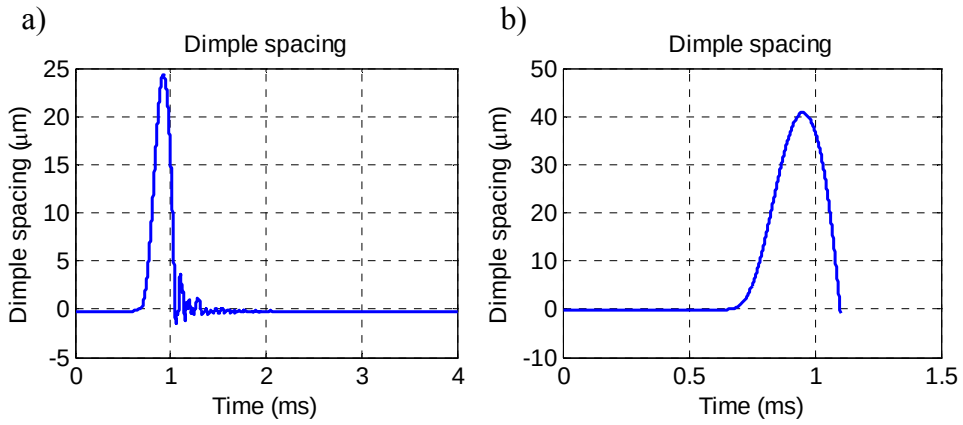

FIGURE 5.13 DIMPLE SPACING FOR SHOCK WITH AMPLITUDE A) 250 G AND B) 280 G, $k_c = 10^8$ N/M

The trend of the HDD shock performance with regards to the changes in the contact stiffness coefficient k_c is given in Figure 5.14. It shows that for stiffer dimple-flexure contact stiffness, smaller shock magnitudes will cause slider-disk contacts. Referring to contact dynamics equation, the contact stiffness can be lowered by reducing the Young's modulus (E) of contacting materials. This suggests that softer material can be used at the dimple/flexure contact region to increase the HDD shock tolerance.

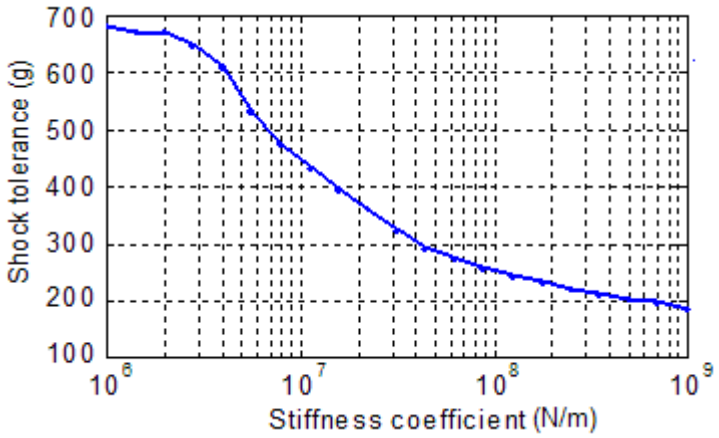

FIGURE 5.14 SHOCK TOLERANCE VS. VARIATION OF CONTACT STIFFNESS COEFFICIENT

Figure 5.15 shows the shock response of the pitch angle of a normal suspension and a suspension with softer dimple/flexure (its contact stiffness is reduced by 99%). By reducing the dimple-flexure contact stiffness, the pitch angle modulation due to shock is also decreased. As a result, the tendency of the slider edge to hit the disk will be less and the shock resistance will increase. The simulation predicted that reducing the original contact stiffness in the HDD that has been modeled by 99% increases its shock tolerance by 80 G.

Additional observation in Figure 5.14 shows that the rate of increase in the HDD shock tolerance is rising when the stiffness coefficient is logarithmically reduced from 10^9 N/m to 4×10^6 N/m. Continuing the reduction shows less increase in the shock performance. A flat slope is indeed detected in the trend curve (around 2×10^6 N/m). But, the shock tolerance still show some increment if the contact stiffness is furthermore decreased. The probable conclusion is that the optimum value for the contact stiffness (in the context of attaining highest shock tolerance) is the lowest feasible value. In reality this value is limited by other factors such as manufacturing cost and availability of material/technology.

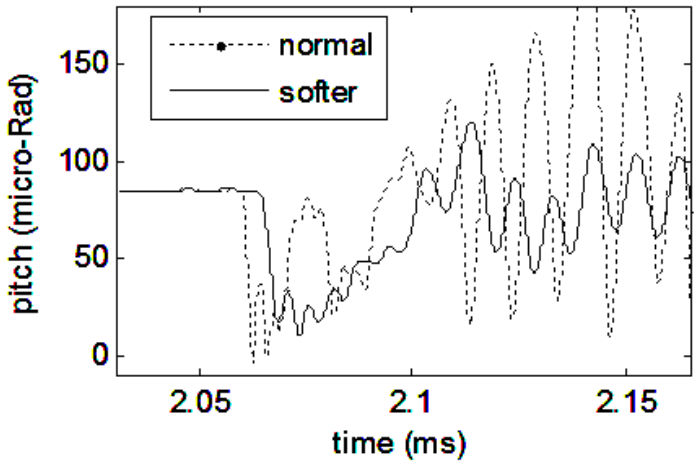

FIGURE 5.15 EFFECT OF DIMPLE-FLEXURE CONTACT STIFFNESS (THE SHOCK STARTS AT 1.5 ms)

5.2.2 Study on the Effect of the Flexibility of the Base Plate

Using flexible multi-body dynamics formulation developed in Chapter 3, the base plate is included in the HDD modeling. The shock simulation is then conducted. The response of first five modes of the original base at 250 G, 1 ms shock is shown in Figure 5.16. It can be seen that the first two modes are relatively more dominant than the other modes. These two modes are shown in Figure 5.17.

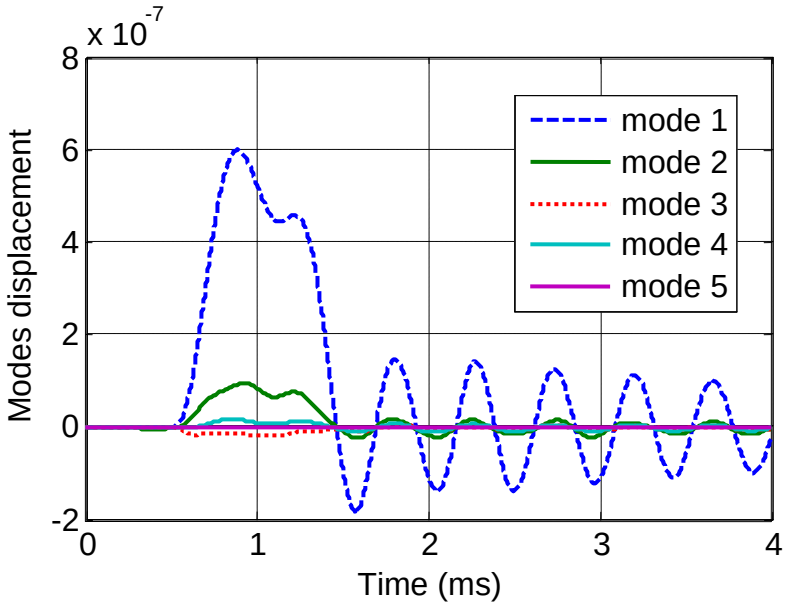

FIGURE 5.16 MODE COORDINATES OF THE BASE DUE TO 250 G SHOCK AT 1 MS

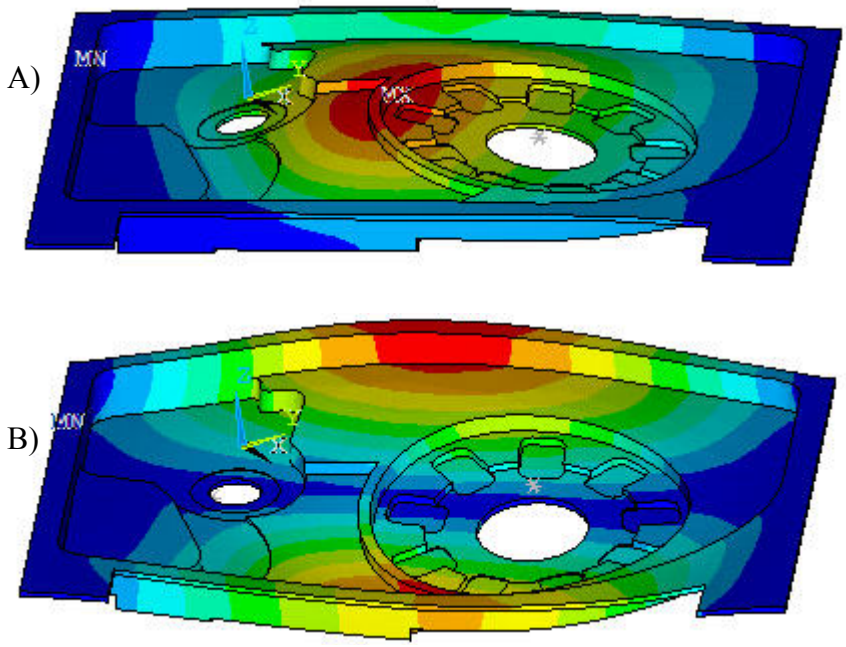

FIGURE 5.17 DOMINANT MODE SHAPES OF THE BASE A) FIRST MODE, B) SECOND MODE

The shock tolerance for different base stiffness and different shock duration is given in Figure 5.18. The base stiffness is varied by modifying its natural frequencies; e.g. '4x stiffer' means that its natural frequencies are increased two times.

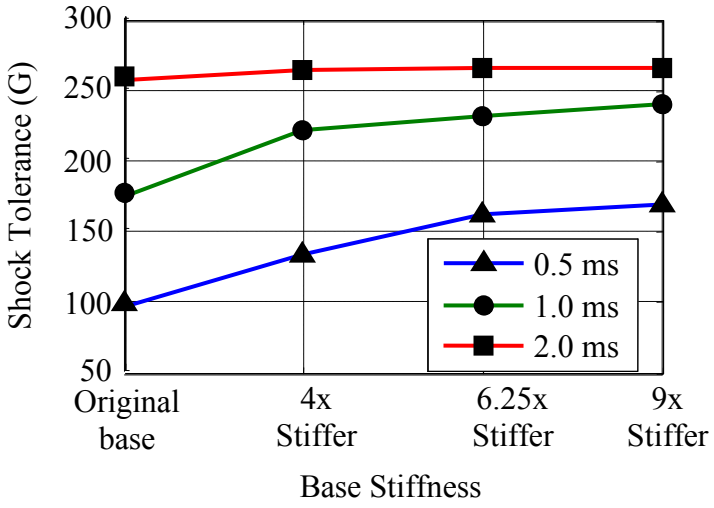

FIGURE 5.18 BASE STIFFNESS EFFECT FOR SHOCKS WITH DIFFERENT DURATION TIME

It can be seen that generally with the increase in the base stiffness, the shock tolerance increases. This is because as the base is getting stiffer, its elastic deformation is

getting less. Less deformation means that the configuration of the HDD components that adhere to the base is also more stable.

Furthermore, the effect of the base stiffness is found to be greater when the shock pulse-width is shorter. This is because the shock with shorter pulse width has significant frequency range that is-closer-to or includes-more-of the base natural frequencies. In our case, the base fundamental natural frequency is ~ 3 kHz. The shock with 0.5 ms pulse width has significant frequency content up to 2 kHz, which is closer to base natural frequency than the shock with 1 ms pulse width. As the results, the 0.5 ms pulse width will have greater effect on the base deformation.

5.2.3 Effect of the Intermolecular Force between the Slider and the Disk

Figure 5.19 depicts flying height response to a shock with amplitude 250 G and 1 ms pulse-width applied on the HDD base. It can be seen that the flying height is smaller when the intermolecular force (IMF) is considered; when the flying height is smaller, the effect of IMF is greater. This is because at lower flying height (before contact happens), the attractive force is bigger.

Overall, for the HDD that we modeled, the effects of intermolecular force are negligible (only ~ 4% at 4 nm flying height). However, for flying height below 4 nm the effect will be higher than 4 % and the intermolecular effect may then be considered.

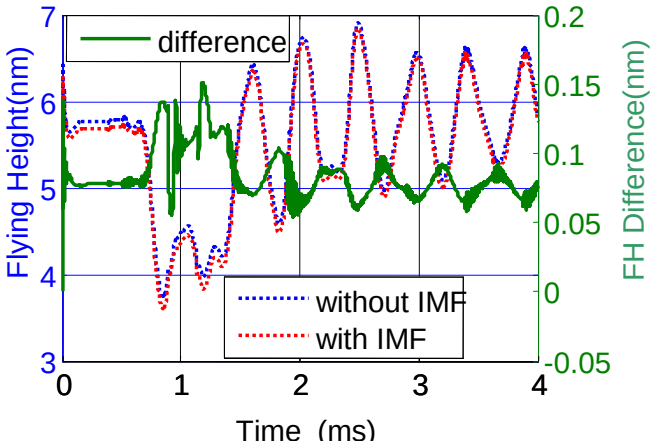

FIGURE 5.19 RESPONSE OF FLYING HEIGHT FOR 250 G, 1MS SHOCK

5.2.4 Effect of Updating the Air Bearing Location at Every Time Step

When the disk rotates, the location of the air bearing (with respect to the disk local coordinates) is moving. Using the second coupled model presented in this chapter, the effect of this location changes can be studied. It appears that the effect on the fly height response is relatively small. Figure 5.20 shows the small difference in phase and magnitude of the fly height shock response between the model that update the air bearing location and the model that does not update it. Overall, the effect of disk spin is negligible.

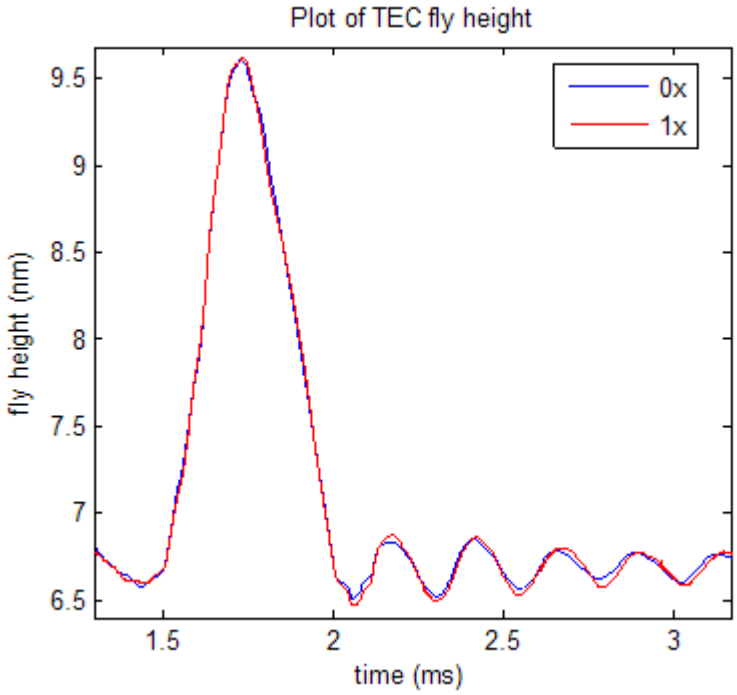

FIGURE 5.20 THE FLY HEIGHT SHOCK RESPONSE (0X → NOT SPINNING, 1X → DISK SPINS)

The summary of design and simulation parametric studies is:

1. Lower dimple/flexure contact stiffness and stiffer base increase the HDD operational shock tolerance significantly.

2. The effect of the intermolecular force on the slider flying height is more than 4% when the clearance is less than 4 nm – at least for the case considered.

3. Updating the air bearing location that moves due to the rotation of the disk does not affect the shock simulation results.

5.3 *Chapter Summary*

The overall summary is given in the following flow diagrams.

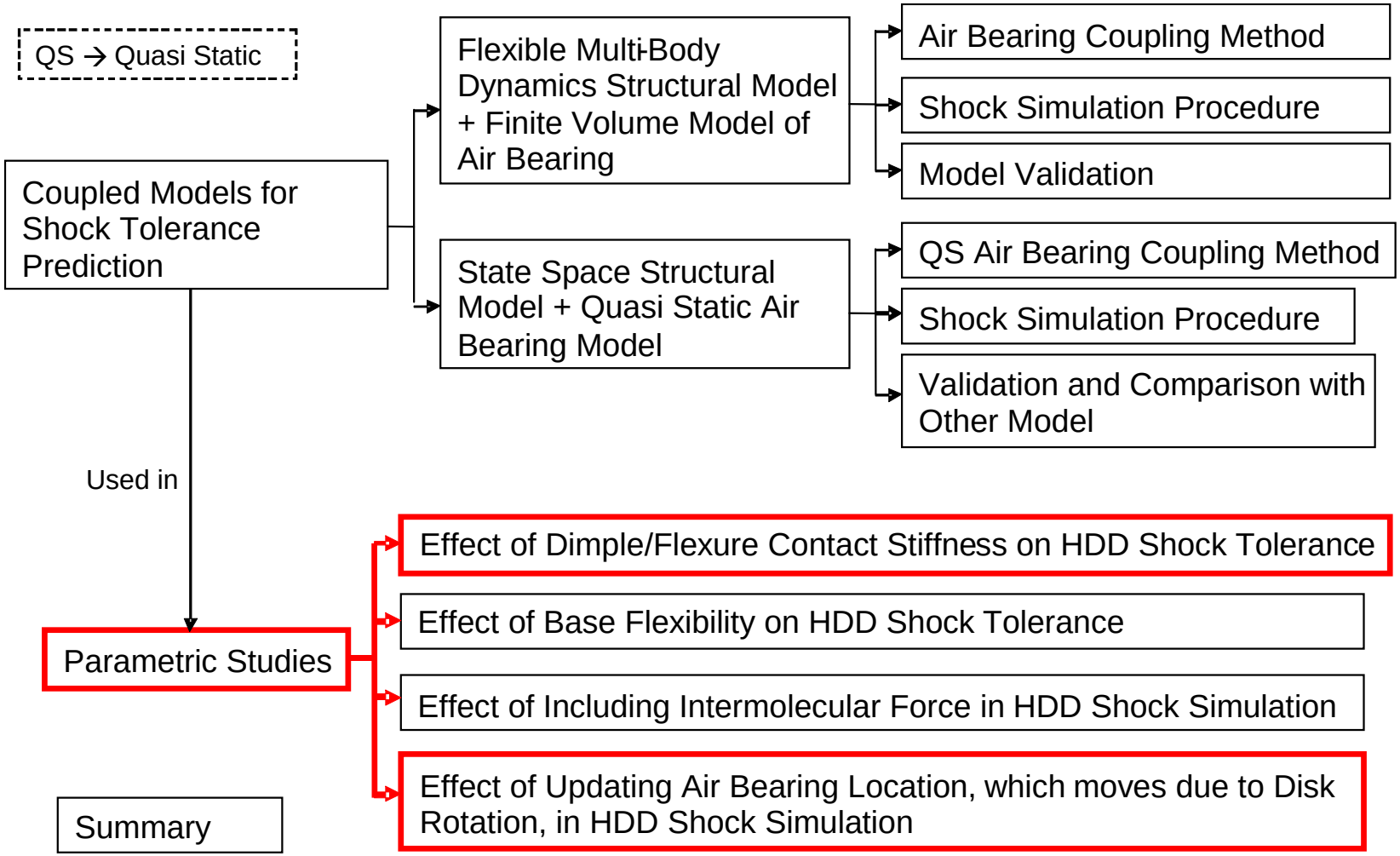

CHAPTER 6 DESIGN AND ANALYSIS OF SHOCK AND RANDOM VIBRATION ISOLATION OF OPERATING HDD

In the previous three chapters, the theoretical models have been developed and used for hard disk drives (HDD) design studies. The results from the studies can be used to increase the mechanical robustness of the HDD internal system (making it more shock/vibration resistant). However, having a strong interior is not enough since the severe shock/vibration excitation comes from the external environment (from outside the HDD). An effective external vibration isolation system is important for the HDD. Hence, this chapter describes how to design, simulate, test and evaluate the external vibration isolation systems for operating HDD subjected to severe shock and random vibrations based on military specifications MIL-STD-810E.

First, the shock and vibration profiles that might be experienced by HDD are described according to Military Standard (MIL-STD) 810E. Next, the authors propose vibration testing and evaluation criteria that can be used to examine the effectiveness of the shock and vibration isolation. Design concepts specially tailored to HDD vibration isolation systems are subsequently proposed in the subsequent section. After that, two case studies are presented to test and augment the concepts.

6.1 *Shock and Random Vibration Profile*

The U.S. Department of Defense has provided a series of guidelines for reliability and environmental testing under MIL STD 810E [169]. Some of the tests given by the standard are vibration, water resistance, humidity, and temperature tests.

The random vibration test in MIL STD 810E is commonly used among mobile electronics manufacturers for ruggedisation testing. The vibration data in the standard is derived based on the interaction of vehicle structures with road and surface discontinuities. Due to the randomness and irregularity of data collected, the data is best simulated by superimposing narrowband random vibration over a broadband random base. Hence, the vibration data consists of random-on-random vibration data in 3 primary axes. Each axis has six phases which correspond to different speed of vehicle during military mission. Figure 6.1 shows a general power spectral density (PSD) profile described by the standard. The standard will be used to investigate the performance of externally isolated HDD. According to the standard, the HDD have to be able to run smoothly under the excitation of each random-on-random vibration profile.

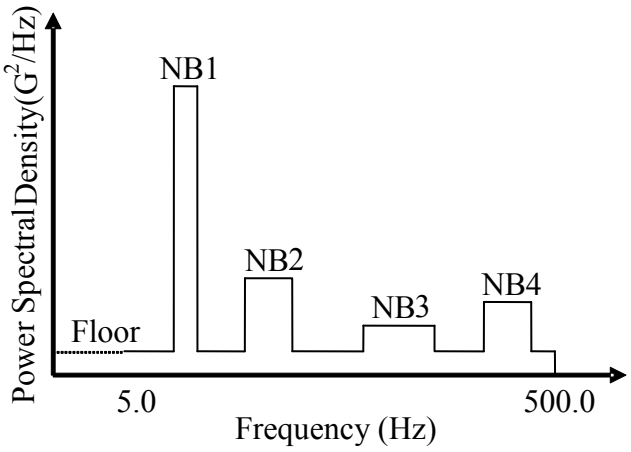

FIGURE 6.1 GENERAL POWER SPECTRAL DENSITY OF RANDOM-ON-RANDOM VIBRATION

The HDD also have to pass the shock tolerance requirements. The purpose of the shock tests is to ensure that the HDD can withstand the relatively infrequent, non repetitive shocks or transient vibration encountered in handling, transportation, and service environments. As described in the MIL STD 810E, the shock tests are intended to assess equipment assemblies which in this case are the HDD together with the shock and

vibration isolator systems, in their functional or operating modes. The applicable shock profiles for functional test are given in Table 6.1.

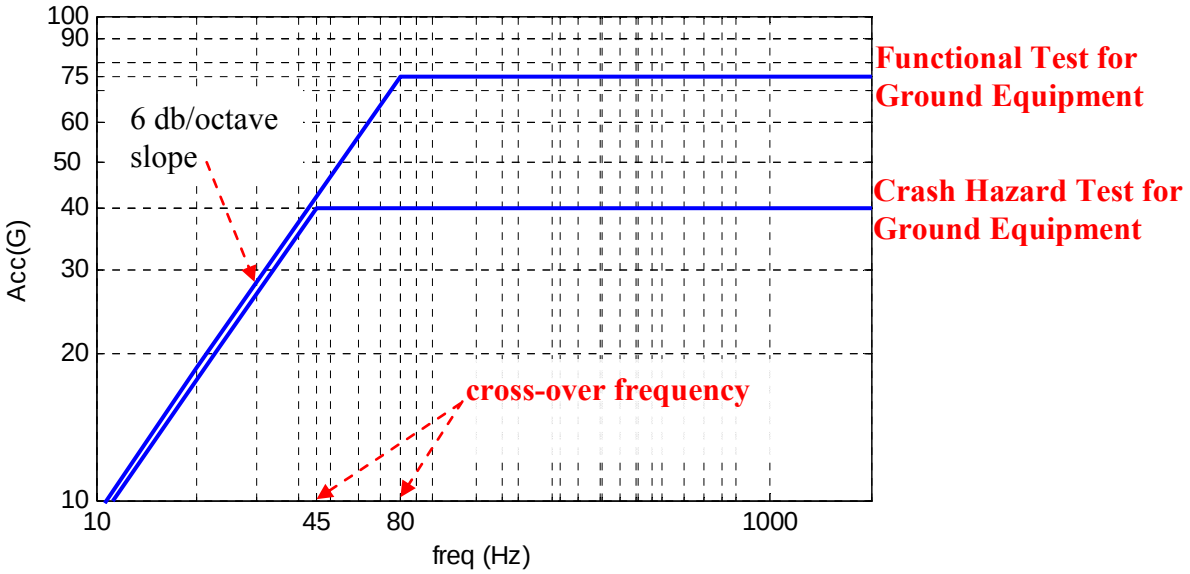

FIGURE 6.2 SHOCK RESPONSE SPECTRUM PROFILE FOR SHOCK TEST

TABLE 6.1 SHOCK PROFILE FOR SHOCK TEST

Test procedure	Half sine peak acceleration	Pulse Width	Cross over frequency
Functional Test For Ground Equipment	40 G (1 G = 9.81 m/s^2)	6-9 ms	45 Hz
Crash Hazard Test For Ground Equipment	75 G	3.5-5 ms	80 Hz

6.2 *Vibration Testing and Evaluation Criteria*

For testing the HDD, random-on-random vibration signals as specified by the power spectral density profiles of MIL STD 810E are generated by a vibration controller (VR8500). The controller then excites a large electrodynamics shaker system to physically produce the random vibration. Figure 6.1 shows a typical experimental setup for random vibration. For shock testing, a programmable shock table and dual-mass shock amplifier (Figure 6.4) is used to produce required shock magnitude and pulse width.

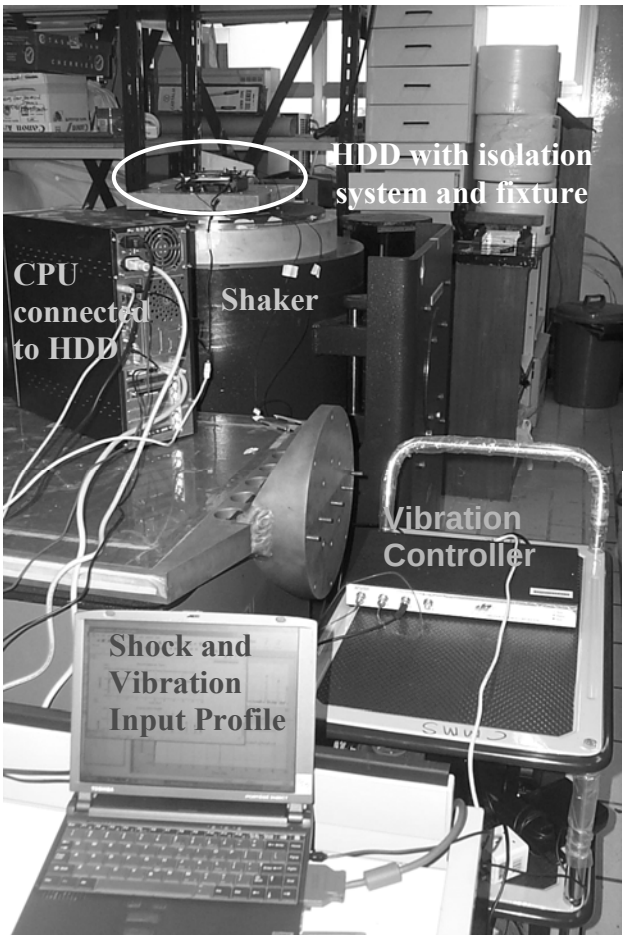

FIGURE 6.3 EXPERIMENT SET UP FOR VERTICAL RANDOM VIBRATION

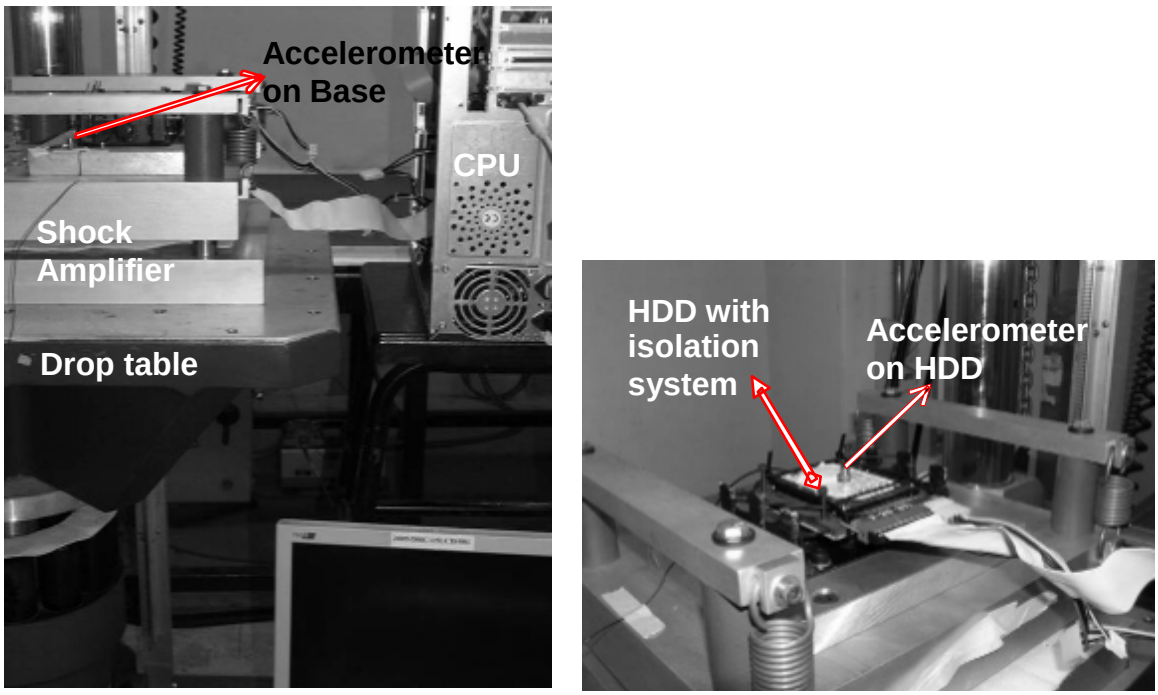

FIGURE 6.4 EXPERIMENT SET UP FOR VERTICAL SHOCK TEST

During shock/random vibration test, the functionality of the HDD is evaluated in terms of

1. Real time data recording to the HDD with constant data transfer rate.

   By using a multi-channel field data recorder, data (e.g. signals from accelerometers) is recorded and streamed in real-time to the HDD. The data transfer rate can be determined from the size of the data and the sampling frequency. The data written to the HDD is then verified. The HDD pass this test if the desired data recording rate can be maintained without loss.

2. Video streaming from HDD

   For example, the movie streamed may be a DVD video having a video bit rate of approximately 4 megabytes per second (MB/s). The HDD are considered to pass this test if there are no pauses in the movie being played continuously during the vibration test.

3. Video capture to HDD

   Using camera with video recording interface, dynamic events are captured to HDD. The HDD pass this test if there is no distortion in the video captured during playback.

6.3 *Design Concept*

6.3.1 Threshold of Bare HDD

This section aims to demonstrate that vibration isolation is necessary for HDD. The vibration tolerances of bare HDD (without vibration isolation system) are determined based on the evaluation criteria given in section 6.2 above. The bare HDD are subjected

to the random vibration defined by uniform power spectral density from 5 Hertz to 500 Hertz. The magnitude of power spectral density is increased until the HDD fail according to the given criteria. Table 6.2 shows the experimentally measured acceptable limits of the bare HDD used in this study (the axes notation is given in Figure 6.5).

TABLE 6.2 MAXIMUM GRMS THAT HDD CAN WITHSTAND WITHOUT VIBRATION ISOLATOR

Manufacturer	Serial No	GRMS		
		x-axis	y-axis	z-axis
Hitachi	F4H23NTD	5.07	5.07	3.47
	F4H23NWD	5.05	5.22	3.47

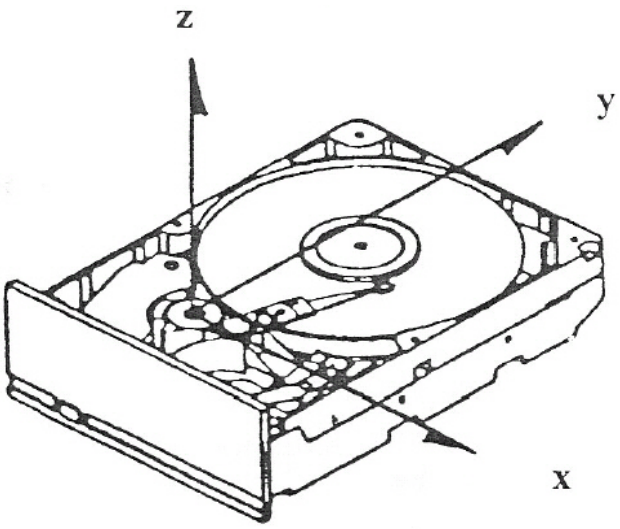

FIGURE 6.5 HDD AXES NOTATION

Since the random vibration inputs specified by MIL STD 810E are up to 8.95 GRMS for z-axis and 12 GRMS for x-axis, the bare HDD would not be able to pass the MIL STD 810E requirements. Hence, vibration isolation is necessary for the HDD.

6.3.2 Shock and Random Vibration Isolation Design

Basically, the isolator design should achieve transmissibilities for all three axes of motion that are low enough to provide the necessary vibration isolation in the 5-500Hz frequency range. Since the HDD cover is relatively stiff (fundamental natural frequencies ~ 3 kHz), the HDD can be treated as a rigid body [122]. This assumption is acceptable in designing the external isolation system because since the cover is relatively very stiff, the elastic deformation of the cover will not affect the response of the isolation system. Referring to Figure 6.6, the RMS value of the HDD acceleration can be predicted by the formula:

$$\text{RMS value} = \sqrt{\int |Tr(\omega)|^2 S_{yy}(\omega) d\omega} \tag{6.1}$$

where $Tr(\omega)$ is the frequency dependent transmissibility function, and $S_{yy}(\omega)$ is the power spectral density function for a random input vibration to the base.

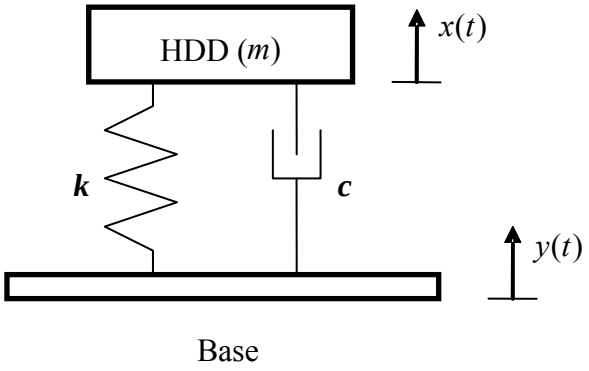

FIGURE 6.6 HDD ON VIBRATION ISOLATOR MOUNT

The objective is to make sure that the RMS value of the HDD acceleration is lower than the acceptable limits given in Table 6.2 above.

Using (6.1), the RMS acceleration response can be predicted if the transmissibility function $Tr(\omega)$ and the power spectral density input $S_{yy}(\omega)$ is known. $Tr(\omega)$ is a function of isolator system natural frequency ω_n and the damping factor ζ.

$$Tr(\omega) = \left(\frac{1+(2\zeta r)^2}{(1-r^2)^2+(2\zeta r)^2} \right)^{\frac{1}{2}}; r = \frac{\omega}{\omega_n} \tag{2}$$

$S_{yy}(\omega)$ is set according to the data given in MIL-STD-810E. The data consists of six phases of random vibration input defined in the z (vertical), x (transverse), and y (longitudinal) directions.

Figure 6.7 to Figure 6.9 show the predicted RMS acceleration response of the HDD versus the isolator's natural frequency for damping factor of 0.1, for the six phases of random vibration input defined in MIL-STD-810E for the z, x and y directions. V1 to V6 correspond to $S_{yy}(\omega)$ in the six phases of vertical random vibration data. T1 to T6 correspond to $S_{yy}(\omega)$ in the six phases transverse of random vibration data. L1 to L6 correspond to $S_{yy}(\omega)$ in the six phases of longitudinal random vibration data.

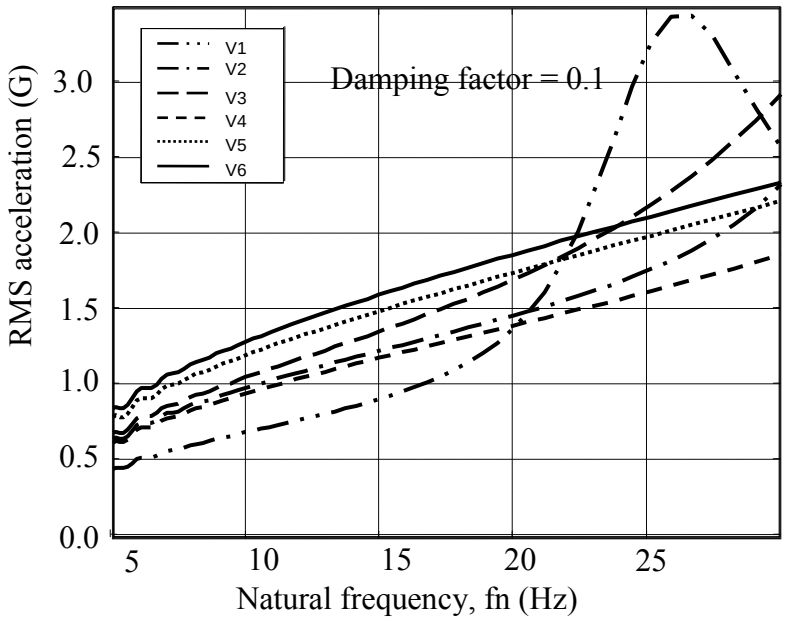

FIGURE 6.7 PREDICTED RMS ACCELERATION RESPONSE OF THE HDD (Z-DIRECTION)

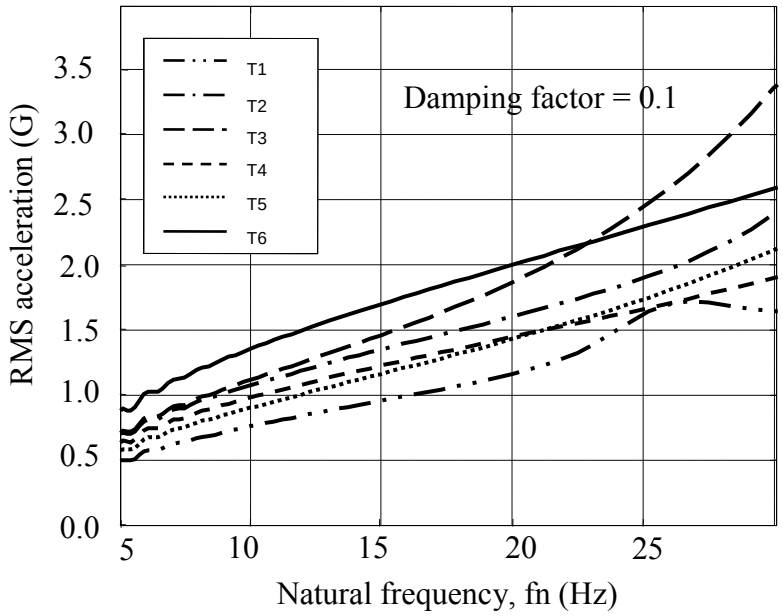

FIGURE 6.8 PREDICTED RMS ACCELERATION RESPONSE OF THE HDD (X-DIRECTION)

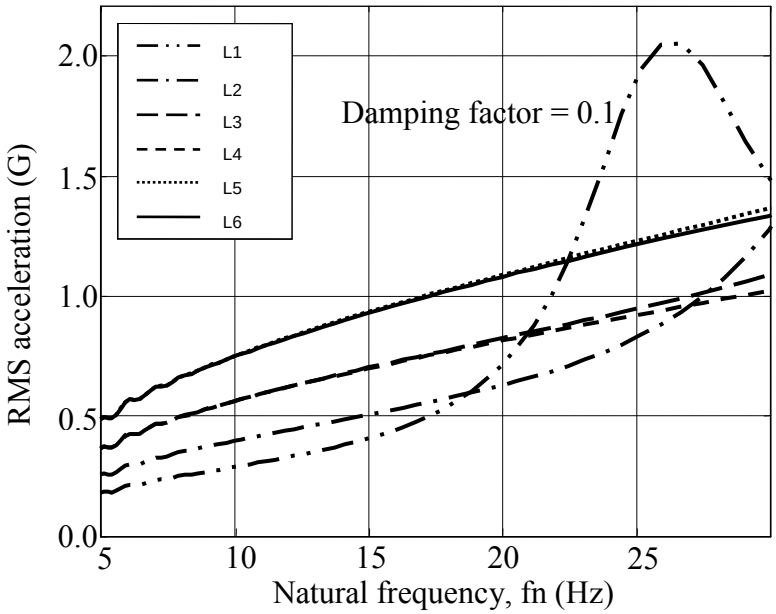

FIGURE 6.9 PREDICTED RMS ACCELERATION RESPONSE OF THE HDD (Y-DIRECTION)

It can be inferred that the vibration isolation design must have relatively low natural frequency. For example, in vertical direction, a natural frequency of 20 Hz or below will give an RMS acceleration response under 2 G. In the *x* and *y* directions, a natural frequency of 30 Hz or below will give an RMS acceleration response under 3.5 G. A well-damped system (damping ratio $\geq$ 0.1) with natural frequencies between 10 to 20 Hz is expected to give good random vibration isolation.

However, a system with low natural frequencies may suffer from high displacement response under a shock input. A high displacement response is not desirable because there may not be enough space around the HDD to accommodate peak-to-peak displacement. In order to restrain displacement response, relatively stiff isolators can be added to the vibration isolation system (Figure 6.10). The HDD can still function normally when it hits the stiff isolator due to its high shock tolerance.

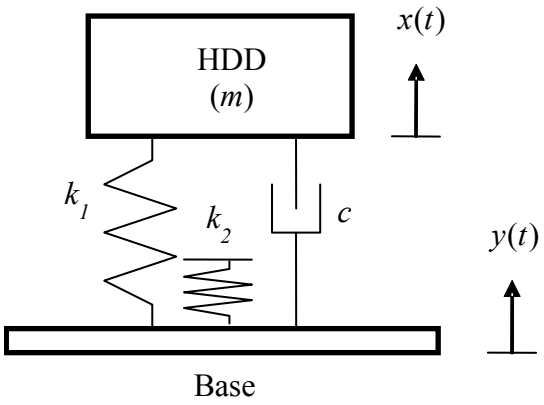

FIGURE 6.10 VIBRATION ISOLATOR MOUNT WITH ADDITIONAL STIFF ISOLATOR

6.4 *Design Case Studies*

6.4.1 Design I

Figure 6.11 shows a vibration isolation system for a 2.5" HDD. The HDD is secured inside an aluminum box. The box is supported by four low damped rubber mounts; two at the left side and two at other side. Figure 6.12 shows the measured transmissibilities of the system in the *x*, *y* and *z* directions. The damping ratios for all three directions are less than the values that are predicted to give satisfactory vibration isolation, as explained in section 6.3. Figure 6.13 shows a typical vibration PSD of the excitation and the corresponding response of the HDD. The HDD isolation system did not pass the random vibration tests according to the criteria defined in section 6.2.

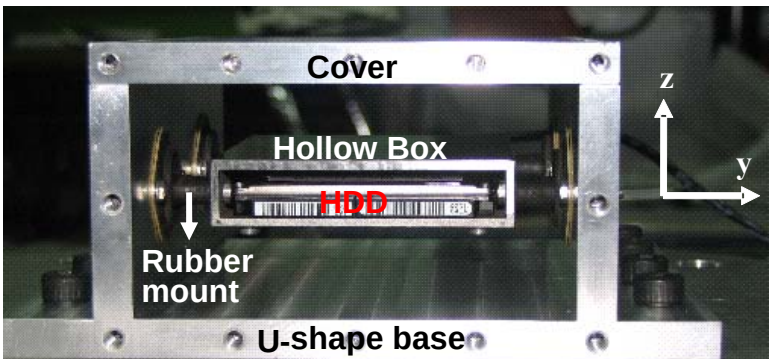

FIGURE 6.11 VIBRATION ISOLATION SYSTEM I

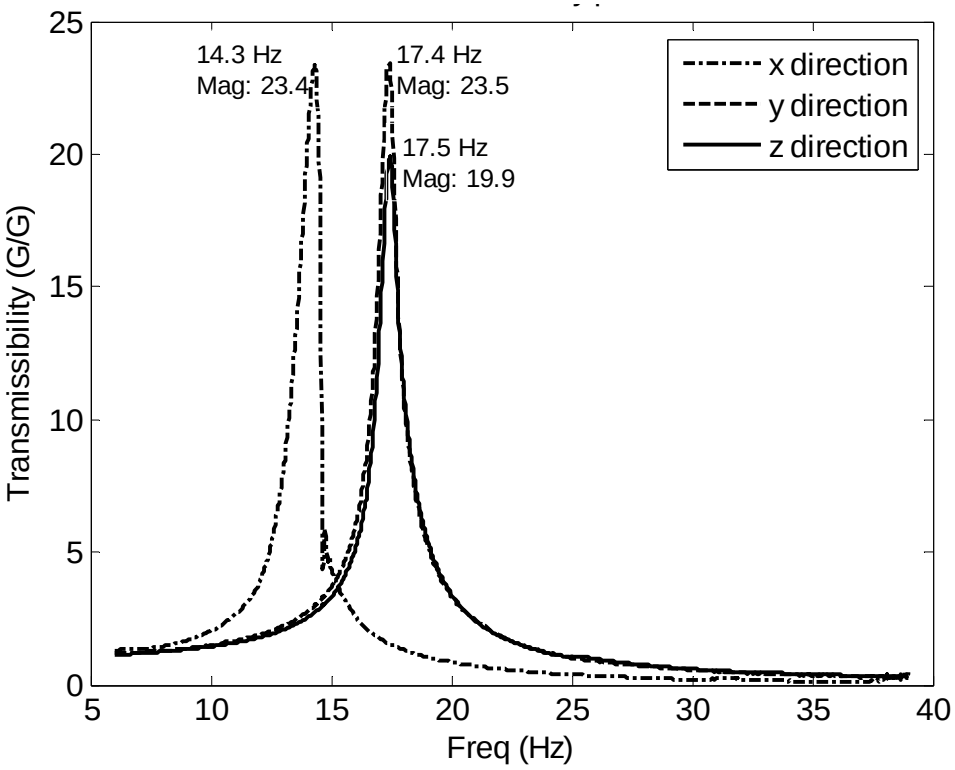

FIGURE 6.12 TRANSMISSIBILITY PLOT FOR VIBRATION ISOLATION SYSTEM I

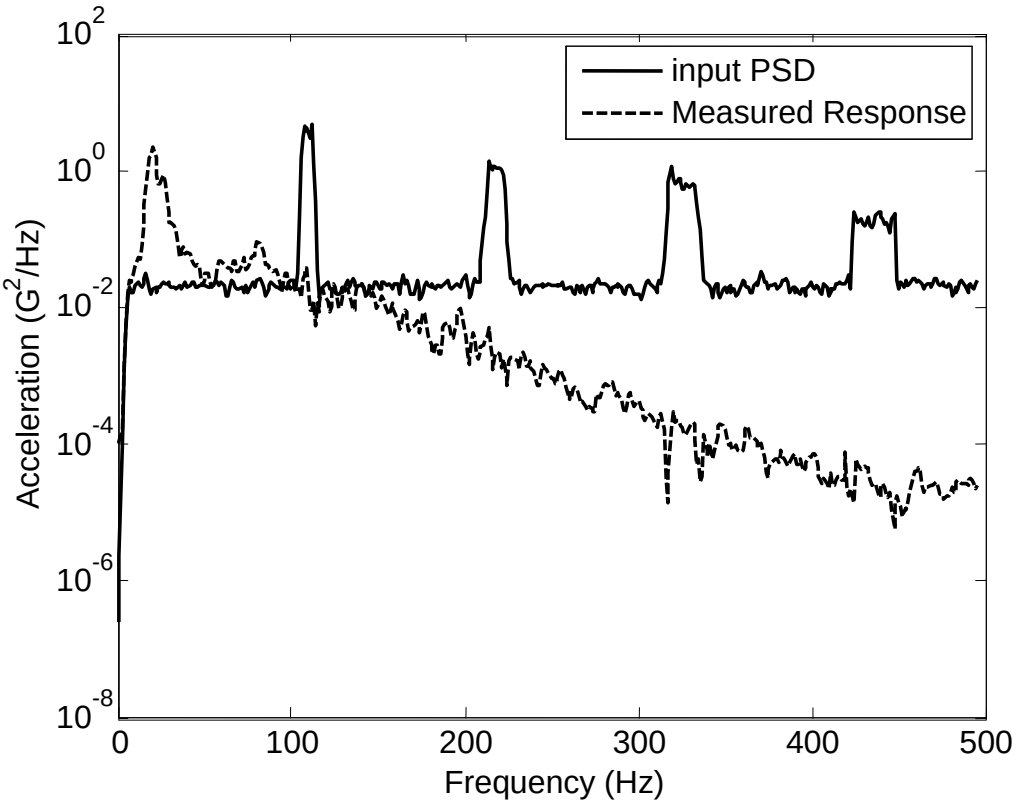

FIGURE 6.13 PSD PLOT FOR VIBRATION ISOLATION SYSTEM I

6.4.2 Design II

Figure 6.14 and Figure 6.15 show another vibration isolation system for a 2.5" HDD. The HDD is secured to a metal base and suspended by rubber O-rings. Figure 6.16 shows the measured transmissibilities of the system in the *x*, *y* and *z* directions. The natural frequencies and damping are well within the ranges that are predicted to give satisfactory vibration isolation. Figure 6.17 shows a typical vibration PSD of the excitation and the corresponding response of the HDD. It is observed that the HDD passes all the random vibration tests according to the specified criteria.

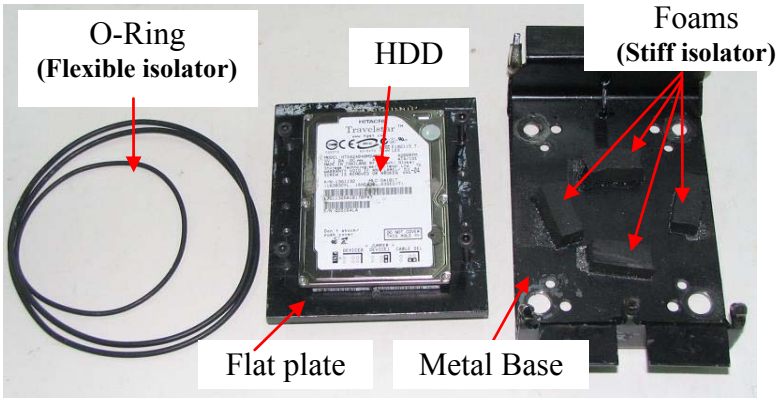

FIGURE 6.14 COMPONENTS OF VIBRATION ISOLATOR SYSTEM II

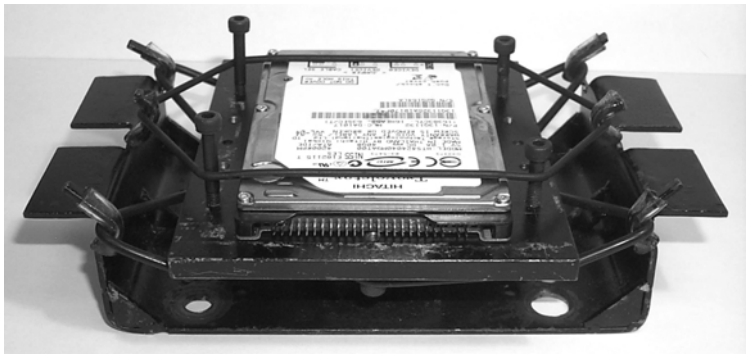

FIGURE 6.15 VIBRATION ISOLATOR SYSTEM II

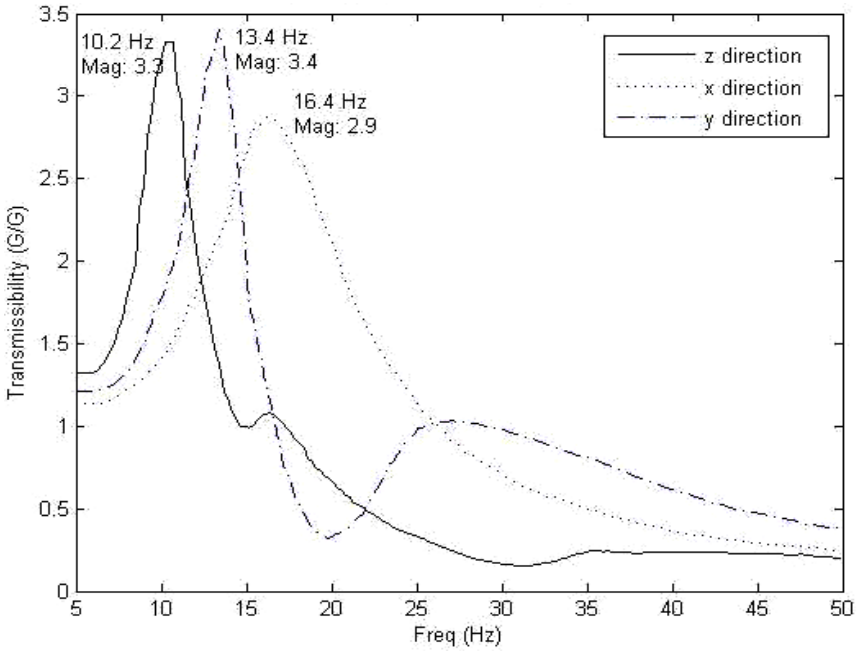

FIGURE 6.16 TRANSMISSIBILITY PLOT FOR VIBRATION ISOLATION SYSTEM II

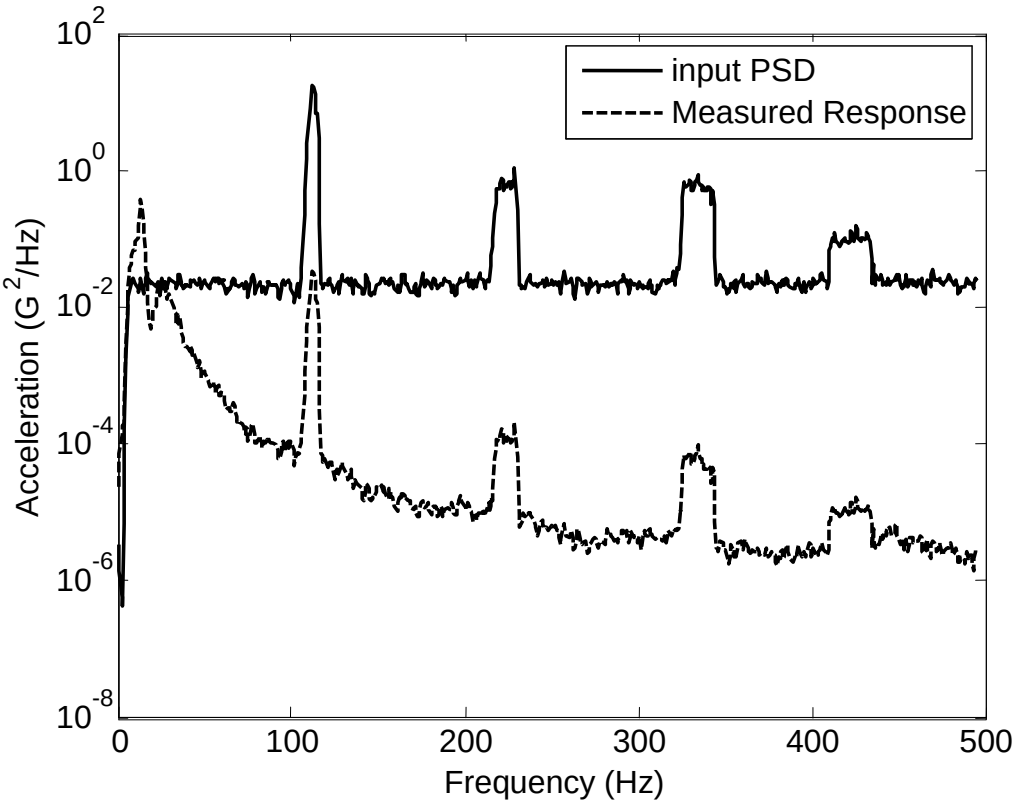

FIGURE 6.17 PSD PLOT FOR VIBRATION ISOLATION SYSTEM II

Figure 6.18 gives the acceleration time history of the base and of the HDD during the crash hazard test. The input acceleration to the base is to 80 G @ 3.5 ms (slightly higher than MIL-STD-810E specification given in Table 6.1). The output acceleration experienced by the HDD is below its critical level (200 G – manufacturer specification). Design II passes the criteria described in section 6.2 in all the shock tests. Figure 6.19 shows the snapshots of the shock response of the HDD. It can be seen that the stiff isolator helps reduce the peak to peak displacement.

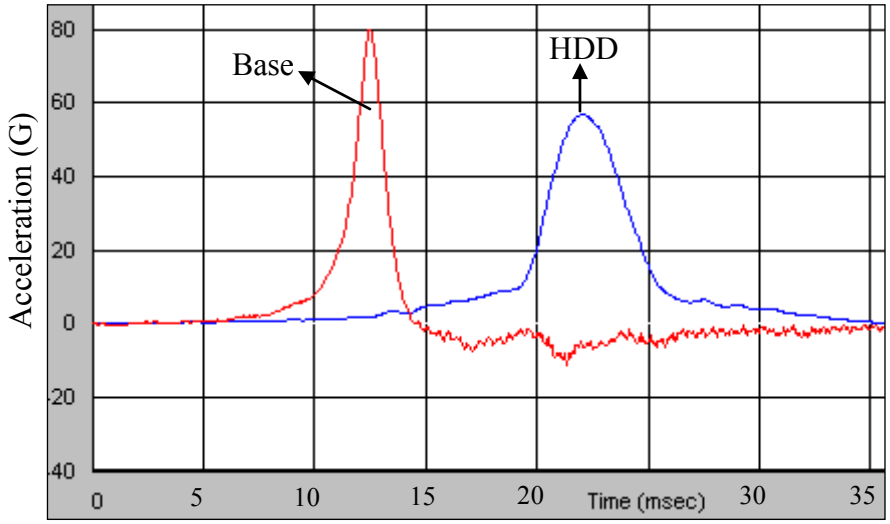

FIGURE 6.18 HDD CRASH HAZARD TEST RESULT

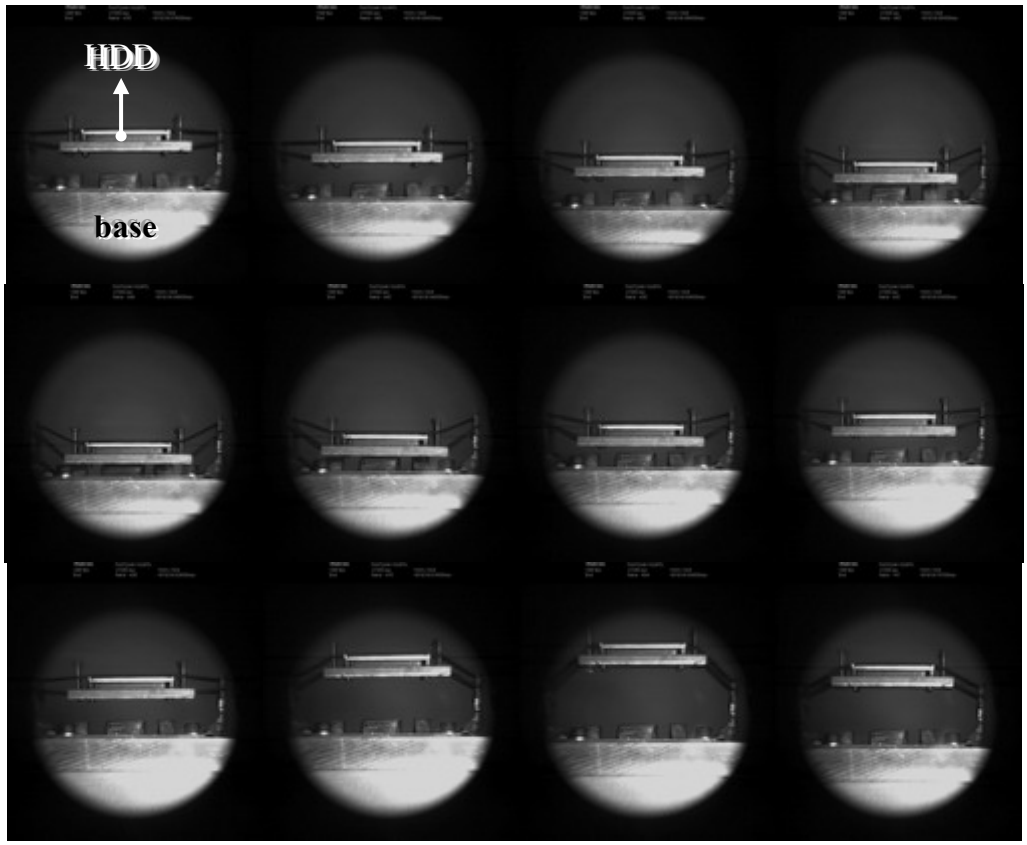

FIGURE 6.19 SNAPSHOTS OF SHOCK RESPONSE OF HDD

A computer simulation model of the HDD vibration isolation system (Figure 6.20) has been developed using SimMechanics. This model takes input in the form of vibration time history data generated from the MIL STD 810E PSD profiles and predicts the output responses. Figure 6.21 shows the measured and predicted RMS acceleration levels of the suspended HDD for the six random vibration test phases in the vertical (z) direction. Comparing with the RMS levels of the input excitation, it can be seen that substantial vibration isolation has been achieved.

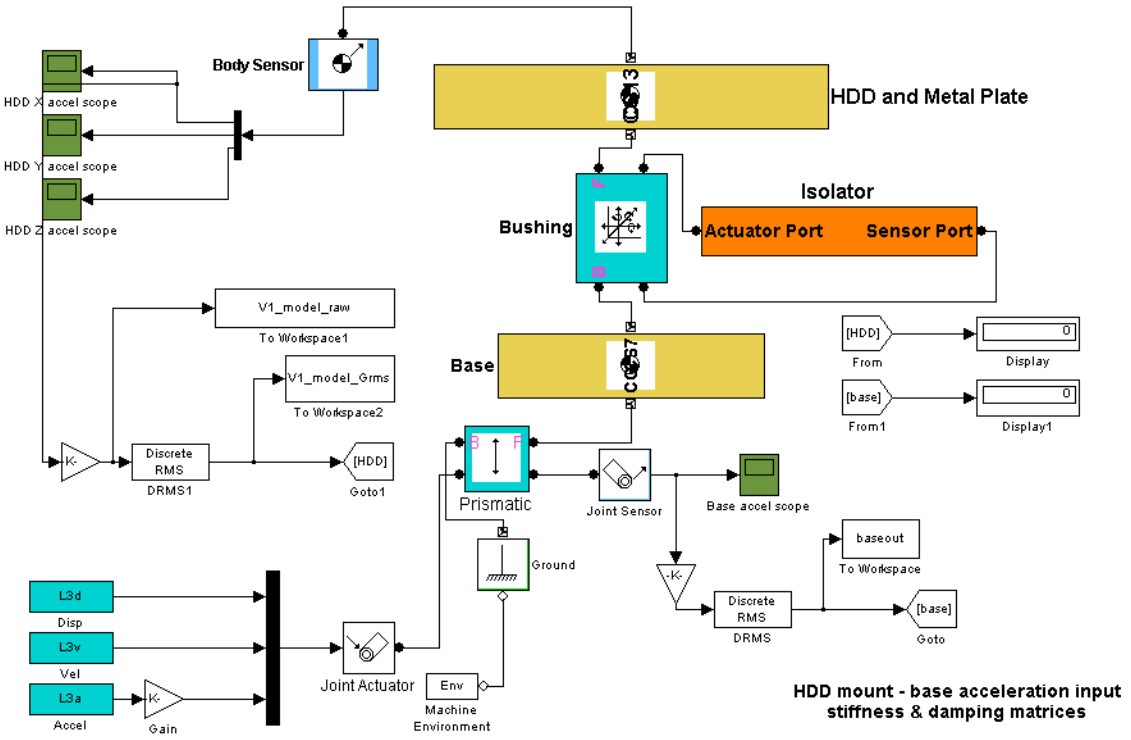

FIGURE 6.20 SIMMECHANICS MODEL OF DESIGN II

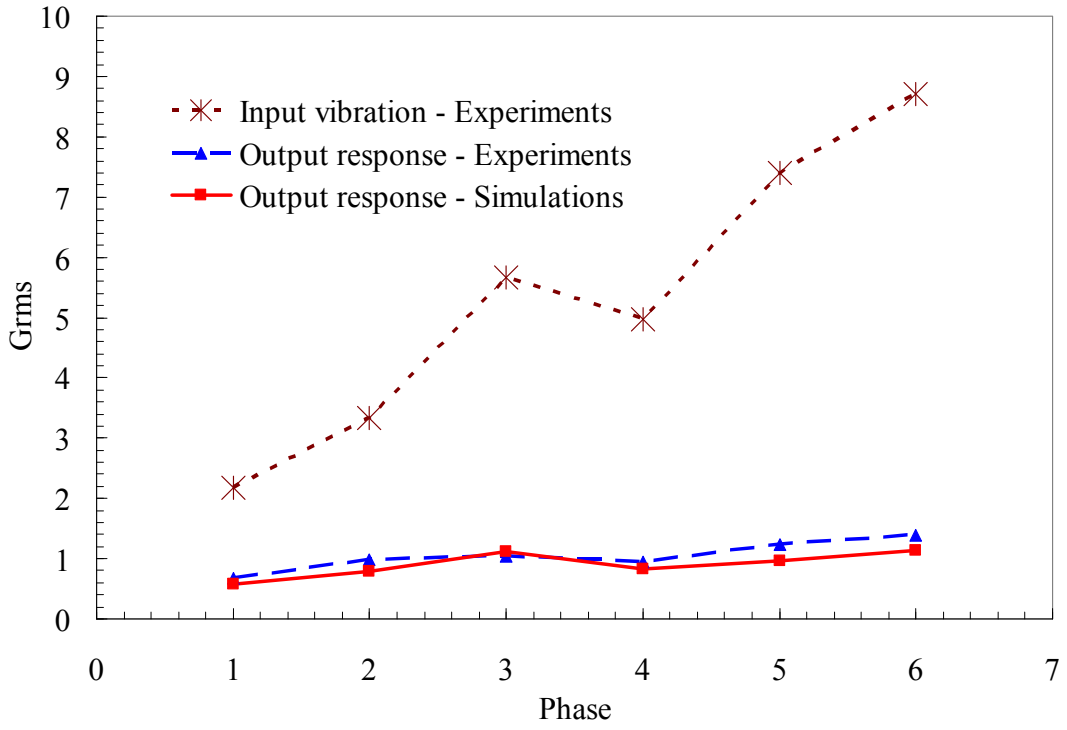

FIGURE 6.21 MEASURED AND PREDICTED RMS ACCELERATION

6.5 *Chapter Summary*

An effective suspension system is necessary to isolate the HDD from the strong vibration transmitted from the ground, vehicle engine, etc. Procedures for vibration testing, evaluation criteria, design concept, modeling and simulation for the external vibration isolation system for the HDD have been presented. Two example designs have been used as case studies to demonstrate and verify the design concepts. The natural frequencies of the external vibration isolation system should be between 10 to 20 Hz. The damping properties of the system is required to be relatively high ($\geq$ 10%). To reduce the peak-to-peak displacement during shock event, relatively stiff isolators can be used. Experiments and simulations have confirmed that effective vibration isolation can indeed be designed to isolate the operating HDD from severe shock and random vibration.

CHAPTER 7 CONCLUSION

The utilizations of the hard disk drives (HDD) in mobile applications require them to have high operational shock and vibration tolerance. The main purpose of this dissertation is to formulate an efficient theoretical model, which incorporates both HDD structural and air bearing models, to predict the HDD operational shock tolerance effectively. The coupled model can be used to investigate the effect of various design parameters on the HDD shock tolerance so as to facilitate optimization and ongoing improvement on the HDD components. In addition, design concepts on how to design, simulate, test, and evaluate the external vibration isolation systems for operating HDD subject to severe shock and random vibrations are developed.

The theoretical models of HDD structures are formulated in Chapter 3. Flexible multi body formulation that can simulate relatively large rotational motion is used to model the dynamic behavior of the structure. A more compact structural model to predict HDD vertical-shock response is developed using a modified state-space formulation based on the mode superposition principle. The state-space model developed can simulate the moving air bearing location due to disk rotation. In the formulation of both theoretical models, Hertz elastic contact theory is used to handle actuator discontinuities.

In Chapter 4 quasi-static concept of the air bearing is introduced and analyzed for its application in the HDD shock simulation. An air bearing model is built based on the quasi-static concept. To investigate the quasi-static concept, a full air bearing model is developed using a finite volume formulation. The finite volume air bearing model is validated by using an established air bearing simulator (CMLAir32).

The quasi static air bearing model is subsequently compared with the full air bearing model. From the comparison, it is found that although the fundamental frequency of the air bearing is much higher than the excitation frequencies, equilibrium condition is not achieved instantaneously due to the squeeze effect dampening the slider shock response. It is also found that by adding optimized damping elements, the quasi-static air bearing model can predict almost the same air bearing force response as the finite volume model.

Chapter 5 presents the coupled models of the structural and the air bearing. In one model, a flexible multi body dynamics structural model is coupled with a full finite volume model of the air bearing. In a second model, the quasi-static air bearing model is attached to the state-space structural model. Efficient coupling methods are developed for each combined model. Model validation shows that both coupled model can effectively predict the shock tolerance of the HDD. Comparison studies with two existing HDD shock models demonstrate that the combination of the state-space structural model and quasi-static air bearing model is the most time-efficient.

By considering the discontinuities of head actuator assembly in the shock simulation, an important design parameter that affects HDD shock performance is identified. It is found that softer contact stiffness between suspension (the dimple) and slider (the flexure) gives higher shock tolerance. A more rigid HDD base cover is also found to increase the predicted shock tolerance. Subsequent shock simulation parameter studies also show that repositioning air bearing location at every simulation time-step (to represent the air bearing that moves with respect to the disk due to disk spinning motion) does not have significant effect on the shock simulation results. Hence, for future shock modeling, the air bearing location can be fixed.

Lastly, the design and analysis of the external shock and vibration isolation for HDD, subject to severe shock and vibration according to MIL STD 810E, is presented in Chapter 6. It is found that the natural frequencies of the external vibration isolation system should be between 10 to 20 Hz. The damping properties of the isolation system is required to be relatively high (> 10%). To reduce the peak-to-peak displacement during shock event, a combination of soft and stiff isolators can be used.

In summary, the new contributions made in this dissertation covers:

1. Shock models of the HDD structures:
    a. Flexible multi body dynamics formulation of operating HDD under shock and considering the nonlinearity of HAA
    b. Modes superposition modeling theory for HDD under shock, considering the disk motion and the nonlinearity of HAA
2. Air bearing shock modeling: introduction, investigation and extension of quasi-static concept for air bearing shock simulation (the author acknowledges Virmani and T. L. Geers as one of the first to introduce this quasi-static concept)
3. Coupled structural and fluid models:
    a. Flexible multi body dynamics structural model + full air bearing model
    b. State-space mode superposition structural model + quasi-static air bearing model

4. HDD vibration isolation: theory/concept on how to design, simulate, test and evaluate the external vibration isolation systems for operating HDD subject to severe shock and random vibrations based on Mil-Std-810E

5. Parametric studies:

    a. Effect of dimple/flexure contact stiffness on HDD shock tolerance

    b. Effect of updating air bearing location, which moves due to disk rotation, in HDD shock simulation

CHAPTER 8 FURTHER WORK

In this last chapter, the author would like to suggest one research work that most probably will generate significant the progress in the HDD shock and vibration field. A brief literature review is first given to explain the needs of this further research work, followed by the objective and the significance of this work. Lastly, two ideas that may meet the research objectives are proposed.

8.1 *Background*

The author realized that the experimental works in operational HDD shock and vibration problem is still lagging compared to the numerical works; the theoretical models have been able to predict the operational HDD shock tolerance (including the slider shock response), but there has not been any experimental technique that is able to measure/identify accurately how the slider-disk contact actually happens when a functioning HDD is being shocked severely. This mostly is because the external shock excitation causes relatively big rigid body motion (at least few centimeters) and a lot of noise (especially during impact), and the physical gap to be investigated (the air bearing spacing) is in nanometer scale and most of the times concealed between the suspension and the disk.

Each existing experimental technique has one or two weaknesses that limit their ability to measure/identify the slider-disk contact due to external shock. Most of precision instruments, such as interferometers [170-173] can operate accurately only when the rigid body motion of the measured object is relatively small. Measurement techniques using acoustic [174, 175] require quiet environment to detect the occurrence of contacts. Electrical resistance methods [176, 177] and piezoelectric transducer methods [178]

require modification of the slider, which cannot be afforded in the modern HDD because the slider is getting smaller and its profile is getting more complex. High speed camera has been used also to capture the HDD shock response [161]. But, due to its coarse resolution (micrometer level), it cannot be used to discern what happens in the nanometer spacing. Laser Doppler Vibrometer (LDV) has been used widely to measure HDD vibrations, such as in [179-182]. In [51] the LDV has been successfully used to determine the slider and the disk response to non-operational shock. It should be possible to extend the method to operational shock through the use of a transparent HDD cover. In addition, there must also be a clear line-of-sight between the LDV and the slider. This requires the modification of the suspension so that the laser light can fall directly onto the slider body. However, it has been observed that during shock the slider may sway horizontally (in parallel plane with the disk surface); this causes the laser point to wander from the intended location. As the result, the measurement may not be correct. Another method is a drive level measurement technique using signal from the write/read head [183]. The limitation is that it can only give the flying height modulation of the head but not the pitch and roll angle, and hence, it is difficult to deduce whether slider-disk contact has happen.

In the HDD industry itself, there are two methods that have been used to detect the slider-disk contact. In the first method, the disk is removed from the drive after shock test and then examined under microscope. Using this method the information on whether a certain shock level damages the disk surface and potential causes for the damage can be inferred. However, how exactly the slider touches the disk is not known. Besides, this method is not practical because it wastes relatively large resources (one drive is required for each shock level) and time (to disassemble the disk and to scan it) [184]. In the second method

the read/write head is used to scan the disk for damages. This is the most efficient way so far, but this method requires additional servo control to enable the read/write head to scan the disk. When there is a need to shock-test a new design, a proper servo control algorithm has to be built first considering the dynamic of the new design. As the consequences, significant amount of time has to be spent on setting up servo control algorithm before the correct scanning can be done to detect the slider disk contact.

8.2 *Objective*

Based on the brief review above, the objective of the further research work is to invent a new technology that can accurately measure/quantify the slider-disk spacing and can detect the slider-disk contact when operational drives are shocked externally.

The potential challenges come from large rigid body movement and a lot of acoustic & mechanical noise generated during the impact. The rigid body movement and the noise are getting bigger as the shock level is getting higher (currently the shock test level is more than 600 G). Furthermore, the air bearing spacing is in nanometer scale and in most drives its position is veiled between the suspension and the disk.

8.3 *Ideas for Further Work*

Three ideas are presented in this sub-section. The first two ideas are the extension from LDV and triple harmonics method, while the third one is a slightly different idea using piezoelectric material.

8.3.1 Extension of LDV method

As mentioned in the brief literature review above, the LDV should be able to measure the slider flying attitude (including pitch and roll angle). However, there are three things to be carried out before the LDV can be utilized properly.

a) There must be a clear line-of-sight between the slider and the LDV sensor; the cover should be made transparent or partly cut to reveal the head disk interface and then the suspension shape should be modified to reveal the slider to the LDV.

b) The HAA should be constrained from swaying during shock. This is because if the actuator swings in the plane direction (parallel to disk surface), the laser points will not stay on the intended position in the slider (note that the slider area is small (~ $1mm^2$). In addition, the shock test rig must be designed in such a way that the HDD only moves in vertical plane (plane perpendicular to disk surface).

c) Three laser points are needed simultaneously at slider body to fully capture its response.

8.3.2 Extension of Triple Harmonic Method

The triple harmonic method has been utilized to measure the flying height. Two spectrum analyzers are used to measure the read signal output of the first and third harmonics. The flying height variation was then obtained by calculating the harmonic ratio using the Wallace spacing loss formula [183].

It may be possible to extend the method to take into account the slider pitch and roll angle also. It means two additional sensors similar to the read head should be added to the

slider. By taking measurement from three different points in the slider body the slider response (flying height, pitch, and roll angle) can be calculated.

The main challenge may come from the complexity in installing two additional read sensors in the small slider; the additional read sensors means that the air bearing profile may need modification. Besides that, their effect on the head-disk-interface shock performance is not yet known.

8.3.3 Using Piezoelectric Sensor

This idea is basically combination of two measurement methods: First, the LDV is utilized to measure the suspension motion. Then, at the same time several piezoelectric sensors, which are installed in the flexure, are used to determine the slider position with respect to the suspension (see Figure 8.1). The LDV measurement on the suspension is much easier to be carried out than on the slider because of its relatively big size and its more accessible position. The main challenge is on deciding the configuration of the piezoelectric sensor that enables accurate measurement of relative position of slider with respect to the suspension. An extra advantage of this concept is that the piezoelectric sensor can later be used as actuator also to help control the slider motion.

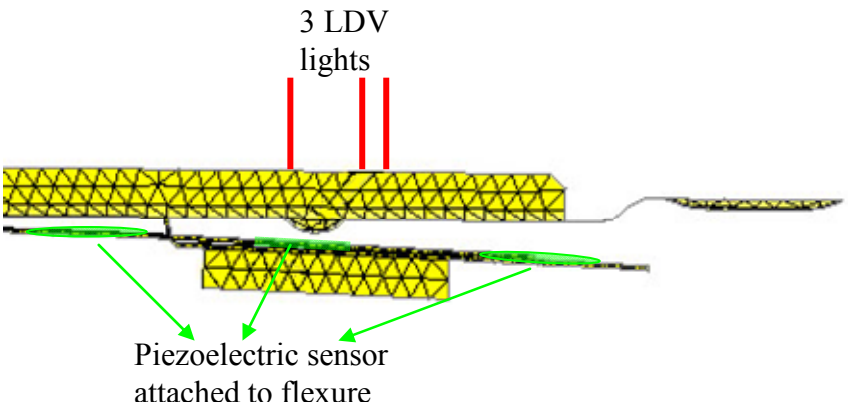

FIGURE 8.1 PIEZOELECTRIC SENSOR

8.4 *Significance*

The research topic of this proposed further work is good because it is focused, it addresses an important problem, and it will create impacts. There are two main impacts that may be created if such technology can be invented. First, many numerical HDD shock models can be verified at a more detailed level. A lot of researchers will use the technology to verify their numerical model. Second, the HDD industries will be very interested with it because they can test the effect of design changes to the HDD shock response more efficiently.

REFERENCES

[1] Wikipedia, "Non-volatile memory," Retrieved Nov 01, 2007, from http://en.wikipedia.org/wiki/Non-volatile_memory

[2] M. Brain, "How Hard Disks Work," Retrieved Nov 01, 2007, from http://computer.howstuffworks.com/hard-disk1.htm

[3] B. Liu, "Advance Technology for Ultra Low Flying Height Head Disk Interface," in *Data Storage Institute Workshop on Head Disk Interface*, Singapore, DSI, 2005.

[4] T. Smith, "Samsung shows 'world's first' hard drive phone," Retrieved Nov 01, 2007, from http://www.theregister.co.uk/2004/09/06/samsung_hdd_handset/

[5] COUGHLIN, "HARD DISK DRIVE CAPITAL EQUIPMENT MARKET & TECHNOLOGY REPORT," Retrieved Nov 02, 2007, from http://www.tomcoughlin.com/Techpapers/Capital%20Spending%20Brochure,%20062606.pdf

[6] G. Keizer, "Toshiba to increase small hard drive capacity to 10GB," Retrieved Nov 02, 2007, from http://www.eetindia.co.in/ART_8800402959_1800009_NT_4bcd2956.HTM

[7] Hitachi, "HDD Roadmap," *HDD Technology Overview* Retrieved Nov 02, 2007, from http://www.hitachigst.com/hdd/technolo/overview/chart01.html

[8] Hitachi, "A brief history of hard drives," Retrieved Nov 02, 2007, from http://www.news.com/2300-1010_3-6031405-9.html?tag=ne.gall.pg

[9] J. Wilcox, "Maxtor buys rival Quantum to become biggest drive maker," Retrieved Nov 02, 2007, from http://www.news.com/2100-1001-246572.html

[10] J. Evers, "Hitachi absorbs IBM hard-disk unit, announces new drives," Retrieved Nov 02, 2007, from http://www.computerworld.com/hardwaretopics/hardware/story/0,10801,77286,00.html

[11] B. Fonseca, "Seagate's Maxtor Grab Expected to Bring Leverage " Retrieved Nov 02, 2007, from http://www.eweek.com/article2/0,1895,1904471,00.asp

[12] "News an Products," *Solid State Technology* Retrieved Nov 02, 2007, from http://sst.pennnet.com/Articles/Article_Display.cfm?Section=Archives&Subsection=Display&ARTICLE_ID=236130

[13] Hitachi, "HGST Areal Density Perspective," *HDD Technology Overview* Retrieved Nov 02, 2007, from http://www.hitachigst.com/hdd/hddpdf/tech/chart02.pdf

[14] Hitachi, "Areal Density Perspective," *HDD Technology Overview* Retrieved Nov 02, 2007, from http://www.hitachigst.com/hdd/technolo/overview/chart02.html

[15] Wikipedia, "Moore's Law," Retrieved Nov 02, 2007, from http://en.wikipedia.org/wiki/Moore's_law

[16] M. MOORE, "German, Frenchman share 2007 Nobel Prize in physics for work on magnetic resistance," Retrieved Nov 06, 2007, from http://peripherals.consumerelectronicsnet.com/articles/viewarticle.jsp?id=192731

[17] Wikipedia, "Perpendicular Recording," Retrieved Nov 06, 2007, from http://en.wikipedia.org/wiki/Perpendicular_recording

[18] Hitachi, "Get Perpendicular," Retrieved Nov 06, 2007, from http://www.hitachigst.com/hdd/research/recording_head/pr/PerpendicularAnimation.html

[19] E. Bangeman, "Seagate hits new heights in disk platter density," Retrieved Nov 06, 2007, from http://arstechnica.com/news.ars/post/20060918-7765.html

[20] J. Reimer, "Toshiba reveals new high-density compact hard drive," Retrieved Nov 06, 2007, from http://arstechnica.com/news.ars/post/20060605-6988.html

[21] Toshiba, "Toshiba Brings Discrete Track Recording Technology to Prototype of 120GB Hard Disk Drive " Retrieved Nov 06, 2007, from http://www.cdrinfo.com/Sections/News/Details.aspx?NewsId=21336

[22] M. Hachman, "Seagate Moves Ahead On HAMR Technology," Retrieved Nov 09, 2007, from http://www.extremetech.com/article2/0,3973,480971,00.asp

[23] T. D. Maesschalck, "300 teraBITS is not 300TB! And 3TB isn't 300TB!," Retrieved Nov 09, 2007, from http://www.dvhardware.net/article16110.html

[24] Fujitsu, "Fujitsu Asia Unveils MHY2BS Series of SATA Hard Disk Drives for ASEAN," Retrieved Nov 06, 2007, from http://www.fujitsu.com/sg/news/pr/archives/month/2007/20070801.html

[25] R. Ambekar, Q. Zeng, and F.-Y. Huang, "System Level Impact Testing of MP3 Players," in *2006 ASME/JSME Joint Conference on Micromechatronics for Information and Precision Equipment (MIPE 2006)*, Santa Clara, California, USA, 2006.

[26] G. Galvin, "Inertial Sensing for Hard Disk Drive Protection," in *IDEMA DISKCON AP 2005*, Asia Pasific, 2005, p. 10.

[27] Hitachi, "Spacing-Areal Density Perspective," *HDD Technology Overview* Retrieved Nov 02, 2007, from http://www.hitachigst.com/hdd/technolo/overview/chart14.html

[28] Dell, "No Spin Zone: Dell Ushers In Better Mobile Storage Reliability With Solid State Drives on Select Notebooks " Retrieved Nov 06, 2007, from http://www.dell.com/content/topics/global.aspx/corp/pressoffice/en/2007/2007_04_24_rr_000?c=us&l=en&s=corp

[29] G. Gasior, "Super Talent's SATA25 128GB solid-state hard drive," Retrieved Nov 06, 2007, from http://techreport.com/articles.x/13163

[30] B. Evans, "Suspension Design Progression for Increasing Shock Performance," in *IDEMA DISKCON AP 2005*, Asia Pasific, 2005, p. 11.

[31] Hitachi, "Head-disk Interface/ Slider Designs for Minimizing Magnetic Spacing," Retrieved Nov 12, 2007, from http://www.hitachigst.com/hdd/research/storage/hdi/minimizingspacing.html

[32] Hitachi, "Evolution of Slider/Air Bearing Surface," *HDD Technology Overview* Retrieved Nov 12, 2007, from http://www.hitachigst.com/hdd/technolo/overview/chart10.html

[33] S. Gan, "Investigation of the effect of voice coil mechanism design on shock performance," H. Harmoko, Ed. Singapore: Seagate Technology International, 2007.

[34] F. F. Yap, N. Vahdati, and H. Harmoko, "Design and analysis of vibration isolation systems for hard disk drives," *Journal of Magnetism and Magnetic Materials; 6th International Symposium on Physics of Magnetic Materials,* vol. 303, pp. e52-e56, 2006/8 2006.

[35] ANSYS, "ANSYS Help," *ANSYS*, 2005

[36] K. L. Johnson, "Hertz theory of elastic contact," in *Contact Mechanics* New York: Cambridge University Press, 1989, pp. 90-104.

[37] N. Baddour and J. W. Zu, "Nonlinearly coupled in-plane and transverse vibrations of a spinning disk," *Applied Mathematical Modelling,* vol. 31, pp. 54-77, 2007.

[38] N. Baddour and J. W. Zu, "Nonlinearly coupled in-plane and transverse vibrations of a spinning disk," *Applied Mathematical Modelling,* vol. In Press, Corrected Proof.

[39] G. H. JANG, S. H. LEE, and M. S. JUNG, "Free Vibration Analysis of A Spinning Flexible Disk-Spindle System Supported by Ball Bearing and Flexible Shaft Using the Finite Element Method and Substructure Synthesis," *Journal of Sound and Vibration,* vol. 251, pp. 59-78, 2002.

[40] N. Tandon, V. V. P. Rao, and V. P. Agrawal, "Vibration and noise analysis of computer hard disk drives," *Measurement,* vol. 39, pp. 16-25, 2006/1 2006.

[41] Girish Naganathan, Satish Ramadhyani, and A. K. Bajaj, "Numerical Simulations of Flutter Instability of a Flexible Disk Rotating Close to a Rigid Wall," *Journal of Vibration & Control,* vol. 9, pp. 95-118, 2003.

[42] A. R. Namcheol Kang, "Aeroelastic Flutter Mechanisms of a Flexible Disk Rotating in an Enclosed Compressible Fluid," *ASME Journal of Applied Mechanics,* vol. 71, pp. 120-130, 2004.

[43] B. C. Kim, A. Raman, and J. Mote, C. D., "Prediction of Aeroelastic Flutter in a Hard Disk Drives," *Journal of Sound and Vibration,* vol. 238, pp. 309-325, 2000/11/23 2000.

[44] M. H. HANSEN, A. RAMAN, and J. MOTE, C. D., "Estimation of Nonconservative Aerodynamic Pressure Leading to Flutter of Spinning Disks " *Journal of Fluids and Structures,* vol. 15, pp. 39-57, 2001/1 2001.

[45] M. Tatewaki, N. Tsuda, and T. Maruyama, "An analysis of disk flutter in hard disk drives in aerodynamic simulations," *IEEE Transactions on Magnetics,* vol. 37, pp. 842-846, 2001.

[46] X. Y. Huang, X. Wang, and F. F. Yap, "Feedback control of rotating disk flutter in an enclosure," *Journal of Fluids and Structures,* vol. 19, pp. 917-932, 2004.

[47] I. Y. Shen, "Vibration of Flexible Rotating Disk," *The Shock and Vibration Digest,* vol. 32, pp. 267-272, 2000.

[48] I. Y. Shen, "Recent vibration issues in computer hard disk drives," *Journal of Magnetism and Magnetic Materials,* vol. 209, pp. 6-9, 2000.

[49] J. Yoon and I. Y. Shen, "A numerical study on rotating-shaft spindles with nonlinear fluid-dynamic bearings," *IEEE Transactions on Magnetics,* vol. 41, pp. 756-762, 2005.

[50] C. W. Tseng, J. Y. Shen, and I. Y. Shen, "Vibration of Rotating-Shaft HDD Spindle Motors With Flexible Stationary Parts," *IEEE Transactions on Magnetics,* vol. 39, pp. 794-799, 2003.

[51] S. Sharma, M. Virmani, and T. L. Geers, "Direct Comparison of Computational and Experimental Head-Slap Data for a Nonoperating Hard Disk Drive," *IEEE Transactions on Magnetics,* vol. 43, pp. 1093-1100, 2007.

[52] D. W. Shu, B. J. Shi, H. Meng, F. F. Yap, D. Z. Jiang, Q. Y. Ng, R. Zambri, and J. H. T. Lau, "The pulse width effect of single half-sine acceleration pulse on the peak response of an actuator arm of hard disk drive," *Materials Science and Engineering: A Mechanical Behaviour of Micro- and Nano-scale Systems,* vol. 423, pp. 199-203, 2006/5/15 2006.

[53] A. N. Murthy, M. Pfabe, J. Xu, and F. E. Talke, "Dynamic response of 1-in. form factor disk drives to external shock and vibration loads," *Microsystem Technologies,* 2006.

[54] A. N. Murthy, B. Feliss, D. Gillis, and F. E. Talke, "Experimental and numerical investigation of shock response in 3.5 and 2.5 in. form factor hard disk drives," *Microsystem Technologies,* vol. 12, pp. 1109-1116, Tuesday, June 20, 2006 2006.

[55] C. C. Lin, "Finite Element Analysis of a Computer Hard Disk Drive Under Shock," *ASME Journal of Mechanical Design,* vol. 124, pp. 121-125, 2002.

[56] E. M. Jayson, J. Murphy, P. W. Smith, and F. E. Talke, "Head slap simulation for linear and rotary shock impulses," *Tribology International,* vol. 36, pp. 311-316, 2003.

[57] G. H. Jang, C. H. Seo, and L. Ho Seong, "Finite element modal analysis of an HDD considering the flexibility of spinning disk–spindle, head–suspension–

actuator and supporting structure," *Microsystem Technologies,* vol. 13, pp. 837-847, May 2007.

[58] P. Bhargava and D. B. Bogy, "Effect of shock pulse width on the shock response of small form factor disk drives," *Microsystem Technologies,* vol. 13, pp. 1107-1115, May 2007.

[59] P. Bhargava and D. B. Bogy, "Numerical Simulation of Operational-Shock in Small Form Factor Hard Disk Drives," *Journal of Tribology,* vol. 129, pp. 153-160, 2007.

[60] A. A. Shabana, *Dynamics of multibody systems*, 2nd ed. Cambridge, U.K. ; New York: Cambridge University Press, 1998.

[61] I. Y. Shen, "Closed-form forced response of a damped, rotating, multiple disks/spindle system," *Journal of Applied Mechanics-Transactions of the Asme,* vol. 64, pp. 343-352, JUN 1997.

[62] I. Y. Shen and C. P. R. Ku, "A nonclassical vibration analysis of a multiple rotating disk and spindle assembly," *Journal of Applied Mechanics-Transactions of the Asme,* vol. 64, pp. 165-174, Mar 1997.

[63] J.-Y. Shen, C.-W. Tseng, and I. Y. Shen, "Vibration of rotating disk/spindle systems with flexible housing/stator assemblies," *Journal of Sound and Vibration,* vol. 271, pp. 725-756, 2004/4/6 2004.

[64] F. Gao, F. F. Yap, Y. Yan, and H. Harmoko, "Shock analysis of non-operating hard disk drives based on a multibody dynamic formulation," *Microsystem Technologies,* vol. 12, pp. 247-257, 2006.

[65] M. R. Hatch, *Vibration simulation using MATLAB and ANSYS*. Boca Raton: Chapman & Hall/CRC, 2001.

[66] M. Suk and T. R. Albrecht, "The evolution of load/unload technology," *Microsystem Technologies,* vol. 8, pp. 10-16, 2002.

[67] P. Kim and M. Suk, "Ramp Load/Unload technology in Hard disk drives," Retrieved Nov 15, 2007, from http://www.hitachigst.com/tech/techlib.nsf/techdocs/9076679E3EE4003E86256FAB005825FB/$file/LoadUnload_white_paper_FINAL.pdf

[68] Q.-H. Zeng and D. B. Bogy, "Effects of certain design parameters on load/unload performance," *IEEE Transactions on Magnetics,* vol. 36, pp. 140-147, 2000.

[69] Q. Zeng, M. Chapin, and D. B. Bogy, "Dynamics of the unload process for negative pressure sliders," *IEEE Transactions on Magnetics,* vol. 35, pp. 916-920, 1999.

[70] Q.-H. Zeng and D. B. Bogy, "Effects of suspension limiters on the dynamic load/unload process: numerical simulation," *IEEE Transactions on Magnetics,* vol. 35, pp. 2490-2492, 1999.

[71] Q. Zeng and D. B. Bogy, "Slider air bearing designs for load/unload applications," *IEEE Transactions on Magnetics,* vol. 35, pp. 746-751, 1999.

[72] Q. H. Zeng and D. B. Bogy, "A Simplified 4-DOF Suspension Model for Dynamic Load/Unload Simulation and Its Application," *Journal of Tribology,* vol. 122, pp. 274-279, 2000.

[73] Q.-H. Zeng, M. Chapin, and D. B. Bogy, "Dynamics of the unload process for negative pressure sliders," *IEEE Transactions on Magnetics,* vol. 35, pp. 916-920, 1999.

[74] S. Yonemura, S. Weissner, L. Zhou, and F. E. Talke, "Investigation of disk damage caused during load/unload using a surface reflectance analyzer," *Tribology International,* vol. 38, pp. 81-87, 2005/2 2005.

[75] S. Weissner, U. Zander, and F. E. Talke, "A New Finite-Element Based Suspension Model Including Displacement Limiters for Load/Unload Simulations," *Journal of Tribology,* vol. 125, pp. 162-167, 2003.

[76] E. M. Jayson, J. Murphy, P. W. Smith, and F. E. Talke, "Effects of Air Bearing Stiffness on a Hard Disk Drive Subject to Shock and Vibration," *ASME Journal of Tribology,* vol. 125, pp. 343-349, 2003.

[77] O. J. Ruiz and D. B. Bogy, "Comparison of slider bearing simulations using different models," *International Magnetics Conference - INTERMAG '88, Jul 12-15 1988, IEEE Transactions on Magnetics,* vol. 24, pp. 2754-2756, 1988.

[78] G. Sheng, B. Liu, and W. Hua, "A nonlinear dynamics theory for modeling slider air bearing in hard disk drives," *Journal of Applied Physics,* vol. 87, pp. 6173-6175, 2000.

[79] S. Fukui and R. Kaneko, "ANALYSIS OF ULTRA-THIN GAS FILM LUBRICATION BASED ON LINEARIZED BOLTZMANN EQUATION: FIRST REPORT - DERIVATION OF A GENERALIZED LUBRICATION EQUATION INCLUDING THERMAL CREEP FLOW.," *Journal of Tribology, Transactions of the ASME,* vol. 110, pp. 253-262, 1988.

[80] S.-C. Kang, R. M. Crone, and M. S. Jhon, "A new molecular gas lubrication theory suitable for head-disk interface modeling," in *43rd Annual Conference on Magnetism and Magnetic Materials, 9-12 Nov. 1998*, Miami, FL, USA, 1999, pp. 5594-6.

[81] S. Fukui and R. Kaneko, "Database for interpolation of Poiseuille flow rates for high Knudsen number lubrication problems," *Journal of Tribology, Transactions of the ASME,* vol. 112, pp. 78-83, 1990.

[82] P. Bahukudumbi and A. Beskok, "A phenomenological lubrication model for the entire Knudsen regime," *Journal of Micromechanics and Microengineering,* vol. 13, pp. 873-84, 2003/11/ 2003.

[83] J. H. Park, A. Beskok, and P. Bahukudumbi, "A unified engineering model for steady and quasi-steady shear-driven gas microflows," *Microscale Thermophysical Engineering,* vol. 7, pp. 291-315, 2003.

[84] S.-C. Kang, R. M. Crone, and M. S. Jhon, "A new molecular gas lubrication theory suitable for head-disk interface modeling," in *43rd Annual Conference on Magnetism and Magnetic Materials, 9-12 Nov. 1998, Journal of Applied Physics*, Miami, FL, USA, 1999, pp. 5594-6.

[85] M. Panzer, "Numerical investigation of the contact force in the head/disk interface," Retrieved May 06, 2006, from http://talkelab.ucsd.edu/matthias/research/research.ppt

[86] B. H. Thornton and D. B. Bogy, "A Parametric Study of Head-Disk Interface Instability Due to Intermolecular Forces," *IEEE Transactions on Magnetics,* vol. 40, pp. 337-344, 2004.

[87] R. Ambekar, V. Gupta, D. B. Bogy, and W. S. Floyd Jr., "Experimental and numerical investigation of dynamic instability in the head disk interface at proximity," in *2004 ASME/STLE International Joint Tribology Conference, Oct 24-27 2004*, Long Beach, CA, United States, 2004, pp. 1463-1470 BN - 0791841812.

[88] V. Gupta and D. B. Bogy, "Dynamics of sub-5-nm air-bearing sliders in the presence of electrostatic and intermolecular forces at the head-disk interface," *IEEE Transactions on Magnetics,* vol. 41, pp. 610-615, 2005.

[89] E. M. Jayson, J. Murphy, P. W. Smith, and F. E. Talke, "Effects of air bearing stiffness on a hard disk drive subject to shock and vibration," *Journal of Tribology-Transactions of the ASME,* vol. 125, pp. 343-349, Apr 2003.

[90] E. M. Jayson, J. M. Murphy, P. W. Smith, and F. E. Talke, "Shock and head slap simulations of operational and nonoperational hard disk drives," *IEEE Transactions on Magnetics,* vol. 38, pp. 2150-2152, Sep 2002.

[91] B. H. Thornton and D. B. Bogy, "Nonlinear aspects of air-bearing modeling and dynamic spacing modulation in sub-5-nm air bearings for hard disk drives," *IEEE Transactions on Magnetics,* vol. 39, pp. 722-728, 2003.

[92] G. Sheng, R. Dukkipati, and J. Pang, "Nonlinear dynamics of sub-10 nm flying height air bearing slider in modern hard disk recording system," *Mechanism and Machine Theory,* vol. 41, pp. 1230-1242, 2006/10 2006.

[93] L. Wu and D. B. Bogy, "Unstructured Adaptive Triangular Mesh Generation Techniques and Finite Volume Schemes for the Air Bearing Problem in Hard Disk Drives," *Journal of Tribology,* vol. 122, pp. 761-770, 2000.

[94] L. Wu and D. B. Bogy, "Effect of the Intermolecular Forces on the Flying Attitude of Sub-5 NM Flying Height Air Bearing Sliders in Hard Disk Drives," *Journal of Tribology,* vol. 124, pp. 562-567, 2002.

[95] S. Lu, "Numerical Simulation of Slider Air Bearing," Berkeley: University of California at Berkeley, 1997.

[96] J. C. Harrison and M. D. Mundt, "Flying height response to mechanical shock during operation of a magnetic hard disk drive," *Journal of Tribology-Transactions of the Asme,* vol. 122, pp. 260-263, Jan 2000.

[97] B. J. Shi, S. Wang, D. W. Shu, J. Luo, H. Meng, Q. Y. Ng, and R. Zambri, "Power Spectrum Analysis of the Excitation Pulse Effects in Drop Test Simulation of Hard Disk Drives," in *Asia-Pacific Magnetic Recording Conference*, Seoul, Korea, 2004.

[98] M. Virmani and T. L. Geers, " Simulation of Operational Shock in a Hard Disk Drive," in *ASME/JSME Joint Conf. on Micromechatronics for Information and Precision Equipment (MIPE)*, 2006.

[99] Y. Wang, "Shock Simulation of HDD," H. Harmoko, Ed. Singapore: Seagate Technology International, 2007.

[100] E. M. Jayson, P. W. Smith, and F. E. Talke, "Shock modeling of the head-media interface in an operational hard disk drive," *IEEE Transactions on Magnetics,* vol. 39, pp. 2429-2431, Sep 2003.

[101] Q. H. Zeng and D. B. Bogy, "Numerical simulation of shock response of disk-suspension-slider air bearing systems in hard disk drives," *Microsystem Technologies,* vol. 8, pp. 289-296, Aug 2002.

[102] Q. Zeng, F. Huang, and H. Tsuchida, "Numerical simulation of shock response of a hard disk drive at operational state," in *Magnetics Conference, 2005. INTERMAG Asia 2005. Digests of the IEEE International*, 2005, pp. 117 - 118.

[103] E. M. Jayson, J. M. Murphy, P. W. Smith, and F. E. Talke, "Shock and head slap simulations of operational and nonoperational hard disk drives," *IEEE Transactions on Magnetics,* vol. 38, pp. 2150-2152, 2002.

[104] Q. H. Zeng, F. Y. Huang, and H. Tsuchida, "Numerical simulation of shock response of a hard disk drive at operational state," in *Magnetics Conference, 2005. INTERMAG Asia 2005. Digests of the IEEE International*, 2005, pp. 117-118.

[105] E. M. Jayson and F. E. Talke, "Optimization of Air Bearing Contours for Shock Performance of a Hard Disk Drive," *ASME Journal of Tribology,* vol. 127, pp. 878-883, 2005.

[106] P. Bhargava and D. B. Bogy, "Effect of Shock Pulse Width on the Shock Response of Small Form Factor Drives," in *ASME/JSME Joint Conference on Micromechatronics for Information and Precision Equipment (MIPE 2006)*, Santa Clara, 2006.

[107] Hitachi, "Track, Areal, Linear Density Perspective," *HDD Technology Overview* Retrieved Nov 19, 2007, from http://www.hitachigst.com/hdd/technolo/overview/chart02.html

[108] K. Usui, M. Kisaka, A. Okuyama, and M. Nagashima, "Reduction of external vibration in hard disk drives using adaptive feed-forward control with single shock sensor," Istanbul, Turkey, 2006, pp. 138-142.

[109] S. Cao, Q. Bi, M. Ding, J. Wang, and K. Ooi, "Effective low frequency disturbance feed forward compensation scheme for mobile HDD application," Singapore, Singapore, 2006, p. 4150382.

[110] R. Oboe, "Use of MEMS based accelerometers in hard disk drives," Como, 2001, pp. 1142-1147.

[111] J. Zheng, C. Du, X. Guo, Y. Wang, J. Zhang, Q. Li, and B. Hredzak, "Phase lead peak filter method to high TPI servo track writer with microactuators," Minneapolis, MN, United States, 2006, pp. 1309-1314.

[112] H. Fujimoto, K. Fukushima, and S. Nakagawa, "Vibration suppression short-span seeking of HDD with multirate feedforward control," Minneapolis, MN, United States, 2006, pp. 582-587.

[113] J. Stoev, K. Cho, J.-S. Shim, and H. S. Lee, "Free fall detection algotithms for hard disk drives," Busan, South Korea, 2006, pp. 2760-2764.

[114] D. S. Lee, "Thermal accelerometer based predictive drop sensor," *Sensors and Actuators, A: Physical,* vol. 135, pp. 889-894, 2007.

[115] Balandin, Bolotnik, and Pilkey, "Review: optimal shock and vibration isolation.," *Shock & Vibration,* vol. 5, p. 73, 1998/// 1998.

[116] J. A. Macinante, "Free or Natural Vibrations," in *Seismic mountings for vibration isolation* New York: Wiley, 1984, pp. 145-176.

[117] P. A. Masterson, "The Basic of Vibration Isoation using Elastromeric Materials," *E-A-R Technical White Papers* Retrieved October 05, 2005, from http://www.earsc.com/HOME/engineering/TechnicalWhitePapers/Vibration/index.asp?SID=61

[118] J. Renninger, "Understanding Damping Techniques for Noise and Vibration Control," *E-A-R Technical White Papers* Retrieved October 06, 2005, from http://www.earsc.com/HOME/engineering/TechnicalWhitePapers/UnderstandingDamping/index.asp?SID=62

[119] P. A. Masterson, "Shock Control for Portable Electronics," *E-A-R Technical White Papers* Retrieved October 06, 2005, from http://www.earsc.com/HOME-Electronic/Engineering/TechnicalReference/TechnicalWhitePapers/ShockControlforPortableElectronics/index.asp?SID=250

[120] P. A. Masterson, "Damping Effects on Shock Response Spectra: 2.5-inch Hard Disk Drives," *E-A-R Technical White Papers* Retrieved October 06, 2005, from http://www.earsc.com/cmsPage/DampingEffectsonShockResponseSpectra2.5-inchHardDiskDrives.asp

[121] P. A. Masterson, "Damping Effects on Shock Response Spectra: 1.8-inch Hard Disk Drives," *E-A-R Technical White Papers* Retrieved October 06, 2005, from http://www.earsc.com/pdfs/Dampingeffects1.8hddFinal.pdf

[122] Balandin, Bolotnik, and Pilkey, "On the optimal shock isolation of a system with one and a half degrees of freedom.," *Shock & Vibration,* vol. 6, p. 159, 1999/// 1999.

[123] S. J. Hwang, "Noise and Vibration Control Technology in Hard Disk Drives," 2004, from http://www.semiconductorfabtech.com/olddatatech/explore/downloads/01.099.pdf

[124] R. B. Gifford, M. C. Strzepa, T. E. MacDonald, and F. W. Bernett, "Damping configuration for improved disk drive performance," US, 1996.

[125] D. T. Landin and S.-L. Hwang, "Constrained layer damper with slits and/or cutouts," US, 1998.

[126] T. Jintanawan, I. Y. Shen, and K. Tanaka, "Vibration analysis of fluid dynamic bearing spindles with rotating-shaft design," *IEEE Transactions on Magnetics,* vol. 37, pp. 799-804, 2001.

[127] C.-W. Tseng, J.-Y. Shen, and I. Y. Shen, "Vibration of Rotating-Shaft HDD Spindle Motors with Flexible Stationary Parts," *IEEE Transactions on Magnetics,* vol. 39, pp. 794-799, 2003.

[128] M. Miwa, H. Miyazaki, R. Kaneko, and H. Unozawa, "Evaluation of fluid dynamic bearing spindle by vibration base," *IEEE Transactions on Magnetics,* vol. 41, pp. 763-768, 2005.

[129] G. H. Jang, J. H. Han, and C. H. Seo, "Finite element modal analysis of a rotating disk–spindle system in a HDD with hydrodynamic bearings considering the flexibility of a complicated supporting structure," *Microsystem Technologies,* vol. 11, pp. 488-498, 2005.

[130] B. Heo and I. Y. Shen, "A parametric study on rocking vibration of hard disk drive spindle motors with fluid-dynamic bearings and rotating-shaft design," *Microsystem Technologies,* vol. 11, pp. 1204-1213, 2005.

[131] J. S. McAllister, "The effect of disk platter resonances on track misregistration in 3.5 inch disk drives," *IEEE Transactions on Magnetics,* vol. 32, pp. 1762-1766, 1996.

[132] A. Sueoka, T. Ayabe, T. Kurahachi, and K. Ohishi, "Vibration Control of a Rotating-Disk Subjected to a Periodic External Force by Dynamic Absorbers," *Jsme International Journal Series Iii-Vibration Control Engineering Engineering for Industry,* vol. 35, pp. 41-49, Mar 1992.

[133] V. Thaveeprungsriporn, K. Sittipongpanich, P. Imoeb, and M. Chayapancha, "Enhancing suspension performance with 3-ply laminated load beam," in *Asia-Pacific Magnetic Recording Conference* Singapore, 2002, pp. 22-02.

[134] L. Xu, S. Zeng, N. Guo, and R. Lin, "Passive vibration control of the head actuator assembly in hard disk drive," Pittsburgh, PA, United States, 2001, pp. 2285-2291.

[135] S. Jin-Seung, H. Min-Pyo, L. Haeng-Soo, and C. Sung-Hoon, "Strategies for improvement of shock performance in hard disk drives," *Journal of Information Storage and Processing Systems,* vol. 3, pp. 229-36, 2001.

[136] T. H. Yan and R. M. Lin, "Dual-mass dynamic absorber for the head actuator assembly in hard disk drives," *Mechanics Based Design of Structures and Machines,* vol. 32, pp. 119-132, 2004.

[137] N. Igata, "Applications of High Damping Stainless Alloy (HIDAS)," *Key Engineering Materials,* vol. 319, pp. 209-216, 2006.

[138] L. Yanning and X. Yanchu, "Dynamics analysis of constrained layer damping treated covers for hard disk drives," in *SPIE - Int. Soc. Opt. Eng.*, San Diego, CA, USA, 2002, pp. 51-62.

[139] S. C. Lim and S. B. Choi, "Vibration control of an HDD disk-spindle system using piezoelectric bimorph shunt damping: II. Optimal design and shunt damping implementation," *Smart Materials and Structures,* vol. 16, pp. 901-908, 2007.

[140] S. C. Lim and S. B. Choi, "Vibration control of an HDD disk-spindle system utilizing piezoelectric bimorph shunt damping: I. Dynamic analysis and modeling of the shunted drive," *Smart Materials and Structures,* vol. 16, pp. 891-900, 2007.

[141] F. F. Yap and N. Vahdati, "Analysis of Vibration Tolerance Level of Hard Disk Drives," Singapore Technology, Singapore April 2004.

[142] N. W. Kim, K. W. Kim, J. R. Lim, and W. Y. Kim, "Numerical simulation and experiment of an antivibration design of slim optical disk drives," *Journal of Information Storage and Processing Systems,* vol. 1, pp. 351-356, Dec 1999.

[143] L. Seungho, C. Young-Bae, P. No-Cheol, and P. Young-Pil, "Optimal design of rubber mounts supporting notebook HDD for shock and vibration isolation," in *Asia-Pacific Magnetic Recording Conference* Singapore, 2006, p. 2 pp.

[144] I. J. Silverman and T. Papadopoulos, "Shock Mount for Hard Disk Drive in a Portable Computer," US: Fujitsu Personal Computer System, Inc., Santa Clara, CA, (US), 1999, p. 10.

[145] M. Liu, F. F. Yap, and H. Harmoko, "Shock response analysis of hard disk drive using flexible multibody dynamics formulation," *Microsystem Technologies,* vol. 13, pp. 1039-1045, May 2007.

[146] H. Harmoko, F. F. Yap, N. Vahdati, S. Gan, and L. Mengjun, "Investigation of effect of various components in HDD on the shock tolerance," in *2006 ASME/JSME Joint Conference on Micromechatronics for Information and Precision Equipment (MIPE 2006)*, Santa Clara, California, USA, 2006.

[147] S. S. Rao, *Mechanical vibrations*, 4th ed. Upper Saddle River, N.J.: Pearson/Prentice Hall, 2004.

[148] V. Chudnovsky, D. Kennedy, A. Mukherjee, and J. Wendlandt, "Modeling Flexible Bodies in SimMechanics and Simulink," *MATLAB Digest* Retrieved May 16, 2006, from http://www.mathworks.com/company/newsletters/digest/2006/may/simmechanics.html?s_cid=MLD0506rowTA2

[149] D. J. Ewins, *Modal testing : theory, practice, and application*, 2nd ed. Taunton, Somerset, England, New York: Research Studies Press; Wiley, 2000.

[150] J. Lau, "HSA modeling," H. Harmoko, Ed. Singapore: Seagate Technology International, 2007.

[151] Y. P. Yang and C. C. Kuo, "Passive and active design of hard disk suspension assemblies using multiobjective optimization techniques," *Computer Methods in Applied Mechanics and Engineering,* vol. 145, pp. 147-166, Jun 15 1997.

[152] O. Ryota, T. Kazuhiro, I. Kenichiro, W. Shigeru, I. Takayuki, and T. Kazuo, "Modal Analysis of HDD's Actuators," *Fujikura Technical Review,* pp. 7-12, 2002.

[153] G. H. Lin, R. Barndt, H. N. Bertram, and J. K. Wolf, "Experimental studies of nonlinearities in high density disk recording," *IEEE Transactions on Magnetics,* vol. 28, pp. 3279-3281, 1992.

[154] B. H. Thornton and D. B. Bogy, "A parametric study of head-disk interface instability due to intermolecular forces," *IEEE Transactions on Magnetics,* vol. 40, pp. 337-344, 2004.

[155] B. H. Thornton and D. B. Bogy, "Head-disk interface dynamic instability due to intermolecular forces," *IEEE Transactions on Magnetics,* vol. 39, pp. 2420-2422, 2003.

[156] Y.A. Chernopyatov, C.M. Lee2, W.J. Chung, and K. S. Dolotov, "A Study on the Influence of Nonlinearity Coefficients in Air-Bearing Spindle Parametric Vibration," *International Journal of Precision Engineering and Manufacturing,* vol. 6, pp. 51-58, 2005.

[157] A. Minikes and I. Bucher, "Comparing numerical and analytical solutions for squeeze-film levitation force," *Journal of Fluids and Structures,* vol. 22, pp. 713-719, 2006.

[158] F. F. Yap, H. Harmoko, M. Liu, and N. Vahdati, "Modeling of hard disk drives for shock and vibration analysis – consideration of nonlinearities and discontinuities," *Nonlinear Dynamics,* vol. 50, pp. 717-731, 2007.

[159] D. Chen and D. B. Bogy, "Dynamics of Partial Contact Head Disk Interface," *IEEE Transactions on Magnetics,* vol. 43, pp. 2220-2222, 2007.

[160] X. Li, "Numerical simulation of slider air bearing in Head-Disk Interface System Based on a Mesh-free Method," in *School of Mechanical & Aerospace Engineering* Singapore: Nanyang Technological University, 2006.

[161] E. M. Jayson, "Numerical and experimental investigations of a hard disk drive subject to shock and vibration," San Diego: University of Calfornia, 2003.

[162] S. Fukui and R. kaneko, "Analysis of ultra-thin gas film lubrication based on linearized Boltzmann equation: First report -- derivation of a generalized lubrication equation including thermal creep flow," *ASME Journal of Tribology,* vol. 110, pp. 253-262, 1988.

[163] S. Fukui and R. Kaneko, "Analysis of flying characteristics of magnetic heads with ultra-thin spacings based on the Boltzmann equation," in *Fourth Joint Magnetism and Magnetic Materials - INTERMAG Conference, 12-15 July 1988*

IEEE Transactions on Magnetics, Vancouver, BC, USA, 1988, pp. 2751-3.

[164] J. A. Francis, L. G. Alejandro, and J. A. Berni, "Direct simulation Monte Carlo for thin-film bearings," *Physics of Fluids,* vol. 6, pp. 3854-3860, 1994.

[165] D. Chen and D. B. Bogy, "Intermolecular force and surface roughness models for air bearing simulations for sub-5 nm flying height sliders," *Microsystem Technologies,* vol. 13, pp. 1211-1217, May 2007.

[166] L. Wu, "Physical modeling and numerical simulations of the slider air bearing problem of hard disk drives," Berkeley: University of California at Berkeley, 2001.

[167] Patankar, *Numerical Heat Tranfer and Fluid Flow*. New York: McGraw-Hill, 1980.

[168] L. F. Shampine and M. W. Reichelt, "The MATLAB ODE Suite," *SIAM Journal on Scientific Computing,* vol. Vol. 18, pp. 1-22, 1997.

[169] DODSTD, "Method 514.4," in *MIL-STD-810E*. vol. Issue DW9901 USA: Information Handling Services, 1989, p. 1 to A88.

[170] X. Liu, W. Clegg, and B. Liu, "Normal incidence polarization interferometer for measuring flying height of magnetic heads," *IEEE Transactions on Magnetics,* vol. 35, pp. 2457-2459, 1999.

[171] W. Clegg, X. Liu, B. Liu, A. Li, C. Chong, and D. Jenkins, "Normal incidence polarization interferometry flying height testing," San Antonio, TX, USA, 2001, pp. 1941-3.

[172] J. Zhou, Y. Ma, B. Liu, Q. Leng, M. Matsumoto, and J. Xu, "Flying height-attitude observation and investigation of sliders in load/unload process," Amsterdam, Netherlands, 2002, pp. 2123-2125.

[173] Y. S. Ma, B. Liu, W. J. Wang, and K. D. Ye, "Slider-bump contact and flying height calibration," *Tribology Letters,* vol. 23, pp. 83-91, 2006.

[174] T. Kita, K. Kogure, Y. Mitsuya, and T. Nakanishi, "New method of detecting contact between floating-head and disk," Boston, MA, USA, 1980, pp. 873-5.

[175] Q. H. Zeng, M. Chapin, and D. B. Bogy, "Two calibration methods of AE measurement channels for slider-disk contact detection," Kyongju, South Korea, 1999, pp. 2367-9.

[176] J. Kishigami, T. Ohkubo, and Y. Koshimoto, "An experimental investigation of contact characteristics between a slider and medium using the electrical resistance method," Brighton, UK, 1990, pp. 2205-7.

[177] B. K. Clark, "An experimental correlation of slider-disk contact detection between piezoelectric and electrical resistance measurements," Pittsburgh, PA, USA, 1991, pp. 5151-3.

[178] T. G. Jeong and D. B. Bogy, "Natural frequencies of sliders and transducers used to detect slider-disk contacts," Washington, DC, USA, 1989, pp. 3725-7.

[179] C. A. Briggs and F. E. Talke, "The dynamics of `micro' sliders using laser Doppler vibrometry," Brighton, UK, 1990, pp. 2442-4.

[180] T. G. Jeong and D. B. Bogy, "Measurements of slider-disk contacts during dynamic load-unload," Pittsburgh, PA, USA, 1991, pp. 5073-5.

[181] Q. H. Zeng and D. B. Bogy, "Experimental evaluation of stiffness and damping of slider-air bearings in hard disk drives," Toronto, Can, 1998, pp. 1-6.

[182] B. Feliss, A. N. Murthy, and F. E. Talke, "Microdrive operational and non-operational shock and vibration testing," *Microsystem Technologies,* 2007.

[183] J. Xu, Y. Shimizu, and L. Su, "Drive level measurement of flying height modulation and control of slider disk contact," *Tribology Letters,* vol. 24, pp. 159-162, 2006.

[184] Terang, "Experimental Investigation of HDD Shock Tolerance," H. Harmoko, Ed. Singapore: Seagate Technology International, 2007.

APPENDIX A: ADDITIONAL DETAILS ON FLEXIBLE MULTI-BODY DYNAMICS FORMULATION

In order to enhance the flexible multi-body dynamics formulations presented in Chapter 3, the detail formulas of the transformation matrix, the mass matrix, and the quadratic velocity vector are described in this appendix.

The appendix is divided into three main parts. The first part covers the development of the transformation matrix based on a successive rotations method, called Euler Angles. The last two parts contain the details on mass matrix and quadratic velocity vector formulations.

A.1 *Transformation Matrix*

A set of reference frames is defined in. The inertial frame XYZ has point O as the origin and has unit vectors of **I**, **J**, and **K**. The rotation sequence of Euler angles θ_x, θ_y and θ_z are selected as (1) θ_x about X axis followed by intermediate coordinates xyz; (2) θ_y about y axis followed by intermediate coordinates $x'y'z'$ which is non-spinning and also called rocking frame; (3) θ_z about z' axis followed by coordinates $x''y''z''$ which is body-fixed to the flexible body. It has point D_i as the origin and has unit vectors of $\mathbf{i}''$, $\mathbf{j}''$ and $\mathbf{k}''$.

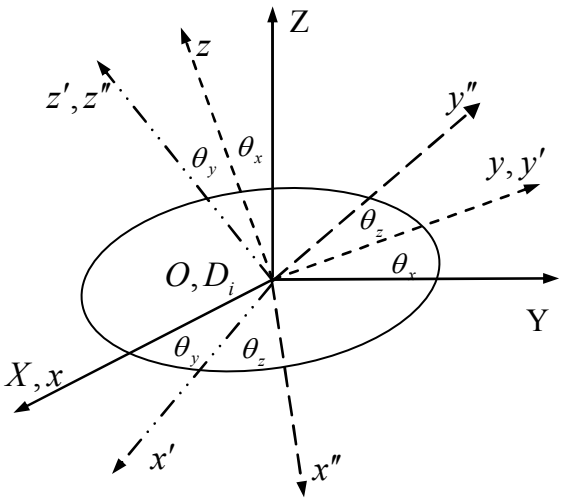

FIGURE A.1 DEFINITION OF FRAMES OF REFERENCE

(1) θ_x about $X \rightarrow xyz$ (2) θ_y about y axis$\rightarrow x'y'z'$ (3) θ_z about z'axis$\rightarrow x''y''z''$

The rocking coordinates $x'y'z'$ and the coordinates $x''y''z''$ body-fixed are related to the inertial coordinates XYZ through the following transformation matrices,

$$\begin{Bmatrix} x' \\ y' \\ z' \end{Bmatrix} = \mathbf{A}_{\text{temp}} \begin{Bmatrix} X \\ Y \\ Z \end{Bmatrix} \tag{A.1}$$

$$\begin{Bmatrix} x'' \\ y'' \\ z'' \end{Bmatrix} = \mathbf{A} \begin{Bmatrix} X \\ Y \\ Z \end{Bmatrix} \tag{A.2}$$

with

$$\mathbf{A}_{\text{temp}} = \begin{bmatrix} \cos\theta_y & \sin\theta_x \sin\theta_y & -\cos\theta_x \sin\theta_y \\ 0 & \cos\theta_x & \sin\theta_x \\ \sin\theta_y & -\sin\theta_x \cos\theta_y & \cos\theta_x \cos\theta_y \end{bmatrix} \tag{A.3}$$

$$\mathbf{A} = \begin{bmatrix} \cos\theta_y \cos\theta_z & \sin\theta_x \sin\theta_y \cos\theta_z + \cos\theta_x \sin\theta_z & -\cos\theta_x \sin\theta_y \cos\theta_z + \sin\theta_x \sin\theta_z \\ -\cos\theta_y \sin\theta_z & -\sin\theta_x \sin\theta_y \sin\theta_z + \cos\theta_x \cos\theta_z & \cos\theta_x \sin\theta_y \sin\theta_z + \sin\theta_x \cos\theta_z \\ \sin\theta_y & -\sin\theta_x \cos\theta_y & \cos\theta_x \cos\theta_y \end{bmatrix} \tag{A.4}$$

A.2 *Mass Matrix Formulations*

A time- and space-dependent matrix $\mathbf{L}^i$ in (3.7) and the partial derivatives $\mathbf{B}^i$ in (3.19) are first formulated below.

$$\mathbf{L}^i = [\mathbf{I} \quad \mathbf{B}^i \quad \mathbf{A}^i\mathbf{S}^i] \tag{A.5}$$

$$\mathbf{B}^i = -\mathbf{A}^i\mathbf{u}^i\mathbf{G}^i \tag{A.6}$$

where $\mathbf{S}^i$ is space-dependent shape matrix, $\mathbf{u}^i$ is local position of arbitrary point P expressed in local body coordinate $x''y''z''$ (as described in Figure A.2).

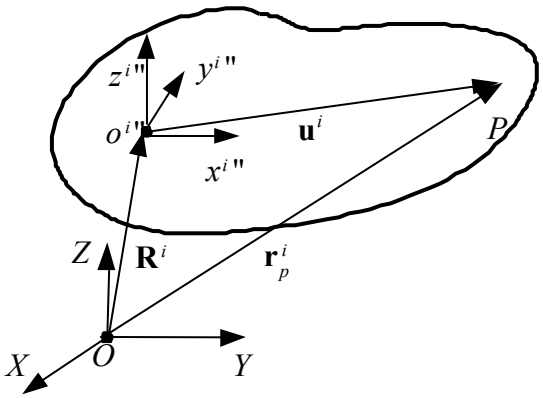

FIGURE A.2 DISPLACEMENT VECTOR OF ARBITRARY POINT *P* ON ONE FLEXIBLE BODY IN THE HDD

The skew symmetric matrix $\tilde{\mathbf{u}}^i$ is defined by

$$\tilde{\mathbf{u}}^i = \begin{bmatrix} 0 & -u_3^i & u_2^i \\ u_3^i & 0 & -u_1^i \\ -u_2^i & u_1^i & 0 \end{bmatrix} \tag{A.7}$$

u_1^i, u_2^i, u_3^i are the components of vector $\mathbf{u}^i$. $\mathbf{G}^i$ is given by

$$\mathbf{G}^i = \begin{bmatrix} \cos\theta_y \cos\theta_z & \sin\theta_z & 0 \\ -\cos\theta_y \sin\theta_z & \cos\theta_z & 0 \\ \sin\theta_y & 0 & 1 \end{bmatrix} \tag{A.8}$$

The mass matrix **M** formulation is as follows

$$\mathbf{M}^i = \int_{V^i} \rho^i \mathbf{L}^{iT} \mathbf{L}^i dV^i$$

$$= \int_{V^i} \rho^i \begin{bmatrix} \mathbf{I} \\ \mathbf{B}^{iT} \\ (\mathbf{A}^i\mathbf{S}^i)^T \end{bmatrix} \begin{bmatrix} \mathbf{I} & \mathbf{B}^i & \mathbf{A}^i\mathbf{S}^i \end{bmatrix} dV^i = \int_{V^i} \rho^i \begin{bmatrix} \mathbf{I} & \mathbf{B}^i & \mathbf{A}^i\mathbf{S}^i \\ & \mathbf{B}^{iT}\mathbf{B}^i & \mathbf{B}^{iT}\mathbf{A}^i\mathbf{S}^i \\ \text{symmetric} & & \mathbf{S}^{iT}\mathbf{S}^i \end{bmatrix} dV^i \quad \text{(A.9)}$$

In symbolic form

$$\mathbf{M}^i = \begin{bmatrix} \mathbf{M}^i_{RR} & \mathbf{M}^i_{R\theta} & \mathbf{M}^i_{Rf} \\ & \mathbf{M}^i_{\theta\theta} & \mathbf{M}^i_{\theta f} \\ \text{symmetric} & & \mathbf{M}^i_{ff} \end{bmatrix} \quad \text{(A.10)}$$

where

$$\mathbf{M}^i_{RR} = \begin{bmatrix} m^i & 0 & 0 \\ 0 & m^i & 0 \\ 0 & 0 & m^i \end{bmatrix}_{3\times 3} \quad \text{(A.11)}$$

$$\mathbf{M}^i_{R\theta} = -\mathbf{A}^i\tilde{\mathbf{S}}^i_t\mathbf{G}^i \quad \text{(A.12)}$$

in which

$$\tilde{\tilde{\mathbf{S}}}^i_t = \int_{V_i} \rho^i \tilde{\mathbf{u}}^i dV^i = \begin{bmatrix} 0 & -s^i_3 & s_2 \\ s^i_3 & 0 & -s^i_1 \\ -s^i_2 & s^i_1 & 0 \end{bmatrix}, \quad s^i_k = \int_{V_i} \rho^i u^i_k dV^i \quad k = 1,2,3 \quad \text{(A.13)}$$

or in vector form

$$\tilde{\tilde{\mathbf{S}}}^i_t = \int_{V_i} \rho^i \mathbf{u}^i dV^i = \int_{V_i} \rho^i \left[\mathbf{u}^i_o + \mathbf{S}^i\mathbf{q}^i_f \right] dV^i \quad \text{(A.14)}$$

where $\mathbf{u}^i_o$ is the position of point *P* in the undeformed state in the body reference and $\mathbf{q}^i_f$ is vector of time-dependent elastic generalized coordinates known as modal coordinates.

To obtain $\tilde{\bar{\mathbf{S}}}_t^i$, the following inertia shape integrals needs to be evaluated:

$$\bar{\mathbf{S}}^i = \int_{V_i} \rho^i \mathbf{S}^i dV^i \tag{A.15}$$

$\bar{\mathbf{S}}^i$ is also needed when calculate the matrix $\mathbf{M}_{Rf}^i$.

$$\mathbf{M}_{Rf}^i = \mathbf{A}^i \int_{V_i} \rho^i \mathbf{S}^i dV^i = \mathbf{A}^i \bar{\mathbf{S}}^i \tag{A.16}$$

$$\mathbf{M}_{\theta\theta}^i = \mathbf{G}^{i\mathrm{T}} \left[\int_{V_i} \rho^i \tilde{\bar{\mathbf{u}}}^{i\mathrm{T}} \tilde{\bar{\mathbf{u}}}^i dV^i \right] \mathbf{G}^i = \mathbf{G}^{i\mathrm{T}} \bar{\mathbf{I}}_{\theta\theta}^i \mathbf{G}^i \tag{A.17}$$

where $\bar{\mathbf{I}}_{\theta\theta}^i$ is called the inertia tensor of the deformable body *i* and is defined as:

$$\bar{\mathbf{I}}_{\theta\theta}^i = \int_{V_i} \rho^i \tilde{\mathbf{u}}^{iT} \tilde{\mathbf{u}}^i dV^i = \int_{V_i} \rho^i \begin{bmatrix} u_2^{i2} + u_3^{i2} & -u_2^i u_1^i & -u_3^i u_1^i \\ & u_1^{i2} + u_3^{i2} & -u_3^i u_2^i \\ \text{symmetric} & & u_1^{i2} + u_2^{i2} \end{bmatrix} dV^i \tag{A.18}$$

$\bar{u}_k^{i2} + \bar{u}_l^{i2}$ and $\bar{u}_k^i \bar{u}_l^i$ for $k, l = 1, 2, 3$ can be expressed as follows.

$$\begin{aligned} u_k^{i2} + u_l^{i2} &= (u_{k0}^i + \mathbf{S}_k^i \mathbf{q}_f^i)^2 + (u_{l0}^i + \mathbf{S}_l^i \mathbf{q}_f^i)^2 \\ &= u_{k0}^{i2} + 2u_{k0}^i \mathbf{S}_k^i \mathbf{q}_f^i + \mathbf{S}_k^i \mathbf{q}_f^i \mathbf{S}_k^i \mathbf{q}_f^i + u_{l0}^{i2} + 2u_{l0}^i \mathbf{S}_l^i \mathbf{q}_f^i + \mathbf{S}_l^i \mathbf{q}_f^i \mathbf{S}_l^i \mathbf{q}_f^i \\ &= (u_{k0}^{i2} + u_{l0}^{i2}) + 2(u_{k0}^i \mathbf{S}_k^i + u_{l0}^i \mathbf{S}_l^i) \mathbf{q}_f^i + \mathbf{q}_f^{iT} (\mathbf{S}_k^{iT} \mathbf{S}_k^i + \mathbf{S}_l^{iT} \mathbf{S}_l^i) \mathbf{q}_f^i \end{aligned} \tag{A.19}$$

$$\begin{aligned} u_k^i u_l^i &= (u_{k0}^i + \mathbf{S}_k^i \mathbf{q}_f^i)(u_{l0}^i + \mathbf{S}_l^i \mathbf{q}_f^i) \\ &= u_{k0}^i u_{l0}^i + u_{k0}^i \mathbf{S}_l^i \mathbf{q}_f^i + u_{l0}^i \mathbf{S}_k^i \mathbf{q}_f^i + \mathbf{S}_k^i \mathbf{q}_f^i \mathbf{S}_l^i \mathbf{q}_f^i \\ &= u_{k0}^i u_{l0}^i + (u_{k0}^i \mathbf{S}_l^i + u_{l0}^i \mathbf{S}_k^i) \mathbf{q}_f^i + \mathbf{q}_f^{iT} \mathbf{S}_k^{iT} \mathbf{S}_l^i \mathbf{q}_f^i \end{aligned} \tag{A.20}$$

where $\mathbf{S}_k^i$ and $\mathbf{S}_l^i$ is the k^{th} row and l^{th} row of the body shape function $\mathbf{S}^i$, respectively ($\mathbf{S}_1^i$ is the body shape function in x"- axis, $\mathbf{S}_2^i$ is the body shape function in y"- axis, and $\mathbf{S}_3^i$ is the body shape function in z"- axis). u_{10}^i, u_{20}^i, and u_{30}^i are the components of vector $\mathbf{u}_0^i$.

In the evaluation of the inertia tensor, the following inertia shape integrals can be defined.

$$I_{kl}^i = \int_{V_i} \rho^i u_{k0}^i u_{l0}^i dV^i \tag{A.21}$$

$$\overline{\mathbf{I}}_{kl}^{i} = \int_{V_i} \rho^i u_{k0}^i \mathbf{S}_l^i dV^i \tag{A.22}$$

$$\overline{\mathbf{S}}_{kl}^{i} = \int_{V_i} \rho^i \mathbf{S}_k^{iT} \mathbf{S}_l^i dV^i \tag{A.23}$$

The (A.21), (A.22), and (A.23) are also used in evaluating $\mathbf{M}_{\theta f}^i$.

$$\mathbf{M}_{\theta f}^i = \mathbf{G}^{i\mathrm{T}} \overline{\mathbf{I}}_{\theta f}^i \tag{A.24}$$

in which

$$\overline{\mathbf{I}}_{\theta f}^i = \int_{V_i} \rho^i \begin{bmatrix} u_2^i \mathbf{S}_3^i - u_3^i \mathbf{S}_2^i \\ u_3^i \mathbf{S}_1^i - u_1^i \mathbf{S}_3^i \\ u_1^i \mathbf{S}_2^i - u_2^i \mathbf{S}_1^i \end{bmatrix} dV^i = \begin{bmatrix} \mathbf{q}_f^{iT} (\overline{\mathbf{S}}_{23}^i - \overline{\mathbf{S}}_{23}^{iT}) \\ \mathbf{q}_f^{iT} (\overline{\mathbf{S}}_{31}^i - \overline{\mathbf{S}}_{31}^{iT}) \\ \mathbf{q}_f^{iT} (\overline{\mathbf{S}}_{12}^i - \overline{\mathbf{S}}_{12}^{iT}) \end{bmatrix} + \begin{bmatrix} \overline{\mathbf{I}}_{23}^i - \overline{\mathbf{I}}_{32}^i \\ \overline{\mathbf{I}}_{31}^i - \overline{\mathbf{I}}_{13}^i \\ \overline{\mathbf{I}}_{12}^i - \overline{\mathbf{I}}_{21}^i \end{bmatrix} \tag{A.25}$$

$\mathbf{M}_{ff}^i$ is a constant matrix and defined by

$$\mathbf{M}_{ff}^i = \int_{V_i} \rho^i \mathbf{S}^{iT} \mathbf{S}^i dV^i = \overline{\mathbf{S}}_{11}^i + \overline{\mathbf{S}}_{22}^i + \overline{\mathbf{S}}_{33}^i \tag{A.26}$$

A.3 *Quadratic Velocity Vector Formulation*

Quadric velocity vector is defined as

$$\mathbf{Q}_v^i = \begin{bmatrix} \mathbf{Q}_{vR}^i & \mathbf{Q}_{v\theta}^i & \mathbf{Q}_{vf}^i \end{bmatrix}^{\mathrm{T}} \tag{A.27}$$

where

$$\mathbf{Q}_{vR}^i = -\mathbf{A}^i \left[\tilde{\boldsymbol{\omega}}^{i2} \overline{\mathbf{S}}_t^i + 2\tilde{\boldsymbol{\omega}}^i \overline{\mathbf{S}}^i \dot{\mathbf{q}}_f^i + \overline{\mathbf{S}}_t^i \dot{\mathbf{G}}^i \dot{\boldsymbol{\theta}} \right] \tag{A.28}$$

$$\mathbf{Q}_{v\theta}^i = -2\dot{\mathbf{G}}^{i\mathrm{T}} \overline{\mathbf{I}}_{\theta\theta}^i \boldsymbol{\omega}^i - 2\dot{\mathbf{G}}^{i\mathrm{T}} \overline{\mathbf{I}}_{\theta f}^i \dot{\mathbf{q}}_f^i - \mathbf{G}^{i\mathrm{T}} \dot{\overline{\mathbf{I}}}_{\theta\theta}^i \boldsymbol{\omega}^i - \mathbf{G}^{\mathrm{T}} \overline{\mathbf{I}}_{\theta\theta}^i \dot{\mathbf{G}}^i \dot{\boldsymbol{\theta}} \tag{A.29}$$

$$\mathbf{Q}_{vf}^i = -\int_{V_i} \rho^i \mathbf{S}^{i\mathrm{T}} \left[(\tilde{\boldsymbol{\omega}}^i)^2 \mathbf{u}^i + 2\tilde{\boldsymbol{\omega}}^i \dot{\mathbf{u}}_f^i \right] dV^i - \overline{\mathbf{I}}_{\theta f}^{i\ \mathrm{T}} \dot{\mathbf{G}}^i \dot{\boldsymbol{\theta}} \tag{A.30}$$

in which

$$\dot{\bar{\mathbf{G}}}^i = \begin{bmatrix} -\sin\theta_y \cos\theta_z \dot{\theta}_y - \cos\theta_y \sin\theta_z \dot{\theta}_z & \cos\theta_z \dot{\theta}_z & 0 \\ \sin\theta_y \sin\theta_z \dot{\theta}_y - \cos\theta_y \cos\theta_z \dot{\theta}_z & -\sin\theta_z \dot{\theta}_z & 0 \\ \cos\theta_y \dot{\theta}_y & 0 & 0 \end{bmatrix} \tag{A.31}$$

$$\dot{\boldsymbol{\theta}} = \begin{bmatrix} \dot{\theta}_x & \dot{\theta}_y & \dot{\theta}_z \end{bmatrix}^{\mathrm{T}} \tag{A.32}$$

$$\begin{aligned} \boldsymbol{\omega}^i &= \begin{bmatrix} \omega_1 & \omega_2 & \omega_3 \end{bmatrix}^{\mathrm{T}} = \mathbf{G}\dot{\boldsymbol{\theta}} \\ &= \begin{bmatrix} \dot{\theta}_x \cos\theta_y \cos\theta_z + \dot{\theta}_y \sin\theta_z \\ -\dot{\theta}_x \cos\theta_y \sin\theta_z + \dot{\theta}_y \cos\theta_z \\ \dot{\theta}_x \sin\theta_y + \dot{\theta}_z \end{bmatrix} \end{aligned} \tag{A.33}$$

$$\tilde{\boldsymbol{\omega}}^i = \begin{bmatrix} 0 & -\omega_3^i & \omega_2^i \\ \omega_3^i & 0 & -\omega_1^i \\ -\omega_2^i & \omega_1^i & 0 \end{bmatrix} \tag{A.34}$$